REPORT DOCUMENTATION PAGE

AFRL-SR-BL-TR-98-

ር 752

1. AGENCY USE ONLY (Leave Blank)	2. REPORT DATE 1991	3. REPOR... ...AND DATES COVERED Final

4. TITLE AND SUBTITLE
On the Application and Interpretation of Coherent Motion Detectors

5. FUNDING NUMBERS

6. AUTHORS
Charles Paul Gendrich

7. PERFORMING ORGANIZATION NAME(S) AND ADDRESS(ES)
Michigan State University

8. PERFORMING ORGANIZATION REPORT NUMBER

9. SPONSORING/MONITORING AGENCY NAME(S) AND ADDRESS(ES)
AFOSR/NI
4040 Fairfax Dr, Suite 500
Arlington, VA 22203-1613

10. SPONSORING/MONITORING AGENCY REPORT NUMBER

11. SUPPLEMENTARY NOTES

12a. DISTRIBUTION AVAILABILITY STATEMENT
Approved for Public Release

12b. DISTRIBUTION CODE

13. ABSTRACT *(Maximum 200 words)*
See Attachment

14. SUBJECT TERMS

15. NUMBER OF PAGES

16. PRICE CODE

17. SECURITY CLASSIFICATION OF REPORT	18. SECURITY CLASSIFICATION OF THIS PAGE	19. SECURITY CLASSIFICATION OF ABSTRACT	20. LIMITATION OF ABSTRACT
Unclassified	Unclassified	Unclassified	UL

DTIC QUALITY INSPECTED 3

ON THE APPLICATION AND INTERPRETATION
OF COHERENT MOTION DETECTORS

By

Charles Paul Gendrich

A THESIS

Submitted to
Michigan State University
in partial fulfillment of the requirements
for the degree of

MASTER OF SCIENCE

Department of Mechanical Engineering

1991

ABSTRACT

ON THE APPLICATION AND INTERPRETATION
OF COHERENT MOTION DETECTORS

By

Charles P. Gendrich

Coherent motions are understood to play an important role in enhancing the momentum transport of turbulent wall-bounded shear flows, but determining whether or not a coherent motion is present in a given volume of space at a particular time is still a difficult task. Although most detection schemes were developed for use within a specific region above the wall, most are ultimately used throughout the entire boundary layer. Three different probe-based algorithms and three different visual detection schemes are applied to combined flow visualization and spanwise vorticity probe data taken in the near-wall region and at y/δ of 0.8. Several new performance parameters have been developed, and they are calculated along with most of the commonly used evaluation parameters as functions of detection threshold and Reynolds number or y^+. The one-to-one correspondence between probe-based detections and visual detections is also evaluated using two parameters already in common use and a new parameter, $P(T,t)$, which is based on the number of event overlaps as a function of time during an event. Inner, outer, and mixed variables are used whenever appropriate to scale all results, but only two Reynolds number-independent curves are found which describe the outer-region response of any detection algorithm as a function of threshold.

ACKNOWLEDGEMENTS

Table of Contents

LIST OF TABLES

LIST OF FIGURES

NOMENCLATURE

Notation	Interpretation
$\underline{A}$	"A" is a vector
$<a>$	a short time average of the quantity "a"
a'	indicates the long-time RMS of "a".
a^+	indicates "a" was normalized with U_τ and ν
a_∞	indicates the value of "a" in the free stream
$\tilde{a}$	indicates the total quantity "a"
A	capital "A" is the mean value of $\tilde{a}$
a	lower-case "a" is the fluctuating component of $\tilde{a}$
	$\tilde{a}(t) = A + a(t)$

Symbol	Interpretation
ν	kinematic viscosity
ρ	density
δ	the same as δ_{99}; the boundary layer thickness
θ	boundary layer momentum thickness
τ_{wall}	shear stress at the wall
$\underline{\omega}$	the vorticity vector
ω_x	the streamwise vorticity component
ω_y	the wall-normal vorticity component
ω_z	the spanwise vorticity component
f	mean event frequency
l^+	a length scale normalized with U_τ and ν
R_θ	Reynolds number based on U_τ, ν, and θ
t^+	time normalized with U_τ and ν
u	streamwise velocity component
$\underline{U}(\underline{X})$	the velocity vector as a function of position
U_τ	friction velocity, $\sqrt{\tau_{wall}/\rho}$
U_∞	free stream velocity
v	wall-normal velocity component
w	streamwise velocity component
x	streamwise coordinate (see Figure 2.2.1)
y	wall-normal coordinate (see Figure 2.2.1)
y^+	height above the wall normalized with U_τ and ν
z	spanwise coordinate (see Figure 2.2.1)

CHAPTER 1

INTRODUCTION

Since the introduction of the Reynolds-decomposed Navier-Stokes equations, researchers of turbulent flows have sought ways to predict values for the Reynolds stress, $-\rho\overline{uv}$, and thereby close the streamwise momentum equation. Some researchers have marked the flow and examined films of what transpires inside and outside the boundary layer. Visual studies by Kline, Reynolds, Schraub, and Runstadler (1967), Corino and Brodkey (1969), Kim, Kline, and Reynolds (1971), and others have shown that the majority of the turbulence production takes place during intermittently-occurring processes located primarily within the inner region of the boundary layer[1]. These events appeared to have a limited spatial extent and an organized velocity or vorticity field, so they were dubbed "coherent motions." For quantitative measurements researchers have used hot wires, hot films, LIPA, LDV, and many other techniques to obtain velocity time histories at one or more points within the flow. Studies of these time series by Blackwelder and Kaplan (1972), Wallace, Eckelmann and Brodkey (1972) followed by Willmarth and Lu (1973), Alfredsson and Johansson (1984), Luchik and Tiederman (1987), Falco and Gendrich (1989), and others have led to the development of numerous probe-based detection schemes which use fluctuating quantities like u, v, and uv to locate when turbulence-producing events occur. Combined

---

[1] In this study the outer or wake region of the boundary layer will refer to that region where $0.2 < y/\delta \leq 0.99$. The region between $0 \leq y/\delta \leq 0.2$ will be called the inner or wall region, and the region below $yU_\tau/\nu = 50$ will be called the near-wall region.

velocity and visual measurements have also been undertaken by Falco (1974, 1977), Bogard (1982), Lovett (1982), Signor (1982), and others to investigate the velocity and vorticity characteristics of visually detected events. All of these studies have in some way addressed the question, "What characterizes a class of events which is important to the production of turbulence in the boundary layer?"

"Coherent motions" are often thought to be associated with the production of negative uv, since quadrants 2 and 4 in the uv-plane provide the largest contributions to the long-time $\overline{uv}$ correlation. In a more general sense, a "coherent motion" is simply a convecting region in space which moves or rotates as a unit in a fashion different from the surrounding fluid. Each realization of a well-defined "coherent motion" generally has a recognizable spatial extent and organization, although random fluctuations in the surrounding fluid will cause differences between each realization. Laufer (1975) suggests that the presence of organized vorticity is the true hallmark of a coherent motion. Kline (1988) summarizes much of the research on the many different coherent motions which have been observed, studied, and classified to date. Although random velocity fluctuations which produce Reynolds stresses are not necessarily caused by a coherent motion, it is generally thought that coherent motions are responsible for the enhanced convective processes present in a turbulent boundary layer.

"Coherent motions," however they are defined, occur intermittently throughout the boundary layer and come in many shapes and sizes[2]. Therefore a "good" detector must be able to determine both the start and stop times of an event[3], not merely that

---

[2] See for example how Signor (1982) used a range of shapes, sizes and orientations to identify "typical eddies".

[3] The start time of an event is generally held to be that time at which an event reaches a given point in space. The stop time of that event is the time at which the upstream end of the event reaches that same point.

an event has occurred. If detection of Reynolds stress-producing events in the inner region is important, a detector must be able to locate both high-speed events (sweeps) in addition to low-speed events (ejections), since almost 80% of the Reynolds stress correlation in the inner region is the result of high-speed, wallward-moving events (Brodkey, Wallace, and Eckelman, 1974).

Probe-based event detection schemes promised to provide the least ambiguous way to locate a coherent motion. Conditional averages[4] have most often been shown as "proof" that a given probe-based detection scheme did indeed locate a specific and unique mechanism which accounted for the majority of the turbulence production. However some authors (Alfredsson and Johansson, 1984) have questioned whether these conditional averages are the result of the detection criterion or if the various methods are indeed detecting distinctly different types of events[5]. Bogard and Tiederman (1987) go further, suggesting that a conditionally-averaged signal always bears characteristics which can be directly related back to the detection criteria. They question whether or not conditional averages derived from velocity-based detection schemes are truly representative of the characteristics of a sweep or ejection[6]. The

---

[4] Conditional averages based on the existence of an event can be calculated in one of two ways: The first approach is to align the centers of the events to be averaged. The average at each point in time before and after the center is calculated out to the desired length of the ensemble. This kind of plot is typically what has been used to decide on how long a VITA event is. The second approach is to align the starting times of the events to be averaged and "stretch" or "compress" the duration of each event so that the end times are also aligned. Averages are then calculated at each normalized point in time. This type of conditional average is commonly used with detectors which produce unique start and stop times for each event. The latter method will be referred to as event averaging or ensembling in this document, while the phrase conditional averaging will refer to the former process, and the context of the phrase will define the conditions under which the averages are to be calculated.

[5] In this document "event type" refers to a specific kind of detection made on a specific data set. For example, one type of uv-quadrant event is a sweep detected at $R_\theta=3120$; this "event type" is different from sweeps detected at $R_\theta=2380$.

[6] A sweep is a high-speed, wallward-moving event. An ejection is a low-speed event moving away from the wall. Sweeps and ejections will be discussed much more thoroughly in chapter 2.

RMS for each point of a conditional average gives a strong indication of how consistently the same thing is happening at each point in time during an "average" event. Unfortunately, very few authors have included this statistic when presenting their ensembles.

The choice of thresholding constant[7] has always been a source of uncertainty for probe-based detection schemes. Quantities such as intermittency, event frequency or inverse event frequency[8], and mean event length have been examined as functions of thresholding constant in the hopes that a plateau would appear, indicating that results in this region should be independent of the threshold chosen. However, Chen and Blackwelder (1978) have shown that when a simple threshold level is applied to a function which has a continuous probability distribution, the frequency of the detections will decrease monotonically with increasing threshold. This conclusion has led Blackwelder and Haritonidis (1983) and others to choose thresholds arbitrarily, arguing that the results are indicative of trends, even if the calculated numerical values are somewhat uncertain. Bogard and Tiederman (1983) and others prefer to select thresholding constants for probe-based detection schemes such that they generate the same number of events as were detected visually.

Velocity-based detection criteria were set aside in favor of visual detections in studies done by Offen and Kline (1973), Falco (1974, 1977), Signor (1982), Lovett

---

[7] "Threshold" and "thresholding constant" will be used synonymously in this document. "Threshold level" will refer to the actual value against which comparisons were made. In general the threshold level equals the thresholding constant times the RMS of the detected variable.

[8] The misnomer "mean time between events" has frequently been applied to this term. The inverse event frequency is the mean time between the beginning of two neighboring events of the same type, while the mean time between events is obviously the average time between the end of one event and the start of the next.

(1982), and many others. Studies by Chen and Blackwelder (1978) and Subramanian, Rajagopalan, Antonia, and Chambers (1982) have attempted to determine the relationship between probe-based detections and detections based on the presence or absence of heat-contaminated fluid coming away from the wall. This technique of heating the viscous sublayer far upstream and then examining the fluid passing over the probe for temperature gradients corresponds very closely to the large-scale motion visual analysis presented in Chapter 2. It suffers from one of the same disadvantages, namely that marked fluid must have been convected away from the wall at some point in time, although it may no longer be part of an active coherent motion.

Visual detections, or detections based on the presence, absence, or concentration gradient of a marker, do not suffer from the problems inherent in analyzing velocity measurements, but that does not mean that there are no problems associated with this detection method. The Schmidt number indicates the ratio between momentum diffusivity and mass diffusivity. If the Schmidt number is significantly larger than unity, marker will diffuse slower than momentum, and instances will occur in which the marker looks like it is being distored although there is no longer any active distortion occurring[9]. A well-defined visual detection criterion is difficult to establish; the easiest one to use is the presence or absence of marker, but high turbulence levels and/or long diffusion times make even this determination a difficult one. Films generally have to be analyzed by eye, and the subjective contribution of the people doing the analysis is difficult to estimate. Furthermore, when combined anemometry and flow visualization is performed, films are rarely exposed at the rate of one frame per digitized data point. Therefore one must not only decide if an active event which was really caused by the physical process under study has passed over the probe, one must

---

[9] This is sometimes referred to as "fossil turbulence".

also attempt to estimate at what point between two consecutive frames the event actually began or ended.

Velocity-based detection schemes will in general produce results which are dependent on the choice of threshold. Although only a subjective "thresholding level" can be applied to visual detections made without image processing equipment, there are a number of different ways in which a film can be analyzed. This will be discussed further in section 2.4, and three methods are presented there which vary in complexity and applicability. Those three methods will be applied to a number of different data sets and the performance of each will be evaluated in subsequent chapters.

Combined velocity and visual data acquisition has led to the comparison of visual and probe-based detection schemes. Bogard (1982) developed a way to measure the long-time correspondence between visual and probe-based detections. This approach has been applied by Luchik and Tiederman (1987) to uv-quadrant, VITA, and modified u-level detections. Most two- or three-dimensional non-intrusive velocity measurement techniques rely on visual data for the generation of velocity vector fields, so the same film which was analyzed for velocity information can also be analyzed to locate coherent motions of interest. These analyses rely primarily on the visual interpretation of films, velocity maps, or circulation contours to find the boundary of an event. Falco, Chu, Hetherington, and Gendrich (1988), Wark and Adrian (1990), and others are currently attempting to locate and characterize coherent motions on the basis of two-dimensional non-intrusive velocity field measurements. Economikos, Shoemaker, Russ, Brodkey, and Jones (1990) are attempting to do the same using three-dimensional velocity measurements. Problems include the fact that enormous amounts of data are generated if these measurements are to resolve a significant volume of

space with fine temporal and spatial resolution, in addition to the fact that an *a priori* concept of what comprises an important coherent motion must be used to locate an event.

The attributes of a good event detector are difficult to quantify, resulting in part from lack of agreement regarding what exactly should be detected; therefore the performance of a detector is difficult to rate quantitatively. A "good" detector is, in fact, one which makes use of whatever information it is given to accurately locate the presence or absence of the physical structure of interest. A detector will obviously perform best if the event to be detected is well defined and a signal directly related to the presence or absence of the event is available[10]. If performance is rated with quantities which are used by the detector itself, the "performance" of the detector will be related to the threshold chosen, and an optimal choice of threshold can always be found which will maximize the detector's performance. If a time series directly related to the physical mechanism of interest is available, it can be used as an effective indicator of a detector's performance. Previously-used performance criteria have consisted of intermittency, average event frequency and average event length calculations. However, the performance of detectors which are supposed to locate Reynolds stress-producing events should also be evaluated on the basis of how well they do that. Performance parameters based on this and other concepts are developed in section 2.6; results of their application to various inner- and outer-region data sets are shown in Chapter 3; comparisons among the various detection criteria employed are presented in Chapter 4.

---

[10] If the event to be detected is simply any motion which generates negative uv, then the optimal detector to use is the uv-quadrant technique with a threshold of 0. This assumes of course that time series of both the fluctuating spanwise and wall-normal velocities are available. As noted above though, a motion which generates Reynolds stress is not necessarily a "coherent motion."

If it is known that an event to be located has a well-defined visual appearance, good agreement should exist between visual and probe-based detection schemes designed to find the same type of event. Conversely, if the visual appearance of a well-defined probe-based detection has been determined, there should be good agreement between both detection methods. The correlation between visual and probe-based detections can be measured using the quantities P(D) and P(E) originally defined by Bogard (1982)[11]. However, a more comprehensive approach would be to see at which points during a visual detection probe-based detections are most (or least) likely to occur. This performance indication concept is also developed further in section 2.6, and the results of its application are shown in Chapter 4.

When the performance of one detector is to be matched to that of another, thresholds must be chosen for each detector as appropriate. Bogard, Luchik, Tiederman, and others have preferred to match the number of events detected and thereby the mean event frequency. However, other performance parameters as discussed above might provide better indicators of what threshold(s) to choose when comparing two different detection schemes. This concept will be explored in more detail in Chapter 4.

The average characteristics of a given detection method are best shown using an ensemble of the variables of interest. However, equally important to the significance of this plot is the standard deviation of the average at each point in time: This indicates how widely variant the events are which comprise the ensemble. The ensembles shown in this document will in general contain plots of u, v, uv, ω_z, and $v\omega_z$ versus normalized time during the "average" event. Plots of $v\omega_z$ are included since the

---

[11] See section 2.6.2.

transport of Reynolds stress, $\partial(\overline{uv})/\partial y$ is proportional to $\overline{v\omega_z}$. At this point in time, the question remains open of whether the motions responsible for $\overline{uv}$ or its transport, $\partial(\overline{uv})/\partial y$, are more important factors influencing the physics of the flow (see for example Hinze, 1975, or Klewicki, 1989). It is hoped that the $v\omega_z$ information provided in these event averages will be of use in resolving this question, but unfortunately its interpretation will remain beyond the scope of this document.

Kline and Falco (1979) posed questions regarding the scaling of events in both the inner and outer regions. Will the detection schemes developed for use in the near-wall region perform similarly in the outer region? Do events last longer and get larger when they are detected further from the wall? Does the intensity of an "average" event in the outer region scale with outer variables? Is an outer-scaled "average" event independent of Reynolds number? It was also asked in that same document whether something other than joint u and v signals can be used to detect events which produce significant amounts of Reynolds stress. These comprise the remaining questions which will be addressed in the coming chapters.

CHAPTER 2

THE EXPERIMENTAL DATA AND THEIR ANALYSIS

In this chapter data sets are described which permit the issues raised in the Introduction to be addressed. These data sets comprise hot wire time series and related films, both of which have been analyzed to produce detection time series indicating when sweeps, ejections, and quiescent periods occurred. The data reduction techniques used to reach this point are described in detail in this Chapter. Parameters for evaluating the long-time performance of each detector are developed, in addition to three parameters which indicate how much overlap there is between the detections of two different schemes.

2.1 THE DATA

Combined flow visualization and hot wire data were obtained in 1979-1982 by D. Signor and J. Lovett, working with R. E. Falco at the Michigan State University Turbulence Structure Laboratory. A total of eight different data sets are available, four taken in the inner region of the boundary layer and four in the outer region. Lovett was responsible for taking the inner region data (Lovett, 1982), and Signor took the

outer region data (Signor, 1982). For the most complete information regarding these data sets and the related data acquisition processes, please see the appropriate document.

2.1.1 Inner-Region Data Parameters

The inner region data sets were taken at an average Reynolds number based on momentum thickness (R_θ) of 720; the probe was positioned between 14.6 and 24.2 viscous units from the wall. The free stream velocity (U_∞) varied slightly from data set to data set, but it was always approximately 1.0 m/s. The friction velocity (U_τ) varied from 0.0497 to 0.0512 m/s. These values are summarized in table 2.1.1.

Data storage limitations prohibited the acquisition of very large contiguous data records. Consequently a number of shorter records were taken, checked for errors, and combined to form the data sets which were actually analyzed. The analog to digital converter (A/D) sampled each each of the four anemometers at 500 to 750 Hz. This produced combined data sets which ranged from 39 to 108 seconds in length, corresponding to 6400-18000 t^+ and 360-1733 tU_∞/δ. These data are summarized in Table 2.1.2.

The probe-based event detection schemes applied to the data produced start and stop times as events of interest passed the probe. These time determinations are at best accurate to one time tick, and the absolute time corresponding to one tick is inversely proportional to the sampling rate. The uncertainty associated with the determination of start and stop times ranges then from 1.3 msec to 2.0 msec, corresponding to 0.21-0.33 t^+ and 0.018-0.031 tU_∞/δ. These data are summarized in Table 2.1.3.

Considerations regarding the uncertainty in the start and stop times of visual detections will be presented in section 2.4.

2.1.2 Outer-Region Data Parameters

The outer region data sets were all taken at $y/\delta = 0.8$ with R_θ varying from 730 to 3120. The flow parameters for all four data sets are summarized in Table 2.2.1. Between 5 and 42 individual data runs were taken at each Reynolds number, and these individual runs comprise the combined data sets which were analyzed. Two different analyses were performed on the visual data; one type of analysis was applied to all of the data available (see section 2.4.1), while the other was applied to approximately 12% of the data (section 2.4.2). Two different combined data sets were created then from all of the data available at each Reynolds number, giving data sets which ranged in length from 2 seconds to 2.5 minutes (Table 2.2.2). A higher digitizing rate was used at higher free stream velocities, so the absolute uncertainty in start- and stop-time determinations decreases at higher velocities. These uncertainty values and their various dimensionless equivalents are shown in Table 2.2.3.

Klewicki[12] showed that first- and second-moment statistics for U, V, UV, and Ω_z will converge to 3% with data sets at least 1000 tU_∞/δ in length. Convergence to 10% will generally be achieved with data sets which are 200 tU_∞/δ in length, a level generally achieved by all the inner-region and large-scale motion outer-region combined data sets but not the ring-like motion data sets (Table 2.2.2).

---

[12] Klewicki (1989), p. 164. Note that convergence to 5% for third- and fourth-moment statistics will only be obtained with data sets which are 4000 tU_∞/δ in length, a level which is achieved by none of the data sets used in this study.

2.2 ACQUISITION OF HOT WIRE AND FLOW VISUALIZATION DATA

As mentioned earlier, the most complete descriptions of the data acquisition processes used are available in Signor (1982) and Lovett (1982); Signor was concerned with the outer-region data, and Lovett was responsible for the inner-region information. However, all of the data sets were taken in the same tunnel using the same laser and optics to generate visual information; the same probes, cameras, and computers were used to store the data. Therefore it makes sense to treat the inner- and outer-region data acquisition all at once, noting differences where appropriate.

The tunnel used was the Michigan State University Turbulence Structure Laboratory 7.3-meter low-speed wind tunnel shown in Figure 2.2.1. Note that the flow was tripped at the entrance of the first working section of the tunnel using either a 12.7 mm circular rod at the lower speeds or a 1.59 mm rod at the highest speed[13]. A four-wire vorticity probe shown in Figure 2.2.2 was driven by four DISA 55M01 anemometers whose outputs were connected to a simultaneous sample-and-hold circuit, digitized by a 50kHz 12-bit A/D converter, and stored on a PDP 11/23 computer. An MKS Baratron model 146H-0.1 pressure transducer was used in conjunction with a total pressure probe and static pressure tap to generate free stream velocity information for calibrations. A clock which incremented after the computer digitized each data point was positioned within the camera's field of view, so that each frame of film can be uniquely associated with a particular instant of the corresponding hot wire time series.

A Redlake Locam model 50-002 16mm pin-registered high-speed movie camera was used with a Schneider-Dreuznach Zenon lens to film the outer region flow

---

[13] See Signor (1982), p. 10.

visualizations. That same camera/lens combination was used to shoot the y^+=15 and y^+=18.9 data. A Photosonics model 35MM-4MLAC high-speed 35mm camera was used to photograph the flow with the probe positioned at y^+=14.6 and 24.2. Only side views are available for the outer region flows; only plan views are available for the y^+=15 flows; but both side and plan views are present in the other three inner-region flow visualization films. See Figure 2.2.3 for the camera and mirror setups which were used to create the different views.

For the outer-region measurements the tunnel was illuminated using both floodlights and a vertical laser sheet. The laser sheet was generated by sending the beam from an 8-watt Coherent CR-8 argon-ion laser into the tunnel from below, where it was focused onto a 3.5" cylindrical mirror. This is shown schematically in Figure 2.2.4. The laser sheet was aimed to pass as close as possible to the vorticity probe in order to maximize the correlation between the visual information and the hot wire data. The only problems arose when the laser sheet actually intersected a wire or two, causing those wires to overheat and fail. The laser sheed did not otherwise affect the hot wire measurements appreciably[14].

For the inner-region films taken with the probe positioned at y^+=15.0, the floor of the tunnel was illuminated from above using three unfiltered floodlights. The y^+=18.9 films were shot with red-filtered floodlighting of the plan view and laser-sheet illumination of the side view. Providing a red filter for the plan view eliminated the bright blue line of the laser sheet from that view, but that reduced the overall illumination of the film. These films had to be push processed with a corresponding increase in image

---

[14] See Lovett (1982), p. 49 for more information on the laser and hot wire setup and qualification.

grain size. The uncertainty associated with analyzing the $y^+=18.9$ films was much larger than that associated with the $y^+=15.0$ films because two views instead of one were present in the former films which started with poorer image density and grain. Poor image quality brought about the decision to use 35mm film for shooting the other two probe positions. A red plan view, a blue side view, and a clock are visible in these films, and the image density and grain are indeed improved over those obtained at $y^+=18.9$.

Smoke was injected upstream of the measurement point using two slits for the inner-region data sets, one far upstream and a tangential slit approximately 80 l^+ upstream of the probe. For the outer-region data sets only the far upstream slit, positioned approximately 4.27 m upstream of the measurement point, was used. See Figure 2.2.5 for a graphic description of the different types of smoke injection slits used and their positions in the tunnel.

2.3 REDUCTION OF VORTICITY PROBE DATA

The vorticity probes used by Signor and Lovett are similar to those described by Foss, Klewicki, and Disimile (1986). The calibration scheme used is a variation of the "effective angle" technique[15]. Applying this calibration technique, the effective angle of the X-wires was determined, along with Collis and Williams coefficients for each of the four wires. These coefficients were applied to the raw data using the programs

---

[15] This technique is described in Klewicki (1989) pp. 34++, Signor (1982), Lovett (1982), and Falco (1980). It has also been recently evaluated in a study by Browne, Antonia and Chua (1989).

CONVOL and CONVEL[16], creating time series of the velocities for each wire at each sampled instant in time. From this point on the data were processed using modified versions of programs created by Klewicki to compute long-time statistics for the data and to create time series of velocities, spanwise vorticity, spatial and temporal derivatives, and various combinations of the above. The processes and assumptions used in these programs are most completely described in Klewicki (1989), along with the inherent uncertainty in the computed values, however a brief summary follows.

The time series required for the detection and evaluation schemes described in section 2.5 are u, v, uv, $\partial u/\partial t$, $u\partial u/\partial t$, ω_z, and $v\omega_z$. The first two time series are derived from the X-array signals, and the third time series is simply the product of the first two. The time derivative of the u signal is calculated by computing a local 5-point least squares fit to a second-order model ($u = a_1 + a_2t + a_3t^2$) and then differentiating the model. The calculation of $\partial u/\partial y$, one component of ω_z, was based on a 2-point finite difference approximation using the fluctuating part of the velocities from the parallel array. The calculation of $\partial v/\partial x$ was analogous to that of $\partial u/\partial t$, that is, a local 5-point least squares fit of a second order model was computed about the point of interest, and then the model was differentiated. The v-component velocities used are those calculated from the X-array data, and Taylor's hypothesis is used to convert time derivatives to streamwise derivatives. Klewicki (1989) notes that this method of computing $\partial v/\partial x$ is preferred to a multipoint finite difference approach, since this method is less sensitive both to the choice of step size and to signal noise. The $v\omega_z$ time series was computed by multiplying $v(t)$ and $\omega_z(t)$ together at each instant of time; the $u\partial u/\partial t$ time series is the product of u and $\partial u/\partial t$.

---

[16] For a description of these programs, see Lovett (1982), pp. 56+ and Signor (1982), Appendix A, pp. 167++.

Since Signor and Lovett did not use the analog filtering circuitry which was available to Klewicki, they developed a number of ways to filter their data digitally. The program VELRED (Lovett, 1982) first eliminated points in the u time series which varied from the previous point by more than u'; these points were replaced by the average of the 2 neighboring points. The v and uv time series were treated the same way. The resulting u, v, and uv time series were then low-pass filtered (averaged or smoothed)[17] by replacing each tick with a local 5- or 7-point average centered on that tick. These then were the time series used to compute spanwise vorticity, temporal and spatial derivatives, and combinations thereof.

The following approach used less filtering than before while eliminating enough low-frequency noise so that the resultant time series were adequate for analysis: Values in the time series for each wire, i.e., the outputs of CONVEL, were checked against the previous point in time for values which changed by more than 2 RMS of a 100-point average about the point of interest. Values which did change so radically were replaced by the average of the two neighboring values in the appropriate time series; this occurred 2864 times out of a total of 878340 data points or 0.33% of the time. The resultant time series were processed as described at the start of this section to generate the u, v, uv, and other time series required for the probe-based detectors and the effectiveness analyses.

After each time series was calculated, it was seen that appreciable jitter was still present in the signals. Using an n-point average to smooth the final time series was an

---

[17] It should be noted that this sort of low-pass filtering prohibits direct calculation of cutoff frequencies, unlike that which can be performed when analog filtering is used. Cutoff frequencies could have been estimated by calculating and comparing "before" and "after" power spectra of the u and v time series.

available option, but it was apparent that the choice of averaging window length would have an effect on the long-time statistics of the resultant data. It was also readily apparent that smoothing the jittery data would significantly change the statistics of those data without giving any indication of whether this was due to the elimination of noise or the introduction of biases by the smoothing process. Therefore smoothing was applied to one of Klewicki's 600,000-point vorticity-vorticity data sets[18] all of which exhibited smoothly continuous time traces for u, v, uv, and ω_z. The long-time statistics for the upper wire fluctuating vorticity time series ($\omega_z(t)$) are shown in Figure 2.3.1 a-c as a function of smoothing window length; note that a smoothing window of one corresponds to no smoothing at all. A window of 5 produced changes of less than 10% in the higher-order statistics[19], so this is the window length which was subsequently used to smooth the final time series calculated from the unsmoothed data of Signor and Lovett.

2.4 REDUCTION OF VISUAL DATA

The visual data obtained (films) were analyzed using a variety of methods which will be described below. The determination of start and stop ticks for each event was complicated by the fact that multiple hot wire data ticks were acquired during the exposure of a given frame of film. Events with an unambiguous visual appearance produced the least uncertain start and stop times; see for example the large-scale motions described in section 2.4.1. More ambiguous visual appearances produced less certain

---

[18] The specific data set used was correlation 10, number 1.

[19] A fluctuating time series was used, so the mean was always zero.

start and stop times, and this is quantified as well as possible below.

The atomized oil droplets ("smoke") used to visualize the flow averaged $1.0\mu m$ in diameter and had a Schmidt number on the order of 38,000, indicating that these particles were satisfactory markers of convective processes but tracked diffusive processes poorly.

The 35mm film was read using a NAC model PH-350B motion analyzer. The 16mm film was read using a NAC model DF-16C analysis projector whose images were displayed on a ground glass screen and read from the reverse side to eliminate the parallax errors associated with using a standard movie screen and viewing from an angle. The 35mm analyzer displayed the images on its own screen; it was not used in projection mode.

2.4.1 Large-Scale Motions

The side views present in all of the outer-region films show dark regions where no smoke is present and lighter regions where smoke has been convected from the injection slit far upstream to the point at which the probe is positioned. If the atomized oil droplets which comprise the smoke had had a Schmidt number of approximately one, the dark regions could be expected to contain the non-vortical fluid from the free stream, while the lighter regions should contain the vortical fluid of the boundary layer. Although it was expected that this would not be the case all the time, the start of a large-scale motion event (LSM) was defined to be the time at which a light, smoke-filled region started to pass over the probe. The end of an LSM was recorded as the time at which a dark region started to pass over the probe.

The LSM visual analysis is simple and easy to perform. The framing rate of the camera produced films in which between 4 and 12 data ticks elapsed between each frame; between 2 and 4 data ticks were taken during each frame. This, in combination with the unambiguous definition of an LSM, produced start and stop times which were accurate to within ± 2–6 data ticks (see Table 2.2.3 for the factors needed to convert data ticks to seconds, t^+, tU_∞/δ, and l^+).

The relatively low ambiguity inherent in LSM visual detections is unfortunately offset by a number of limitations. First, there is no provision for classifying an event, so this analysis cannot be used to show whether modifications which induce changes in the boundary layer structure are affecting the sweep process or the ejection process. Second, application of this analysis to the near-wall region would be difficult, since the presence or absence of marker there is rarely as unambiguous as it is in the outer region. Third, this approach exacerbates non-unity Schmidt number effects since the marker must be injected close to the working section inlet if it is to mark the entire boundary layer. The entire development length is then available for the differences between convection and diffusion of both marker and momentum to make themselves apparent.

The simplicity of this approach makes it a desirable candidate for use in the outer region if it can be shown that the disadvantages noted above do not affect the results too much. Therefore LSM detections from the outer-region films were analyzed as described in section 2.6, and the results from those analyses are presented in the next chapter.

2.4.2 Visual Detections of Ring-Like Motions in the Outer Region

Falco (1974, 1977) and Signor (1982) proposed that vortex ring-like motions of intermediate scale[20] were a plausible mechanism for momentum transport in the outer region of a turbulent boundary layer. Flow visualization and hot wire anemometry were used in an iterative process to define the visual characteristics of this intermediate-scale ring-like motion (RLM) which they called a "typical eddy." The model RLM was then divided into eight separate zones as shown in Figure 2.4.1. The existence of an RLM event in zones 1-6 passing over the probe was based in the shape of the RLM with respect to the shape shown in Figure 2.4.1, the orientation of the RLM, the existence of fluid motion within the eddy, and a location above $y/\delta=0.5$. The same criteria were applied to zones 7 and 8 for film taken at the two lowest Reynolds numbers, but conditional sampling at the higher two velocities was performed with reference to both the film and the u, v, uv, and ω_z time traces.[21] The start of an RLM event was recorded as that time at which the structure intersected the vorticity probe.

Signor's grand ensembles of u and v as a function of zone within the model coherent structure[22] were used in conjunction with the usual concept of a sweep and ejection to determine which RLM detections could be classified as a sweep and which as an ejection. Without this step RLM detections cannot readily be compared to the results of detection schemes which locate sweeps and ejections.[23] The average

---

[20] "Intermediate scale" in this case is something on the order of $\delta/10$. In the flows studied the average vertical extent of a typical eddy was of the same order as the Taylor microscale (Tennekes and Lumley, 1972, p. 66).

[21] See Signor (1982), pp. 21-23.

[22] These are Figures 3.35 and 3.36, p. 99 and 100, in Signor (1982). Note that the data from all four Reynolds numbers were ensembled to produce these plots.

[23] It would be possible to compare the detections from each zone to sweep, ejection, inward

streamwise velocity in zones 1 and 2 was always higher than the mean; in the other 6 zones it was generally less than the mean. The average wall-normal velocity in zones 1 and 2 was generally negative, while in the other 6 zones it was positive. Events from zones 1 and 2 were therefore generally high-speed and wallward moving, so they were called sweeps. Events from the other zones were generally low-speed and outward moving, so they were called ejections.

The same film was used for both RLM and LSM analysis. Therefore an uncertainty of between ±2–6 ticks existed because of the way the film was exposed. The event was well defined, and the selection criteria were applied conscientiously. However, the blurring in the higher-velocity films which required the combined use of film and hot wire data for identification also increased the uncertainty in the start and stop times of those events. For $R_\theta=730$ and $R_\theta=1400$ the start and stop times are therefore uncertain to ±2 and 3 ticks, respectively. The other times are probably uncertain to ±7 ticks at $R_\theta=2380$ and ±8 ticks at $R_\theta=3120$. Using values from Tables 2.2.3 and 3.2.1, the uncertainty in average RLM event length is between 0.3% and 1.2%.

The RLM visual analysis is both complex and time consuming. With adequate illumination and framing rates, its uncertainty is comparable to that of the LSM visual analysis, but blurred images in combination with the tight RLM sampling criteria produce both a higher uncertainty in start and stop times and a larger rejection rate than that obtained for the LSM approach. However, the RLM analysis relies on the relative motion of smoke particles from frame to frame to verify that each RLM is active when it reaches the probe. This reduces the effect of a high Schmidt number on the results,

---

interaction, and outward interaction detections due to other schemes. However, since the focus of this work is on sweeps and ejections, it seems more reasonable to determine which RLM zones contain events that behave like sweeps and ejections for comparison purposes.

since it has been shown that the particles used were small enough to mark convective processes within the flow, while the time between frames (12 data ticks or less) was short enough so that diffusive processes would not be a significant factor in that interval.

2.4.3 Inner-Region Visually-Detected Events

The velocity signatures of sweeps and ejections were used to define the visual characteristics of those events when their effects penetrated into or rose out of the visualized inner-region of a turbulent boundary layer. The visual detections were based primarily on the plan view of atomized oil droplets ("smoke") used to mark the viscous sublayer. The concentration of smoke in the sublayer was greater than the overlying fluid, so a high-speed, wallward-moving event appears to move the smoke particles out of the way, creating a region darker than its surroundings which rapidly advances on and passes the probe. Low-speed, outward-moving events appear as bright areas (most often "ridges") which move slowly over the probe. The side view, illuminated by laser sheet, was used as a secondary source of information when it was available. Ejections in the side view appear as slow-moving bright regions rising away from the wall and passing over the probe.

The existence of an event at the probe was based on a number of criteria: Was the smoke moving faster (or slower) than it did in the surrounding fluid? Was the smoke density just upstream of the probe steadily decreasing (or increasing) from frame to frame? Did the event intersect the X-array?[24] The start of an event was

---

[24] This criteria was applied since the X-array was the source of u and v information. As noted in section 2.3, the parallel array was only used for calculating $\partial u/\partial y$.

recorded as that time at which the boundary of the higher-velocity (or lower-velocity) region intersected the X-array. The end of a sweep was occasionally difficult to determine, since strong sweeps did have the ability to remove all of the smoke from the region around the probe. The precise end of an ejection was difficult to determine on those occasions when the smoke density slowly relaxed back to its average value. Generally an accurate determination of start and stop times could be made by playing a sequence of frames and looking for changes in particle velocities; when this did not work, the existence of an event was noted but not used in the analysis.

It was recognized that this method of analysis had a certain amount of subjectivity in it, so two methods were employed to improve the consistency of this analysis' application. The first method involved reading the same film at different times and comparing the results. During the first two weeks of film analysis, this author read many films, but the same film (5200 frames)[25] was read every other day. That day's results were compared with those of the previous reading. After the same events were found in two consecutive readings and their start and stop times agreed to ±1 tick, film analysis started all over again; old results were discarded, and only subsequent results were saved. In the second method, two practiced film readers analyzed the same film, and the results were compared[26]. The same events were located, with a couple exceptions, and their start and stop times agreed to ±3 ticks.

Framing rates and film speed varied from data set to data set, so the uncertainty of the start- and stop-time determinations also varied. Sometimes the film was still accelerating up to speed within the camera during the initial frames of a data run;

---

[25] This was the $y^+=15.0$ film.

[26] My thanks go to Dr. Falco who took the time to sit and stare at films with me. We used the first film of the $y^+=18.9$ data set for this.

event times could generally be determined to within 10 data ticks for this part of a film. Sometimes the camera was started late or ran out of film early; in these instances, quiescent periods were recorded during those times for which no visual information was available. If more than 40% of the data run was affected in this way, the entire data run was discarded[27]. The y^+=14.6, y^+=18.9, and y^+=24.2 data sets all were filmed with approximately 8 data ticks between frames when the camera was up to speed. Three or four data ticks were taken while each frame was exposed, giving a total uncertainty in start and stop times for these data sets of ±6 ticks. Approximately 4 data ticks elapsed between frames of the y^+=15.0 film, and two to three ticks were taken during each frame. Therefore the total uncertainty in start and stop times from this film is about ±3.5 data ticks. Using information from Tables 2.1.3 and 3.3.1, the uncertainty in average event length varies from 0.6% to 3.1%.

2.5 PROBE-BASED EVENT DETECTION SCHEMES

Three of the more frequently used probe-based coherent event detection schemes have been implemented in this study. A goal of the implementations has been to use detectors which are capable of locating the start and stop times of coherent motions which contribute to Reynolds stress production. Since it has been shown that sweeps are responsible for the majority of the Reynolds stress production in the near-wall region (Brodkey, Wallace, and Eckelman, 1974), each detector as implemented must provide for the detection of high-speed events, a constraint which led to a modification of the u-level technique. The detectors as used in this study will be described below

---

[27] This includes 1 out of 9 of the y^+ = 14.6 data runs, none of the y^+=15.0 data runs, none of the y^+=18.9 data runs, and 4 out of 18 of the y^+=24.2 data runs.

in some detail. The computer programs used to generate detection time series were presented in Gendrich, Falco, and Klewicki (1989); specific questions regarding the implementations used in this study may be answered by referring to that document.

2.5.1 The uv-quadrant breakdown technique

Perhaps the most common detector used when time-resolved streamwise and wall-normal velocity measurements are available is the uv-quadrant breakdown technique first proposed by Wallace, Eckelman, and Brodkey (1972) and subsequently expanded by Willmarth and Lu (1972). The start of an event is said to occur when the product of u times v exceeds a given threshold[28], equal to $cu'v'$. The u and v time series are used to classify events as sweeps, ejections, inward interactions, or outward interactions. A sweep is a high-speed coherent event moving toward the wall, so a sweep is an event that has u>0 and v<0 by definition. Similarly, ejections have u<0 and v>0; both u and v are negative during an inward interaction; and both are positive during an outward interaction. Since this study focuses on the nature of sweeps and ejections, the detections from quadrants 1 and 3 will not be analyzed.

---

[28] Some write H as the thresholding constant symbol for this detection technique; this is intended to refer to the size of the hyperbolic "hole" in the uv-plane which is created by non-zero thresholding constants. k is frequently used as the thresholding constant for the VITA technique, L for the u-level technique. Since thresholding constants are used similarly in all of these detection schemes, they will all be called c in this document. Note that $c \geq 0$.

2.5.2 The TERA technique

The essence of the Turbulence Energy Recognition Algorithm was proposed by Zoran Zaric' in 1981 and simplified by Falco and Gendrich (1989). The underlying idea of the TERA technique is that a turbulence event will produce a change in the magnitude of the streamwise turbulence kinetic energy. This will be accompanied by an increase in the magnitude of the temporal derivative of u^2, and $\partial(u^2)/\partial t$ equals $2u\partial u/\partial t$. Therefore the start of a TERA detection is said to occur when the magnitude of $\partial u/\partial t$ exceeds the threshold level, $c(\partial u/\partial t)'$. The event ends when both $|\partial u/\partial t|$ and a short-time average of that same quantity fall below the threshold level.

Events are classified as a sweep or ejection based on the sign of u. High-speed events (u>0) are called sweeps, and low-speed events (u<0) are called ejections. An event is also said to end if u changes sign before the short-time average described above falls below its cutoff level. The TERA implementation for this study does not differ significantly from what was described in Falco and Gendrich (1989).

2.5.3 The u-level technique

The u-level technique was first proposed by Lu and Willmarth (1973) and subsequently modified by Luchik and Tiederman (1987). Events started when u dropped below $-cu'$; they ended when u rose above $(-cu')/4$. Since this approach forced u to be negative, only low-speed events (called ejections) could be detected by this approach. Therefore the modified u-level technique of Luchik and Tiederman (1987) did not meet this study's requirements for a detection scheme, i.e., the detector was not able to determine the start and stop times of both sweeps and ejections.

The modified u-level technique was further modified for this study so that high-speed events could also be detected. An event is said to begin when the magnitude of u rises above the threshold level cu′, and it ends when |u| falls below one quarter of the threshold level or when u changes sign. Events are classified as sweeps or ejections depending on the sign of u; low-speed events are called ejections, and high-speed events are called sweeps.

2.5.4 Grouping of Events

All of the event detection schemes presented above have the capability of producing very short events or very short quiescent periods between events of a similar nature. A grouping procedure similar in nature to that used by Bogard and Tiederman (1986) was used to cluster shorter events which likely comprised one individual burst. Bogard and Tiederman (1986) used the probability distribution of their ejection statistics to decide on the grouping window to use. Falco and Gendrich (1989) showed that the size of the grouping window had little effect on the correlation between TERA and inner-region visual detections if the grouping window was $5 \, t^+$ or larger. Therefore events of the same type separated by pauses shorter than about $5 \, t^+$ were connected and the intervening pauses eliminated.

Very short events posed another problem. The signature of events one or two t^+ in length is bound to be significantly different from that of more average events which range from 100-400 t^+ in length. The inclusion of many short events therefore has the potential to affect the ensemble average appreciably. Furthermore, it is questionable whether a very short detection was caused by noise in the signal or a real physical process. Consequently, it was decided to eliminate very short detections after grouping

was applied to the signal but before ensembles and other results were calculated. This was implemented by eliminating sweeps or ejections which were shorter than three data ticks in length (less than 1 t⁺; see Tables 2.1.3 and 2.2.3).

2.6 PERFORMANCE PARAMETERS

Quantitative evaluation of a detection scheme's performance depends on the availability of a signal which gives a good indication of the presence or absence of the physical structure under study. This signal can be in the form of an intermittency function, from a visual analysis for example, or it can be in the form of another time-resolved quantity like vorticity. If the signal used to locate events is also used to evaluate how well the detections were made, the level of performance achieved will be directly related to the choice of threshold. In this case one can easily optimize the performance of the detector by making the correct choice of threshold. It is not frivolous to obtain a signal which shows whether or not something is going on and then not use that signal in the detector itself; simple detection schemes need to be evaluated on the basis of more complex ones which give the most nearly correct detections possible.

This leads back to the question of what a coherent motion is, which one cannot know until it has been detected and analyzed; yet the adequacy of the detections cannot be evaluated until the motion has been characterized. A simple definition of an interesting coherent motion is used in this study; more complex definitions will not change the methods by which the performance of a given detection scheme is evaluated. Iterating the process of defining an event, figuring out how to detect it, and then evaluating how well those detections have been made should lead to the most

well-refined definitions of both the event and the best way in which to detect it.

As mentioned in the Introduction, previously used performance evaluations have often consisted of only average event frequency and average event length calculations. These values may give some information regarding a range of thresholds within which the detected event lengths or frequencies are threshold independent, but by themselves frequency and length are not good performance indicators: Even if the average length and frequency of occurrence are known, it is possible to generate detections having these characteristics which locate absolutely nothing of interest.

Sweeps and ejections are the focus of this study; consequently the definitions of these events will be used to construct parameters which should aid in evaluating the performance of the various detection schemes used. The nature of both events is that the product of uv is negative; they are Reynolds stress producers. Ejections should induce negative fluctuations in the spanwise vorticity as the more vortical fluid from near the wall is convected upwards. Similarly, sweeps should induce positive fluctuations in ω_z. In either case the RMS of ω_z is likely to be higher during these events than it is on average.

Other event definitions will suggest different performance indicators. For example, if the event to be located has a well-defined visual appearance, the one-to-one correspondence between visual and probe-based detections will be a strong indicator of detector performance. The factors P(D) and P(E) as defined by Bogard (1982) indicate the level of one-to-one correspondence between any two detection schemes. The factor P(T) as defined below gives a time-resolved[29] indication of how well the detection

---

[29] Actually, P(T) is an event-resolved indicator, since the average likelihood of a correct detection is determined at each point in time during an event's ensemble.

scheme under test locates the presence of the correct event when it is "known" that such an event is occurring. P(D) and P(E) yield scalar quantities, while P(T) yields a time series; all of these will be dependent on the threshold level chosen for the probe-based detector. One-to-one event correspondence will be dealt with in section 2.6.2 and applied in Chapter 4. Some additional analysis concerns will be dealt with in section 2.6.3.

2.6.1 Long-time statistical performance parameters

Old and new performance parameters are defined here which can be used to rate how well a detector locates the presence of a sweep or ejection. The older parameters will be presented first, followed by ones specific to the nature of the sweep and ejection as discussed above. The mean event frequency indicates how many events occur per unit time. It is calculated by dividing the number of detected events by the total data set length:

$$f = \frac{(\text{\# of events}) \times (\text{sampling rate})}{(\text{total \# of ticks in the data set})}$$

When inner variables are used to normalize this value, $f^+ = f\nu/U_\tau^2$; if outer variables are used, the dimensionless quantity is $f\delta/U_\infty$. The mixed normalization factor is always defined to be the geometric mean of the inner- and outer-normalization factors, so in this instance the mixed normalization factor is $\sqrt{(\nu\delta)/(U_\tau^2 U_\infty)}$. For comparison purposes, results will only be given in dimensionless form, although all three normalizations will be presented.

The average event length is calculated by multiplying the average event duration by an appropriate convection velocity. In the outer region it is generally assumed that

the convection velocity of a coherent motion is approximately $0.9U_\infty$. Falco[30] measured an average speed for pockets of $0.6U_\infty$. In either case the convection velocity is proportional to U_∞, so as long as this speed is only weakly dependent on distance from the wall, U_∞ can be used to give event lengths suitable for comparison purposes. This will permit us to determine whether or not a given normalization eliminates the dependency of event length on Reynolds number or probe distance from the wall. Average event lengths are then calculated by dividing the total detection time by the number of events and multiplying by U_∞:

$$l = \frac{\Sigma(\text{Individual event durations})}{\text{total number of events}} \times U_\infty$$

U_τ/ν is the inner-variable normalization factor, and $1/\delta$ is the outer-region factor used[31].

Sweeps and ejections produce negative uv (by definition). A parameter which indicates how often the detector is "ON" during periods in which negative uv is being generated would be useful in evaluating the performance of that detector. Since large magnitudes of uv contribute more to the long-time $\overline{uv}$ correlation, those times should be weighted more heavily than ones which only produce minimal contributions to $\overline{uv}$. This suggests that the percent of Reynolds stress "captured" should be defined as follows:

$$\%\text{negUV} \equiv \frac{\int_{\text{during events}} u(t)\, v(t)\, dt}{\int_{\text{all time}} u(t)\, v(t)\, dt}$$

[30] Private communication, 1988. See also Falco and Gendrich (1989).

[31] It was suggested by C. Wark and H. Nagib of I.I.T. (private communication, 1990) that θ would be a more accurately determined estimate of the outer-region length scale than δ. Unfortunately, insufficient time was available to incorporate their suggestion into this study.

If sweeps actually convect fluid with a lower vorticity intensity, $|\tilde{\omega}_z|$, from the outer region down to the level of the probe, they will cause positive fluctuations in vorticity during an event (given our coordinate system and measurement location). Ejections should behave in the opposite fashion, bringing up fluid with a higher vorticity intensity from nearer the wall, inducing a negative fluctuation which should show up in the vorticity event average for ejections. A long-time performance indicator which deals with the vorticity should deal with either the average fluctuation or the average intensity of the fluctuations (RMS). Since the average fluctuation can be shown in an ensemble, the intensity of the fluctuations will be the long-time performance indicator used.

$$\omega_z \text{ parameter} \equiv \frac{(\omega_z{'})_{\text{during events}}}{(\omega_z{'})_{\text{all time}}}$$

If high-intensity fluctuations are present, this parameter should be greater than one, unless only the event under consideration produces all of the vorticity fluctuations experienced by the probe or the vorticity changes occur before the detector turns "ON" or after it has turned "OFF."

The energy associated with an event is a function of the the turbulence kinetic energy and the enstrophy. Vorticity has already been dealt with above, but kinetic energy has not yet been considered. Since the spanwise velocity, w, was not measured, only two out of three components of the turbulence kinetic energy are available. Therefore the event intensity parameter to be considered will be approximated by $u^2 + v^2$, and this value will be non-dimensionalized by the long-time RMS of that quantity.

$$\text{TKE parameter} \equiv \frac{\langle u^2 + v^2 \rangle_{\text{during events}}}{(u^2 + v^2){'}}$$

Note that the quantities used in calculating the TKE parameter are the fluctuating velocity components after the mean components have been subtracted out. Furthermore, the TKE parameter is based on the average value of the turbulence kinetic energy during the events under consideration, not an RMS of that quantity. Therefore strong events whose velocity components vary substantially from the mean during an event will produce higher values for the TKE parameter than events whose velocity components oscillate about the mean.

2.6.2 Visual-correspondence performance parameters

Bogard (1982) proposed two different ways to gauge the long-time correspondence between visual and probe-based detections. These parameters, called P(D) and P(E), were the probability that a visual detection would occur during a given probe-based detection and vice versa, respectively. P(D) and P(E) are defined as follows (after Luchik and Tiederman, 1987):

$$P(E) \equiv \frac{N_{ED}}{N_E}$$

$$P(D) \equiv \frac{N_{DV}}{N_D}$$

N_E is the total number of visual detections, N_D is the total number of probe-based detections, N_{ED} is the number of visual detections which correctly correspond[32] to a probe-based detection, and N_{DV} is the number of probe-based detections which

---

[32] "Correct 1:1 correspondence" as used in this study means only that the same event is detected by both methods at some overlapping point in time. No penalties are assessed for detecting the wrong type of event or detecting no event at all. P(E) and P(D) therefore have a range between zero and one.

correctly

correspond to a visual detection. If either N_E or N_D is zero, both P(E) and P(D) are defined to be zero.

A new quantity, P(T, t), is required to indicate how good the one-to-one correspondence is at each point in time during an ensemble averaged reference detection. If we choose visual detections to be our reference, we can define P(T) as follows:

$$P(T, t) \equiv \frac{N_{DV} \text{ at this t}}{N_E}$$

This variable shows the relative frequency of occurrence of probe-based detections as a function of time during the reference (visual) detections. Within this context one can think of P(T) as an event-resolved P(E) value. When P(T) equals P(E), all of the probe-detected events which corresponded to any visual event overlapped at that event-resolved point in time. P(T) in combination with the probe-based detection criteria used will allow more specific limits to be set on flow variables at certain points during the visual detection without needing to calculate the ensemble average of those variables. For example, if a high-threshold uv-quadrant detection frequently occurs at a given point during a visual event, one can conclude that the magnitude of uv at that point is usually large.

The event-resolved correlation between visual events and probe-based detections can show a number of interesting details regarding the relative location of those detections with respect to each other. If the P(T) plot is a horizontal line, the probe-based detections either occurred at exactly the same point relative to the visual detections or they must not be correlated with each other at all. That is, a horizontal line on a P(T)

plot indicates either perfect correlation or no correlation at all; P(D) will indicate which. If P(T) varies significantly with time relative to the start and end points of the "average" visual event, a certain level of correlation is present, indicated by P(T)/P(E). For example, given a P(D) of 43%, P(E) of 40%, and the P(T) plot (threshold=0.7) as shown in Figure 4.2.7a, one sees a) that 43% of the uv-quadrant ejections overlapped with an RLM ejection, b) that 40% of these visual events overlapped with a probe-based detection, and c) that three quarters of those overlaps occurred at $5/6^{ths}$ of the way through the visual event, at the peak in the plot where P(T) is about 30%.

2.6.3 Additional Considerations

Statistics are calculated for those periods during which detections are said to be occurring. Therefore, one must consider how well those statistics will have converged to their long-time values given the number of data points which are used. Using a Weak Law of Large Numbers formulation and 95% confidence interval, Klewicki (1989) has calculated the convergence of different statistical moments for data taken with these probes in flows between $1000 < R_\theta < 5000$. As long as the sampling rate is large enough[33], the number of samples required is not the prime concern; it is rather the time over which values are summed. This is due to the fact that independent samples are needed to assure convergence of the statistics to their correct values. Normalizing these sampling times with outer variables provides a Reynolds number

---

[33] The Kolmogorov frequency is an adequate lower bound on the frequency for the purposes of this analysis.

independent approximation to how much data must be taken in order to assure a given level of convergence for the statistics.

The mean and RMS velocity and vorticity statistics should converge to within 3% by the time tU_∞/δ exceeds 1000. Velocity-vorticity correlations will probably not converge until over 3000 tU_∞/δ has elapsed. Skewness values require as much as 3500 to 6000 tU_∞/δ in order to converge to within 5%; flatness values generally require between 2000 to 5000.

The performance indicators outlined above require only average and RMS values, and convergence to 10% would be considered acceptable for the purposes of this study. Convergence of velocity and vorticity average and RMS values to within 10% should be obtainable with measurements taken over as little as $200tU_\infty/\delta$[34]. Therefore if events have a length scale of $O(\delta)$, then averaging over 200 events should produce statistics converged to ±10%.

The scaling of events in the outer region[35] of the boundary layer is to be considered in Chapter 3. Inner, outer, and mixed variables will be used to scale each variable in the "average event" ensembles calculated from either visual detections or probe-based detections made with a given thresholding level. The trends of each variable during the ensemble will not be affected, but the scaling between data sets will change. Since the length of each event is stretched or compressed until it fits into the desired length of the ensemble, no special scaling will have to be done to the time axis

[34] Klewicki (1989), pp. 164, 183-8, and private communication.

[35] Inner-region events will not be scaled since the data sets were all taken at approximately the same Reynolds number ($R_\theta \approx 720$). This applies especially to Figures 3.3.1 and 3.3.2.

before ensembles from different Reynolds numbers can be compared.

It is expected that the length of events in the inner region will scale with inner variables, and that those events will grow larger the further they are from the wall. In order to test this hypothesis, the inner-scaled average event length will be calculated and then divided by the non-dimensional probe height above the wall. It should be noted that some normalization needs to be used, since the flow parameters for each data set are not quite identical, however the choice of normalization should not significantly affect the results.

CHAPTER 3

EVALUATION OF VISUAL AND PROBE-BASED DETECTION SCHEMES

The event detection schemes described in sections 2.4 and 2.5 were applied to the data sets described in sections 2.1-2.3, and the appropriate performance parameters were calculated as described in section 2.6. Those results are presented in this chapter, and Chapter 4 presents comparisons of the results from different detection schemes.

Results from all of the probe-based detection schemes depend on the thresholding constant, c. This variable can take any non-negative value, and results were calculated for increasing values of the thresholding constant until no events were detected for at least three of the data sets used. This resulted in a thresholding range of 0-3 for the u-level technique, 0-6 for the TERA approach, and 0-7 for the uv-quadrant analysis.

The TERA technique also depends to a certain extent on the choice of a short-time averaging window length. Falco and Gendrich (1989) showed that using a window of $5t^+$ or greater would create a situation in which the threshold has a much greater effect on the results than the window length. Therefore the window was chosen to be at least $5t^+$ (generally 25 ticks; see Tables 2.1.3 and 2.2.3) for this detector when applied in both the inner and outer regions.

Long-time statistical performance parameters were calculated for all six detection schemes employed[36]. Four inner- and four outer-region data sets[37] were available for analysis, and both sweeps and ejections were located by all except the LSM visual detection method. For each performance parameter (e.g., inner-scaled average event length) sixteen curves are required to describe the response as a function of threshold, event type, and y^+ or R_θ. It was found that this was too much to put on one plot, so figures are divided according to whether inner-region or outer-region results are plotted. Performance of sweep and ejection detections from the same data set are plotted using similar symbols, and the same symbols are used consistently throughout all of the figures. This means, for example, that results associated with sweep detections on the y^+=24.2 data set will always be plotted with the open diamond symbol, and the corresponding ejection detection results will be shown by the crossed diamond symbol.

For each detection scheme the number of events and total event time will be shown first in order to give an indication of the the statistical uncertainty present in the subsequent results. Long-time average values will then be shown, including mean event frequency, average event length, percent of Reynolds stress "captured," RMS spanwise vorticity during events, and turbulence kinetic energy level. Finally, event averages of u, v, uv, ω_z, and $v\omega_z$ will be presented in conjunction with the RMS for each variable, to give an indication of the average events' characteristics, and how variable each turbulence quantity is during that particular kind of detection. Plots which will be compared from detector to detector are in general plotted on coordinates

---

[36] These six are the LSM, RLM, and inner-region visual detection methods, the uv-quadrant breakdown technique, TERA, and the u-level technique.

[37] Table 2.2.2 shows that the entire R_θ=1400 data set is probably not long enough to generate long-time statistics significant to 10%, however this is also the case for the R_θ=3120 RLM data set. It is seen that some of the results calculated from these data sets do not conform to trends established by the other data sets, however those results are nevertheless shown for comparison purposes.

whose y-axes are scaled differently. This allows for the most precise determination of Reynolds number or y^+ trends, but it enjoins caution when making comparisons from plot to plot.

The performance parameters presented in this chapter will be evaluated on the basis of Reynolds number or y^+ trend for a given type of event and whether or not differences exist between results corresponding to sweep and ejection detections for a given data set. The analysis results will be presented in the same order in which the analyses were presented in Chapter 2. Sections 3.1-3.3 will be devoted to results from the three different visual detection approaches, and sections 3.4 through 3.6 will contain results from each of the different probe-based detection schemes.

3.1 LARGE-SCALE MOTION (LSM) RESULTS

The films resulting from Signor's outer-region ring-like motion study were analyzed in 1984-5 by Falco, et. al. (unpublished) to determine the start and stop times for LSM events as described in section 2.4.1. This analysis resulted in a database of visual detections which corresponded to the entire available database of hot wire data. The most detections (647) were available for the lowest speed (R_θ=730), and the fewest were available for the shortest data set (37 detections for R_θ=1400). This gave an outer-normalized total event time between 52 and 753 tU_∞/δ. Consequently we can expect fairly well-converged results for all except perhaps the R_θ=1400 data set. See Table 3.1.1.

Rao, Narasimha, and Badri Narayanan (1971) suggest that the frequency of inner-region bursts should be Reynolds number independent when scaled with outer variables; Blackwelder and Haritonidis (1983) suggest that inner variables will provide a Reynolds number independent scaling, while outer variables will provide a non-dimensional frequency which increases as $R_\theta^{0.6}$. These detections were all made by applying the VITA technique to inner-region hot wire data.

Since fewer than 200 LSMs were found at R_θ=3120, the frequency calculated at that Reynolds number is only marginally significant; with only 34 events, the usefulness of the R_θ=1400 frequency calculations is doubtful. For the three longer outer-region data sets then, inner scaling provides a dimensionless frequency which increases then decreases with Reynolds number. Outer and mixed scaling give dimensionless frequencies which decrease monotonically with increasing Reynolds number. It should be noted that the probes used had a spatial scale shorter than the $20U_\tau/\nu$ cutoff noted by Blackwelder and Haritonidis (1983), therefore spatial averaging should not have adversely affected these results.

The average event lengths scale poorly with inner or mixed variables, but when scaled with outer variables, the average event is approximately one boundary layer thickness in length[38] and relatively Reynolds number independent. Even the R_θ=1400 events which were detected averaged around 1δ in length.

_____

[38] Recall that a convection velocity of $1.0 \times U_\infty$ was used. A convection velocity of $0.9 \times U_\infty$ makes the outer-scaled lengths very close to one indeed, although the R_θ=3120 events are still a little longer than expected.

The most common long-time normalization of <uv> is to divide the average uv during events by the long-time RMS of uv. This normalization is presented in Table 3.1.1 for comparison with the percent Reynolds stress "captured". LSM detections capture between 45% and 60% of the Reynolds stress present in the outer region. The average turbulence kinetic energy during LSMs is 77% to 89% of the long-time RMS of the TKE. The RMS spanwise vorticity during LSMs from the three lower Reynolds number data sets is close to the long-time RMS of ω_z, while the RMS of ω_z during R_θ=3120 LSMs is only half of ω_z'.

The event averages for an LSM detection are shown with outer, mixed, and inner normalizations in Figures 3.1.1 through 3.1.3. One quarter of the ensemble's standard deviation at each point in time[39] is plotted as an error bar about each curve. Unfortunately the high variability of the LSM ensembles yields plots which have quite a messy appearance; see for example Figure 3.4.32 in which there is quite a large range of variability between the different quantities which were ensembled. The LSM ensembles show a relatively constant RMS which for each variable is almost an order of magnitude larger than the peak-to-peak variation in the average. The relative variation of the ω_z and $v\omega_z$ ensembles is larger than the others, though. Furthermore, the larger the sample size, the more nearly the ensemble average approaches zero as a limit.

These results suggest that the typical LSM event is not an active producer of the same kinds of turbulent motions throughout its entire lifetime. The high variability of u

---

[39] The mean ± 1/4 RMS for a Gaussian distribution gives limits within which only 20% of the samples will fall. Although the distribution at each point in time of these ensembles is not in general Gaussian, the high RMS values are strong indicators of the high variability of each variable at each point in time.

and v throughout the life of an "average" LSM indicates that high-intensity turbulent motions occur at random between the start and stop of an LSM. Outer scaling of the ensembled quantities produces values whose maxima have approximately the same magnitude; outer scaling does this better than mixed or inner scaling. However, the event averages show no agreement or consistent Reynolds number trend between all four data sets. This is probably attributable to the high variability shown by these averages.

3.2 RING-LIKE MOTION DETECTION RESULTS

The results of Signor's (1982) RLM analysis were converted into sweep and ejection start and stop times as described in section 2.4.2, and the long-time statistical performance parameters associated with those detections are shown in Table 3.2.1. Since six of the eight zones comprising a "typical eddy" are generally low-speed, outward-moving regions, it is not surprising that ejections generally outnumber sweeps 4:1. Unfortunately, even the ejections for each data set are fewer than 200 in number; the outer-normalized total event time varies from 4-10 for sweeps and 23-58 for ejections[40]. The events presented below should be considered in this light; they represent an indication of what this detection scheme might do on average if more samples were available.

---

[40] Detections from all four Reynolds numbers comprised Signor's "grand ensembles," so those results did not suffer from a paucity of data as do these.

Falco (1974) and Signor (1982) observed that the intermediate-scale ring-like motions which were observed had a length which was generally on the order of the Taylor microscale. Therefore it is not completely surprising that a mixed-variable scaling of the mean event frequency and mean event lengths produces results which exhibit the least Reynolds number dependence. The mixed-scaled frequency for ejections ranges from $100\text{--}124\text{x}10^{-6}$; the corresponding sweep frequency range is $20\text{--}34\text{x}10^{-6}$. Mixed-scaled ejections are slightly longer than sweeps, and this is probably a consequence of the length of zone 1 versus the other zones (see Figure 2.4.1). Since the RLMs were contained within the LSMs[41], it was expected that these events would be shorter than one boundary layer thickness in length, and they are.

The RLM contains a fairly low percentage of the Reynolds stress generated in the outer region, somewhere around 30%. Note that the 63% total detected in the RLMs at $R_\theta=3120$ must be a consequence of the different data set lengths; the 139 LSMs detected at this Reynolds number only contained 57% of the negative uv, and the long-time RLM percentage must be less than or equal to this, since RLM detections are a subset of LSM detections. Greater stresses are at work on average within an RLM, as shown by higher fluctuations in ω_z and higher average turbulence kinetic energy levels. This is also indicated by the fact that the average magnitude of uv as normalized by $(uv)'$ is greater for RLM's (about 0.6) than it is for LSM's (about 0.48).

Normalized ensembles of u, v, uv, ω_z, and $v\omega_z$ during an RLM sweep are shown in Figures 3.2.1-3.2.3; the outer-, mixed-, and inner-normalized ejection event averages are shown in Figures 3.2.4 through 3.2.6. High RMS levels are present once again,

---

[41] Smoke is required to detect an RLM, and since presence of smoke is the only LSM detection criterion, all RLMs must occur within an LSM detection time.

but the relative magnitude of the RMS compared to the peak of the average is lower than it was for the LSM. The peaks in the RMS generally fall on local minima or maxima in each plot; minimum RMS levels generally occur near zero-crossings. It is interesting to note that the RMS values for sweeps are usually lower than the corresponding ejection RMS values, even though (or perhaps because) there are significantly more ejections than sweeps. The negative average values for u during sweeps at R_θ=2380 are accompanied by the highest RMS values of all four data sets. This is not inconsistent with the results of Signor (1982), but it certainly is unexpected. As mentioned earlier though, Signor's results (especially Figure 3.33) are averaged over all four Reynolds numbers and have a correspondingly higher number of samples.

The rotational nature of the RLM tends to induce a sign change in v during the event, at which point uv goes to zero. This is doubtless a contributor to the reduction in Reynolds stress captured during RLMs versus LSMs. The positive ω_z fluctuations for the R_θ=730 and 2380 sweeps are not expected based on a consideration of Figure 2.4.1; fairly strong vorticity fluctuations of the sign of the mean are expected from both zones 1 and 2. However, those results are consistent with Figure 3.40 in Signor (1982). The negative peaks in the ω_z ensembles for both sweeps and ejections are also consistent with Signor's results. Note in Figure 2.4.1 that positive vorticity fluctuations are expected only from zones 7 and 8, while zones 3-8 have the u and v averages characteristic of an ejection. The contributions from the events of zones 1, 7, and 8 are undoubtedly the largest cause of the high RMS values present in the ω_z ensembles for both sweeps and ejections. The large variability in u during an RLM at the different heights associated with the different zones probably causes the very high variance seen in the <u> plots.

The RLM is a more active event on average than the LSM, and it appears to capture about half of the Reynolds stress which is present within the LSM. As noted in section 3.1 though, the LSM accounts for less than 60% of the negative uv present at $y/\delta=0.8$. The peak level of vorticity within an RLM averages 2 to 4 times higher than that present in the LSM, with a corresponding increase in the RMS vorticity. The RLM ejection generally has more energy than the corresponding LSM or RLM sweep. Once again outer variables produce normalized ensembles whose minima and maxima are of approximately the same magnitude. While there is poor agreement between the average behavior of u, v, uv, ω_z and $v\omega_z$ during sweeps at the four Reynolds numbers considered, those variables do have similar trends during the average RLM ejection event. It should also be remembered that these results may be preliminary in nature because of the relatively small number of events which were analyzed.

3.3 INNER-REGION VISUAL DETECTION RESULTS

The inner-region visual analysis described in section 2.4.3 was applied to all of the film available, and 96-530 sweeps and ejections were located with the probe at each different height above the wall. The shortest data set, $y^+=15.0$, gave the fewest detections, and the $y^+=14.6$ data set was taken with the probe almost at the same height above the wall in viscous units. Although the $y^+=15.0$ results are shown, it is expected that the $y^+=14.6$ results will provide a more accurate indication of what occurs around that location in the near-wall region[42]. The total detection times range

---

[42] Recall that detections from the $y^+=15.0$ film had the least uncertainty with respect to start and stop times. The only problem with this data set is that only one roll of film was shot, so the data set is smaller than one might like.

from 50–630 tU_∞/δ; the y^+=18.9 ejection detections have a statistical significance which is marginal. These data are summarized in Table 3.3.1.

Note that although the probes were moved, the event detection "point" was not. Small differences might also be inherent in the results, since the Reynolds number of these data sets did vary between 704 and 744. If the results are truly converged to their long-term values, the inner-scaled frequency and event length values should be accurate to ±10%. Results which vary by more than this amount should be due to differences in temporal and spatial resolution between the films which comprise the visual record of these data sets. These differences were discussed in section 2.4.3.

Blackwelder and Haritonidis (1983) show that bursting frequency increases from the edge of the viscous sublayer out to $y^+\approx40$, giving values for f^+ between 0.0018 and 0.0028. The events detected were ejections, and both the bursting frequencies and trend agree very well with the y^+=14.6 and 18.9 data shown in Table 3.3.1. As noted in section 2.4.3, there were problems with film graininess and temporal resolution which limited the scale of events that could be detected when the probe was positioned at y^+=24.2. This should have resulted in fewer events with generally longer length being detected, and one can see here that the y^+=24.2 frequency is indeed lower than what was expected. More sweeps than ejections were located using the inner-region visual analysis, resulting in a higher sweep detection frequency.

Ejections not only occurred less often, they also had a shorter average length than the visually detected sweeps. In appearance the sweeps most often looked like "pockets" as described by Falco (1980) and Lovett (1982). Ejections most often looked either like a ridge of low-speed fluid pushed up and out by a sweep or like a long streak which frequently appeared to be induced by a motion on one side or another

which contained streamwise vorticity[43]. Although the streaks were significantly longer than the streamwise spatial extent of the "pockets," it seldom happened that a streak moved lengthwise over the X-array while continuing to develop. This is what caused the calculated length of an "average" ejection to be shorter than the "average" sweep. The events detected at $y^+=18.9$ were shorter than the corresponding events at 14.6, but those lengths seemed to increase marginally from 18.9 to 24.2. This apparent length increase was probably due to the analysis difficulties discussed above and in section 2.4.3; an increase in length was the expected effect of these analysis problems.

Visually detected ejections capture about a quarter of the Reynolds stress in the near-wall region, while sweeps account for another 40% or so. This is a little more than the RLM and LSM detections in the outer region and corresponds roughly to the performance of the uv-quadrant technique with a threshold of 1. Both sweeps and ejections contain spanwise vorticity fluctuations which are about as intense as the long-time RMS of ω_z. The average turbulence kinetic energy associated with an ejection is higher than the TKE RMS and increases with distance from the wall, while the sweep's average TKE is less than the RMS and decreases with increasing y^+.

Ensemble averages of u, v, uv, ω_z, and $v\omega_z$ during inner-region visual detections are shown in Figures 3.3.1 and 3.3.2. The level of variance in these averages as indicated by the RMS of those values is high, but again not as high as that for the LSM ensembles. This detection scheme was designed to locate sweeps and ejections on the basis of visual information, and the ensembles show that this is indeed what was done on average. The average streamwise velocity of these motions is higher around $y^+=15$

---

[43] Here is a good instance of two uniquely identifiable motions which contribute to turbulence production, have attributes of an "ejection", yet have quite dissimilar physical characteristics like spatial extent and temporal duration.

than it is further out in the boundary layer; the wall-normal velocity is highest at $y^+=18.9$. The ω_z plot shows that on average an increase in vorticity[44] occurs just before the passage of a sweep at the lower probe positions. This correlates nicely with the observation that an ejection often preceded a sweep, and that ejection can be expected to have a higher vorticity intensity than the mean. A decrease in vorticity is associated with the passage of a visually detected sweep when the probes are higher up, although the magnitude of this change is less for the $y^+=24.2$ case. This tends to support the observation that these visually detected events most often looked like the "pockets" described by Falco (1980) and Lovett (1982).

Peaks in the v ensemble reveal that visual detections tend to miss the earlier part of the event. The smoke which was observed in order to make the visual detections marked only the viscous sublayer, whereas the probes were always located above $y^+=7$. Sweeps, moving wallward as they do, should have passed the level of the probes before reaching the viscous sublayer where they would act on the smoke. Therefore it is logical that the v excursion for sweeps should begin well before the start of a visual detection. It is however surprising that the wall-normal velocity also tends to be fairly high by the time a visual ejection starts, and that the v peak at $y^+=18.9$ occurs before the start of visually detected ejections. This suggests that the motions which are classified as ejections by probe-based schemes might not originate in the viscous sublayer; rather an upward motion starting further out entrains fluid from the sublayer which subsequently appears to be an ejection.

---

[44] Recall that the mean shear stress produces an average spanwise vorticity which is negative, therefore negative excursions of ω_z about the mean produce an increase in the magnitude of the spanwise vorticity.

There are a number of other possible explanations for the behavior of the v ensemble during ejections: The inertia of the oil droplets might have induced a delay in the response of those particles, but that should also have caused non-zero u and v ensembles at the end of the visual events which is not the case. The uncertainty associated with determining the start and stop of a visual event might have been biased toward later in the event, although that should also have resulted in an offset at the end of the event which isn't apparent. The criteria for locating the start of an event might have been applied too strictly, forcing the presence of strong motions to cause the smoke activity which was required before an event was said to exist. However, even the latter explanation does not account for the fact that the peak in the $y^+=18.9$ ensemble occurs before the start of the event. Therefore, it seems most likely that the explanation at the end of the previous paragraph is the correct one, that is, events frequently originating above the viscous sublayer entrain fluid from the sublayer to produce the visual signature which the present analysis classifies as an ejection.

The "average" inner-region visually detected event is a fairly vortical structure which loses its turbulent energy as it gets closer to the wall. The sweeps usually penetrate to at least $y^+=15$, and the ejections tend to rise at least that high but not usually up to $y^+=18.9$, although the strongest vertical motions are generated at that point, occurring *before* the start of the average visual ejection. A total of 60% to 70% of the Reynolds stress generated in the near-wall region is contained within events located by applying the inner-region analysis described in section 2.4.3. The requirement that an event be active before it is said to exist results in an asymmetric ensemble, with peak values in u and v occurring near the start of an "average" event.

3.4 uv-QUADRANT ANALYSIS RESULTS

The uv-quadrant analysis technique was applied to both the inner- and outer-region data sets, and the results from these analyses are shown as a function of thresholding constant in the figures of this section. Figures 3.4.1 - 3.4.3 show the number of events detected when this technique was applied to the data sets used for inner-region, RLM, and LSM visual detections. Note that fewer than 200 events are detected for the $y^+=15.0$ data set, but the corresponding results will be included anyway. For thresholding constants larger than 1.0, fewer than 200 of each type of event are detected at any probe height in the inner region. In the outer region that point is reached after c exceeds 3.6. Outer-region events must be of shorter duration[45] than inner-region events detected with the same threshold, since fewer events in the inner region produce total event times of greater than 200 tU_∞/δ until c goes above 1; the corresponding outer-region threshold limit is 0.7. As expected because of the brevity of the RLM data sets, this analysis produced only a very limited number of events to be compared with the RLM detections in Chapter 4. Total event times are shown under inner, outer, and mixed normalizations in Figures 3.4.4-3.4.12.

Note that when the threshold is zero, the number of sweeps for a given data set is approximately the same as the number of ejections. As the threshold increases, fewer sweeps are eliminated in the near wall region, in contrast to the wake region where fewer ejections are eliminated. Since the Reynolds stress is the detected variable in this scheme, an incremental increase in the thresholding level should eliminate fewer events from the quadrant containing the Reynolds stress peak. Therefore the event frequency as a function of threshold is a result of the detection criterion used and the

---

[45] That is, outer region events are of shorter duration under outer variable normalization.

probe location.

The number of events and the total time during which a detector is "ON" are functions of the data set length as well as threshold, so agreement between data sets is not expected. As noted earlier though, it is expected that inner-region event frequency (Figures 3.4.13 - 3.4.15) should be approximately constant for a given threshold when scaled with inner variables. The sweep and ejection frequency for each data set is about the same, but neither good agreement nor the slight increase with y^+ which was observed by Blackwelder and Haritonidis (1983) using the VITA technique is seen with this technique using any scaling.

In the outer region however, inner variables do appear to do a good job of scaling uv-quadrant detection frequency (Figures 3.4.16 - 3.4.18), with the exception of the R_θ=2380 data. Note that the sweep frequency is lower than the ejection frequency in the outer region for uv thresholding constants greater than 1.0, and recall that we expect frequency results to be significant through thresholds of 3 or so.

Event lengths (Figures 3.4.19 - 3.4.24) were scaled with inner, outer, and mixed variables. It can be seen that sweep events are longer than ejection events for $y^+\leq15$. Inner-scaling suggests that inner-region events get shorter with increasing y^+, however this trend is not observed under mixed or outer normalizations. One expects the inner-region event length to scale with inner variables, though, and the lack of agreement noted above may be a result of the event convection velocity chosen. As indicated earlier, it was assumed that convection velocity is only weakly dependent on distance from the wall. R. E. Falco[46] argues that coherent motions would not remain

---

[46] Private communication.

recognizable as such if they experienced a convection velocity which varied significantly from top to bottom. A. Naguib[47] indicates his data support the notion that convection velocity is not approximately constant at $0.6U_\infty$ throughout the near-wall region[48]. If convection velocity does indeed increase with distance from the wall, it might be seen that average event length scales with inner variables and is not a function of distance from the wall (Figure 3.4.25).

The essence of the uv-quadrant breakdown is that events are classified by the magnitude of the Reynolds stresses they generate. The events considered here are only those which generate negative uv, and the percentage of the negative uv "captured" by these events is shown in Figures 3.4.26 and 3.4.27. The first of these figures shows good agreement with results from $y^+=50$ presented by Alfredsson and Johansson (1984). Note that those authors plotted the total $-\overline{uv}$ as a consequence of +138% from quadrants 2 and 4 and -38% from quadrants 1 and 2; their 78% contribution from the second quadrant[49] would be shown as 57% in Figure 3.4.27. These results are undeniably a consequence of the detection criterion used.

The RMS vorticity fluctuations are shown in Figures 3.4.28 and 3.4.29. It is clear from Figure 3.4.28 that both sweeps and ejections in the inner region, with the exception of ejections occurring at $y^+=14.6$,[50] produce spanwise vorticity fluctuations which are about as intense as the long-time RMS of ω_z. Figure 3.4.29 offers a much less

---

[47] Private communication, supported by comments from C. Wark and H. Nagib.

[48] It is interesting to note that Naguib uses the uv-quadrant breakdown with a threshold of 3 to detect events downstream of a wall-mounted shear stress sensor. He calculates convection velocity for sweep events by noting the average time required for them to travel from the upstream detection point to the one downstream.

[49] Alfredsson and Johansson (1984), p. 331.

[50] The $y^+=15$ ω_z' values do not show good agreement with the $y^+=14.6$ results, however this may be due to the different data set lengths as discussed above.

straightforward interpretation. Among the ejection detections, vortical intensity varies by a factor of five as it increases from R_θ=3120 to 730 then to 2380 and 1400. The ω_z RMS associated with R_θ=3120 sweep detections increases initially but then falls, while the vortical intensity of R_θ=2380 and 730 sweep detections increases monotonically with threshold. About the only consistent conclusion which can be drawn from Figure 3.4.29 is that for thresholds of 0.9 or higher, ejections have larger fluctuating spanwise vorticity intensities than sweeps in each data set.

The turbulence kinetic energy of events detected by the uv-quadrant technique is shown in Figures 3.4.30 and 3.4.31. Events corresponding to the quadrant in which the Reynolds stress peak is located should, on average, produce a greater level of TKE[51]. As noted above, sweeps are the dominant Reynolds stress producers at $y^+ \leq 15$, so the results shown in these two figures are simply what was expected based on the detection criterion and the distribution of the detected variable as a function of y^+.

Calculating event averages requires that a threshold be chosen which can be applied at the four different Reynolds numbers to be plotted. Some authors (e.g., Bogard and Tiederman, 1984) have chosen their threshold levels so that the number of probe-based detections is the same as the number of visual detections. Authors who are not looking for a high level of correspondence with visual data (e.g., Alfredsson and Johansson, 1983) tend to choose higher thresholds in an effort to select only the strongest events for analysis. To achieve the same number of probe-based detections as visual detections would require a threshold of 0.2 in the inner region, 2.0 for the ring-like motion data, and a value increasing with Reynolds number from 0.2 to 3.0

---

[51] Recall that in the absence of the spanwise fluctuating velocity component, w, TKE is calculated as the square of u plus the square of v.

for the large-scale motion data. The statistics based on number of events (as opposed to total detection time) were well-behaved generally up to thresholds of 3, and stronger events were more interesting than weaker ones, so a threshold of 2.45 was used to calculate the event averages shown in this section.

Ensembles of the uv-quadrant sweep detections are shown in Figures 3.4.32-3.4.34, while the ejection ensembles are presented in Figures 3.4.35-3.4.37. The detection algorithm used specifies that the magnitude of uv will have a given value at the start and end of an event. Therefore the uv plot crosses the start and stop time marks at the threshold level, resulting in a variance for uv which is zero at those times with a peak in the middle of the event. Both u and v had to be fairly large for their product to exceed the threshold, and this resulted in a significantly lower variance for <u> and <v> when compared to the visual detection ensembles.

Outer scaling of both sweeps and ejections produces v ensembles which are noticeably grouped into two curves, R_θ=730 & 1400 and R_θ=2380 & 3120. The low variance for all of these curves suggests that this is more than just coincidence, that uv-quadrant events in the outer portion of the boundary layer have <v> magnitudes which scale with the free stream velocity and that those relative magnitudes become larger at higher Reynolds numbers. Inner scaling produces a clear Reynolds number trend in the v ensembles while causing the <uv> curves to group in the same way that the <v> curves did under outer scaling. It was not expected that any variables would cause universal scaling of the <uv> curves since the threshold level is the product of u′ and v′, both of which are Reynolds number-dependent quantities (Klewicki, 1989).[52] Inner scaling is the clear choice for <uv>, and it should be related to a Reynolds

---

[52] See also Wei and Willmarth (1990).

number shift in $\overline{uv}$ statistics at $y/\delta=0.8$, but inner scaling effectively eliminates comparisons of ω_z and $v\omega_z$ ensembles.

The ω_z variance is fairly large, especially for the ejection detection ensembles. However, all four Reynolds numbers follow the same trend (seen best under outer scaling in Figures 3.4.32 and 3.4.35), that of a strong vortical pulse at the start of the event which relaxes toward zero. Recalling that Ω_z is less than zero in the near-wall region, the negative vorticity fluctuation during an ejection is likely to result from the upward convection of more intense ω_z from nearer the wall at the start of the event. Similarly, inward convection of less vortical fluid from outside the boundary layer during a sweep would result in the positive fluctuation observed on average at the start of a sweep.

The "average" uv-quadrant detection is either a sweep or ejection whose frequency, event length, turbulence kinetic energy, and u, v, & uv event averages can be directly related back to the distribution of Reynolds stress throughout the boundary layer and the choice of thresholding constant. The outer-region event is characterized by a fairly strong initial peak in the spanwise vorticity[53] which relaxes toward zero as the event progresses.

---

[53] Note that the ω_z peak is larger than the RMS of the average at that point in the normalized event time.

3.5 TERA ANALYSIS RESULTS

The TERA analysis was applied to both the inner- and outer-region data sets described in Chapter 2, and the results of these analyses are shown in this section. All but the shorter 3 data sets (R_θ=1400, y^+=15.0 and 18.9) produced an adequate number of events (Figures 3.5.1 - 3.5.3) for thresholds up to 2 in the inner region and 3.5 in the outer region. As was the case with the uv-quadrant analysis, slightly lower thresholds (just less than 2 for both inner and outer regions) produced total event times (Figures 3.5.4 through 3.5.12) which exceeded $200tU_\infty/\delta$ in duration.

No set of variables scales the inner-region detection frequency (Figures 3.5.13 - 3.5.15) so that it is independent of y^+, although outer scaling does appear to minimize the differences. One can see most readily in Figure 3.5.14 the effects of grouping on the frequency of TERA detections. Note that the frequency of y^+=14.6 ejections, y^+=15.0 ejections, and y^+=24.2 sweeps *increases* initially with increasing threshold. This is accompanied however by a steadily decreasing total event time. The cause of this is a combination of grouping and low threshold: At low threshold events are long and close together, so the grouping process joins them up into a number of very long events. As threshold increases, fewer of the events are close enough to be grouped, so the total number of bursts detected increases, while the total event time goes down. The apparently constant frequency of the y^+=14.6 sweep, y^+=15.0 sweep, and y^+=24.2 ejection detections may also be a result of the grouping process and not some underlying physical mechanism. As shorter events are eliminated with increasing threshold, some grouped events are splitting up, thereby creating a relatively constant total number of events, again with steadily decreasing total event time.

Outer-region TERA detection frequencies (Figures 3.5.16 - 3.5.18) behave in a fashion very similar to the outer-region uv-quadrant detection frequencies. They scale well with inner variables for thresholds of one or more. Sweeps occur less often than ejections, and the R_θ=2380 detections seem to occur more often than any others. High-speed events in the outer region seem to have less turbulence kinetic energy than their low-speed counterparts, and the Turbulence Eenergy Recognition Algorithm detects this.

Inner-region event lengths (Figures 3.5.19 through 3.5.21) seem to scale well with inner or mixed variables, but again the events further out in the boundary layer appear to be shorter than those nearer the wall. This may be a result of the convection velocity chosen; see the discussion in section 3.4 above. The strongest events appear to have relatively constant lengths varying with y^+ and ranging from 30 to 80 viscous units (0.2-0.4 δ)[54]. However, this appearance may be deceptive because of the relatively few number of events detected at thresholds above 2.

Inner scaling of outer-region sweep detections (Figure 3.5.22) produces good agreement between the R_θ=730, 1400, and 3120 results. Mixed scaling (Figure 3.5.23) produces relatively good agreement between all data sets except R_θ=3120. In any event, TERA-detected sweeps in the outer region are longer than the corresponding ejections, and those sweeps appear to have a length scale of around 50 viscous units. It is interesting to note that under outer scaling (Figure 3.5.24), all events tend to a length between 0.05 and 0.15.

---

[54] Recall that the convection velocity used was 1.0U_∞.

Since TERA-detected inner-region events decrease in length with increasing y^+, it is not surprising that event length divided by height above the wall (Figure 3.5.25) is strongly dependent on y^+.

It is very interesting to note that at a threshold of zero, the TERA detector was "ON" approximately 50% of the time in both the inner and outer regions[55]. During this time, 100% of the total Reynolds stress was generated in both regions (Figures 3.5.26 and 3.5.27). Although wall-normal velocity information was unavailable to the TERA detector, its negative uv performance is very similar to the uv-quadrant technique.

The intensity of the spanwise vorticity fluctuations during detected events is shown as a function of the TERA thresholding constant in Figures 3.5.28 and 3.5.29. In the inner region sweeps appear to have a higher level of vorticity fluctuation, but this level increases for all detected event types well past the limit of statistical significance (c=2). In the outer region TERA-detected sweeps and ejections stemming from the same data set have about the same level of vorticity fluctuations, but no clear Reynolds number trend is seen.

It is not at all surprising that the turbulence kinetic energy (TKE) of TERA-detected events increases with increasing threshold. TERA detections are based on the temporal derivative of the streamwise TKE, so requiring a higher level of this value at the start of events must result in a higher level of TKE during the event. The threshold dependence of this result is a consequence of the detection criterion, but the distribution of TKE between high-speed and low-speed events and the differences

---

[55] Compare for example, Figures 3.5.3 and 3.5.5 with Tables 2.1.2 and 2.2.2.

between those distributions from the inner to the outer regions is caused by the physics of the flow.

The plots of Reynolds stress "captured" and turbulence kinetic energy present during uv-quadrant and TERA detections show clearly that there is a strong correlation between high TKE and large Reynolds stress values. Regardless of whether one looks for a large magnitude for uv or $\partial(u^2)/\partial t$, one will find both high Reynolds stress and high TKE levels. This seems to be a result of the flow physics more than a consequence of the detection criteria employed.

Once again it was impossible to choose a threshold level for creating ensembles which would give the same number of events as were detected visually, although a threshold of 1.5 yielded approximately the same total number of TERA detections as LSMs at $R_\theta=730$. The 1.5 threshold was also generally within the level of statistical significance both in terms of total detection time and in terms of the number of events detected, so that value was used to create Figures 3.5.32 through 3.5.37. It can be seen in those figures that outer variables scale these variables best for comparison purposes, especially ω_z and $v\omega_z$.

The u trace is the one most directly influenced by the detection criterion used; the characteristic upward (or downward) slope through the beginning of the event, peak, and slow decline through the end are all a result of how the start and end of an event are defined. On the average the wall-normal velocity, v, behaves opposite u, and this behavior is not "programmed in" by the detection scheme. However the RMS values show that v occasionally does have the same sign as u for both sweeps and ejections; the higher average v peak shown in Figures 3.5.35-37 is simply accompanied by higher RMS levels. The behavior of v strongly affects the average and variance in

plots of uv and $v\omega_z$.

Inner scaling produces the same kind of grouping in the <u> curves which was seen in the <uv> curves for uv-quadrant detections. This is seen in the good agreement for the R_θ=730 & 1400 <u> plots versus the R_θ=2380 & 3120 plots. Furthermore, the v and uv ensembles for TERA ejections exhibit the same Reynolds number trend when scaled on inner variables (see Figure 3.5.37). The threshold level for the TERA detector is based on $u\partial u/\partial t$, suggesting that the Reynolds number dependencies noted above are related to a correlation between the long-time $u\partial u/\partial t$, u, v, and uv statistics at y/δ=0.8. If no such correlation exists, then the observed trends must be related to changes in the outer-region motions detected by the TERA algorithm.

What is an "average" TERA event? At lower threshold levels TERA events contain a great deal of Reynolds stress. At higher threshold levels both sweeps and ejections throughout the boundary layer are about around 50 viscous units long[56]. TERA-detected events have high vorticity fluctuations around an essentially zero mean value, implying uniform distribution of positive and negative spanwise vorticity fluctuations during an "average" event. Even strong TERA-detected sweeps do not usually penetrate to y^+=15; strong TERA ejections do not generally rise above that level. In Reynolds stress capture and TKE versus threshold performance, the TERA detector is very similar to the uv-quadrant approach, but this is not entirely reflected in the "average" events calculated using event-based conditional averaging.

---

[56] That is, assuming a convection velocity of $0.6U_\infty$ in the inner region and $0.9U_\infty$ in the outer region.

3.6 u-LEVEL ANALYSIS RESULTS

The u-level analysis as modified to detect sweeps (see section 2.5.3) was applied to all the data sets available, and those results are presented in this section. The number of events (Figures 3.6.1 through 3.6.3) is of the same order of magnitude as the number of events detected by the TERA and uv-quadrant techniques. This means that something other than number of events must used to pick a thresholding constant with which to generate ensembles, since it is impossible to pick one threshold which will provide the same number of u-level detections as visual detections for all data sets. A threshold of 0.5 or less provides more than 200 events and more than $200tU_\infty/\delta$ for most of the inner region data sets; 1.3 is a reasonable cutoff to use with the detections made on the LSM database. Normalized total detection times are presented in Figures 3.6.4 - 3.6.12.

Inner-region event frequency (Figures 3.6.13-3.6.15) is once again an irregular function of y^+ which does not scale with inner variables as noted by Blackwelder and Haritonidis (1983). Outer variables provide reasonable agreement between the inner 2 and outermost event detection frequencies, but the cause of the $y^+=18.9$ behavior remains an enigma. Note that the sweep event frequency is the same as the ejection event frequency regardless of threshold; the number of sweeps detected does not decrease faster than the number of ejections as it did with the TERA and uv-quadrant detection schemes.

Outer-variable scaling of outer-region detections gives a dimensionless event frequency which decreases with increasing Reynolds number. Other than that, no consistent Reynolds number trends are the result of scaling with inner, outer, or mixed variables. Outer-region event frequencies are shown in Figures 3.6.16 through 3.6.18.

Note that all of the inner- and outer-region event frequencies are steadily decreasing functions.

Average event lengths are shown in Figures 3.6.19-24. The most curious result is the fact that the average event length is relatively constant for each event type, regardless of thresholding constant. Also, all sweep detections are at least as long as the corresponding ejection detections, regardless of probe height. It was seen that the number of events and therefore event frequency both decrease steadily as threshold increases, yet the remaining events have the same average length. This stands in contrast to the results of Luchik and Tiederman (1987) who found that a parabolic profile best described the average event frequency. (They didn't report on event length, however.)

None of the scalings used generated a dimensionless frequency which was either independent of probe height or consistently dependent on y^+ or R_θ. The u-level detections are long events, 350-550 viscous units in length in the inner region and 250-650 viscous units in the outer region. In the inner region between 1.5 and 3 boundary layer thicknesses pass during the average u-level detection; in the outer region the average length is $0.45 - 1.3\delta$. Inner-scaled event lengths in the inner region already have approximately the same value, although the ejections located further than $y^+=15$ from the wall tend to be shorter than the rest. Normalizing these values by height above the wall (Figure 3.6.25) creates a non-dimensional length which is inversely proportional to y^+, just as it happened with the uv-quadrant and TERA detections.

At zero threshold the u-level detection function is on 100% of the time, detecting either a sweep or an ejection. Consequently, at zero threshold the u-level technique must detect 100% of the Reynolds stress generated throughout the boundary layer.

More interestingly, over 80% of the total Reynolds stress[57] is still being detected at threshold levels of up to 0.7 in both the inner and outer regions (Figures 3.6.26 and 3.6.27).

The inner-region ω_z fluctuation intensity during events is about the same as the long-time RMS of ω_z in the inner region, regardless of threshold. Outer-region sweeps detected with threshold levels of 1 or less have an RMS which is about 80% of the overall vorticity intensity, while the vortical intensity of ejections is 120%-130% of the long-time RMS. However, this does not apply to the $R_\theta=3120$ data set, even though such large irregularities in ω_z intensities are not observed with the uv-quadrant and TERA techniques[58]. In any event, u-level detections seem to have vorticity fluctuations which are generally of the same order as the long-time ω_z' values at each probe location and Reynolds number.

The mean turbulence kinetic energy plots (Figures 3.6.30 and 3.6.31) are almost identical to those associated with the TERA detection scheme, and they are also a result of the detection scheme itself. As noted above, the level of TKE with respect to threshold is a function of the detector, but the *distribution* of TKE between high-speed and low-speed events must be a result of the flow physics and not the detection criteria. Requiring higher levels of u during an event will inevitably raise the turbulence

---

[57] The total Reynolds stress captured is the sum of the contributions made by both sweep and ejection detections made on the same data set.

[58] Close examination of Figure 3.6.29, the u-level ensembles, the profile of ω_z during VITA detections, the VITA sweep ensemble, and the $<\omega_z>_{events}/\omega_z'$ calculated on the basis of the RLM data set (Table 3.2.1) suggests that there are one or two points late in the $R_\theta=3120$ data set at which a massive jump in vorticity occurs. This point occurs within detections made only by the VITA and u-level techniques, but it is buried in over 50,000 data points, so it has not been found yet. It is apparently these one or two points which cause such strange behavior in the VITA and u-level event averages, as well as the excessively high ω_z' value which makes the normalized ω_z RMS during $R_\theta=3120$ events so low.

kinetic energy associated with those events, since TKE is directly related to the square of the streamwise velocity fluctuations. These figures show results one would expect from this detection algorithm.

A threshold had to be chosen before the ensembles for the u-level detector could be calculated. It was decided to use the highest threshold which still permitted over 80% of the Reynolds stress to be "captured" by u-level detections. The threshold 0.7 was also acceptable in terms of number of events and total detection time. That threshold was low enough so that the anomaly which affects the vorticity RMS for sweeps was still included. However, eliminating the ω_z anomalies would have required a threshold in excess of 1.8, and that would have produced unacceptably low total event times.

The event averages of the outer region u-level sweep detections are shown in Figures 3.6.32-34; the corresponding ejection plots are presented in Figures 3.6.35 through 3.6.37. Outer variables once again provide the best normalization for comparing magnitudes of ω_z and $v\omega_z$, and it is not at all surprising that outer variables scale <u> best at $y/\delta=0.8$. Inner-variable scaling produces the same Reynolds number trends discussed in the two previous sections, including the grouping of <uv> and <v>, although those are not variables used by the detection algorithm. One notable difference is the fact that outer variables scale the <uv> ejection ensemble fairly well, a feature not present in TERA or uv-quadrant detections.

Similar to the TERA detection scheme, the average character of the u signal is determined by the detection criteria used: At the start and end of the event, u is equal to the threshold levels used to initiate and terminate events, so the RMS of the average goes to zero at these points. The magnitude of u is large during an event, peaks

before the midpoint, and relaxes to zero slightly after the event ends. The average trend of v during an event is such that Reynolds stresses will be produced most of the time. The RMS of the v average is large though, indicating that v occasionally has the same sign as u. Although the shape of the Reynolds stress curve is similar to that associated with the "average" uv-quadrant detection, the level of the standard deviation is the same while the average value is one order of magnitude smaller (compare Figure 3.4.32 with 3.6.32). The shape of the R_θ=3120 ω_z plot has already been discussed above.

The "average" u-level event is a long event, regardless of the threshold used. Like TERA detections, u-level events contain a very large percentage of the Reynolds stress generated when lower threshold levels are used. Unlike TERA though, the u-level detector is always "ON" at thresholds of zero, so not only is all of the negative uv "captured" then, but all of the positive contributions to the Reynolds stress correlation are also accounted for. The "average" u-level ejection has a higher level of vorticity fluctuations above y^+=15 than the corresponding sweep. It is quite interesting to note that the spanwise vorticity intensity during u-level events is generally independent of threshold (Figure 3.6.29). Even strong u-level sweeps do not usually get down as far as y^+=15, while strong u-level ejections do not generally rise above that level. Like uv-quadrant and TERA detections, a u-level event will have a level of turbulence kinetic energy which is directly related to the thresholding constant used.

CHAPTER 4

A COMPARISON OF VISUAL- AND PROBE-BASED DETECTIONS

Several different notions of what characterizes an important event have led to the development of methods to detect those motions as well as parameters to measure how well those detections were performed. The best-defined average characteristic of the motions studied is the streamwise velocity signature, which generally was a result of the detection scheme applied[59], although even the u-signature was poorly defined in the case of the LSM. In broad terms, the detection schemes have been applied in an attempt to locate the presence of sweeps (high-speed, wallward moving events) and ejections (low-speed, outward-moving events). Ensembles have shown that these are indeed the "average" events being detected, so the question naturally arises as to whether or not the *same* events are being detected by these different approaches.

If one knows that a particular scheme does indeed locate the physical process of interest but wishes to use a simpler detector to locate those same events, the problem of threshold choice for the second detector scheme arises. Bogard and Tiederman (1983), Luchik and Tiederman (1987), and others have chosen thresholds for the second detector such that the number of events and thereby the mean event frequency

---

[59] In the instance that detections were made visually, the apparent velocity could be directly related to the best-defined characteristic, which in this case was visual in nature.

are the same. However, one cannot argue that the same events are being located simply because the same number of events have been found. If one wishes to compare long-time statistical quantities in order to optimize threshold choice, it would make sense to compare parameters which are related to the physics of the events to be detected, e.g., the percentage of Reynolds stress located.

The other method available to optimize threshold relies on an evaluation of the one-to-one correspondence between detections made by the two schemes under examination. P(E) and P(D) give an indication of the long-time correspondence; P(T) gives an indication of the event-resolved correspondence between detections. The general problem with these three, although it applies particularly to P(E), is that the longer the events are which the second detector locates, the greater the likelihood that there will be some overlap with an event found using the first scheme. It will be seen in coming sections that P(E) and P(T) have their highest peaks when the second detector's threshold is zero. Therefore, something other than maximizing these two functions must form the basis for the choice of threshold if P(E) and P(T) are to be used. Luchik and Tiederman (1987) selected thresholds which gave the same average event frequency, but this was also the point where P(E) and P(D) had the same value. Since P(T) gives information about how often detections occur before, during, and after the reference events, the combination of a high peak during and low peaks before and after could be used to set limits on the threshold for the second detector.

Reynolds stress-producing events are obviously located best by the uv-quadrant technique, but events which produce high uv magnitudes are not necessarily "coherent motions." Economikos, Shoemaker, Russ, Brodkey, and Jones (1990) have recently been working on the assumption that the general location of a coherent motion is best detected visually, after which the velocity and vorticity fields associated with that

region in space are determined. In any event, the velocity and vorticity signatures associated with a coherent motion cannot be determined from an *a-priori* examination of only those time traces. Therefore if the goal is to locate a particular coherent motion, it makes sense to start with visual detections and compare the long-time performance and event-to-event correspondence of those visual detections with probe-based detection schemes that are intended to locate the same kind of event[60]. In this chapter that approach will be taken, and the correspondence of probe-based detections to the three different kinds of visual detections presented in chapters 2 and 3 will be evaluated.

For each of the three visual detection criteria applied in Chapter 3, the long-time statistical performance of the visual detections will be compared with that of the probe-based detection schemes in an effort to determine whether any threshold can be chosen which makes the probe-based detector perform the same as the visual-based detector, regardless of Reynolds number or probe height. The correspondence between the visual detector and the three different velocity-based detection schemes will also be evaluated. Altogether, this should give a good indication of how different the events really are which these six detection methods locate.

---

[60] It should be noted however that these comparisons can be applied to any two intermittency functions, one of which should already be able to locate the events of interest. For example, it would be interesting to compare the zero-threshold TERA and uv-quadrant detection correspondences, since both of those approaches detect 100% of the Reynolds stress in the boundary layer with approximately the same level of intermittency.

4.1 LARGE-SCALE MOTIONS AND THE PROBE-BASED DETECTORS

Before addressing the one-to-one correspondence issue, it is useful to consider what conclusions can be drawn regarding differences in detections based on differences in the long-time performance parameters presented in chapter 3. As mentioned in Chapter 3, it was impossible to select a thresholding constant for any of the probe-based detectors used which consistently yielded the same number of events as were detected visually. Referring to Figure 3.4.3 and Table 3.1.1, one can see that the total number of events[61] detected by the uv-quadrant technique with a threshold of 2.45 is fewer than the number of LSMs detected at $R_\theta=730$ or 2380, but it is more than the number of LSMs detected at the other two Reynolds numbers. The TERA detector with a threshold of 1.5 located approximately the same number of events as LSMs at $R_\theta=730$, although more events were located at the three other Reynolds numbers. The u-level detector with a threshold of 0.7 located between two and three times as many events as LSMs for all four Reynolds numbers. For all of the probe-based detectors used, it would be impossible to match the number of detections to the number of LSMs for more than one data set at a time. Since mean event frequency is directly proportional to the number of events detected, the frequency of LSM detections will be higher (or lower) than that of probe-based detections at a given Reynolds number if more (or fewer) LSMs were detected.

The inner-scaled average LSM length varied from 300 to 1500, a range even wider than that exhibited by the u-level detections. The TERA and uv-quadrant

---

[61] "Total number of events" refers to the sum of the number of sweeps and the number of ejections for those detectors which can locate both. Recall that the ensembles presented in Chapter 3 were made with the following thresholds: uv-quadrant, 2.45; TERA, 1.5; u-level, 0.7.

detections were generally between 30 and 150 viscous units in length; the u-level detections ranged between 150 and 700. Surprisingly, the average u-level sweep from the R_θ=730 data set was longer than the average LSM at that Reynolds number; otherwise all of the probe-based events had an average length shorter than that of the corresponding LSMs. In any event, mean event length cannot be used as an indicator of the correct threshold to choose for any of the three probe-based detectors under consideration.

For the uv-quadrant technique, a threshold of 1.9 would match the Reynolds stress "captured" by this technique at R_θ=730 to that located by the LSM visual detections. However, that threshold is 2.3 for the R_θ=1400 data and about 1.5 for the R_θ=2380 and 3120 data sets. For the TERA technique thresholds between 0.8 and 1.8 are required to match this parameter; for the u-level technique the threshold range is $1.5 \leq c \leq 2.1$.

As noted earlier, the TERA and uv-quadrant techniques had very similar vorticity intensity and TKE distributions at least up to the limiting thresholds for each detector (Figures 3.4.29 and 3.5.29). At thresholds of zero, the vorticity and TKE levels are about the same for these three detectors, but only the vorticity associated with R_θ=3120 ejection detections can be matched with LSM detections at that Reynolds number for non-zero threshold levels. As with event frequency, a different u-level threshold is required for each data set in order to match vorticity or TKE performance with the corresponding LSM value. One can therefore conclude that none of the parameters considered, including number of events and average event length, can be used to decide on a threshold independent of R_θ for any of the probe-based detection schemes under consideration. Matching probe- and visual-based performance at one Reynolds number (when possible) only produces a performance mismatch at the other

Reynolds numbers.

Although the magnitude of the average LSM streamwise velocity peak is a factor of 2-4 times smaller than that obtained with the probe-based detection schemes used in this study, the average LSM event is low-speed in nature. Therefore it was decided to study the correspondence between LSMs and ejections located with the uv-quadrant, TERA, and u-level techniques. The reader is reminded that a significant number of events were detected up to thresholds of 3.5 for the uv-quadrant and TERA techniques; the cutoff for u-level detections is about 1.3. Please recall also that only 34 and 139 LSMs were detected in the R_θ=1400 and 3120 data sets, respectively, versus over 500 events each for the other two Reynolds numbers.

P(D), the probability of a visual detection occurring during a probe-based detection, is shown as a function of threshold in Figures 4.1.1 through 4.1.3. The most notable feature of these plots is that the value is so nearly constant, remaining between 45% and 75% from zero up to the threshold limits for all three detectors. One should also note however that the value of P(D) for a given data set does vary with threshold, going up and down without any particular trends. Luchik and Tiederman (1987) observed a steadily increasing trend for P(D) when visual detections were compared with uv-quadrant, u-level, and VITA probe-based detections made at y^+=30; this trend is not apparent in any of these results[62]. The same authors also observed a linearly decreasing trend in P(E) in their study, and while a strictly linear threshold dependence cannot be seen in Figures 4.1.4 through 4.1.6, a monotonic decrease is present. Note that P(E) does not start at 100% for any of the detectors, implying that events are

---

[62] See however section 4.3 for a comparison between the inner-region visual detections made in this study with probe-based detections made between y^+=14.6 to 24.2.

being located by all three probe-based schemes which occur entirely outside the smoke-marked outer region of the boundary layer.

P(T) is plotted versus normalized event time in Figures 4.1.7-4.1.9 for a number of different thresholds for each detector. The constant value of this function for the uv-quadrant detections at R_θ=730 and 2380 shows that a uv-quadrant event was just as likely to occur at any point during an LSM as it was to occur before or after an LSM. This implies that no correlation exists between uv-quadrant and LSM detections at those two Reynolds numbers. While encouraging, Figures 4.1.7b and d are probably misleading due to the small number of events which were used to create those plots. Figures 4.1.8 and 4.1.9 show essentially the same trends as Figure 4.1.7, although the zero-threshold mean value of P(T) is higher for both TERA and u-level events, reaching as high as 50% for u-level detections at R_θ=2380.

In summary, a probe-based detection is likely to occur at any point during an LSM; this is supported by the invariant nature of P(D) as well as Figures 4.1.7-9. The jagged character of the P(T) plots from the R_θ=1400 and 3120 data sets, when compared to the smooth nature of the other two P(T) plots, suggests that 140 events are not enough to characterize this distribution, while 500 appears to be an adequate number. None of the long-time statistical performance parameters considered, including frequency and event length, suggest that there is a single threshold which will cause any probe-based detection scheme to generate the same performance as LSM detections for all Reynolds numbers.

4.2 RING-LIKE MOTIONS AND THE PROBE-BASED DETECTORS

A comparison similar to the one presented above was performed on the RLM detections from section 3.2, and the results are given below. The reader is referred to Figures 3.4.2, 3.5.2, and 3.6.2, as well as Table 3.2.1, in which it is shown that no particular type of visual detection exceeded 200 in number, and only zero threshold levels produced more than 200 detections from any probe-based detector. As a consequence, the results shown below will be more qualitative in nature than those given in sections 4.1 or 4.3.

A consideration of the different detection criteria employed should suggest whether or not one can expect the visually detected events to be located by the probe-based schemes under scrutiny. The RLM "sweeps" and "ejections" were derived from visual detections of ring-like motions which were required to display an actively rotating character before the event was confirmed. Although the grand ensembles of RLM zones 1 and 2 showed that these parts of an RLM were high speed and wallward moving on average, the rotational aspect of these detections (especially from zone 2) tends to induce a sign change in v from the start to the end of a "sweep". The wall-normal velocity during "ejections" is very similar to that during "sweeps" as seen in Figures 3.2.1-6. Although confusing at first, this is almost certainly a result of combining zones 3-8 and calling them all "ejections." As summarized in section 3.2, the visually detected events were generally high or low speed as appropriate to sweeps or ejections, but v usually goes from negative to positive at some point during each event, with the exception of detections from zones 7 and 8 where the opposite occurred.

The probe-based detection schemes under consideration do a good job of locating only high-speed or low-speed events. The uv-quadrant technique does a very good job

of locating only those events which generate Reynolds stress. Since this kind of event generally occurs near the start of an RLM "sweep" or the end of an RLM "ejection," it is expected that P(T) between RLMs and uv-quadrant events will show peaks near the start of sweep detections and the end of ejection detections. TERA events key on the streamwise velocity and its derivative; peaks in the P(T) between RLMs and TERA events should occur throughout the entire event, since changes in u occur at the ends, and large values of u generally are present in the middle of RLM events. The u-level detector also uses large excursions in the streamwise velocity to locate events, so the P(T) peak should occur in the middle of RLM events where u is generally a maximum.

The more complex nature of the RLM detections makes it unlikely that any of the probe-based detectors under consideration will locate the same events, having approximately the same starting and ending points (which would be indicated if P(T) had the appearance of a square-wave). However, a consideration of the average RLM and probe-based detections suggests that P(T) peaks might occur at predictable locations during the RLM detections. Since it is anticipated that the starting and ending times of the visual and probe-based detections will in general be different, it is not reasonable to assume that the performance parameters developed in section 2.6 will yield an optimal threshold for any of the detection schemes under consideration.

With higher Reynolds numbers, lower uv-quadrant thresholds will allow the uv-quadrant technique to "capture" the same percentage of negative uv as generated during RLMs. However, in general this threshold is not the same for sweeps as it is for ejections; the range is 0.4 to 3.7. The same is true for the TERA technique, although the applicable threshold range is smaller, $0.5 \leq$ range is from 0.8 to 2.3. Essentially the same problem occurs when one tries to match any of the three remaining RLM

performance indicators to those generated by another detection scheme: A wide threshold range is required to match the different performance levels associated with all of the available RLM event types.

The long-time correspondence between RLMs and velocity-based detections is shown in Figures 4.2.1 through 4.2.6. The reader is once again reminded that Figures 3.4.2, 3.5.2, and 3.6.2 show these P(D) plots are the result of at most 200 probe-based detections, while the P(E) figures (see Table 3.2.1) are based on between 13 and 111 visual detections, with the fewest events present in the $R_\theta=1400$ data set. As with the LSM, these P(D) values remain within a relatively constant range, although the range itself is larger than it was for the LSM. The majority of the uv-quadrant detections produce P(D) values around 40%, while the $R_\theta=3120$ data set produces higher values for both sweeps and ejections. The same is true of the TERA detections, but the range for the lower Reynolds number P(D)s is from 20% to 60%. P(D) for u-level detections exhibits a steadily increasing trend similar to that shown by Luchik and Tiederman (1987); the minimum non-zero P(D) value is 38%. The P(E) values for the uv-quadrant and TERA techniques once again decrease monotonically with threshold, while P(E) for u-level detections decreases almost linearly. It is interesting to note that P(E) for sweeps is invariably lower than P(E) for ejections from the same data set. This suggests that RLM sweeps generally have lower streamwise velocity peaks than RLM ejections, since the u-level scheme requires the same u magnitudes for sweeps as for ejections.

Event-resolved probabilities of the correct event being located are shown for the uv-quadrant technique in Figures 4.2.7 through 4.2.10. It was expected that uv-quadrant ejections would be located most often toward the end of an RLM ejection, and at zero threshold the peak was indeed located there with a magnitude of 55%.

More encouraging is the fact that a peak exists at all, that Figure 4.2.7a is not comprised of straight lines like Figure 4.1.7a. This variation, especially the fact that the P(T) magnitudes are significantly lower at the ends of the visually detected events, suggests that the correlation between RLMs and uv-quadrant detections is better than that between LSMs and any probe-based detections. However, it is disappointing that the peaks which are so evident at Reynolds numbers of 730, 3120, and even 1400 (see Figures 7a, 10a and 8a),[63] are not as apparent at R_θ=2380. Instead of a variation from 25% at the start of an event to 55%-65% near the end, Figure 4.2.9a varies only from an initial value of 30% to a peak value of 40%.

The expected P(T) trend between RLM and uv-quadrant sweeps was for the P(T) peak to be located near the start of the RLM event. Although this is the generally the case, the P(T) plots are ragged, and this result may be more fortuitous than factual.

The probability of TERA events occurring during RLMs is shown in Figures 4.2.11 - 4.2.14; the u-level P(T) plots comprise the next four figures. The u-level and TERA plots for each event type are almost identical, with the exception of P(T) for ejections at R_θ=2380, where the magnitude of the u-level response exceeds that for the TERA technique. Furthermore, these figures do not show the variation which was seen in Figures 4.2.7-11, but have instead almost the character of the LSM plots 4.1.8 and 4.1.9. The differences between the RLM and LSM plots for these two probe-based detectors could very well lie in the fact that almost five times as many events are in the LSM data sets at R_θ=730 and 2380. Insomuch as there is any peak to the P(T) plots, the peak is located near the center of the RLM, as expected. Also as expected, this applies to both sweeps and ejections. Since the level of correlation is

---

[63] Only 38 events are present in the P(T) distribution shown in Figure 4.2.8a.

about the same before, during and after an "average" RLM, one must conclude again that a TERA or u-level detection is likely to occur at any point during this type of visual event.

Considering the "average" RLM event and the probe-based detection criteria suggested that the RLM is different in nature from those events located only on the basis of their velocity signatures. This might be different if a spanwise vorticity-based detection scheme were used. A comparison of the performance indicators generated by RLM, uv-quadrant, TERA, and u-level events yielded no obvious threshold levels to use with any of the probe-based schemes. The long-time correlations between visual- and probe-based detections suggested that a relatively constant proportion of the probe-based events overlapped at least somewhat with a visual event; unfortunately this was a fairly small percentage, on the order of 40%. P(D) for the u-level detector with these data sets exhibited approximately the same behavior as shown by Luchik and Tiederman (1987), although that similarity was not seen with the uv-quadrant detections. Even with thresholds of zero, at most 80% of the visual detections corresponded with the appropriate type of probe-based event, as shown in the P(E) plots. The combination of P(E) and P(T) indicated that the overlap between uv-quadrant events and RLMs almost always occurred near the end of the RLM, although the extent of the overlap was widely variable. Contrary to initial expectations, the overlap between TERA or u-level and RLM events is likely to occur at any point during the RLM.

4.3 INNER-REGION VISUAL AND PROBE-BASED DETECTIONS

The inner-region visual detections have also been compared with the probe-based detections made from the same data sets, and those results are presented below. The difference between these detections and the ones discussed above is that the data sets were all taken at approximately the same Reynolds number ($R_\theta \approx 720$), but the probe was positioned at four different heights above the wall. Although the hot wires were moved, the visual detection point did not shift; the plan view was almost exclusively used to determine when events were occurring. The visual detection criteria were the visual equivalents of what a sweep and ejection should be (see section 2.4.3), so these detections should correspond most closely with the events located by the three different probe-based detection schemes. However, little consideration could be given to the vertical location or extent of the visual detections, so it is possible that the visually detected events did not produce velocity changes at the probe at the same times at which the visual events were said to occur. A number of factors affect this issue, including angular orientation and vertical velocity of the observed feature, height of the probe, and the vertical extent of any overlying motions which caused or were caused by the observed motion. Since the visual detections capture the entire event regardless of vertical development with respect to the probe, it is not logical to assume that the performance parameters of the visual-based detections can be "matched" to those from a given threshold for any probe-based scheme[64]. In section 3.3 it was suggested that sweeps tended to remain above $y^+=15$, while ejections did not usually extend above that same point. Therefore it seems most likely that the best correlation between visual- and probe-based detections will occur with sweeps at $y^+=18.9$ and

---

[64] This is indeed the case, with threshold ranges between 0 and 1.5 required for the TERA and uv-quadrant techniques, between 0 and 1 for the u-level technique, depending on the parameter.

24.2 and ejections at y^+=14.6 and 15.

A comparison of the ensemble averages shown in Figures 3.3.1 and 3.3.2 with those shown in sections 3.4-6 suggests that there should be a good correlation between u-level or TERA and visual detections throughout the duration of the visual event. On average the visual events generate a fairly constant level of Reynolds stresses before, during, and after the events, therefore the correlation between visual and uv-quadrant detections is expected to be poor. The uv ensemble shows that a slightly higher level of uv is generally present near the beginning of the "average" visual events, so if there are any peaks in the uv-quadrant P(T) distributions, it should be near the start of the visual events.

Since sweeps move wallward, they should reach the outermost probe position first; ejections should contact the innermost probe sooner than the others, assuming the events started at about the same height and that that height was less than y^+=14.6. This suggests that the P(T) profiles comparing inner-region visual events to detections based on the streamwise velocity should have peaks which occur earlier for the $y^+\approx15$ ejections and the y^+=24.2 sweeps than for other event types. That is, with the probe in the outermost position, the P(T) peak should occur closer to the start of the visual sweeps than it does with the probe elsewhere, and similarly for visually detected ejections with the probe at its innermost position.

Long-time correspondence between visual- and probe-based detections are shown in Figures 4.3.1 through 4.3.6. Figure 4.3.1 shows that the visually detected ejections above y^+=14.6 account for about half of all the low-speed events which generate Reynolds stresses. Ejections at y^+=14.6 and all of the visually detected sweeps account for about 70% of the sweeps or ejections at that point which generate negative uv. Figure

4.3.2 shows that the strongest high-speed and low-speed events all correspond to visual detections. The range on P(D) for TERA detections is fairly constant, between 40% and 80% through the significant thresholding limit.

Only 65% to 90% of the visual events correspond to probe-based detections, even at zero thresholds. Therefore, some of the visually located events of both types had the wrong sign of u (and perhaps v, also) throughout their entire durations as measured at the probe. Considering Figure 4.3.4, it is surprising that 83% of the visually detected sweeps correspond to events in quadrant 2 of the uv plane at $y^+=15$, although this is offset by the 72% observed at $y^+=14.6$. Recalling that the TERA detector is only on 50% of the time with c=0, while the u-level detector is always "ON" with a zero threshold, it is interesting to note that P(E) for both detectors at zero threshold is practically identical for each data set; see Figures 4.3.5 and 4.3.6. The TERA algorithm with a threshold of zero must therefore generate detections which correctly correspond to every inner-region visual sweep with positive streamwise velocity fluctuations and every visually detected ejection with negative streamwise velocity fluctuations. However, these are not the only TERA detections made with that threshold, as indicated by the P(D) plot (Figure 4.3.3).

The event-resolved correlations between visual events and uv-quadrant detections are shown in Figures 4.3.7 through 4.3.10. There is a surprisingly large variation in P(T) from the start to the end of each event type, showing that uv-quadrant detection overlaps are about twice as likely to occur near the start of all visual detections. The variation in P(T) follows the variation in the uv ensemble for each event type as shown in Figures 3.3.1 and 3.3.2, and in general the P(T) profiles are as expected.

Profiles of P(T) for TERA detections are shown in Figures 4.3.11-14. Over 85% of the TERA events which overlap do so at the center of the corresponding visual event, and the TERA events tend to occur earlier than the visual events as shown by the high level of P(T) before and at the start of each average visual event. The strong correspondence between TERA sweeps and visually detected sweeps must be tempered by the fact that only 113 events comprise those P(T) curves. At the nearby y^+=14.6 location, 530 events give a much less pronounced profile. Although it was expected that P(T) would have the highest peaks near the start of ejections at $y^+\approx$15 and sweeps at y^+=24.2, it can bee seen that all of the P(T) peaks are about the same, with the highest P(T) magnitude present near the start of sweeps detected at y^+=15.

The correspondence between u-level detections and inner-region visual detections is shown in Figures 4.3.15 through 4.3.18. As with the TERA P(T) profiles, the peaks are shallow and tend to occur near the start of the "average" visual events, regardless of event type. The highest peak is once again present in the y^+=15 sweep distribution, potentially a result of P(E) for u-level detections being highest for y^+=15 sweeps and ejections. A difference between the P(T) profiles for the u-level technique versus the other two techniques is the high level of correspondence between detections at higher threshold levels. Over 90% of the c=1.6 probe-based detections which overlap with visual events do so over the entire length of the visual event. The average length of a u-level event is significantly larger than that of a visual events, so it is not surprising that u-level detections tend to extend past both the start and end of the visual events with which they correspond.

Consideration of the detection criteria and the ensembled inner-region visual detections of sweeps and ejections suggested that a fairly high level of correspondence would be present between these events and probe-based detections. A high level of

correspondence (over 75% with zero thresholds) was achieved, with velocity-located events tending to overlap most often near the start of the visual events. However, fewer than 80% (and as few as 45%) of the events located with a probe-based scheme corresponded to visual events in the thresholding ranges for which a significant number of events were available. P(D) had no consistent y^+ or thresholding trends. Since information regarding the vertical extent of the visual events was generally not used, it was expected that a single thresholding constant would not work to generate probe-based detections that had the same characteristics of the visual detections. This was indeed the case.

CHAPTER 5

SUMMARY AND CONCLUSIONS

Six different coherent motion detection schemes have been applied to eight different data sets, and the performance characteristics of those different schemes have been compared. Outer region data in the range $730 \leq R_\theta \leq 3120$ were used; inner region data sets all had an average Reynolds number based on momentum thickness of 720, while the probe was positioned in the range $14.6 \leq y^+ \leq 24.2$. The performance parameters used will be discussed below, followed by a summary of what those parameters indicated when applied to the different detection sets. Visual detections formed the reference data sets for the event-overlap analysis presented in Chapter 4. The overall indications of P(T), a new parameter proposed in Chapter 2, will be discussed, in addition to some general comments on the detection schemes used.

Combined hot wire and flow visualization data taken in 1981 and 1982 by Signor (1982) and Lovett (1982) comprised the raw data which was used in this study. The hot wire data was processed by routines developed by Klewicki (1989) and Gendrich, resulting in time series that were brief but adequate for the analyses to be performed. All the routines which generated the probe-based detections were written by this author and presented in Gendrich, Falco, and Klewicki (1989). The probe-based detections are the result of applying the conventional uv-quadrant technique, the TERA technique,

and a modified modified u-level approach[65] to all eight hot wire data sets. The outer-region film was read by Signor, who located the presence of ring-like intermediate-scale motions (RLMs, called "typical eddies" by Signor and Falco). Those same films were read by Falco and others to determine the times during which smoke was passing over the probe. These detections comprised the LSM database used in this study. This author read the inner-region films to locate the presence of sweeps (high-speed, wallward-moving events) and ejections (low-speed, outward-moving events) penetrating into or rising out of the viscous sublayer at the probe's streamwise location. These detections comprise the inner-region visual database used in this study.

Parameters were proposed in Chapter 2 which should indicate how well a given detection scheme locates the presence of sweeps and ejections. These parameters included the mean event frequency and length, in addition to a spanwise vorticity parameter, a turbulence kinetic energy parameter, and a parameter indicating the percent of Reynolds stress which was generated while the detector was "ON." Event frequency and length were scaled using inner, outer, and mixed normalizations, and those results were presented in Chapter 3. Neither of those parameters under any of these scalings yields a parameter which is independent of Reynolds number or y^+. Ensemble averages for the outer-region visual detections were also scaled using these normalizations. While it was expected that outer variables would best scale the minima and maxima of all five variables, $<u>$, $<v>$, and $<uv>$ scaled equally well with inner, outer, and mixed variables.

---

[65] This version of the u-level technique could locate the start and stop times of both sweeps and ejections.

The vorticity parameter indicated the RMS of the spanwise vorticity fluctuations during events, normalized by the long-time $\omega_z{}'$. For each data set this parameter either remained fairly constant or increased with threshold, but the performance tended to vary irregularly with Reynolds number or probe height. The TKE parameter showed the unsurprising result that the average of (u^2+v^2) increases with threshold for all three probe-based detectors. However, the threshold dependence was a function of event type (sweep or ejection) and *not* Reynolds number in the outer region for all three detectors. Furthermore, the threshold dependence was linear with slope 1 for both the uv-quadrant and TERA techniques.

The percent Reynolds stress "captured" parameter varied predictably with threshold for the uv-quadrant technique, since the Reynolds stress was the detected variable. The inner-region variability of Reynolds stress with y^+ accurately reflects the shift of the uv-quadrant PDF peak from quadrant 4 below $y^+=15$ to quadrant 2 above that level. The u-level "% Reynolds stress" plots are very similar to those for the uv-quadrant technique, although the 0-threshold performance of the u-level technique can be predicted from the fact that the u-level detector is always "ON" when c is 0. It is more remarkable that the TERA plots are also similar to the uv-quadrant plots, duplicating the 100% captured result at zero threshold, even though the TERA detector is only on approximately 50% of the time then.

Criteria were suggested for determining adequate sample size on the basis of the number of events located and the total event time. The distributions of u, v, uv, and ω_z in the data sets considered indicate that convergence of the mean and variance to $\pm 10\%$ of the true values can be achieved with 95% confidence in the results if samples from $200tU_\infty/\delta$ are present in the summation. It was apparent from the results presented in Chapter 3 that data sets longer than the ones used are required to provide

better statistical convergence and a higher level of certainty in the ensemble averages shown. Longer data sets would not, however, guarantee that the variance of those averages would be reduced[66]. To a rough approximation, 200 events should provide enough data so that the event length and event frequency also converge to within 10% of the true values. Results from Chapter 4 suggests that 140 events are too few, while 500 seem to be adequate to characterize the one-to-one correspondence between events located by two different detection schemes.

Ensemble averages for u, v, uv, ω_z and $v\omega_z$ were presented for sweeps and ejections located by each detector. As discussed in the Introduction, it has been suggested that the choice of detection criteria strongly influences the "average" characteristics of the located events. The symmetry (or asymmetry) of the detection criteria certainly seems to cause the ensemble of the detected variable to be symmetric (or asymmetric). The low variability of <u> during TERA events suggests that the ensemble of a variable related to the one which forms the basis for detections is influenced by the detection criteria. On the other hand the TERA detector had no information regarding v during detections, yet v was almost always positive during ejections and negative during sweeps. It seems most probable that this is an indicator of a correlation between $u\partial u/\partial t$ and v rather than a result predicated by the choice of detection criteria.

The variability[67] of each ensemble average was shown as a function of normalized event time in the ensemble plots of Chapter 3. The limits thus depicted represent bounds on the maximum likelihood region within which the true average value should

---

[66] Since only the top parallel wire of the R_θ=1400 data set generated bad data, it would be possible to extend the length of that data set as far as LSM and probe-based detections are concerned, although vorticity and strain rate information would be missing.

[67] One quarter of the RMS of the average at each point in time comprised the variability which was shown in the ensemble plots.

fall. Alternatively, these regions can be seen as indicators of how widely variant the different time signatures are which comprise the event's ensemble. Note that the ensemble averaging process appears to be an unbiased but not consistent estimator for the expected value of a particular variable at a given normalized event time, since the variance does not tend to zero as the number of events in the average increases. This is either due to the estimation technique or the lack of convergence for the expected value itself. Since the expected value of a random variable is well defined, perhaps the process of stretching variable-length events to one size should be evaluated with this problem in mind. In any event, the RMS was generally much larger than the average value, even with as many as 650 events present in the ensemble. Although there was so much variance about the average value of an ensemble, the ensembles of a visual event were successfully used in conjunction with the detection criteria of a probe-based scheme to predict when the greatest number of probe-based detections were likely to overlap with the visual event; see for example sections 4.2 and 4.3.

The one-to-one correspondence between visual and probe-based detections was considered in Chapter 4 using P(D), P(E), and a new variable, P(T, t), as the evaluation parameters. Visual data provide more complete information regarding the spatial organization of motions in the flow than do multipoint hot wire measurements. Consequently, visual detections frequently comprise the reference database against which probe-based detections are compared. In keeping with this common practice, visual detections were used as the basis for comparison in this document. However, sweeps and ejections were the events which we wished to locate, and they have a well-defined Reynolds stress signature which is accurately detected by the uv-quadrant technique. It might be worthwhile to consider the correspondence between uv-quadrant detections and those made by other detection schemes, perhaps as a function of two different threshold levels[68]. This is particularly indicated for the TERA detector, whose long-

---

[68] In this case P(E) and P(D) become surfaces in the threshold space. P(T,t) would become a volumetric response plot unless a threshold for one of the detectors could be decided upon in

time performance parameters correspond very closely to those of the uv-quadrant technique.

As seen in Chapter 4, the long-time overlap parameters P(D) and P(E) were not smooth, monotonic functions of threshold for any of the combinations of probe-based and visual detectors considered in this document. This stands in contrast to the results of Bogard (1982) and Luchik and Tiederman (1987); it is perhaps caused by the brevity of the data sets which were used in this study. P(T, t) was a well-behaved function of normalized event time and threshold, except at the highest threshold levels where the number of overlapping events was very small. Falco[69] suggests that P(T) should be redefined to indicate how many out of all the overlapping events overlap at each given point in time. This modified version of P(T) would then be defined as:

$$P(T_2, t) \equiv \frac{N_{DV}(t)}{N_{DV} \text{ overall}}$$

where $N_{DV}(t)$ is the number of probe-based detections which correctly correspond to a visual detection at a given point in normalized event time, and N_{DV} overall is the total number of probe-based detections which correctly correspond to a visual detection. Unfortunately $P(T_2)$ no longer indicates the overall correlation between visual and probe-based detections in addition to the variance of that correlation over the ensemble, both of which can be read from P(T) plots.

The LSM results suggest that the LSM visual analysis should not be applied when the marker used has a Schmidt number significantly different from unity. In this particular instance (Schmidt number greater than 30,000), events which happened

advance.

[69] Private communication.

upstream of the probe could move the smoke around and lose their momentum through diffusion long before the smoke could relax back to its undisturbed condition. Classifying events on the presence or absence of smoke resulted in detections which occurred at random with respect to uv-quadrant, TERA, and u-level detections. The percent Reynolds stress captured is approximately equal to the percentage of time that the detector is "ON" (see Table 3.1.1). The spanwise vorticity parameter is approximately constant at 1. The ensemble averages of fluctuating parameters are very close to zero when compared against the variance of those same variables. These are approximately the results one would expect when making random detections averaging 1δ in length in the outer region of the boundary layer.

The RLM detections are based on the same data that produced the LSM detections (i.e., the same films were used), but the key difference is the requirement that the smoke must be seen to move in a distinct manner from frame to frame. It is practically certain that the smoke did not mark all of the coherent convective processes occurring in the outer region of the boundary layer, so it is quite likely that "typical eddies" are also present in the unmarked regions of the flow. If the entire flow field were marked with smoke, all of the RLMs in the flow could be located; alternatively, use of a marker with a Schmidt number of 1 would probably alleviate this problem.

The kinematic constraint on the RLM is vortical in nature, so the comparison drawn between probe-based detections and those visual results was slightly forced, since those results had to be cast into a classification scheme based on linear instead of angular momentum. Future studies might consider the correspondence between the different zones of a "typical eddy" and various probe-based schemes in an effort to determine the correlation between those vortical processes and what is typically classified as a sweep or ejection.

The inner-region visual detection technique described in Chapter 2 was demonstrated as capable of locating the start and stop of sweeps and ejections. The temporal gradient in the smoke intensity and the motion of a distinct region faster or slower than its surroundings were used as the indicators of whether or not an active event was passing over the probe. A small percentage of "ejections" were located whose absolute velocity never fell below the mean, although subsequent examination of the time traces revealed there was always a decrease in the streamwise velocity magnitude (and an increase in the wall-normal velocity) during these events. "Sweeps" with a similar problem were also detected. It seems most likely that these detections resulted from considering only the temporal gradient of the smoke intensity and not the absolute intensity itself.

Plan views of the flow were used to make the detections, because that information was available for all of the data sets of interest. Although it was difficult to infer event height above the wall on the basis of the plan view, that view did give the best indication of the spanwise and streamwise extent of the active events. There was a very poor correlation between dark (no smoke) regions in the side view and sweeps detected using the plan view. Bright ridges rising out of the sublayer as seen in the side view always corresponded to ejections in the plan view[70], but the plan view generally indicated the event started before and ended after the side view's ridge intersected the probe. This suggests that the plan view is the best view to use when atomized oil droplets are the marker and inner-region sweeps and ejections are to be detected.

---

[70] They did as long as the laser sheet was positioned right next to the X-array. This is partly dependent on the definition of an ejection (see 2.4.3) and the generally narrow aspect of the ejections.

None of the detectors located all of the same events, as seen in Chapter 4. The percent Reynolds stress "captured" and TKE parameter plots were the only Reynolds number independent parameters calculated. The former is directly related to how effectively a detection scheme locates sweeps and ejections, so it is an appropriate parameter to use when attempting to match the performance or threshold of two different detectors. Unfortunately, neither percent Reynolds stress "captured" nor the average turbulence kinetic energy during events was independent of Reynolds number as far as the outer-region visual detections were concerned. Although either of those two parameters could be used to match performance among the probe-based detection schemes, no parameters could be used to match probe-based detections at a given threshold to any visual detections.

Kline and Falco (1979) suggested that the "intensity" of an event in the outer region should scale with outer variables. If "intensity" is understood to be the turbulence kinetic energy in the flow, $\frac{1}{2}(u^2+v^2+w^2)$, then the intensity does not become Reynolds number independent when normalized with U_∞^2. It does, however, scale with the RMS of the TKE, at least in the approximation that the TKE is equal to $\frac{1}{2}(u^2+v^2)$.

Consideration of the performance of the uv-quadrant detector led to the conclusion that the amount of negative uv "captured" during uv-quadrant events is a result of the threshold chosen and the PDF of u versus v. For uv-quadrant events the dependence of frequency, turbulence kinetic energy, and event length on threshold seems to be a function of the probe height and the detection criterion, in combination with the distribution of u versus v. As discussed above, the uv ensembles are a consequence of the detection criterion. The uv initial and final values are dictated by the start/stop limit, and the upward slope/ peak in the middle character follows from requiring the events to have uv magnitudes greater than the start/stop criterion.

The TERA detection criteria cause the threshold dependence of the turbulence kinetic energy during events; the higher the threshold, the higher the change in TKE at the start and during events, leading to higher overall TKE levels. However the distribution of TKE between high-speed and low-speed events seems to be a consequence of the flow physics. Event averages of u during TERA events are the consequence of the start and stop criteria in the same way that $<u>$ and $<v>$ ensembles are caused by the uv-quadrant criterion.

The u-level technique as modified by Luchik and Tiederman was further modified for this study in order to detect sweeps as well as ejections. The performance of this version of the u-level technique as indicated by the parameters presented in this study is similar to that of both the uv-quadrant and the TERA techniques. Furthermore, the u-level technique is the simplest of all 6 detection methods considered, both in terms of data required and the analysis of that data. However, it should be noted that u-level events are significantly longer than those located by all except the LSM approach, even in the inner region of the boundary layer where events are most likely shorter than one δ in length.

Grouping was applied to all probe-based detections, and this also had an impact on the apparent performance of the detectors. Long events which were close together tended to group. As threshold was increased, those events grew further apart and could no longer be grouped. This caused an apparent increase in number of events and event frequency, although the total detected time continued to decrease. The resultant dependence of event frequency on threshold was a combination of the detection criteria, which had to permit long events, and grouping.

Outer-scaled event lengths provided a check on the hypothesis that events are around one boundary layer thickness in length; it turns out that almost all detected events were less than one δ long on the average, with the shortest events occurring in the near-wall region. Plots of event length versus y^+ were shown in Chapter 3, with the conclusion that events as detected by the three probe-based schemes considered do not get longer the further they are away from the wall. This was true regardless of threshold and regardless of the detection scheme[71]. It is important to note, though, that the event convection velocity was assumed to be constant in the near-wall region, so this conclusion follows directly from the inner-scaled average event duration. If the convection velocity is dependent on y^+, events may indeed grow larger the further they are away from the wall.

If a coherent motion is simply one which generates Reynolds stresses, then the parameter presented in Chapter 2 which best evaluates a detector's performance is obviously the percentage of negative uv "captured" by the detector. The best detector of these events is the uv-quadrant breakdown technique, however it was seen in section 3.5 that the TERA technique is very similar to the uv-quadrant approach with respect to this performance parameter. Kline and Falco (1979)[72] posed the question of whether or not something other than high uv could be used to detect "significant motions" in the flow. If a significant motion is one which generates Reynolds stresses, then the TERA approach, which requires only streamwise velocity information, can be used to detect those motions. The exact relationship between TERA and uv-quadrant detections as indicated by P(D), P(E), and P(T) still must be determined, though.

---

[71] Since the inner-region visual analysis did not generate information regarding event size as a function of distance from the wall, information from that analysis cannot contribute to an answer to this question.

[72] See Kline and Falco (1979), p. 11.

Sweeps and ejections are simply-defined events, but five minutes' contemplation of flow visualization or u, v, and uv time traces will at least partially reveal the complexity of the motions within a turbulent boundary layer. In order to more completely understand these motions, one must be able to distinguish between more than these three states of Nature: {sweep, ejection, and quiescent periods}. As discussed by Kline (1988), such distinctions are already being drawn, and detection schemes are being designed to locate those events. In this document some new approaches to evaluating the performance of a detector have been presented and compared to many of the older performance parameters currently in use. The one-to-one correspondence of events located by two different detection schemes has also been considered. It is hoped that the new tools developed in this document will be of use in the community-wide efforts to understand the interplay of coherent motions and the detectors designed to locate and characterize them.

TABLES

Table 2.1.1 Inner-region Flow Parameters

y^+	U_∞ (m/s)	δ (mm)	U_τ (m/s)	ν $\times 10^5$ (m^2/s)	R_θ
14.6	0.975	61.0	.0512	1.55	744
15.0	0.920	101.5	.0497	1.55	704
18.9	0.951	61.0	.0506	1.55	726
24.2	0.920	61.0	.0497	1.55	704

Table 2.1.2 Inner-region Combined Data Set Lengths

y^+	event type	total ticks	total sec	total t^+	total tU_∞/δ
14.6	S/E	65000	108.3	18309	1733
15.0	S/E	20000	40.0	6364	362
18.9	S/E	19500	39.0	6435	609
24.2	S/E	58800	78.4	12473	1184

Table 2.1.3 Inner-region Time Uncertainty - the Length of One Time Tick

y^+	sampling rate (Hz)	1 tick (msec)	1 tick (t^+)	1 tick (tU_∞/δ)	1 tick (l^+)
14.6	600	1.67	0.282	0.0267	3.22
15.0	500	2.00	0.318	0.0181	3.54
18.9	500	2.00	0.330	0.0312	3.72
24.2	750	1.33	0.212	0.0201	2.36

Table 2.2.1 Outer-region Flow Parameters

R_θ	U_∞ (m/s)	δ (mm)	U_τ (m/s)	$\times 10^5$ ν (m^2/s)
730	0.997	82.9	.0494	1.56
1400	1.86	102.0	.0811	1.55
2380	3.26	106.0	.136	1.55
3120	5.33	74.4	.196	1.55

Table 2.2.2 Outer-region Combined Data Set Lengths

R_θ	event type	total ticks	total sec	total t^+	total tU_∞/δ
730	LSM	153000	153.0	23900	1836
	RLM	31500	31.5	4920	378
1400	LSM	22500	9.0	3813	168
	RLM	13500	5.4	2288	101
2380	LSM	175500	35.1	42184	1081
	RLM	36000	7.2	8653	221
3120	LSM	108000	6.8	16711	484
	RLM	27000	1.7	4178	121

Table 2.2.3 Outer-region Time Uncertainty - the Length of One Time Tick

R_θ	sampling rate (Hz)	1 tick (msec)	1 tick (t^+)	1 tick (tU_∞/δ)	1 tick (l^+)
730	1000	1.00	0.156	0.0120	2.84
1400	2500	0.40	0.169	0.00747	3.50
2380	5000	0.20	0.240	0.00616	5.17
3120	16000	0.063	0.155	0.00448	3.79

Table 3.1.1 Outer-region LSM Detection Performance Indicators

parameter	R_θ=730	R_θ=1400	R_θ=2380	R_θ=3120
number of events	647	34	557	139
total time (in)	9802	1170	24911	7497
total time (mix)	2717	246	3987	1276
total time (out)	753	52	638	217
frequency (in)	661e-6	256e-6	763e-6	199e-6
frequency (mix)	183e-6	54e-6	122e-6	34e-6
frequency (out)	507e-7	113e-7	195e-7	58e-7
event length (in)	306	789	1070	1470
event length (mix)	18.9	34.6	35.0	47.9
event length (out)	1.16	1.52	1.15	1.56
% "ON" time	.410	.307	.590	.449
<uv>/RMS (uv)	-0.408	-0.454	-0.426	-0.508
% (-) uv	.447	.366	.591	.570
RMS ω_z	1.02	1.06	.953	.465
average TKE	.774	.92	.837	.889
average strain	.023	.024	-.020	-.001

(in)   indicates inner variables were used to normalize the results.

(mix) indicates mixed variables were used.

(out) indicates outer variables were used.

Table 3.2.1 Outer-region RLM Detection Performance Indicators

parameter	$R_\theta=730$ E	S	$R_\theta=1400$ E	S	$R_\theta=2380$ E	S	$R_\theta=3120$ E	S
# of events	90	24	38	13	110	24	111	21
total t (in)	761	136	527	91	1696	283	1379	211
total t (mix)	211	38	111	19	272	45	235	38
total t (out)	58	10	23	4	43	7	40	6
freq (in)	446e-6	119e-6	477e-6	163e-6	734e-6	160e-6	636e-6	120e-6
freq (mix)	124e-6	33e-6	100e-6	34e-6	118e-6	26e-6	108e-6	20e-6
freq (out)	343e-7	91e-7	210e-7	72e-7	188e-7	41e-7	184e-7	35e-7
ev len (in)	171	114	318	161	368	281	338	287
ev len (mix)	10.5	7.0	13.9	7.1	12.1	9.2	11	9.4
ev len (out)	.649	.434	.611	.310	.395	.302	.360	.305
<uv>/RMS (uv)	-.732	-.483	-.372	-.148	-.518	-.528	-.695	-.352
% (-) uv	.265	.033	.268	.028	.240	.036	.587	.050
RMS ω_z	1.34	.832	1.32	1.21	1.07	.961	1.28	1.33
avg. TKE	1.15	.922	1.10	.973	1.04	.985	1.01	.642
avg. strain	.434	-.293	.158	.237	.041	-.186	.202	.447

(in)   indicates inner variables were used to normalize the results.
(mix) indicates mixed variables were used.
(out) indicates outer variables were used.

Table 3.3.1 Inner-region Visual Detection Performance Indicators

parameter	$y^+=14.6$ E	S	$y^+=15.0$ E	S	$y^+=18.9$ E	S	$y^+=24.2$ E	S
# of events	490	530	96	113	157	220	271	352
total t (in)	4631	6638	867	2241	1062	2223	2565	5165
total t (mix)	1425	2042	207	535	327	684	790	1591
total t (out)	438	628	49	128	100	210	243	490
freq (in)	212e-5	230e-5	153e-5	180e-5	266e-5	372e-5	98e-5	127e-5
freq (mix)	653e-6	707e-6	364e-6	429e-6	817e-6	1150e-6	301e-6	391e-6
freq (out)	201e-6	217e-6	87e-6	102e-6	251e-6	352e-6	93e-6	121e-6
ev len (in)	180	239	167	368	127	190	175	272
ev len (mix)	12.7	16.8	9.3	20.4	9.0	13.5	12.6	19.5
ev len (out)	.895	1.19	.515	1.13	.64	.96	.898	1.39
<uv>/RMS (uv)	-.299	-.646	-.745	-.734	-.899	-.560	-.698	-.466
% (-) uv	.245	.464	.155	.383	.25	.33	.285	.40
RMS ω_z	1.04	.966	1.06	.987	1.06	.985	1.03	1.02
avg. TKE	1.11	.992	1.08	1.05	1.46	.72	1.31	.67
avg. strain	-.147	-.13	-.128	-.080	.47	-.39	.197	-.126

(in)   indicates inner variables were used to normalize the results.
(mix) indicates mixed variables were used.

(out) indicates outer variables were used.

FIGURES

Plan View

Side View
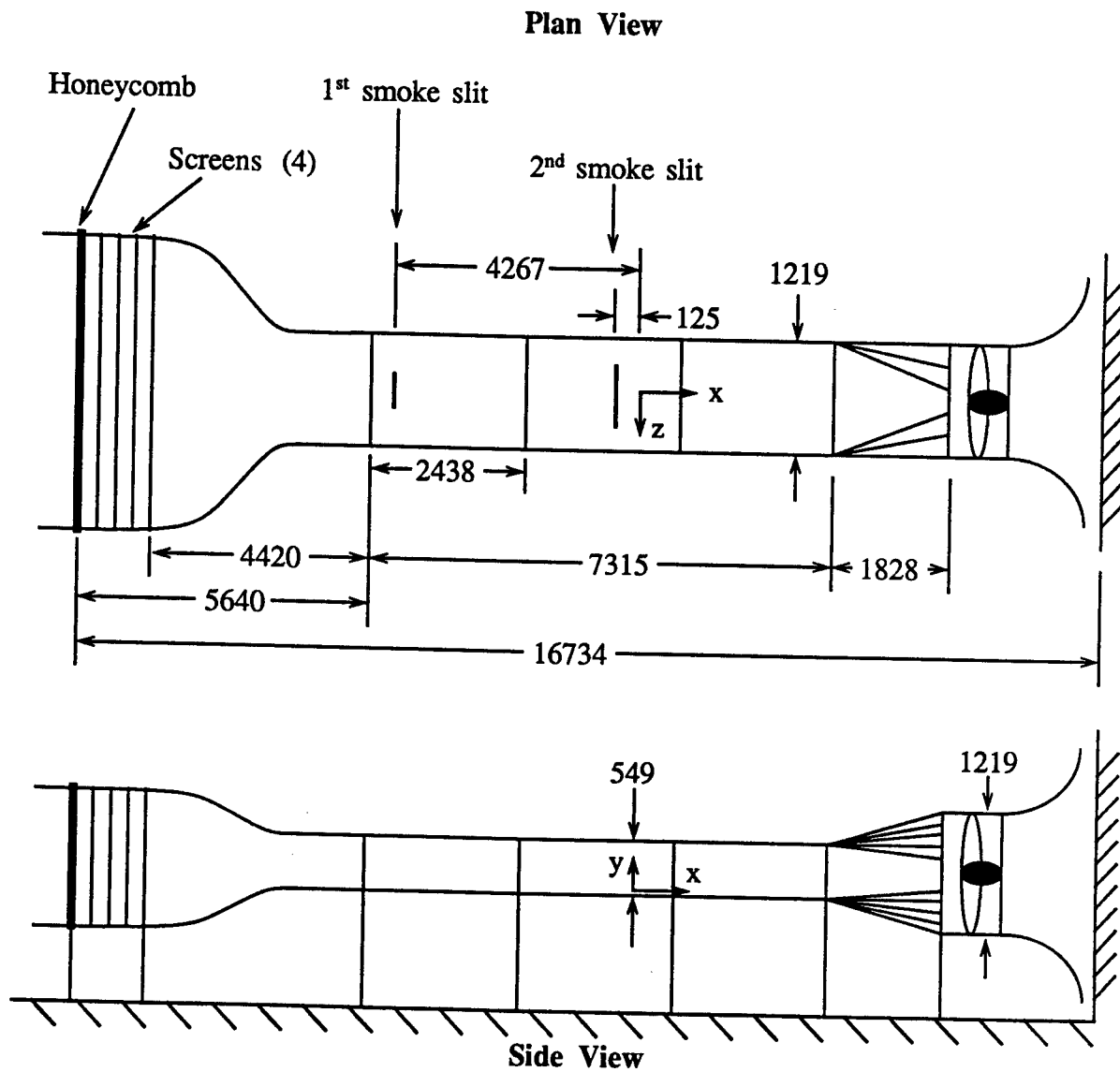
NOTE 1: All dimensions are in millimeters. Drawing is not to scale.
NOTE 2: The data acquisition point is at the origin as shown above.
NOTE 3: The entrance contraction has an area ratio of 13:1.

Figure 2.2.1 The 7.3m boundary layer wind tunnel in Michigan State
University's Turbulence Structure Laboratory.
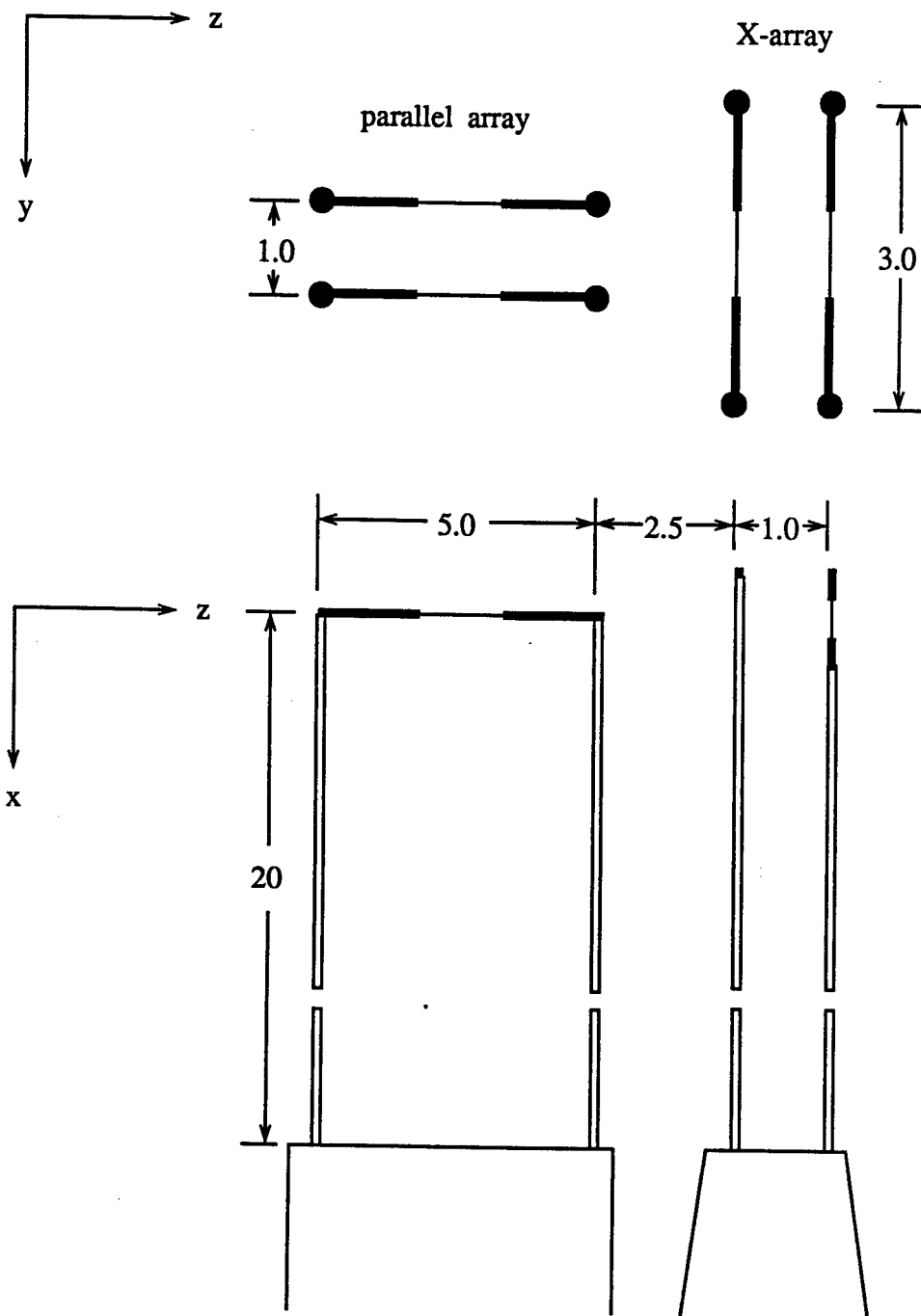
NOTE 1: All dimensions are millimeters. Drawing not to scale.
NOTE 2: Axes indicate directions only, not the location of the origin.

Figure 2.2.2 The spanwise vorticity probe.

Side View Mirrors
(most films)

Plan View

Clock View

Camera

z

x

Clock

Clock View Mirror

Top View Mirror

Red Filter

45°

Plan and
Clock View

45°

Mirror

Side View
(most films)

Green
Filter

y

z

Mirror

45°
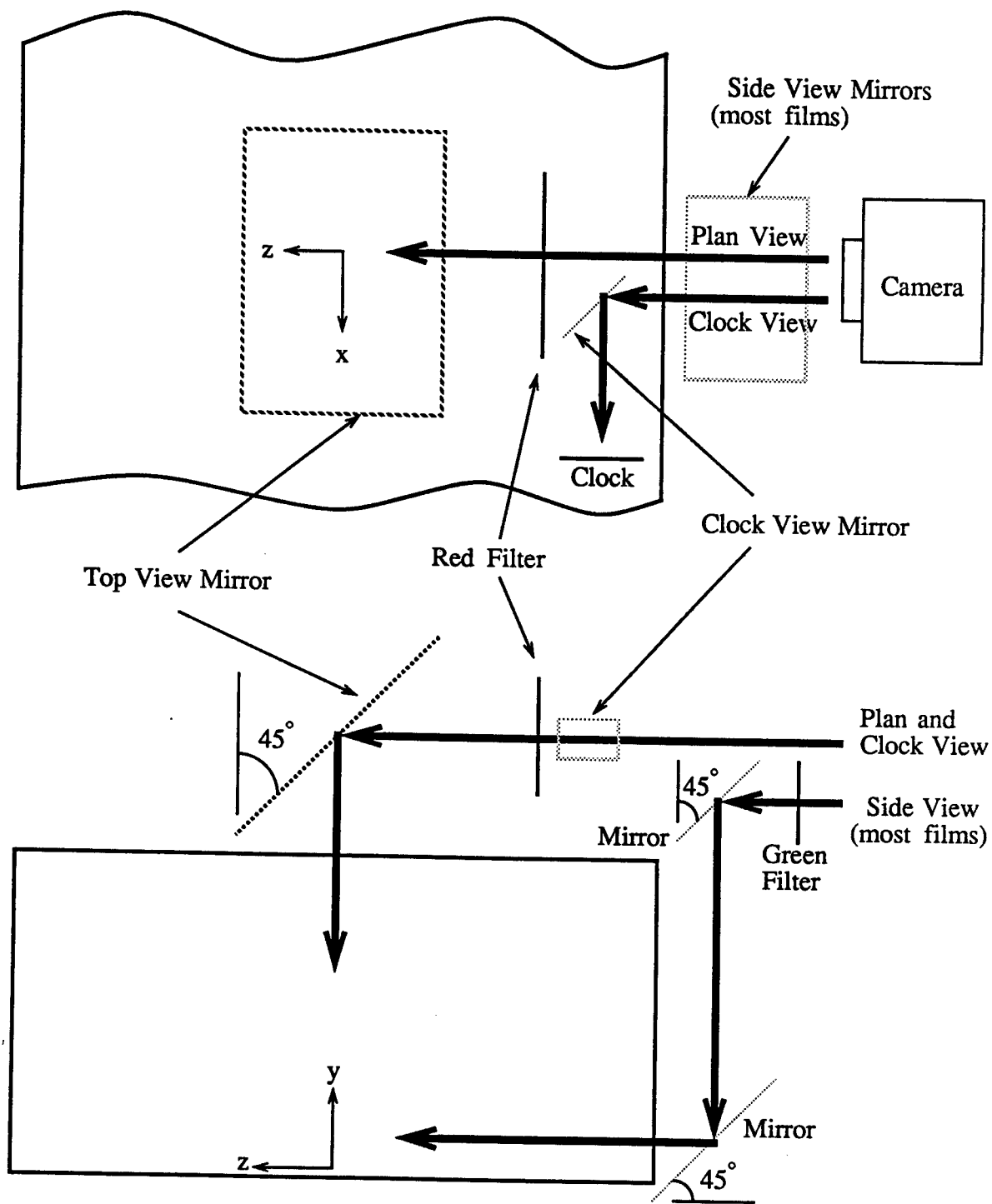
NOTE 1: The red filter was only used when the side view was present.
NOTE 2: The spanwise vorticity probe was located at the origin. The
         laser sheet passed through the X-Y plane.
NOTE 3: Dark arrows indicate lines of sight.

Figure 2.2.3 Camera and mirror setup.
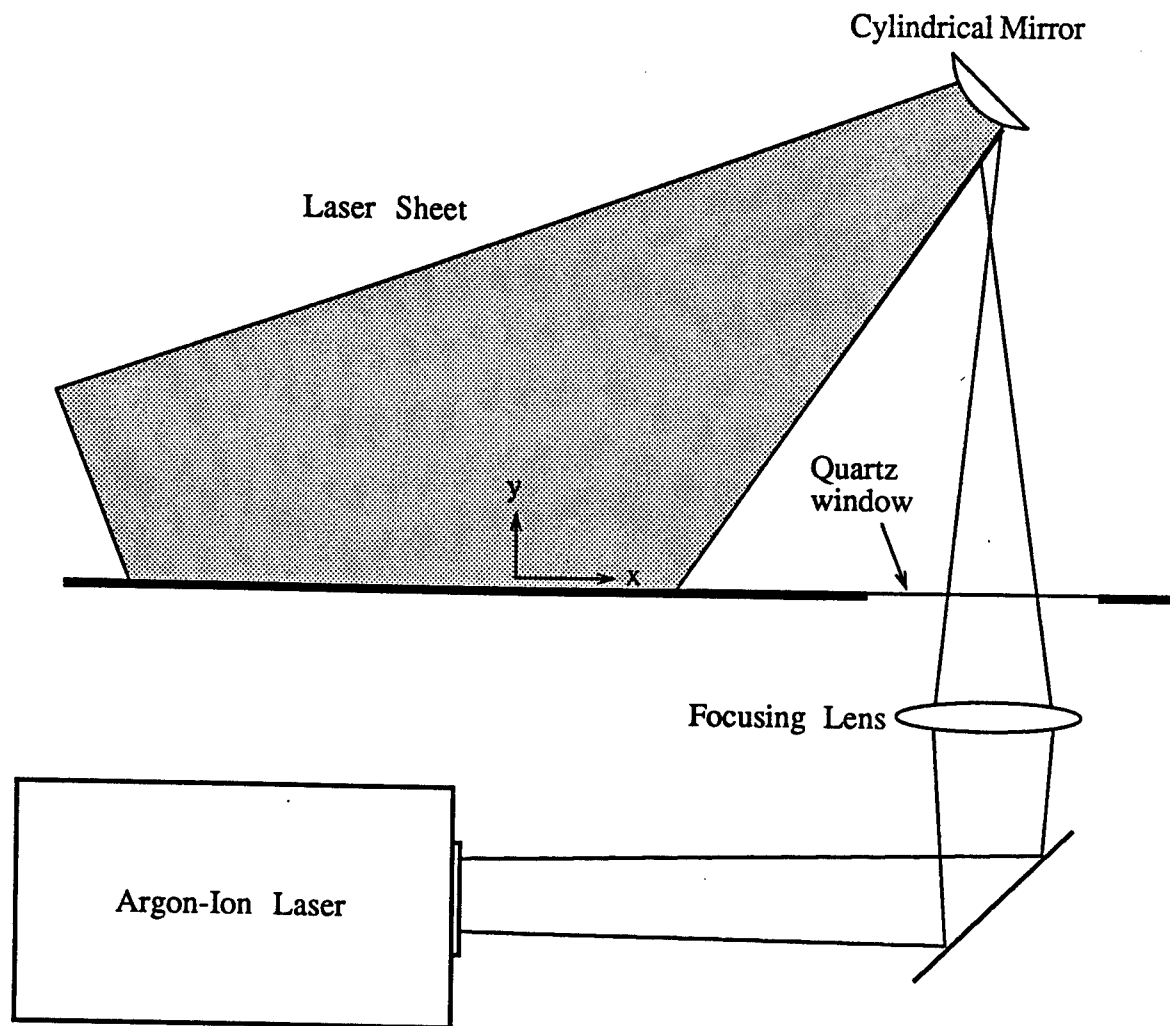
Figure 2.2.4 Laser and laser optics setup.

1st smoke slit (see Figure 2.2.1)

Fairing

y

x

Smoke

2nd smoke slit (see Figure 2.2.1)

y

x

Smoke Injected Tangential to the Flow
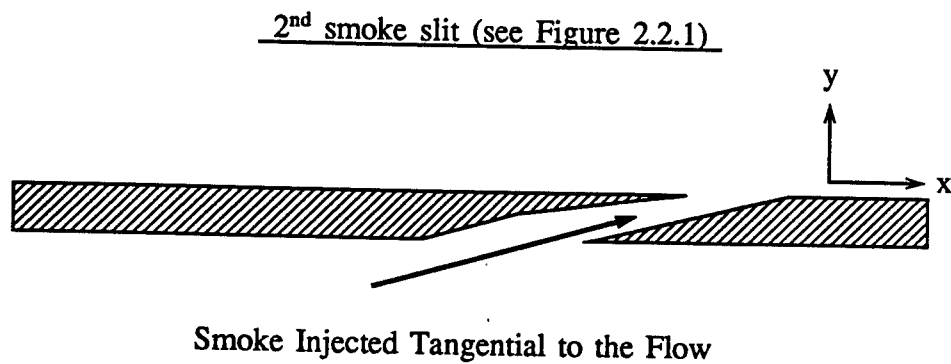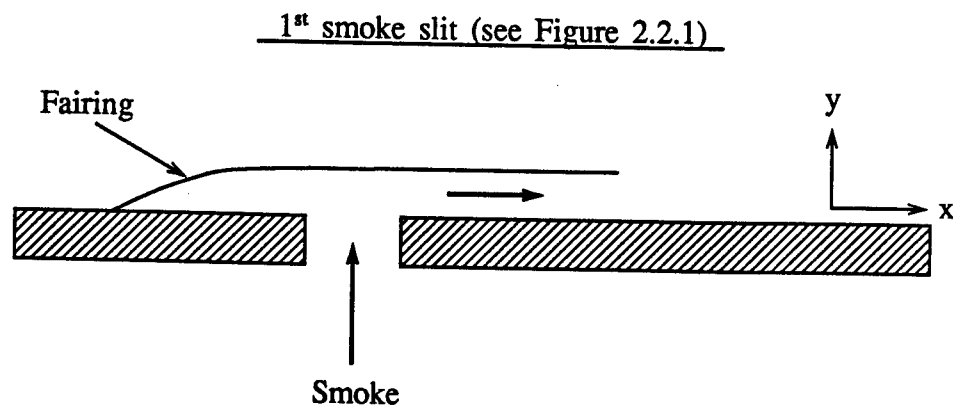
NOTE: Axes indicate directions only, not the location of the origin.

Figure 2.2.5 Smoke injection slit configurations (after Lovett, 1982)
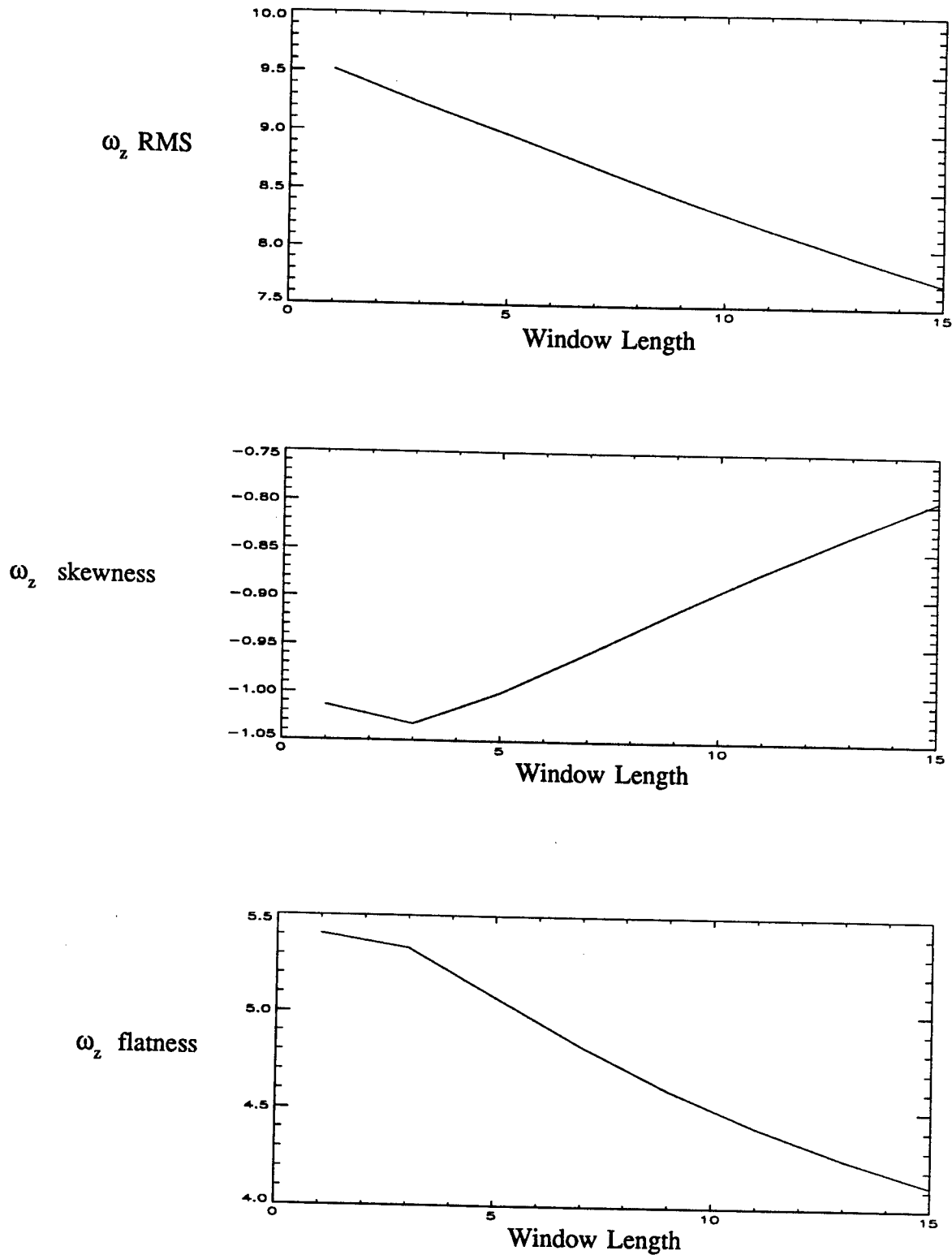
Figure 2.3.1 Changes in spanwise vorticity statistics for different averaging window lengths.

$\longleftarrow$ U_∞

Smoke Boundary.
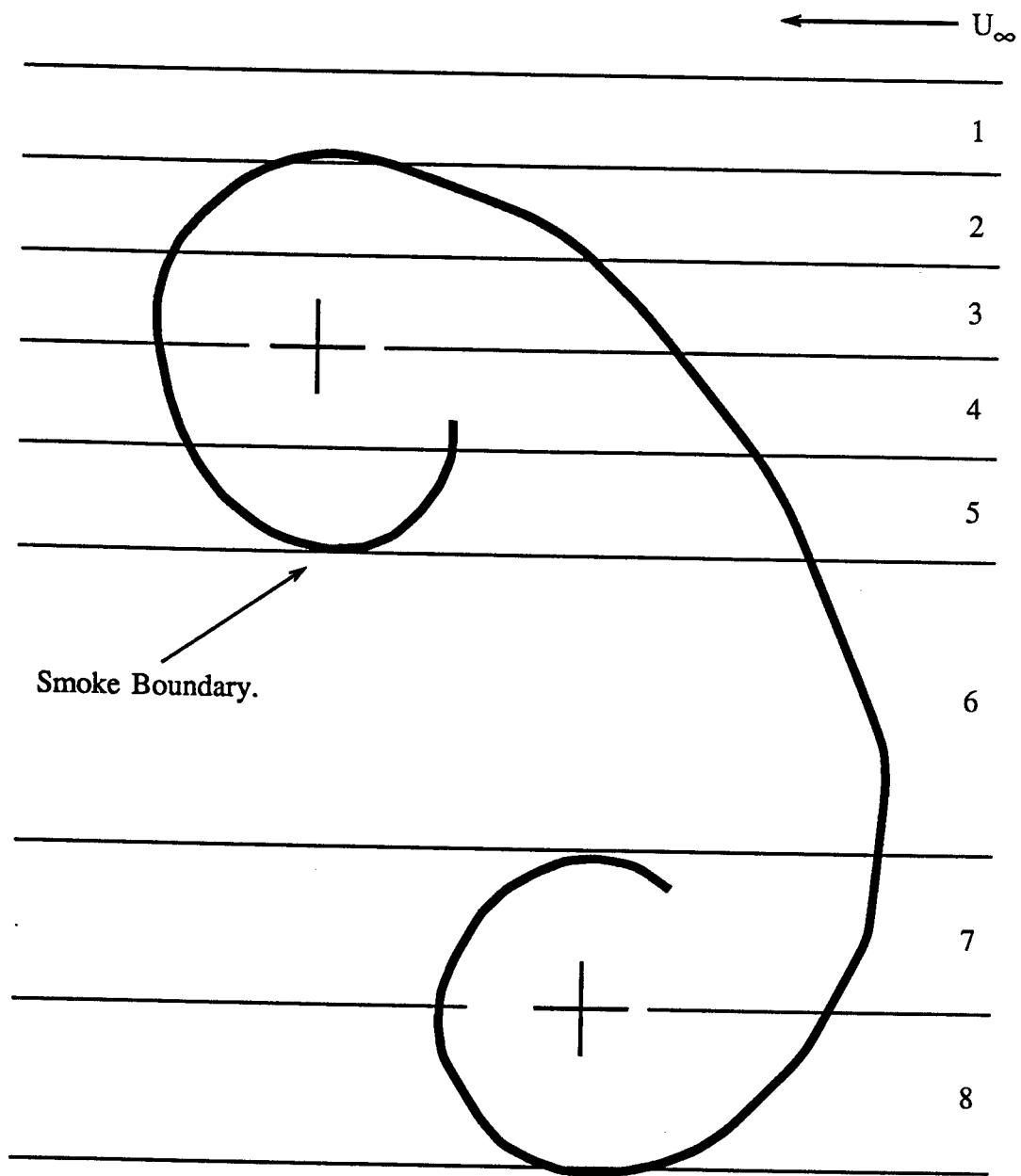
Figure 2.4.1 Zones of a "Typical Eddy" (after Signor, 1982)
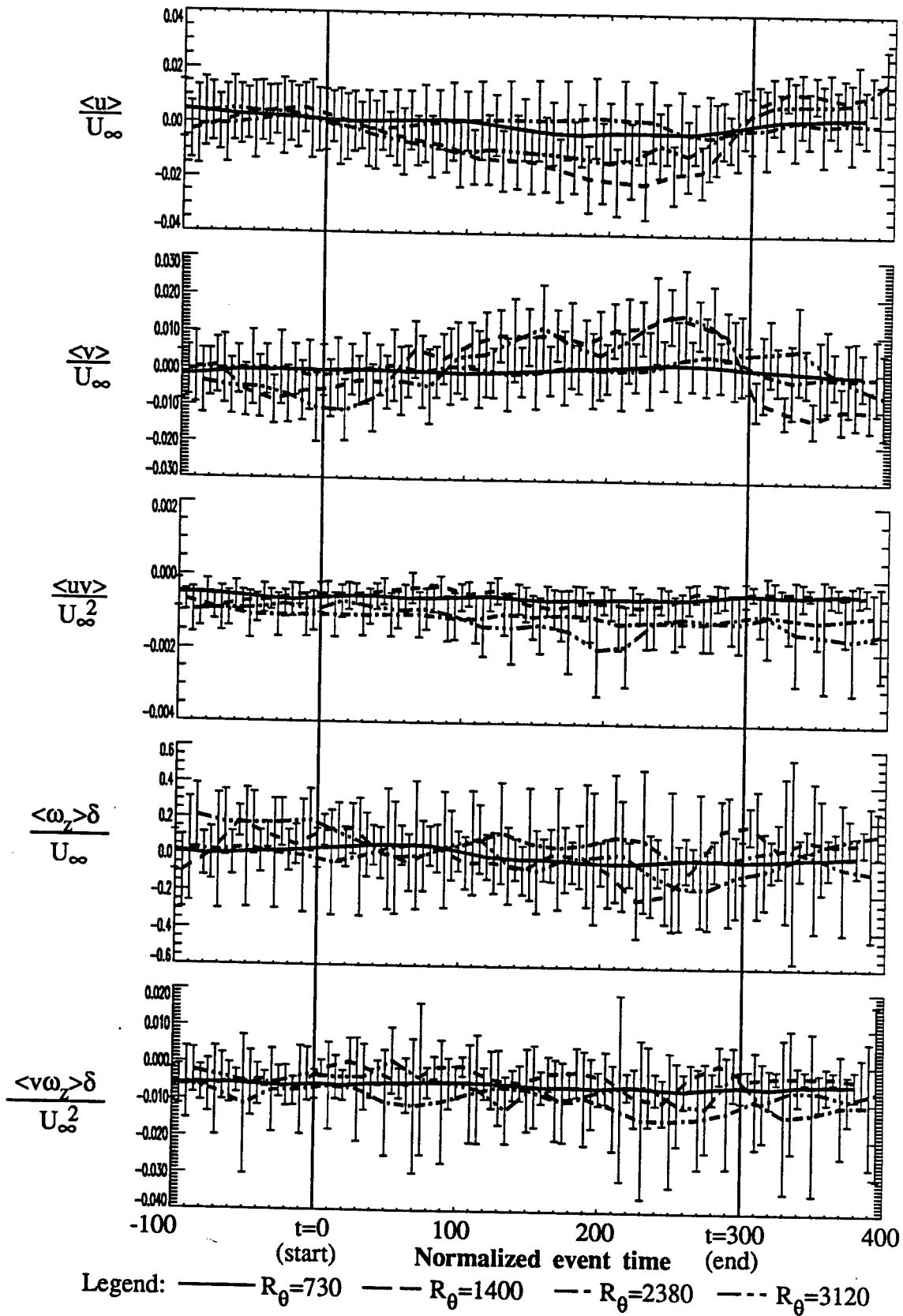
Figure 3.1.1 Outer-scaled LSM ensembles. Error bars indicate 25% of an ensemble's standard deviation at each point in time
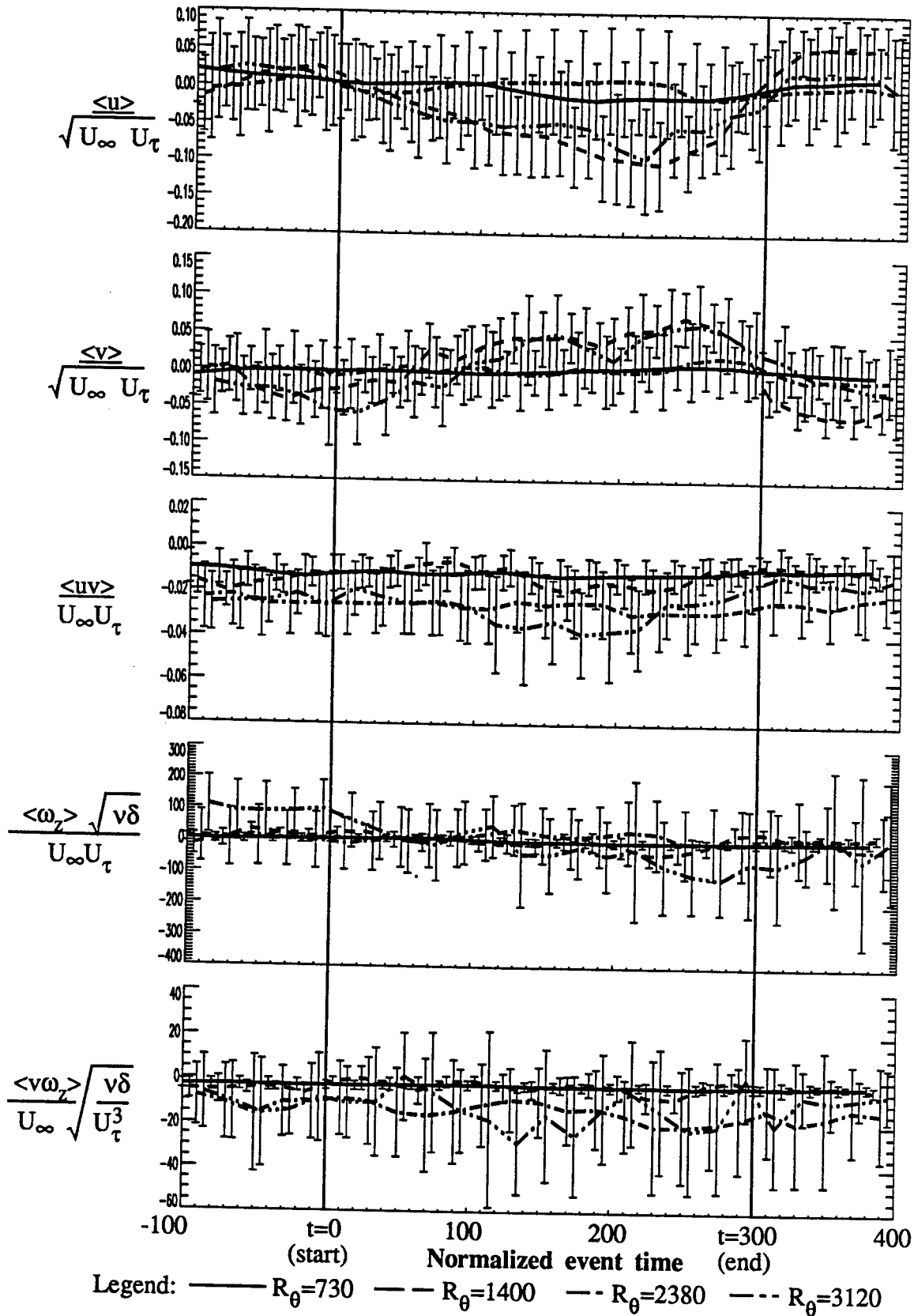
Figure 3.1.2 Mixed-scaled LSM ensembles. Error bars indicate 25% of an ensemble's standard deviation at each point in time
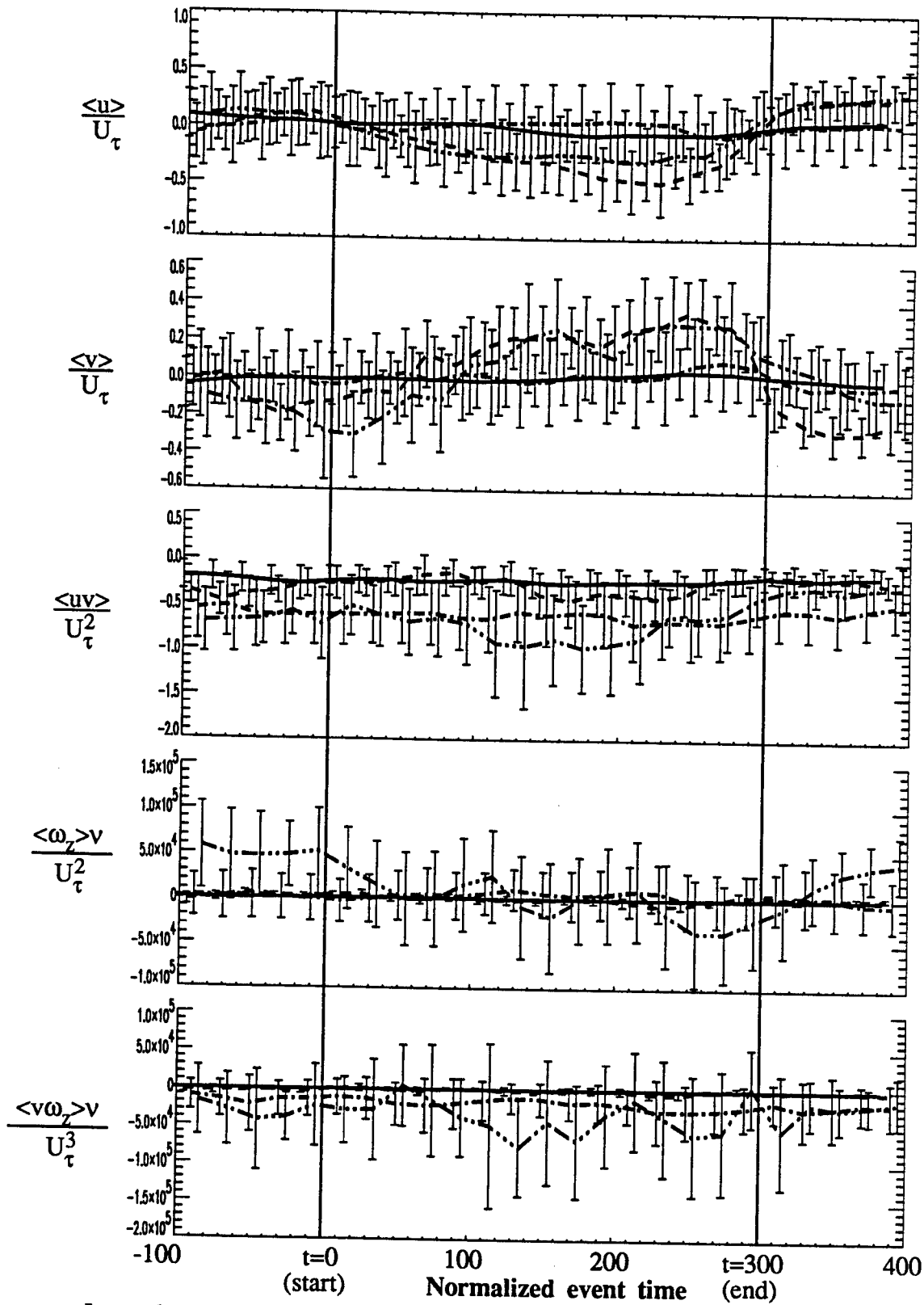
Figure 3.1.3 Inner-scaled LSM ensembles. Error bars indicate 25% of an ensemble's standard deviation at each point in time
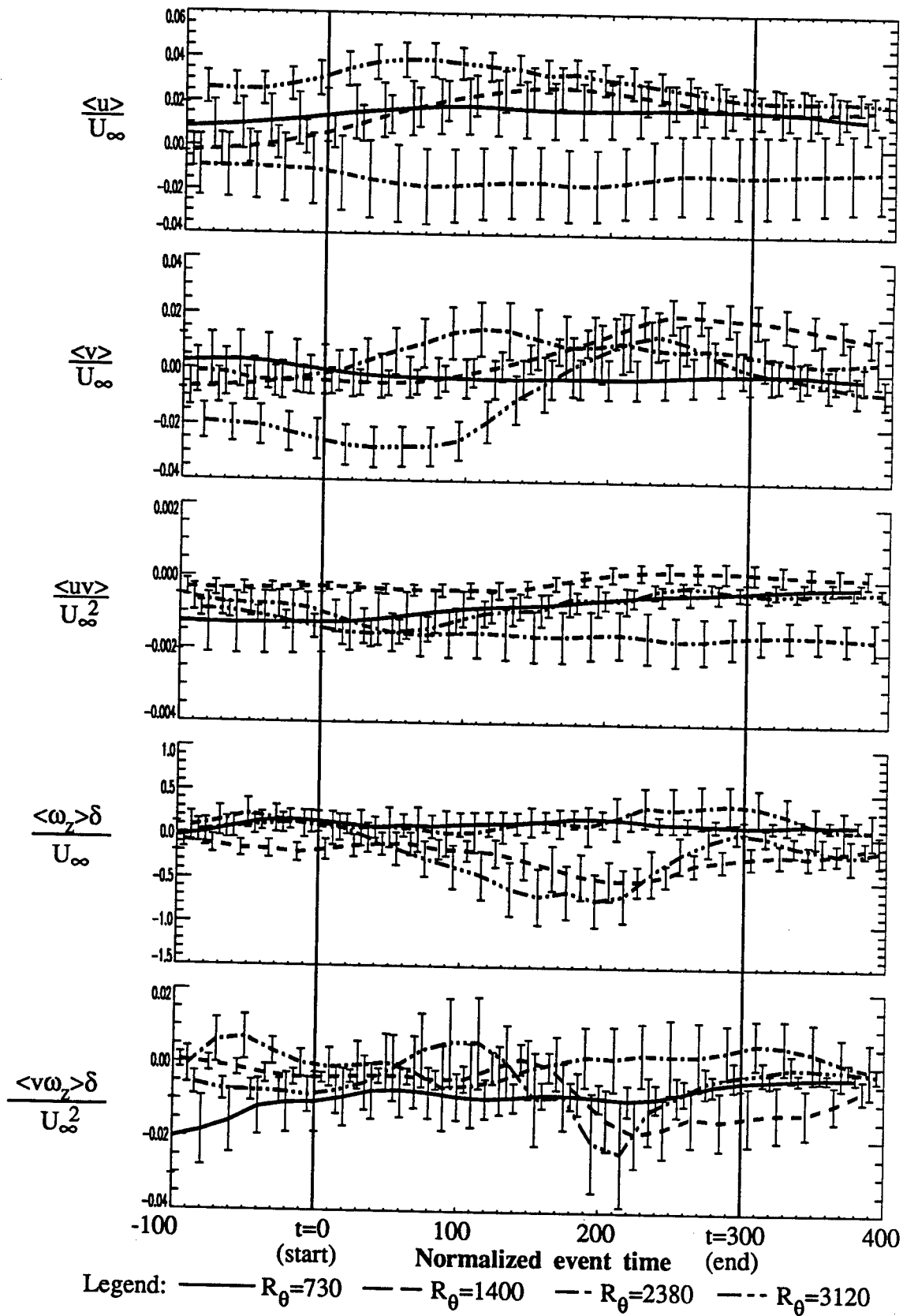
Figure 3.2.1 Outer-scaled RLM sweep ensembles. Error bars indicate 25% of an ensemble's standard deviation at each point in time
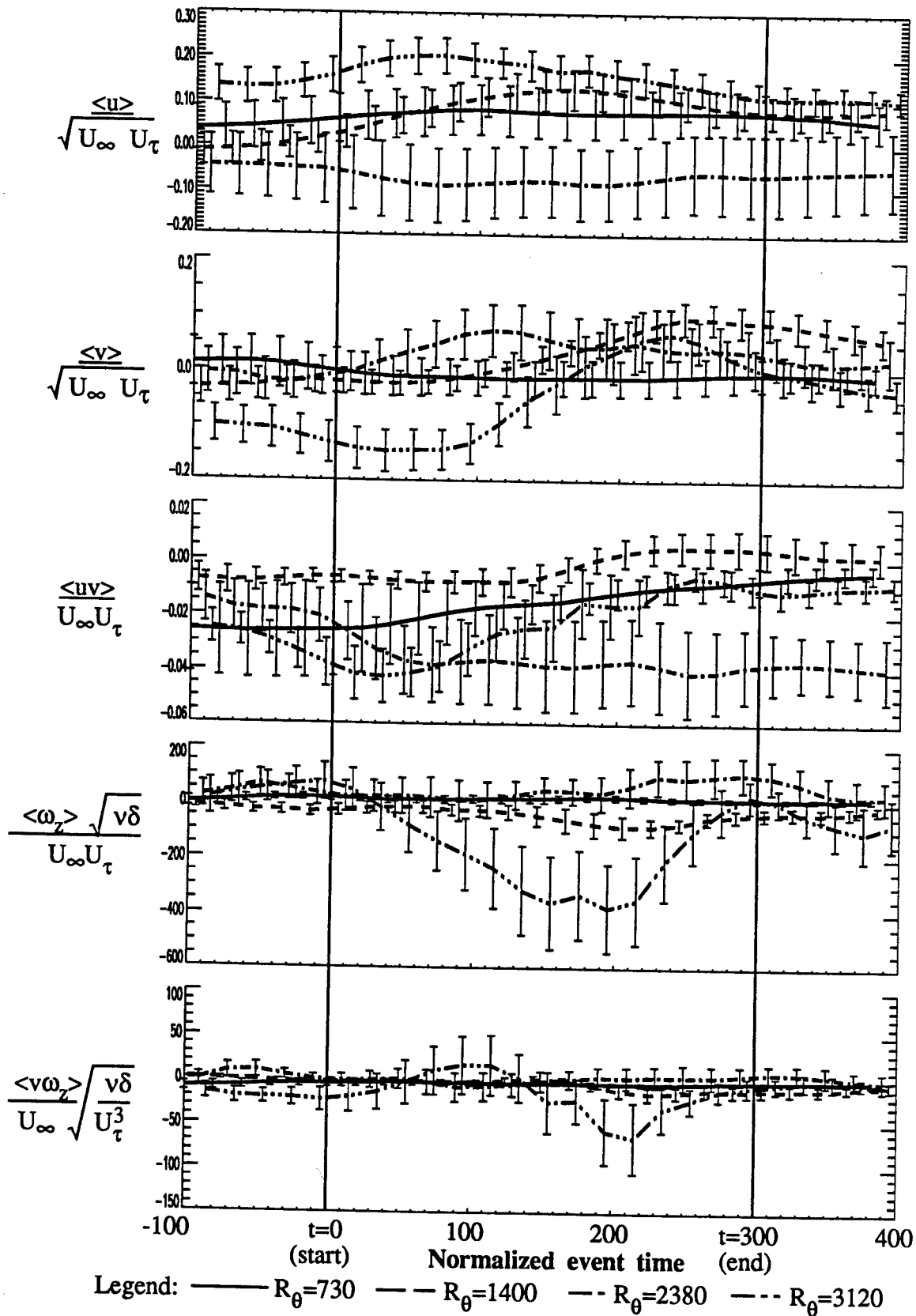
Figure 3.2.2 Mixed-scaled RLM sweep ensembles. Error bars indicate 25% of an ensemble's standard deviation at each point in time
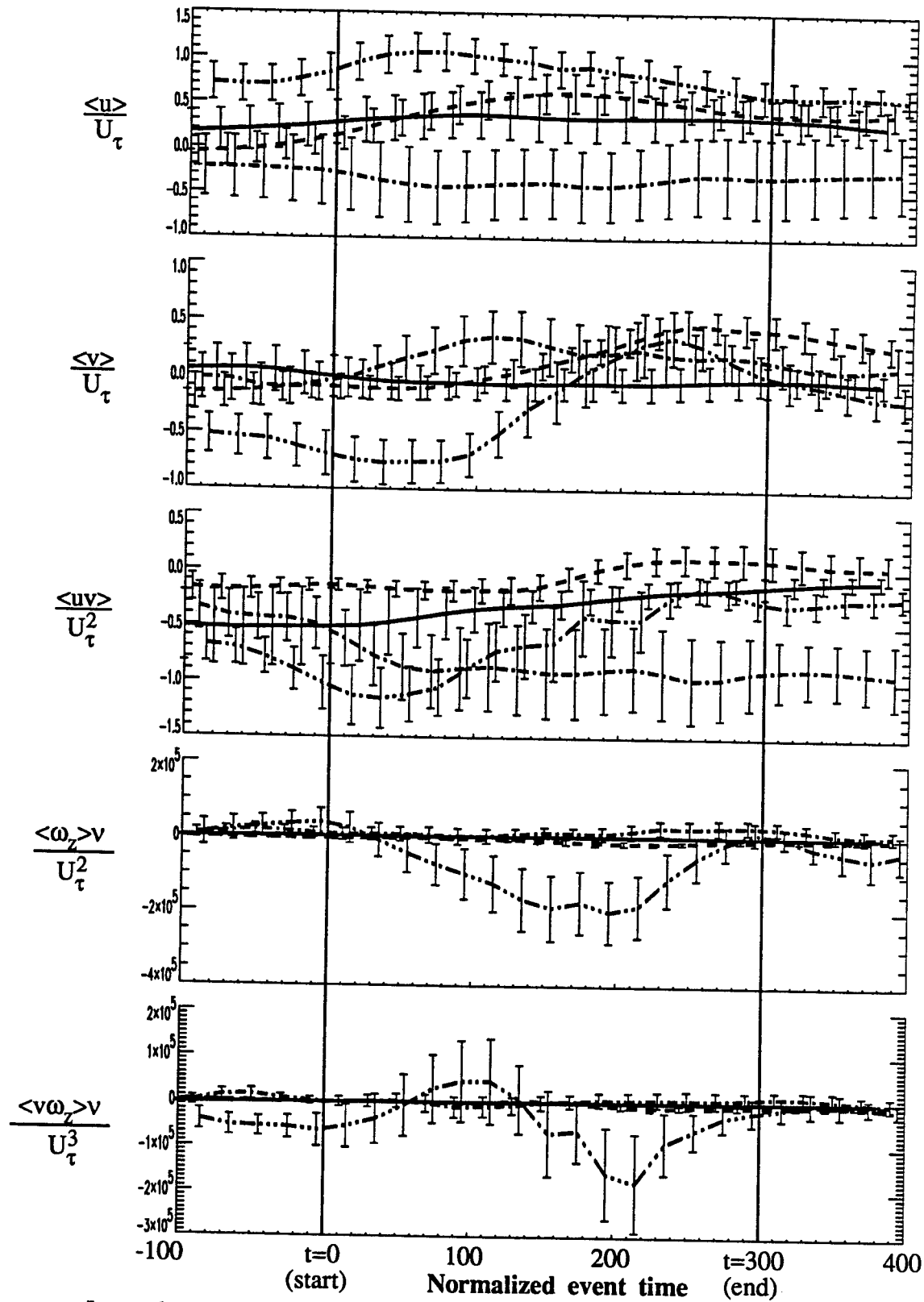
Figure 3.2.3 Inner-scaled RLM sweep ensembles. Error bars indicate 25% of an ensemble's standard deviation at each point in time
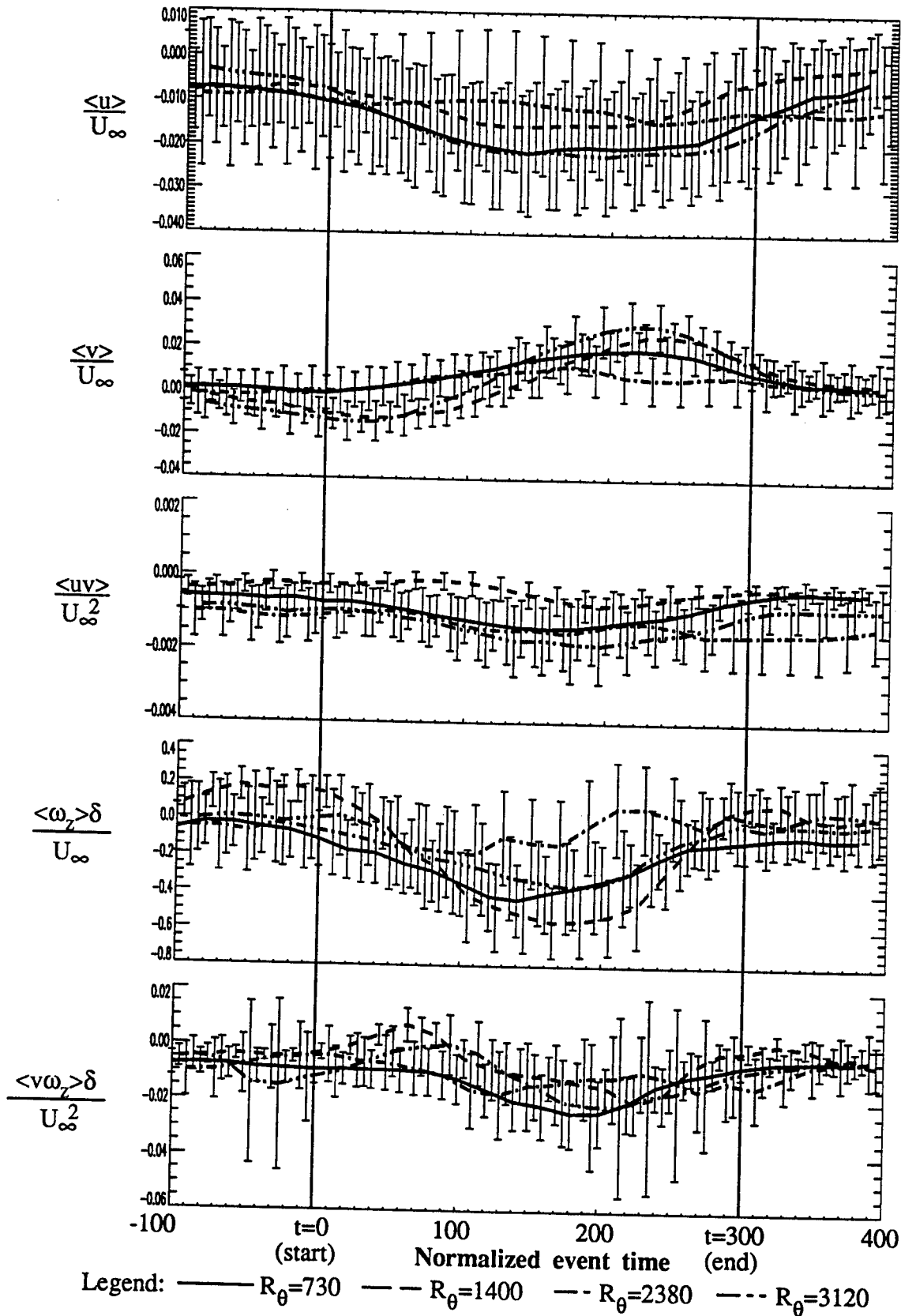
Figure 3.2.4 Outer-scaled RLM ejection ensembles. Error bars indicate 25% of an ensemble's standard deviation at each point in time
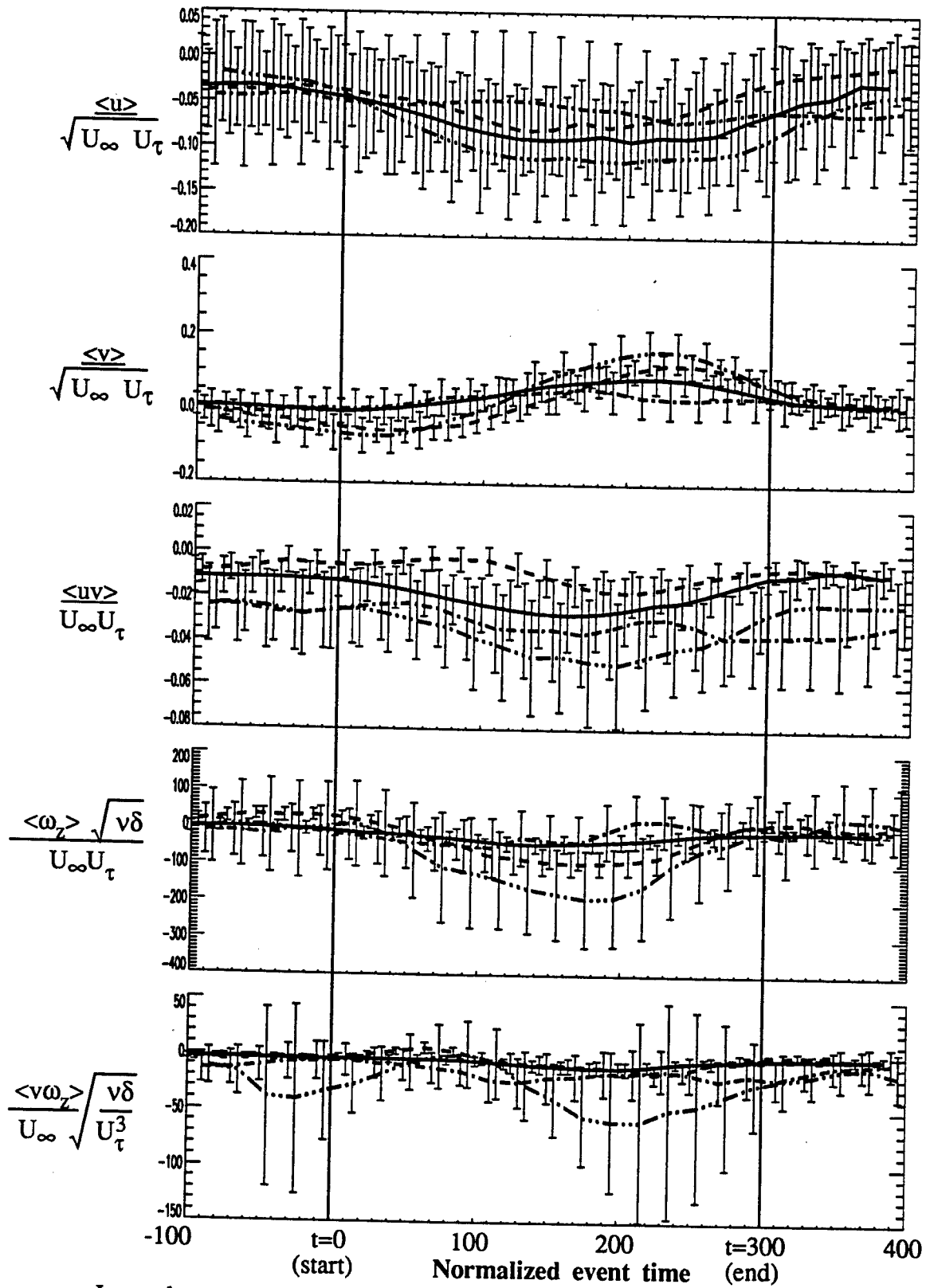
Figure 3.2.5 Mixed-scaled RLM ejection ensembles. Error bars indicate 25% of an ensemble's standard deviation at each point in time
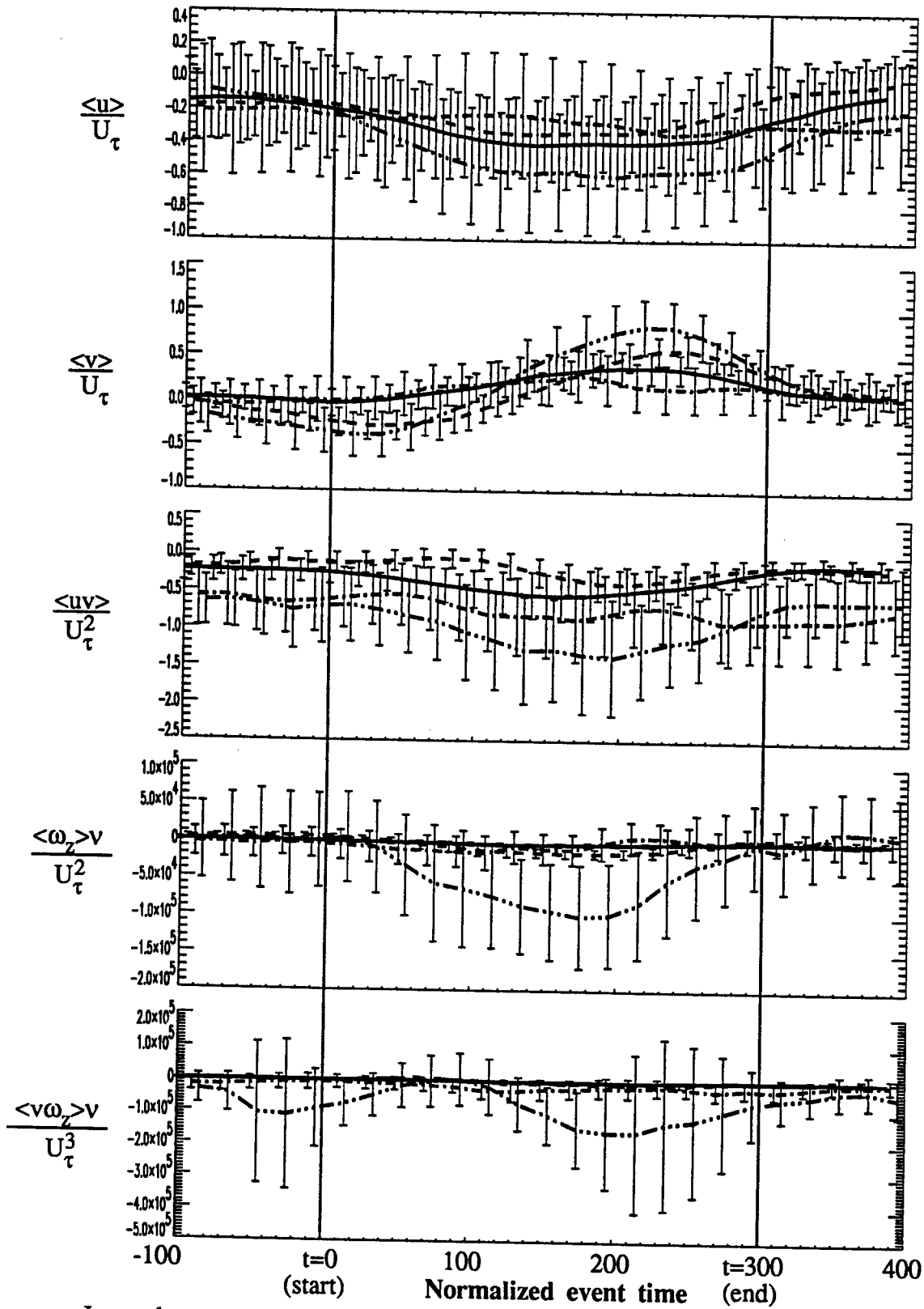
Figure 3.2.6 Inner-scaled RLM ejection ensembles. Error bars indicate 25% of an ensemble's standard deviation at each point in time
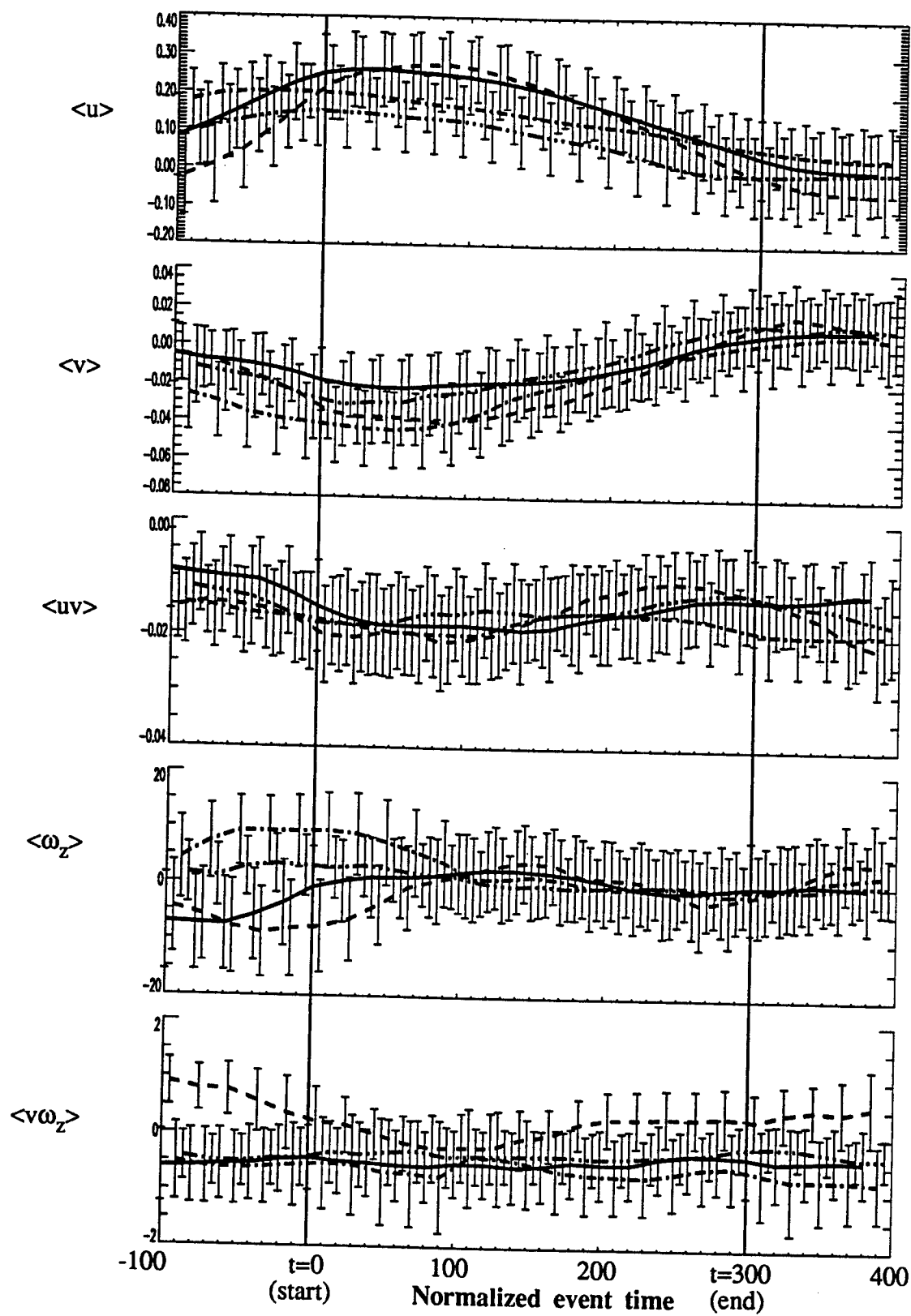
Figure 3.3.1 Ensembles of inner-region visually detected sweeps. Error bars indicate 25% of an ensemble's standard deviation at each point in time
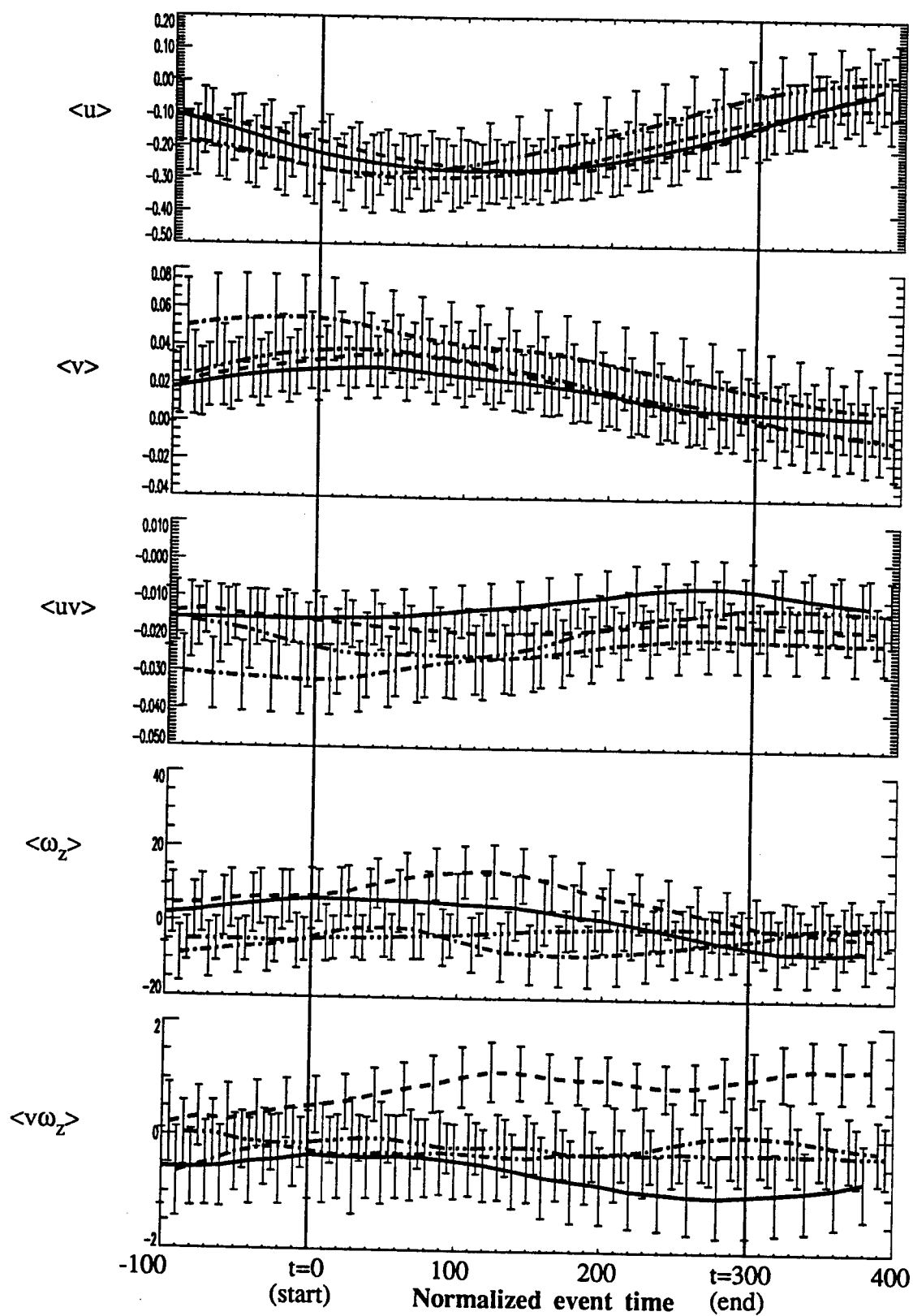
Figure 3.3.2 Ensembles of inner-region visually detected ejections. Error bars indicate 25% of an ensemble's standard deviation at each point in time

Number
of Events

uv-quadrant technique threshold level
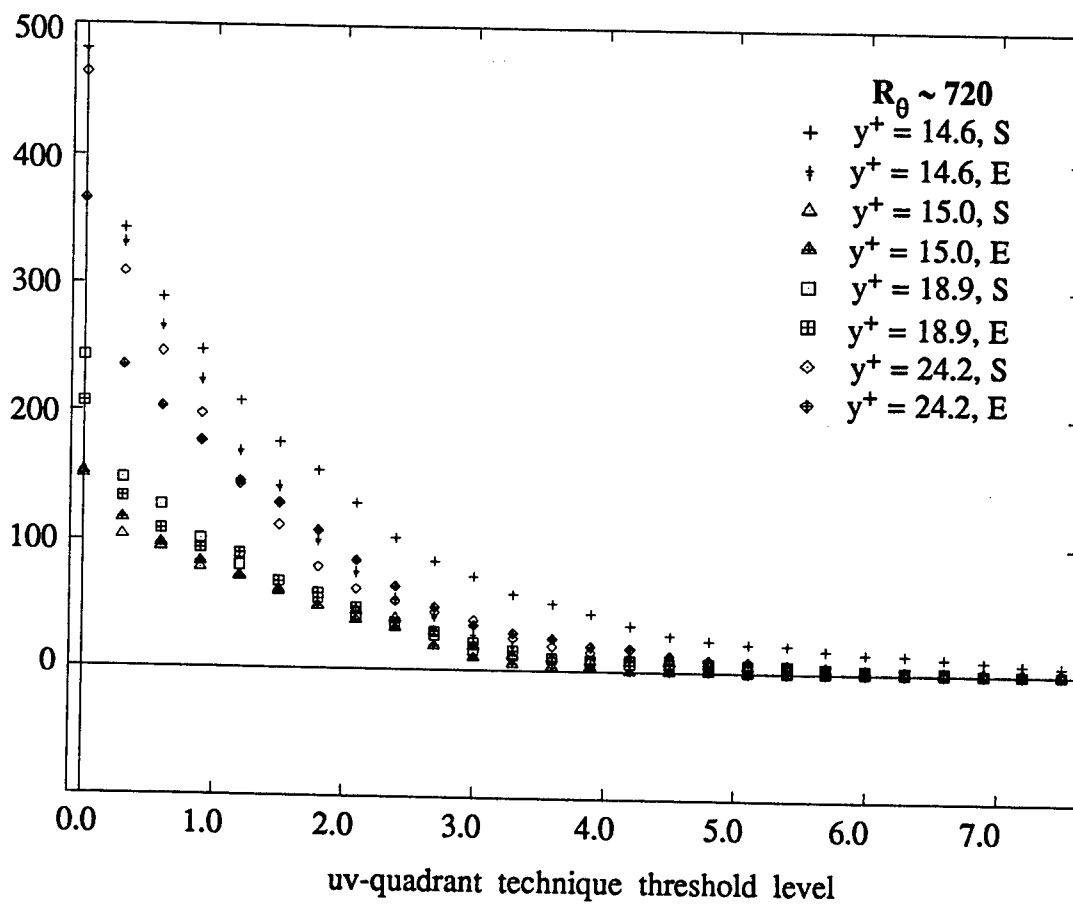
Figure 3.4.1
Number of uv-quadrant Events
vs. Threshold level (Inner-region data)
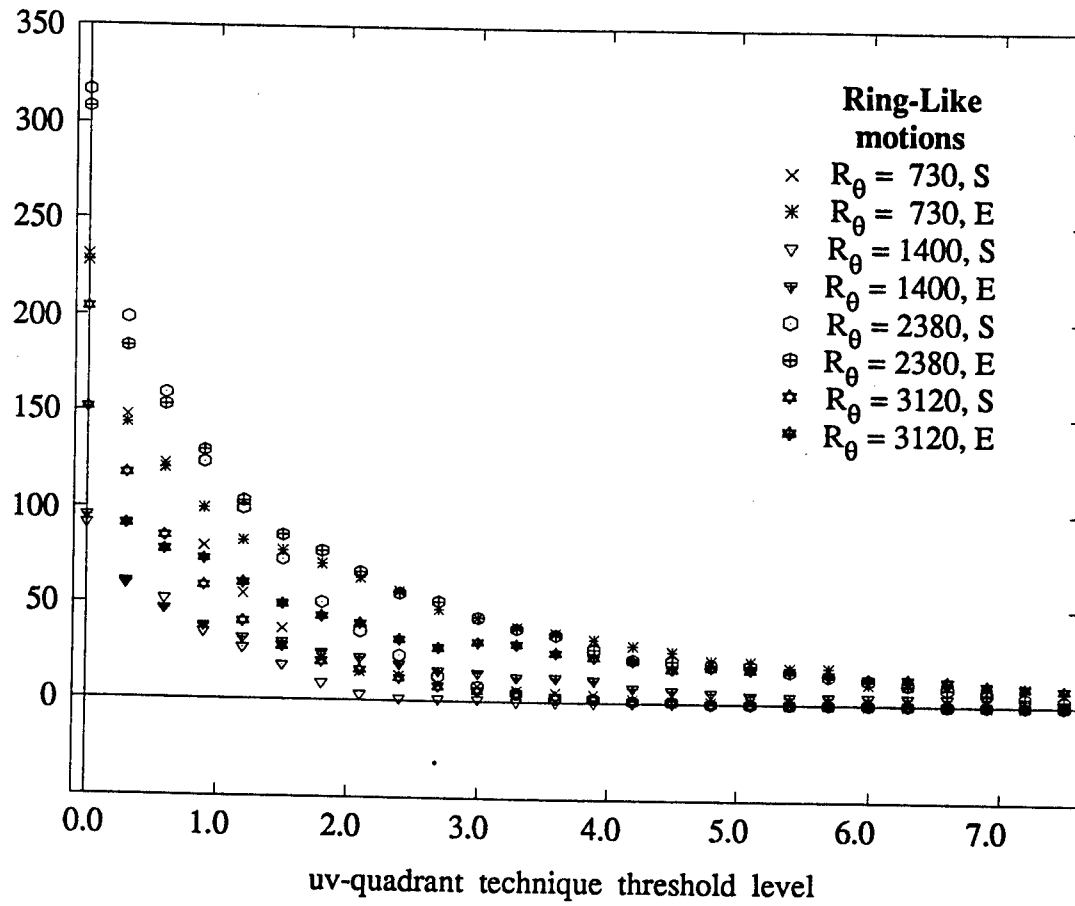
Number
of Events

Figure 3.4.2
Number of uv-quadrant Events
vs. Threshold level (RLM data set)

Number
of Events

uv-quadrant technique threshold level
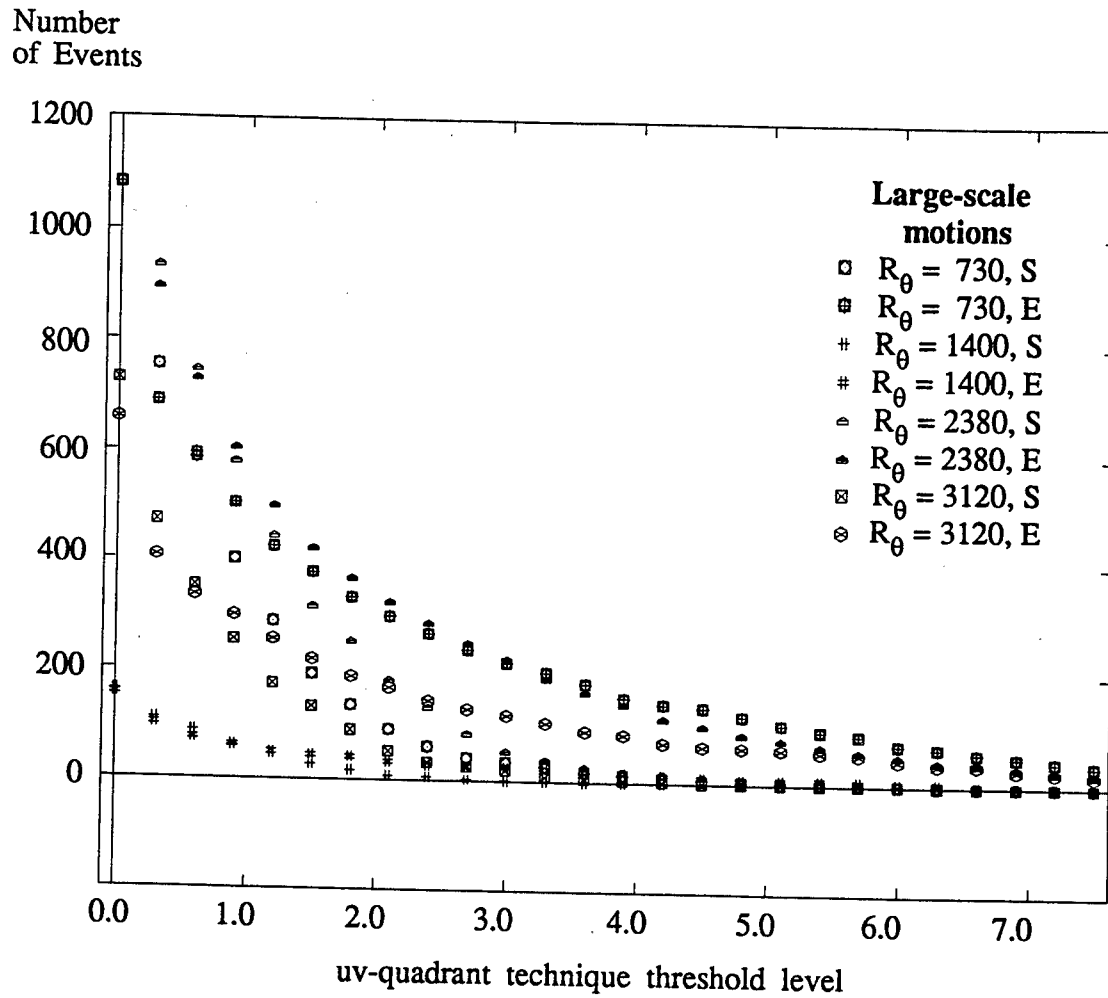
Figure 3.4.3
Number of uv-quadrant Events
vs. Threshold level (LSM data set)
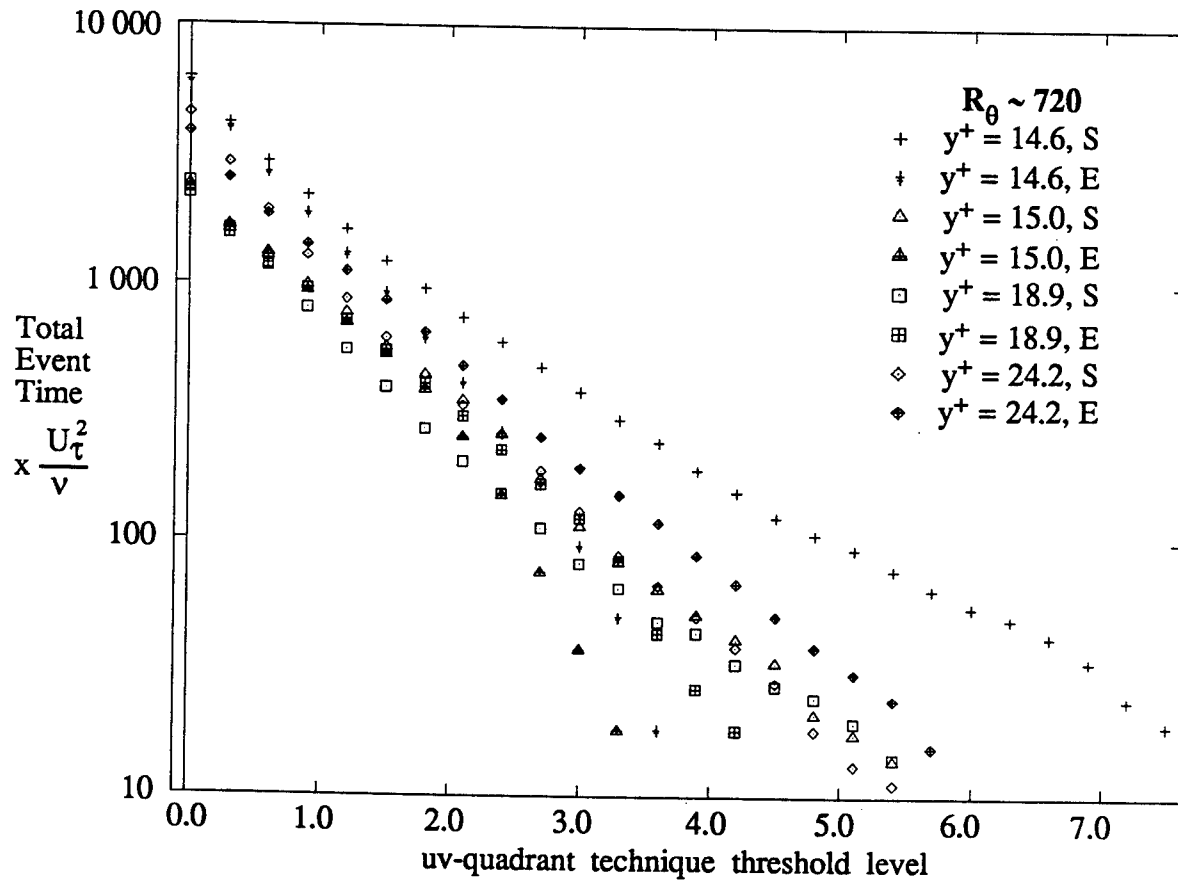
Figure 3.4.4
Inner-Scaled Total uv-quadrant Event Time
vs. Threshold (Inner-region data)
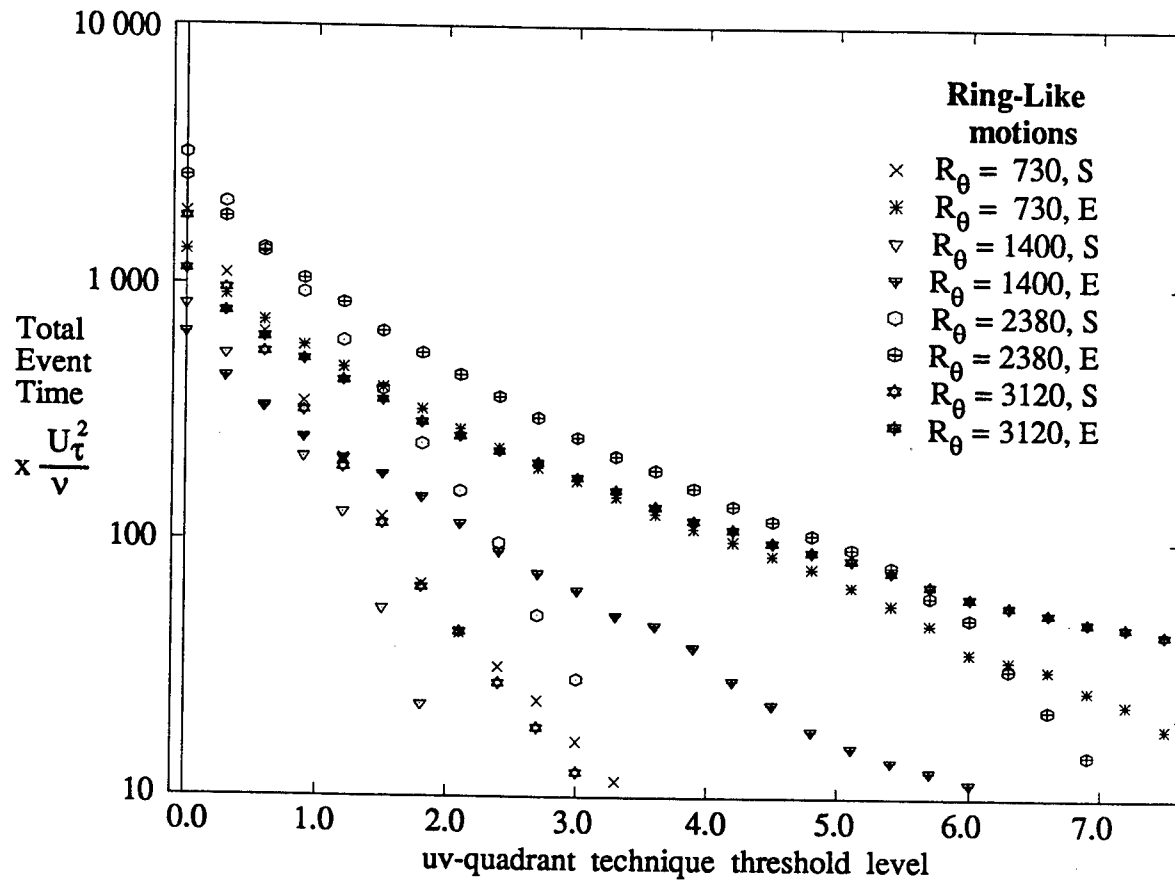
Figure 3.4.5
Inner-Scaled Total uv-quadrant Event Time
vs. Threshold (RLM data set)
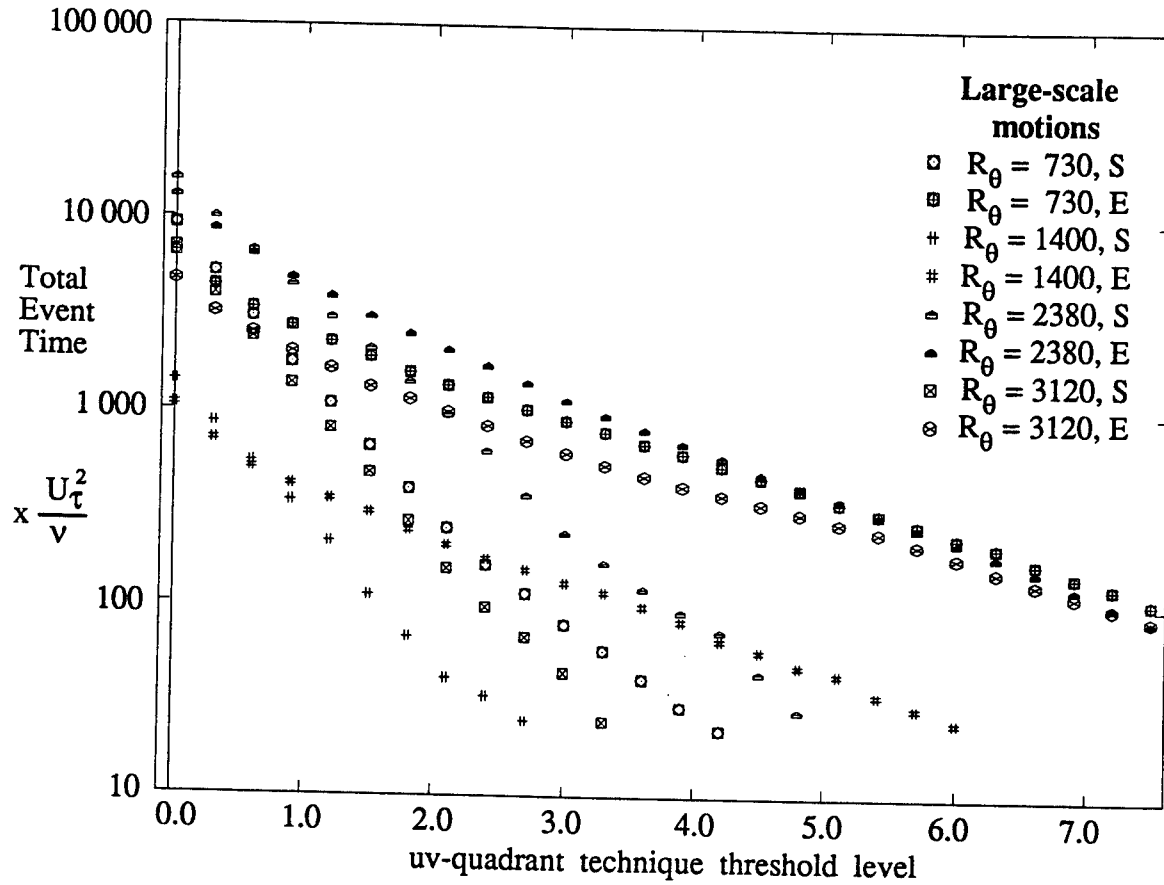
Figure 3.4.6
Inner-Scaled Total uv-quadrant Event Time
vs. Threshold (LSM data set)
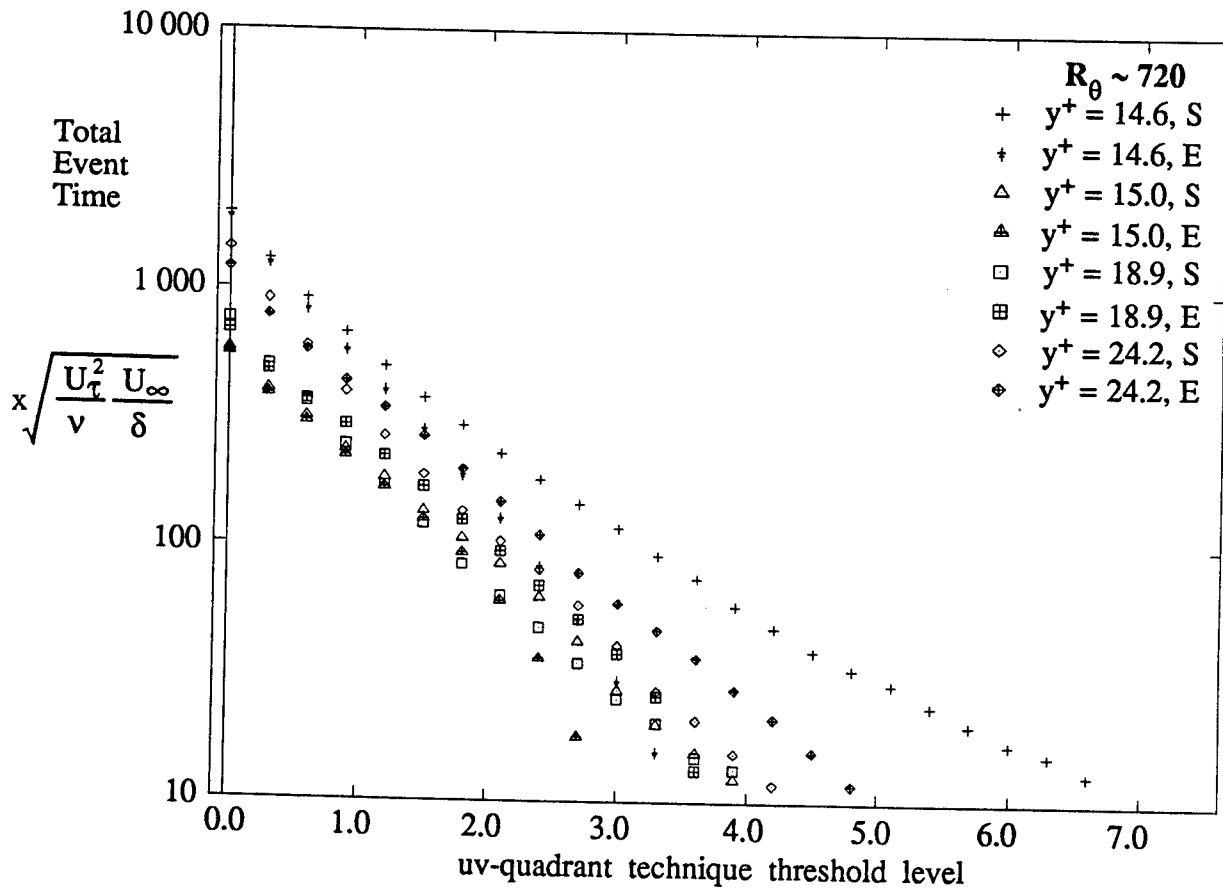
Figure 3.4.7
Total uv-quadrant Event Time (Mixed Scaling)
vs. Threshold (Inner-region data)
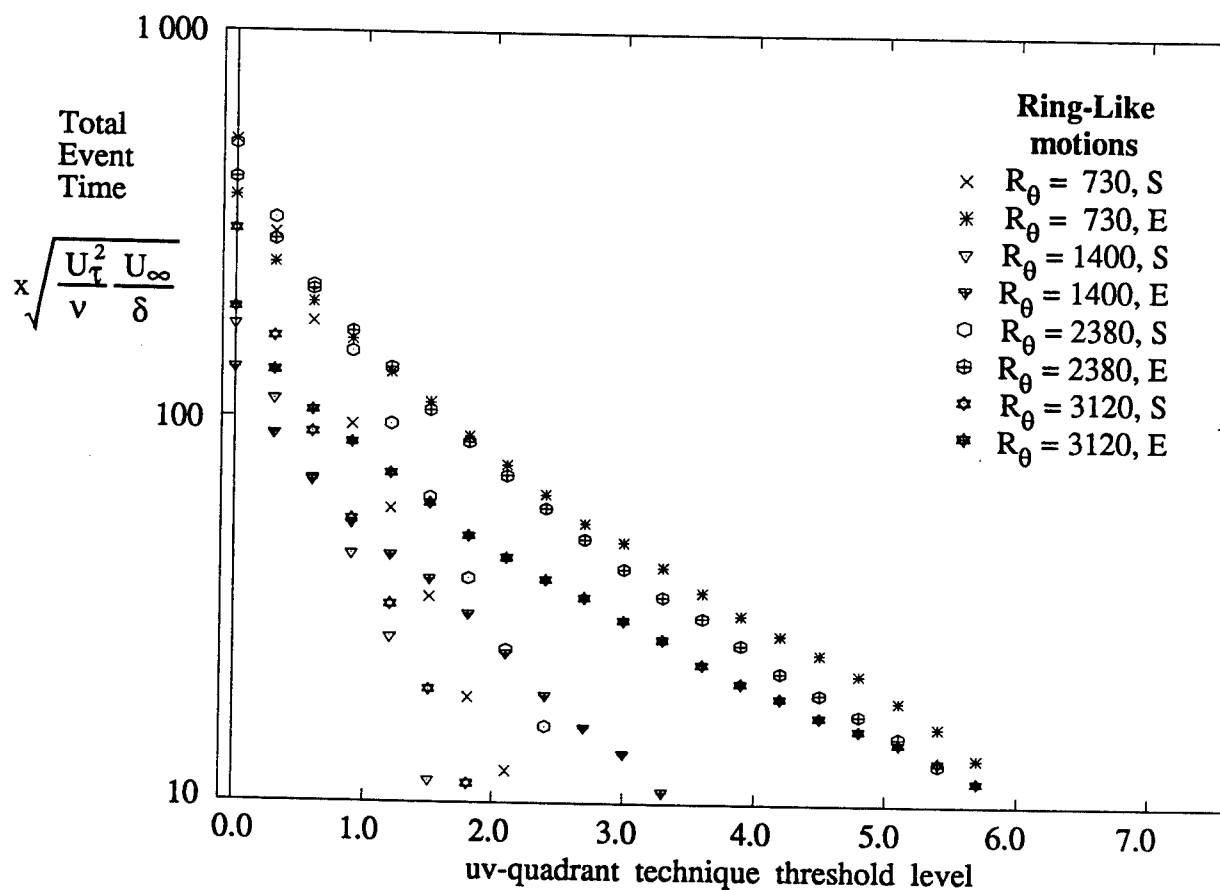
Figure 3.4.8
Total uv-quadrant Event Time (Mixed Scaling)
vs. Threshold (RLM data set)
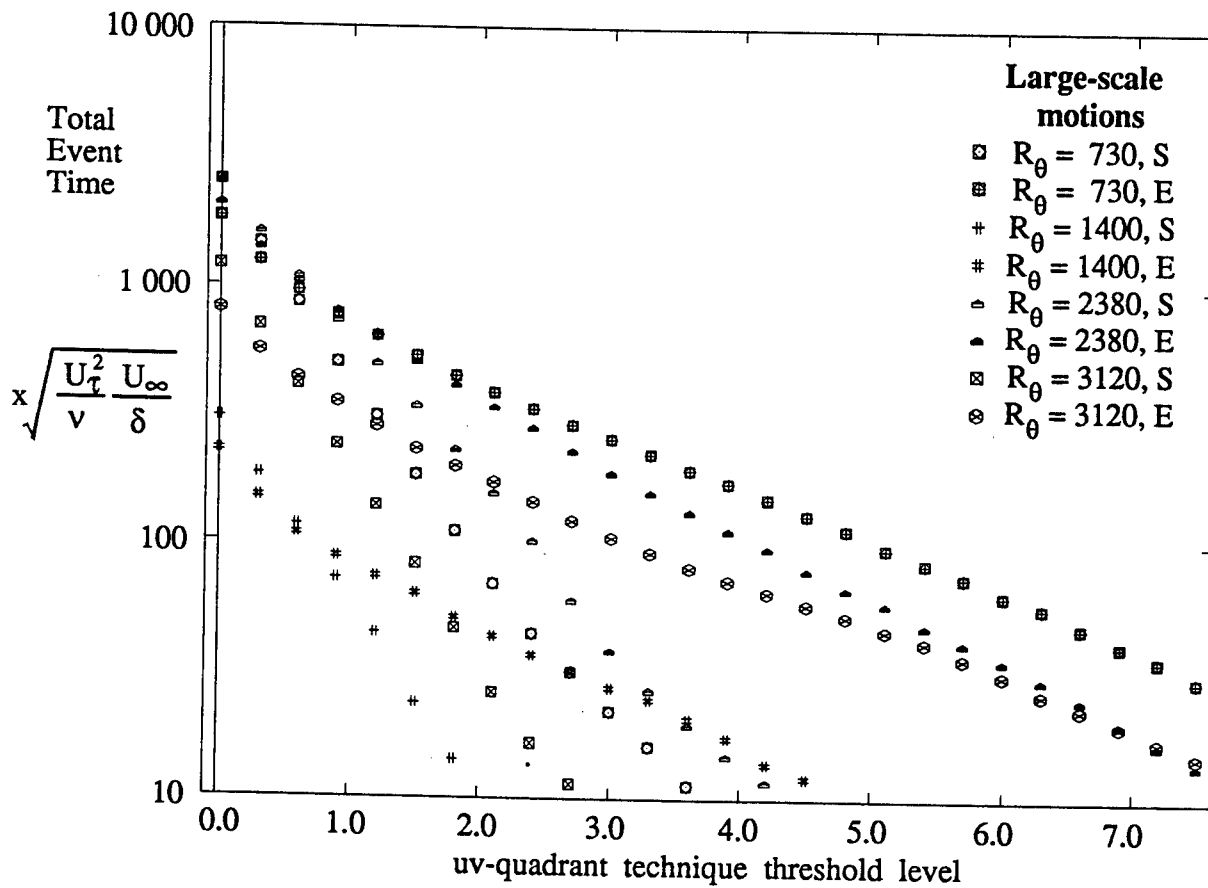
Figure 3.4.9
Total uv-quadrant Event Time (Mixed Scaling)
vs. Threshold (LSM data set)
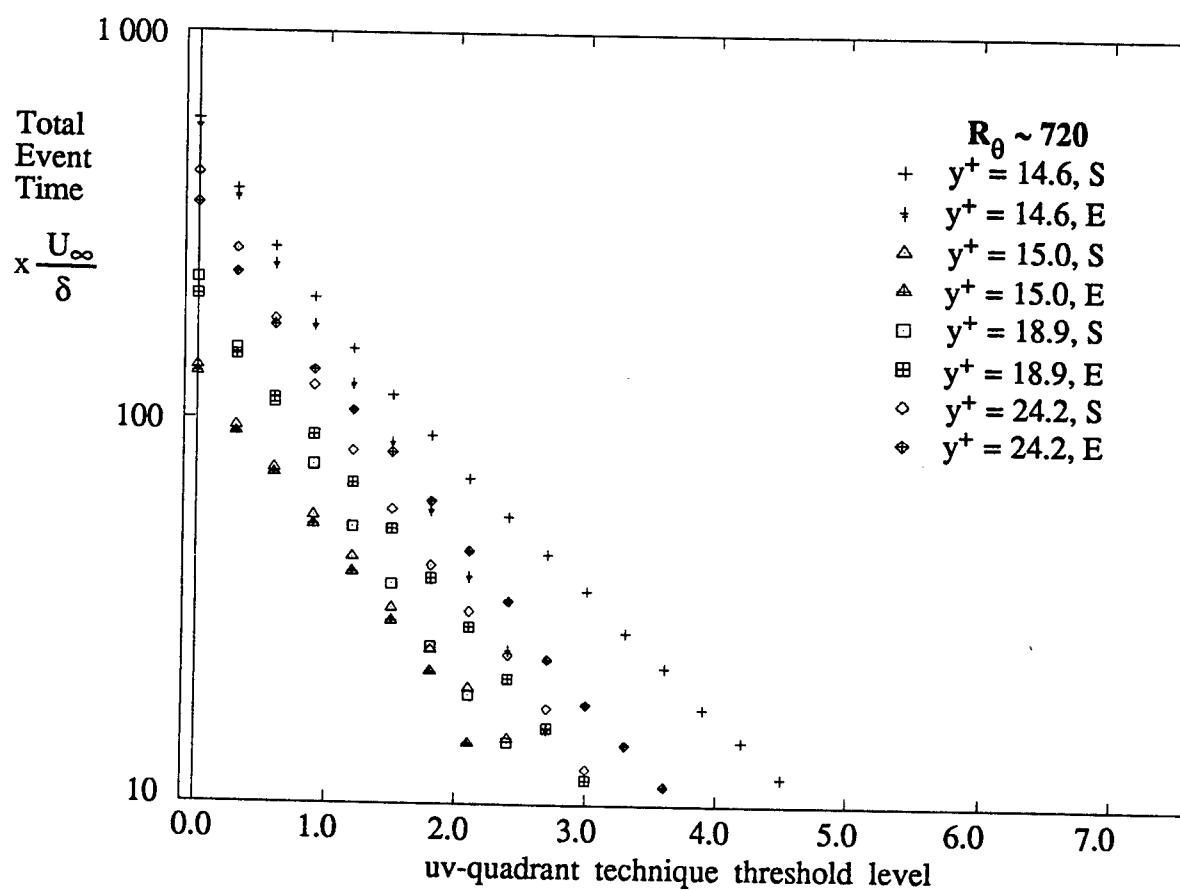
Figure 3.4.10
Outer-Scaled uv-quadrant Total Event Time
vs. Threshold (Inner-region data)
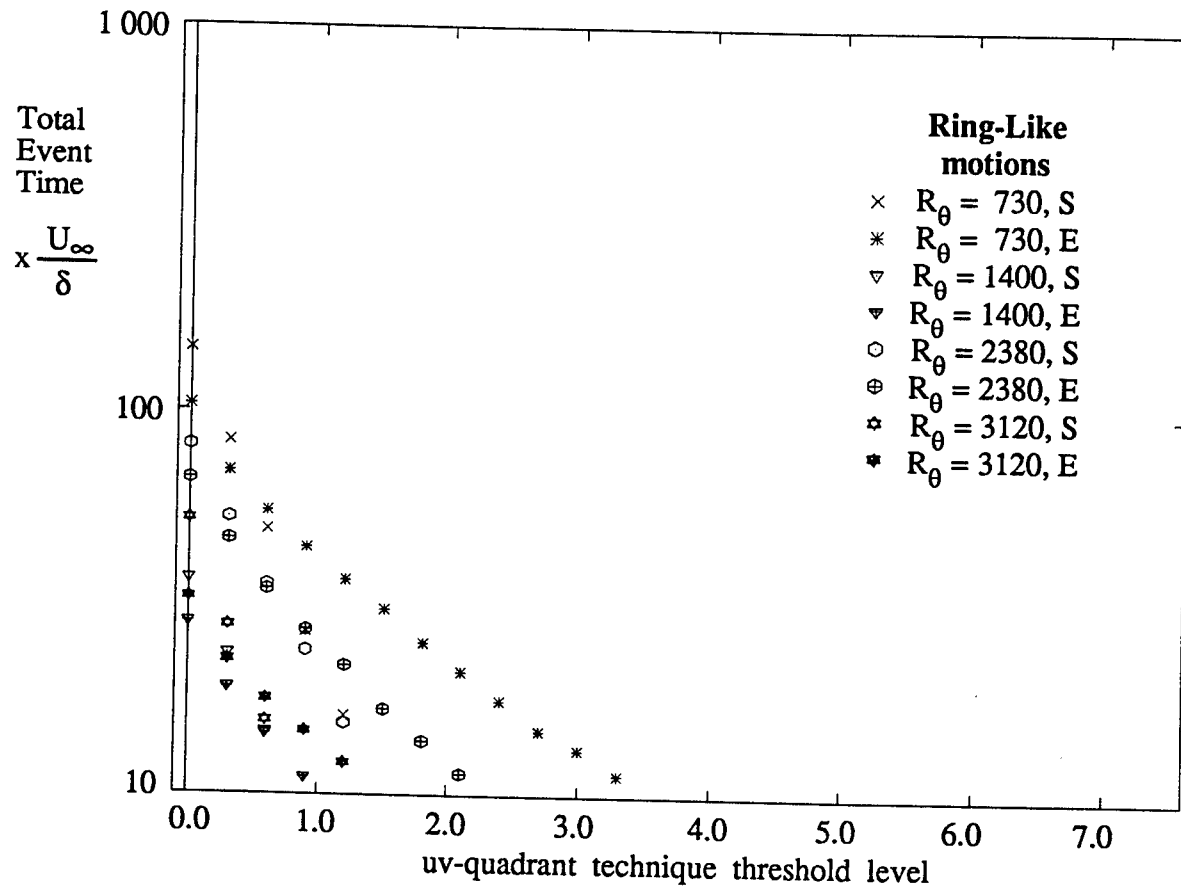
Figure 3.4.11
Outer-Scaled Total uv-quadrant Event Time
vs. Threshold (RLM data set)
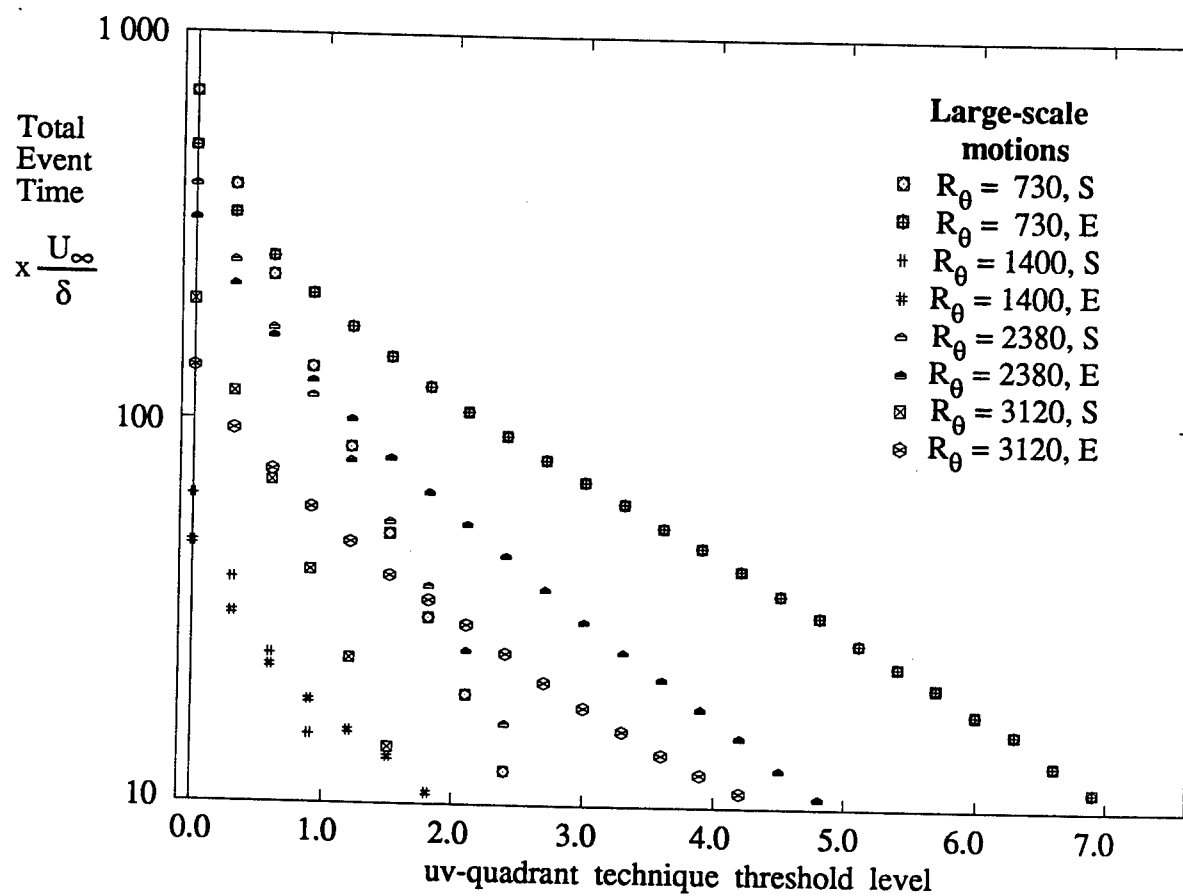
Figure 3.4.12
Outer-Scaled Total uv-quadrant Event Time
vs. Threshold (LSM data set)

Number
of Events
――――――― $\times \dfrac{\nu}{U_\tau^2}$
Total Sample
Time
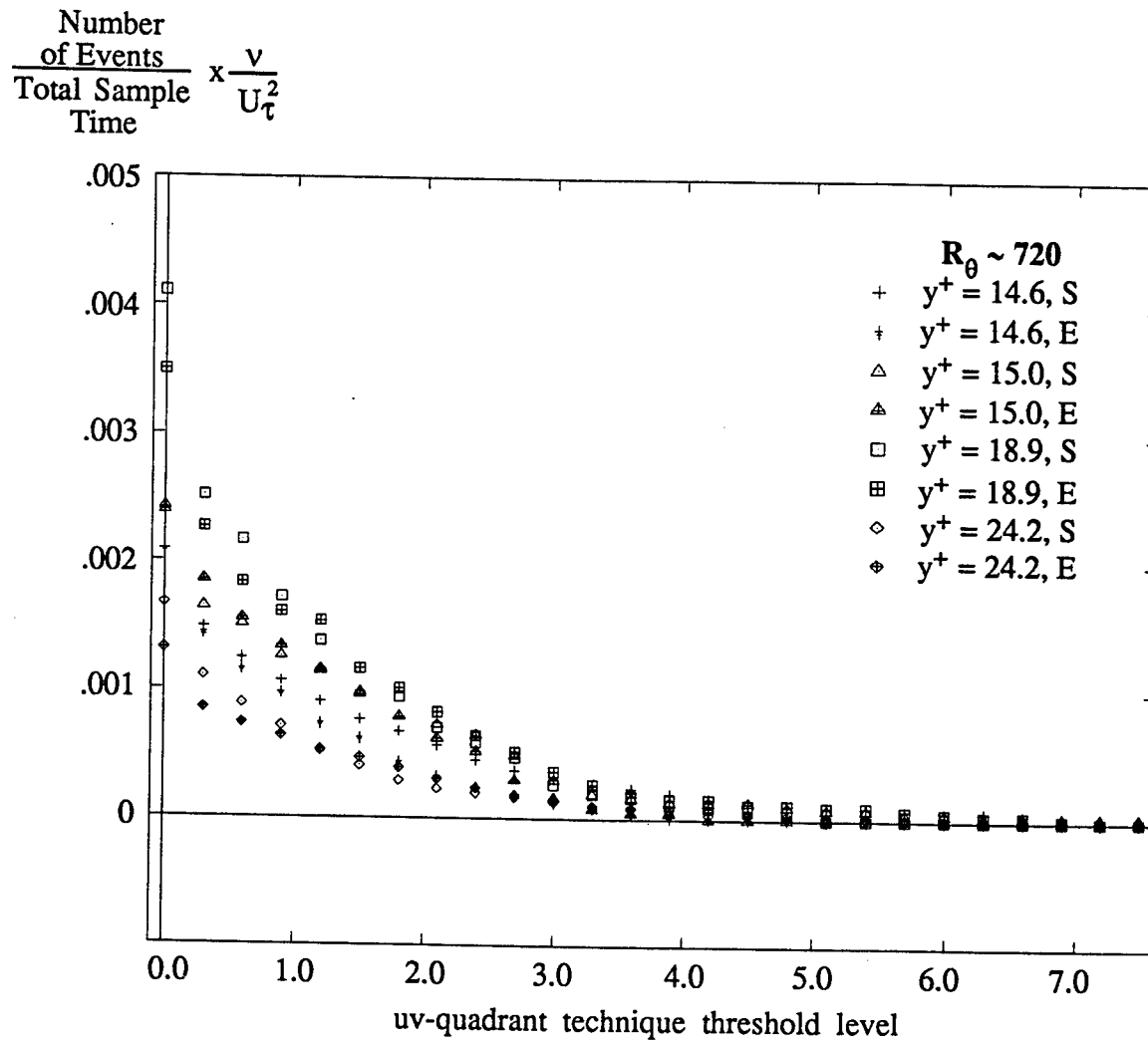
Figure 3.4.13
Inner-scaled uv-quadrant Event frequency
vs. Threshold level (Inner-region data)

$$\frac{\begin{array}{c}\text{Number}\\\text{of Events}\\\hline\text{Total Sample}\\\text{Time}\end{array}}{}\; x \sqrt{\frac{\nu}{U_\tau^2}\;\frac{\delta}{U_\infty}}$$
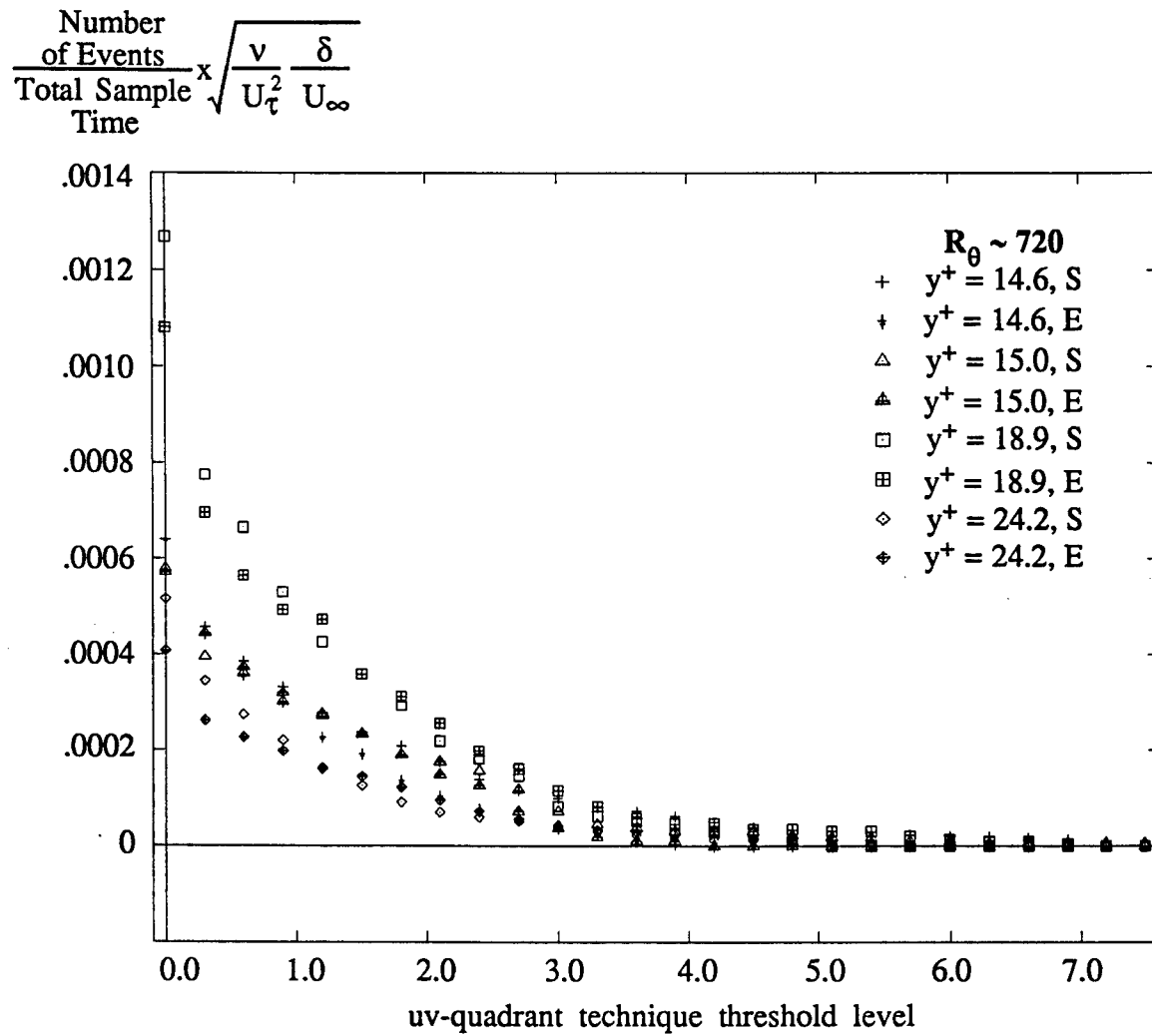
Figure 3.4.14
uv-quadrant Event frequency (Mixed-scaling)
vs. Threshold level (Inner-region data)

$$\frac{\text{Number of Events}}{\begin{array}{c}\text{Total Sample}\\\text{Time}\end{array}} \times \frac{\delta}{U_\infty}$$
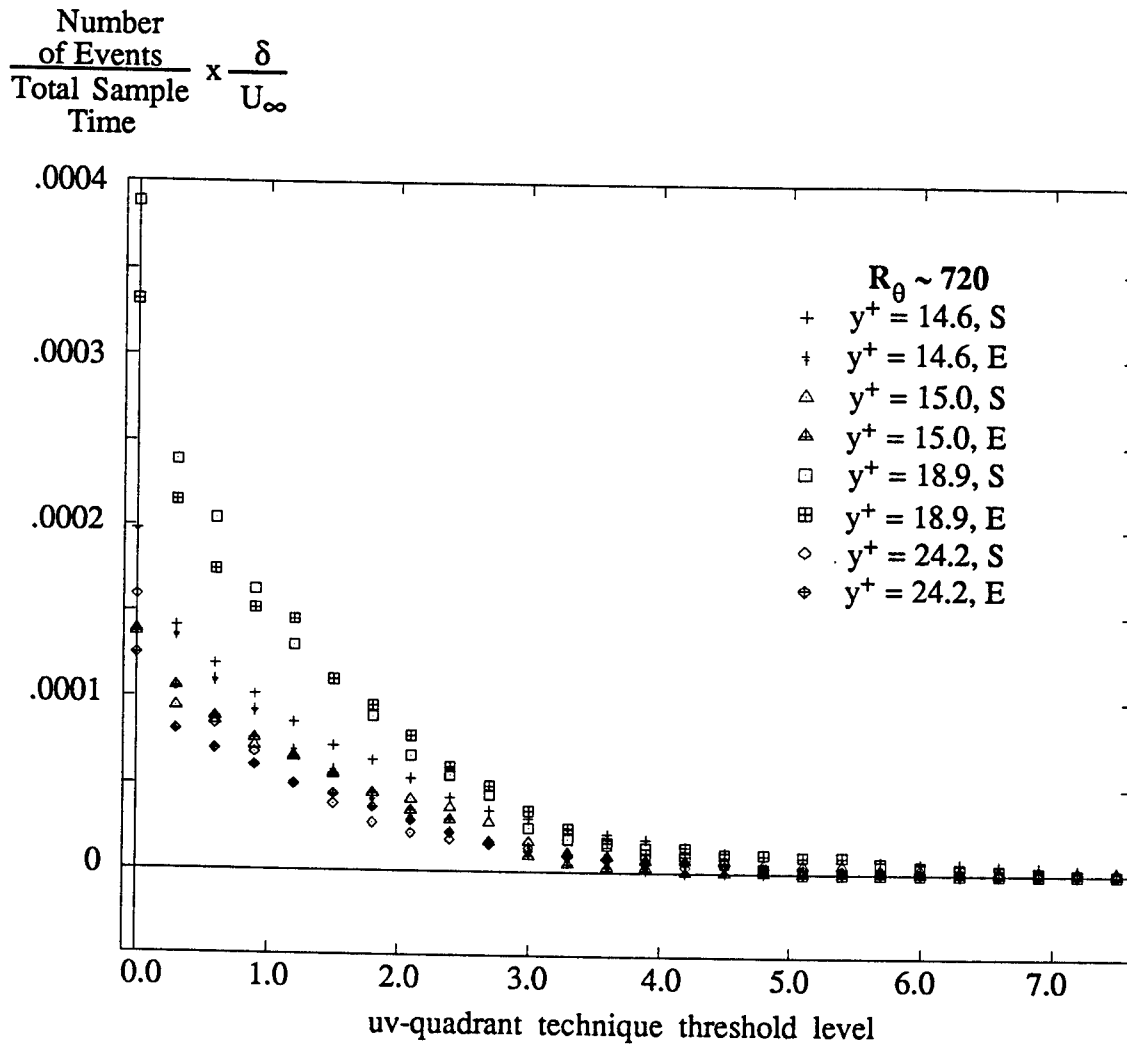
Figure 3.4.15
Outer-scaled uv-quadrant Event frequency
vs. Threshold level (Inner-region data)

$$\frac{\text{Number}}{\text{of Events}} \times \frac{\nu}{U_\tau^2}$$
Number of Events / Total Sample Time
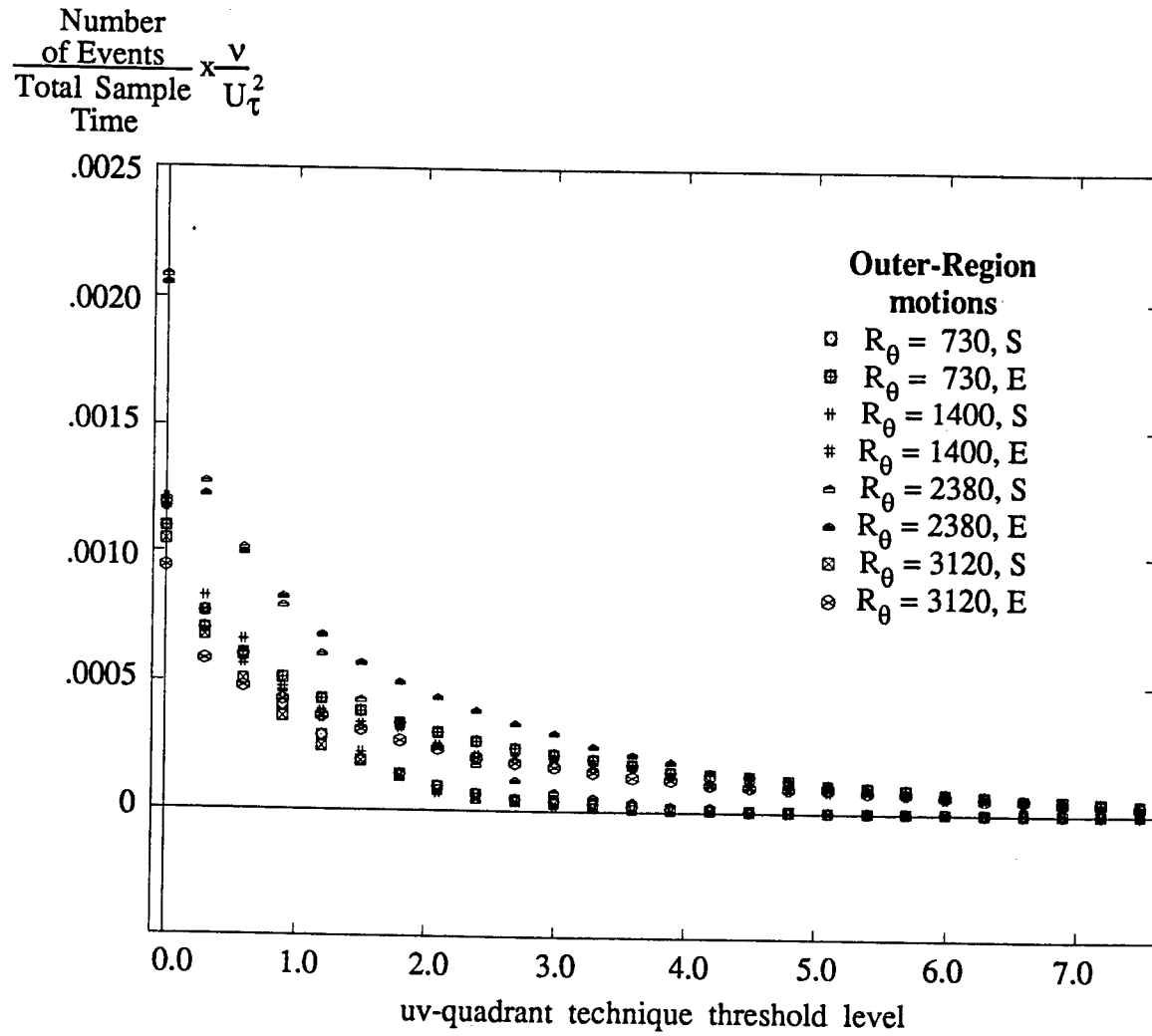
Figure 3.4.16
Inner-scaled uv-quadrant Event frequency
vs. Threshold level (LSM data set)

$$\frac{\text{Number of Events}}{\substack{\text{Total Sample} \\ \text{Time}}} \times \sqrt{\frac{\nu}{U_\tau^2} \frac{\delta}{U_\infty}}$$
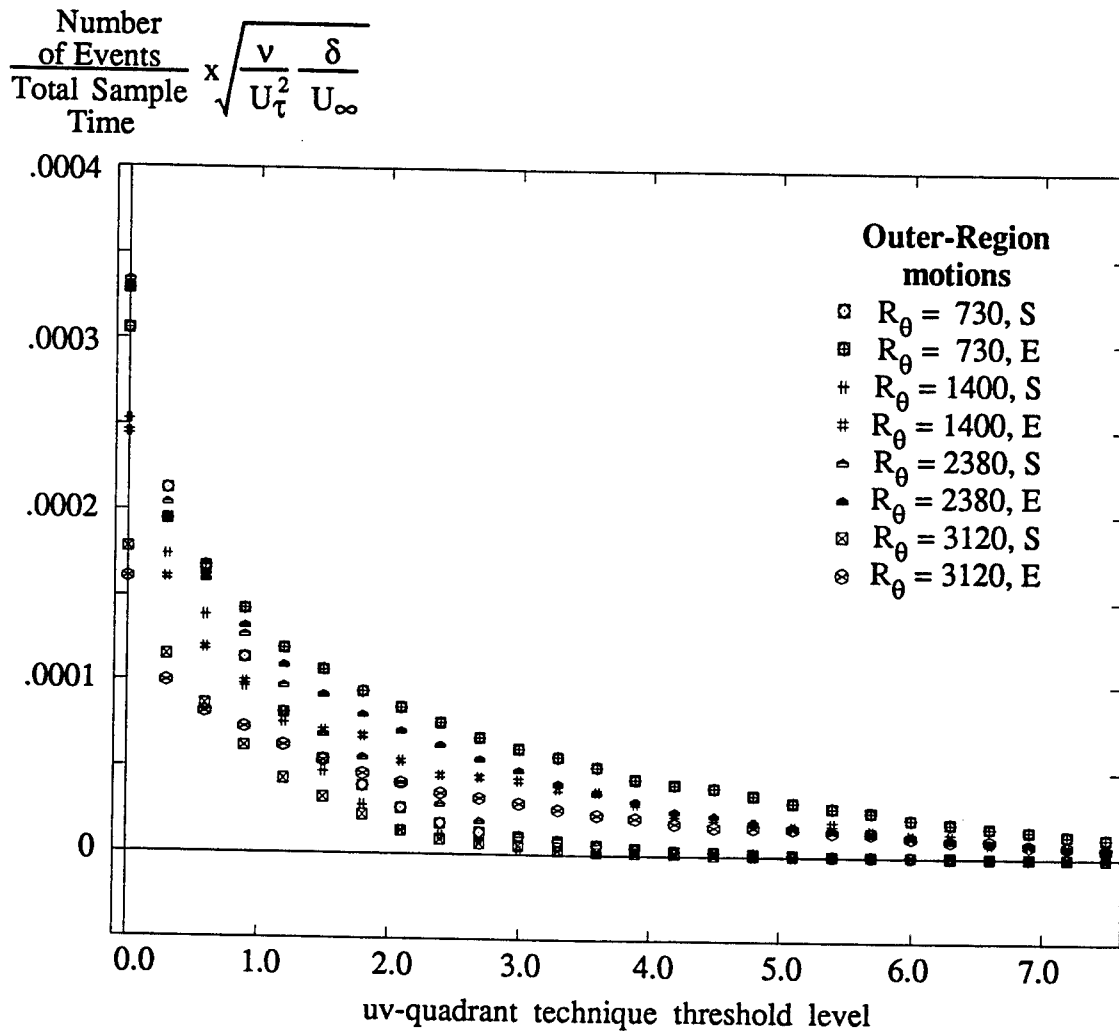
Figure 3.4.17
uv-quadrant Event frequency (Mixed-scaling)
vs. Threshold level (LSM data set)

$$\frac{\text{Number of Events}}{\text{Total Sample Time}} \times \frac{\delta}{U_\infty}$$
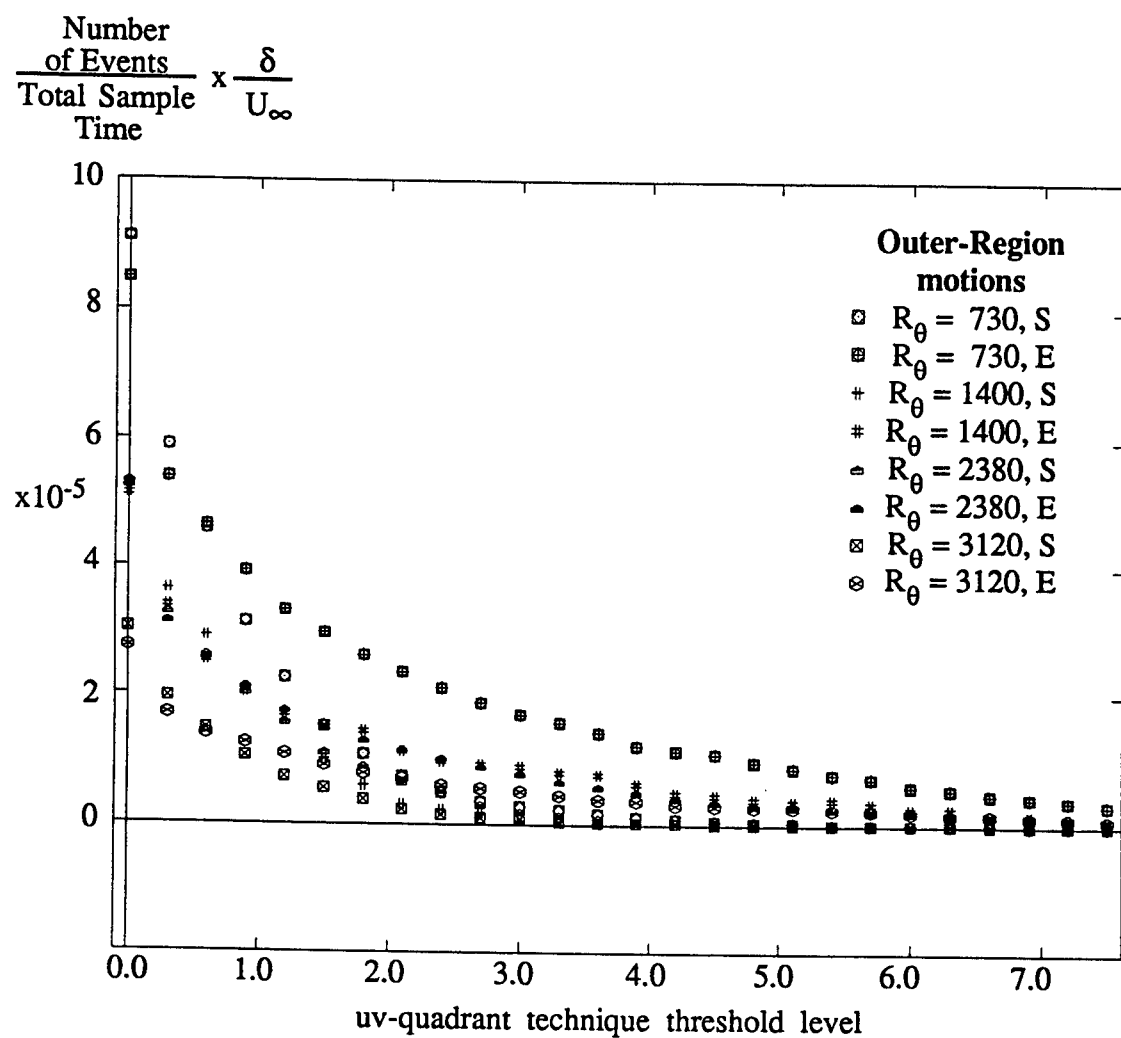
Figure 3.4.18
Outer-scaled uv-quadrant Event frequency
vs. Threshold level (LSM data set)
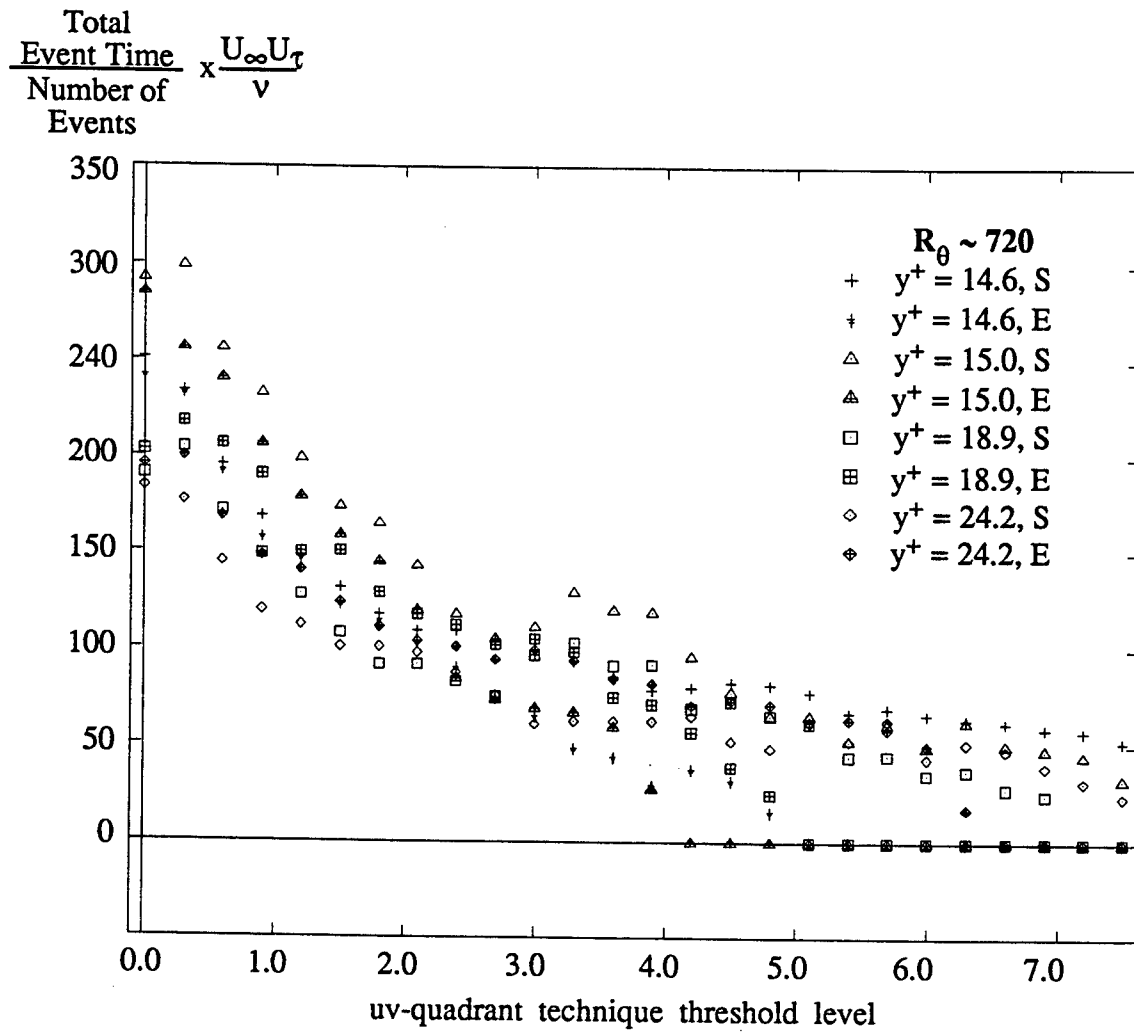
Figure 3.4.19
Inner-Scaled Average uv-quadrant Event Length
vs. Threshold (Inner-region data)

$$\frac{\text{Total}}{\frac{\text{Event Time}}{\text{Number of}}} \times \sqrt{\frac{U_\infty^2 \, U_\tau}{\delta \, \nu}}$$
Events
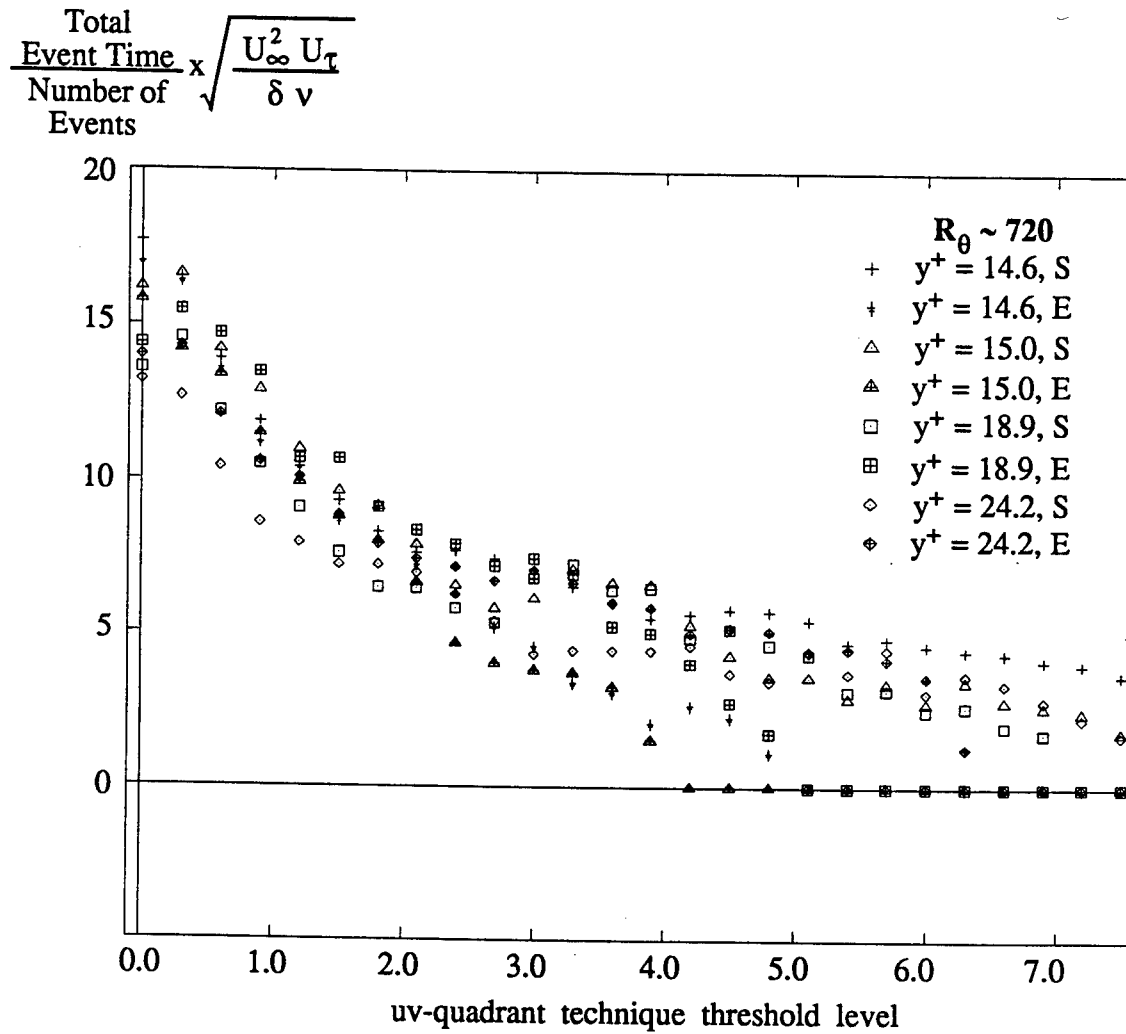
Figure 3.4.20
Average uv-quadrant Event Length (Mixed Scaling)
vs. Threshold (Inner-region data)

$$\frac{\text{Total}}{\text{Event Time}} \times \frac{U_\infty}{\delta}$$
Number of
Events
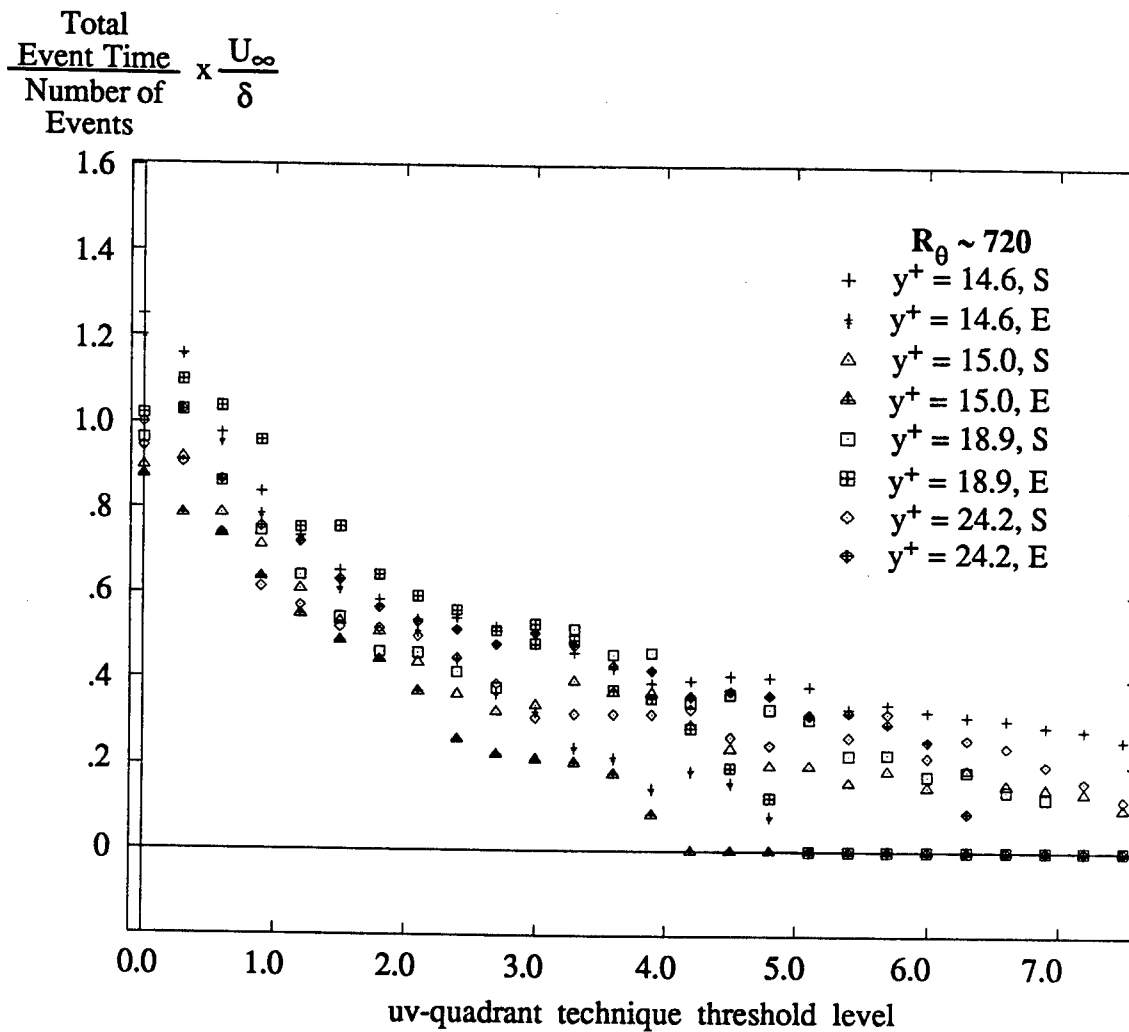
Figure 3.4.21
Outer-Scaled Average uv-quadrant Event Length
vs. Threshold (Inner-region data)

$$\frac{\text{Total Event Time}}{\text{Number of Events}} \times \frac{U_\infty U_\tau}{\nu}$$
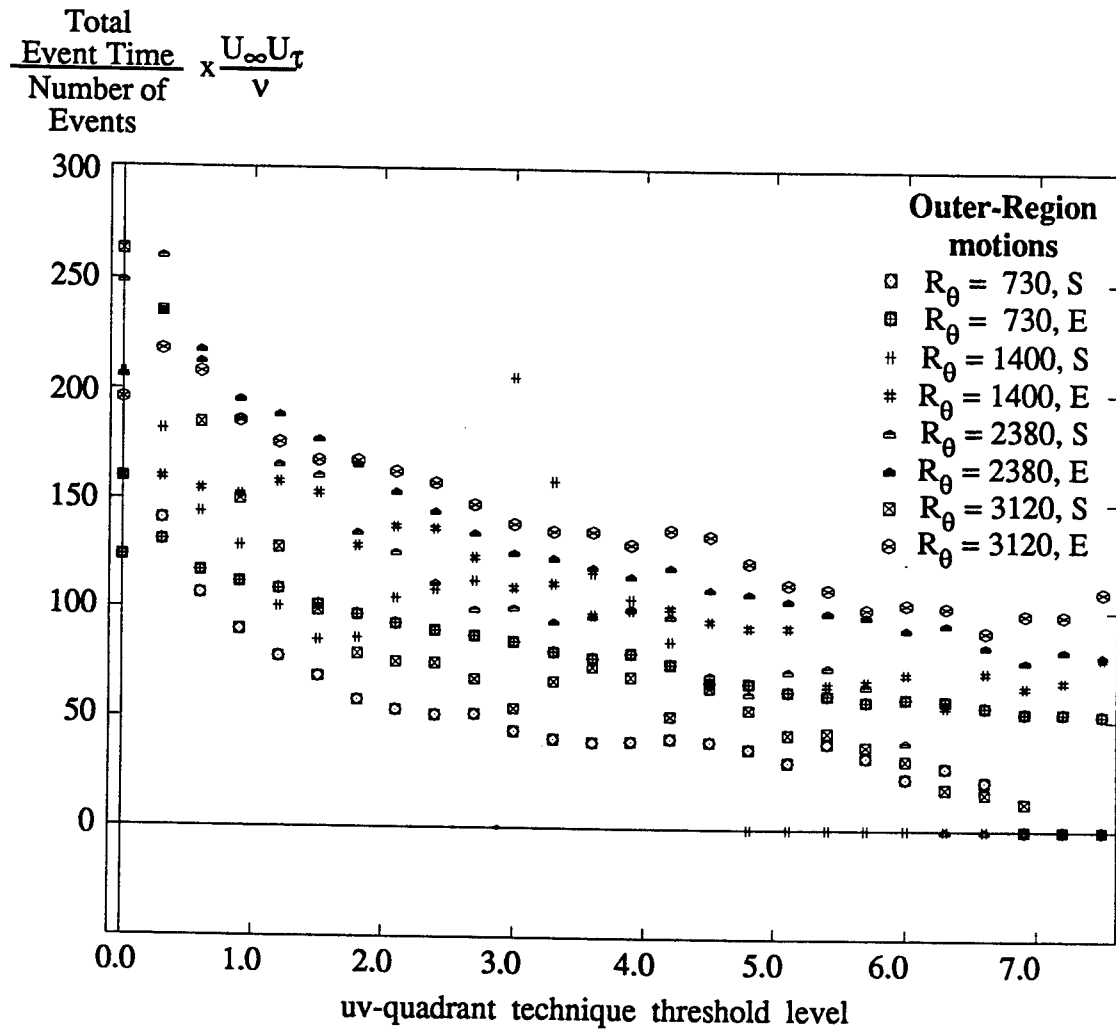
Figure 3.4.22
Inner-Scaled Average uv-quadrant Event Length
vs. Threshold (LSM data set)

$$\frac{\text{Total}}{\text{Event Time}} \times \sqrt{\frac{U_\infty^2 \, U_\tau}{\delta \, \nu}}$$

Number of Events
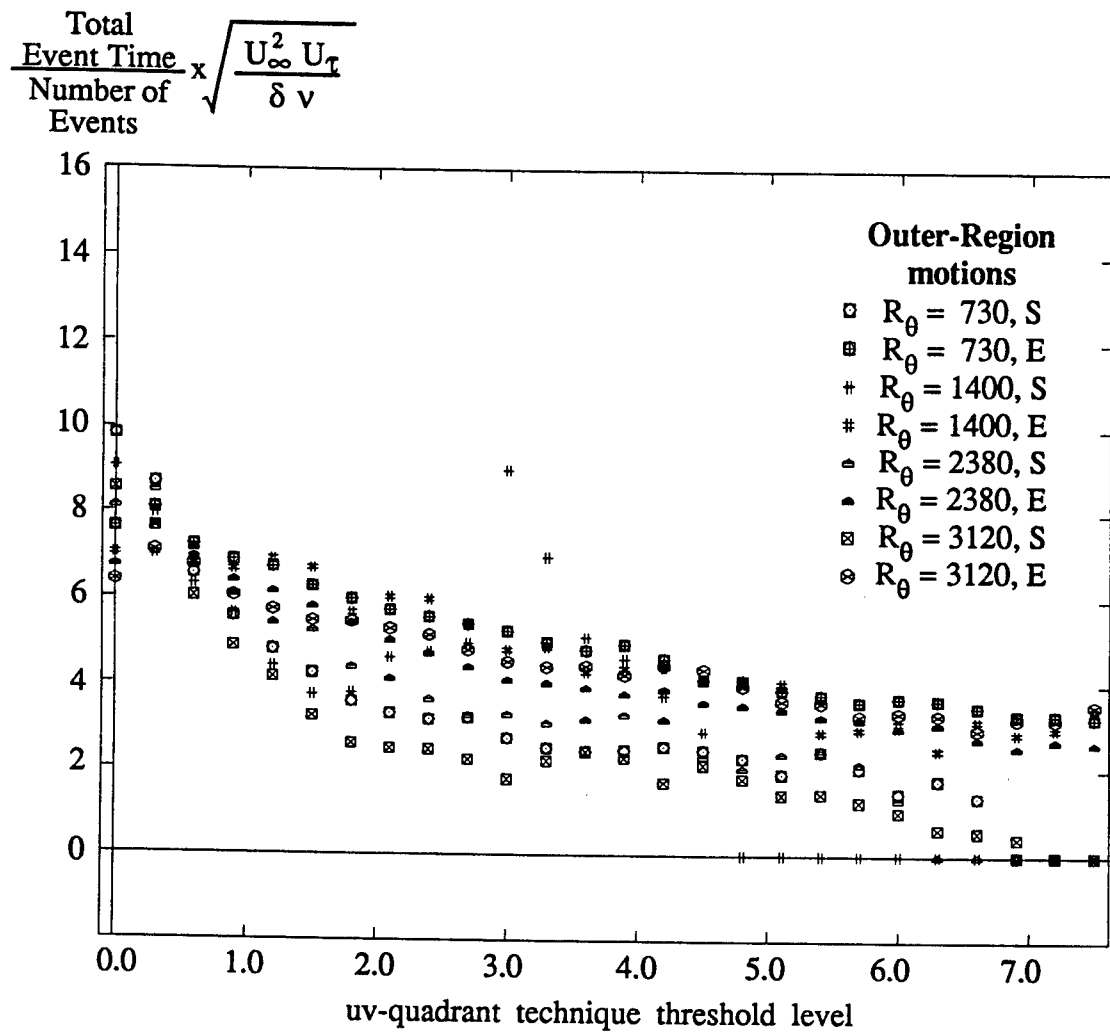
Figure 3.4.23
Average Event uv-quadrant Length (Mixed Scaling)
vs. Threshold (LSM data set)

$$\frac{\text{Total Event Time}}{\text{Number of Events}} \times \frac{U_\infty}{\delta}$$
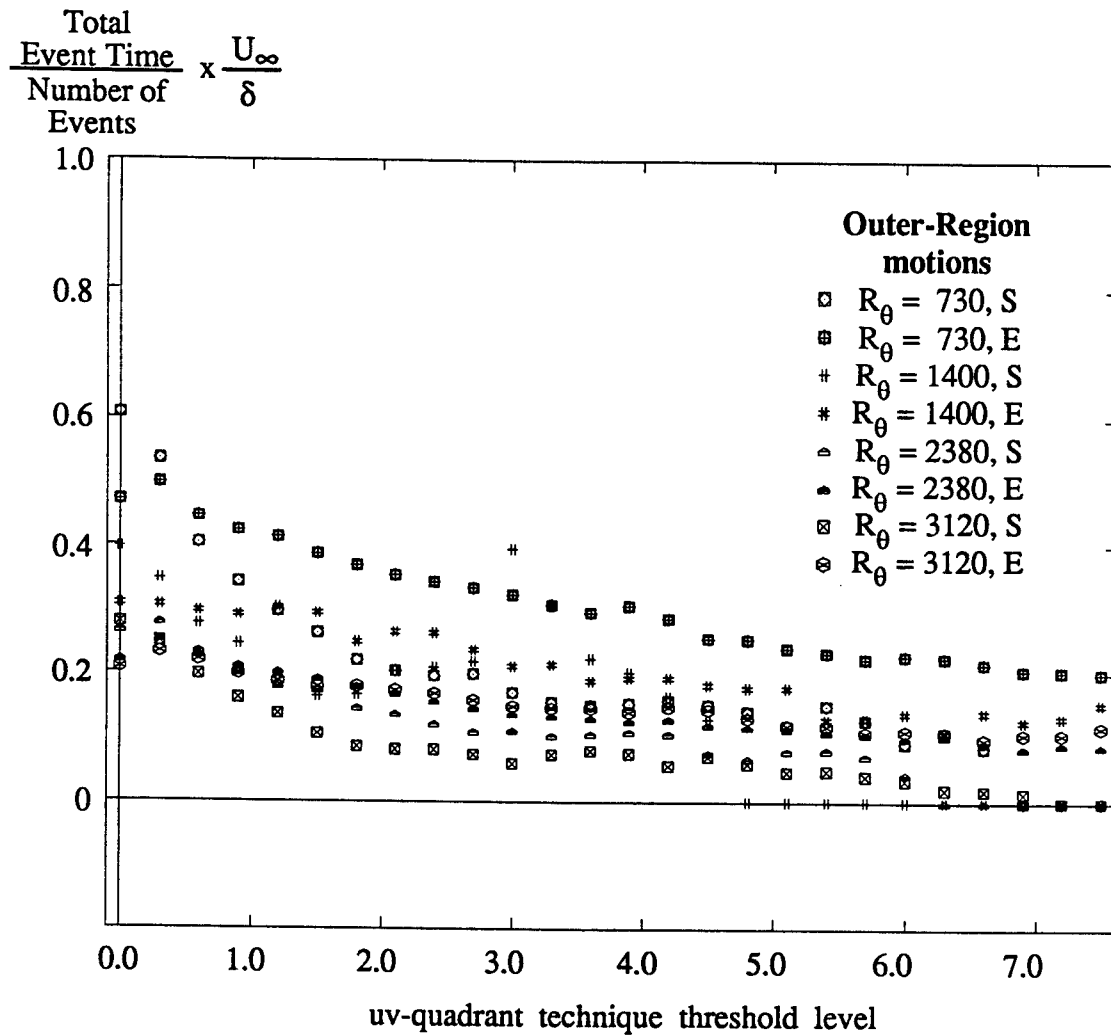
Figure 3.4.24
Outer-Scaled Average uv-quadrant Event Length
vs. Threshold (LSM data set)

$$\frac{\text{Total}}{\frac{\text{Event Time}}{\text{Number of}}} \times \frac{U_\infty U_\tau}{\nu \; y^+}$$
Events
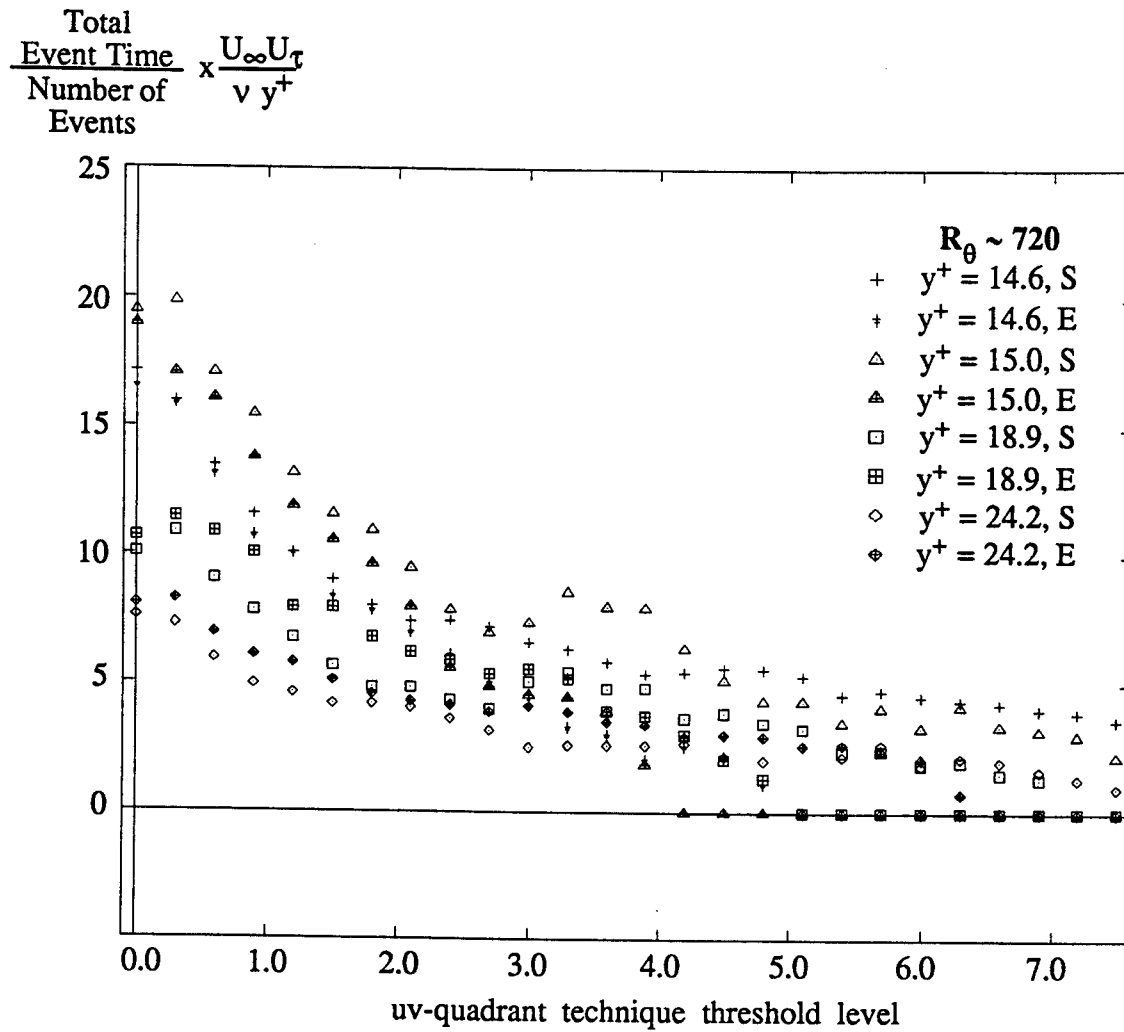
Figure 3.4.25
Average Inner-Scaled uv-quadrant
Event Length over y^+
vs. Threshold (Inner-region data)

$\int uv<0 / \int uv<0$
during   all times
events
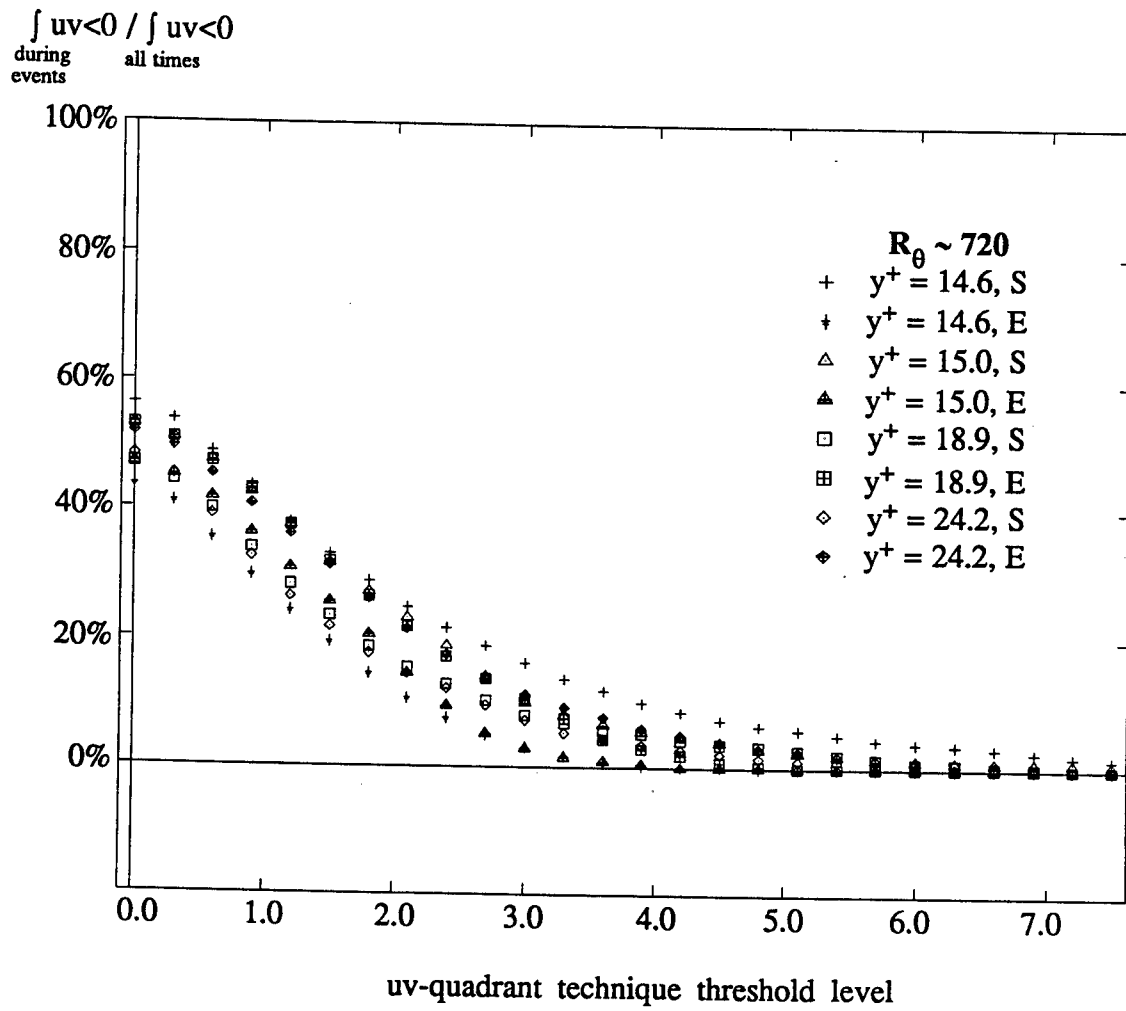
Figure 3.4.26
Percent Reynolds Stress "captured" during
uv-quadrant events vs. Threshold
(Inner-region data)

$\int uv<0$ / $\int uv<0$

during   all times
events
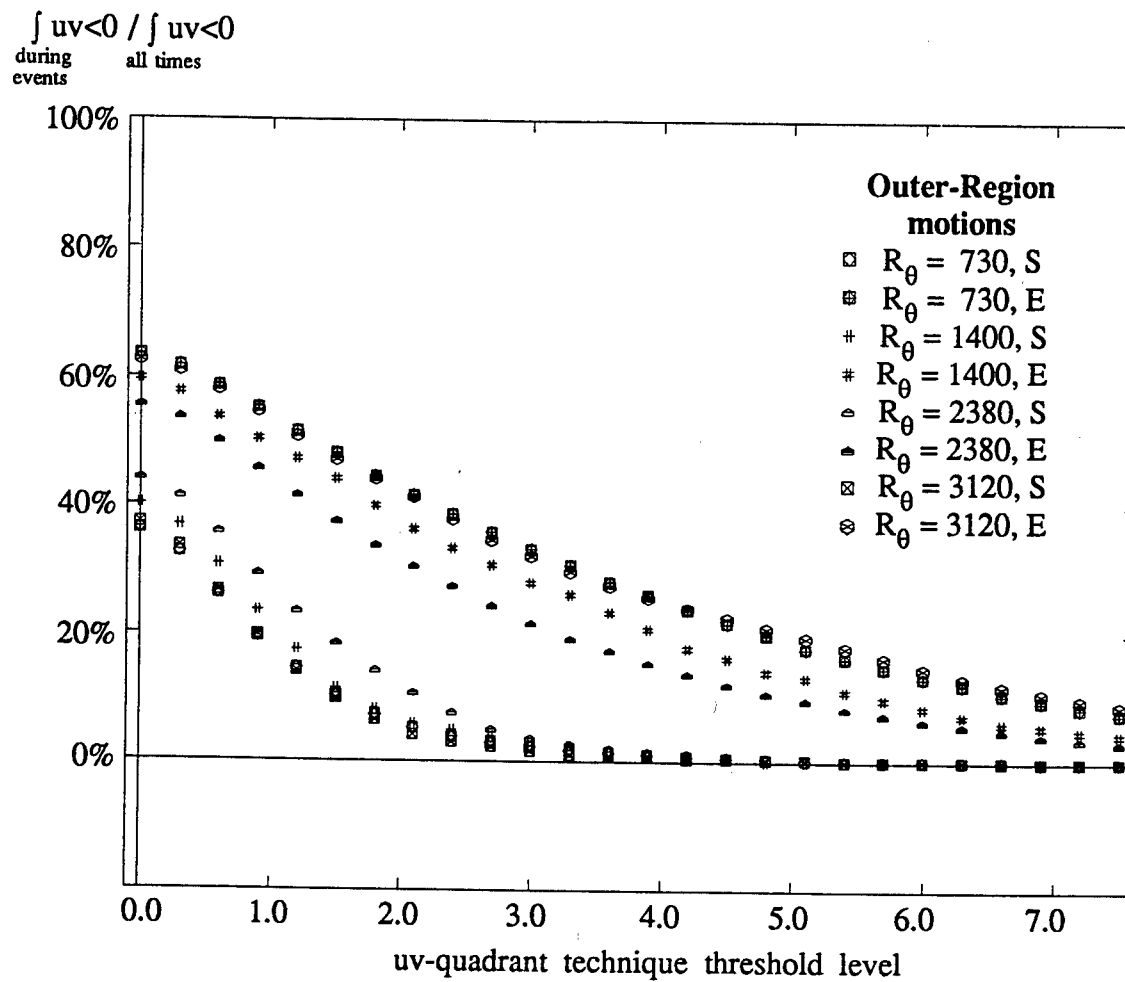
Figure 3.4.27
Percent Reynolds Stress "captured" during
uv-quadrant events vs. Threshold
(LSM data set)
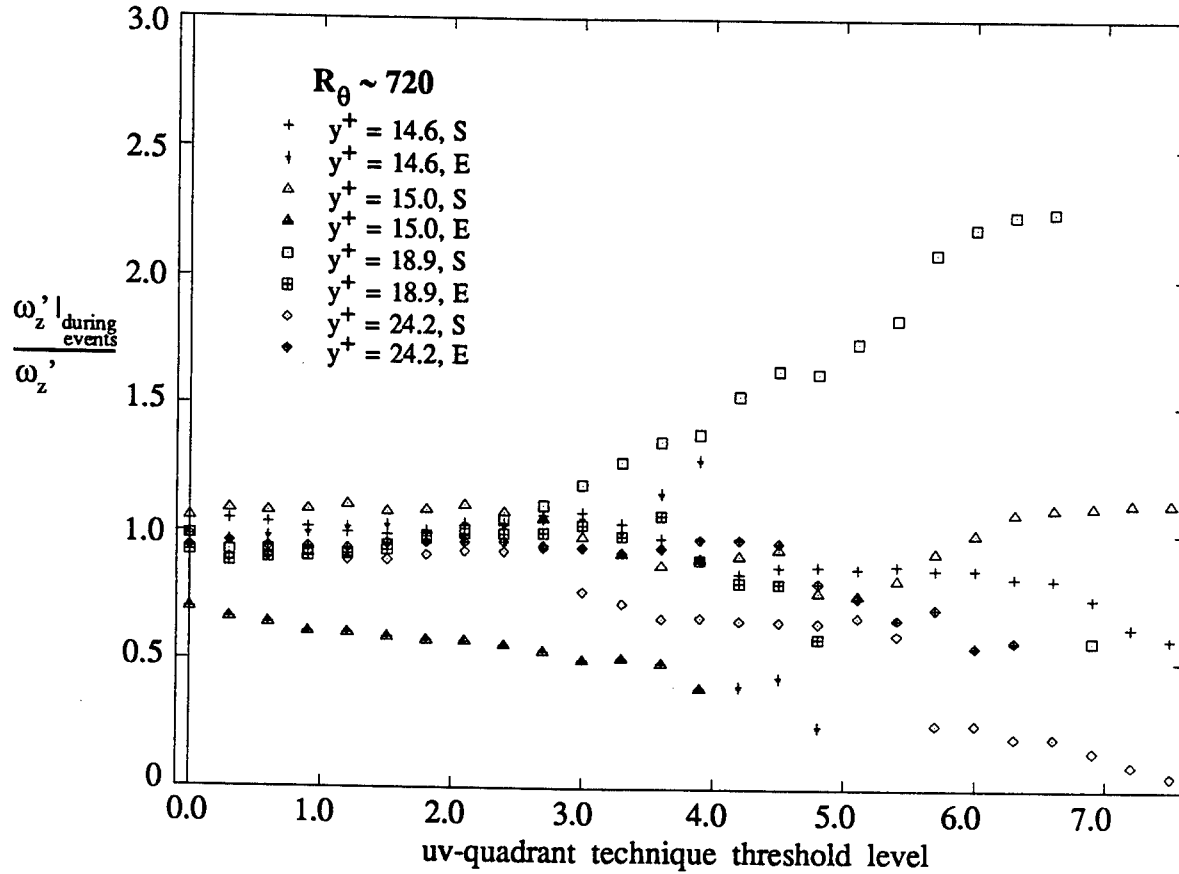
Figure 3.4.28
RMS ω_z During uv-quadrant Events
Normalized by ω_z'
vs. Threshold (Inner-region data)

Figure 3.4.29
RMS ω_z During uv-quadrant Events
Normalized by ω_z'
vs. Threshold (LSM data set)

$$\frac{<u^2+v^2>|_{\substack{during \\ events}}}{(u^2+v^2)'}$$

R$_\theta$ ~ 720

+ $y^+ = 14.6$, S
✦ $y^+ = 14.6$, E
△ $y^+ = 15.0$, S
▲ $y^+ = 15.0$, E
□ $y^+ = 18.9$, S
⊞ $y^+ = 18.9$, E
◇ $y^+ = 24.2$, S
◆ $y^+ = 24.2$, E

uv-quadrant technique threshold level
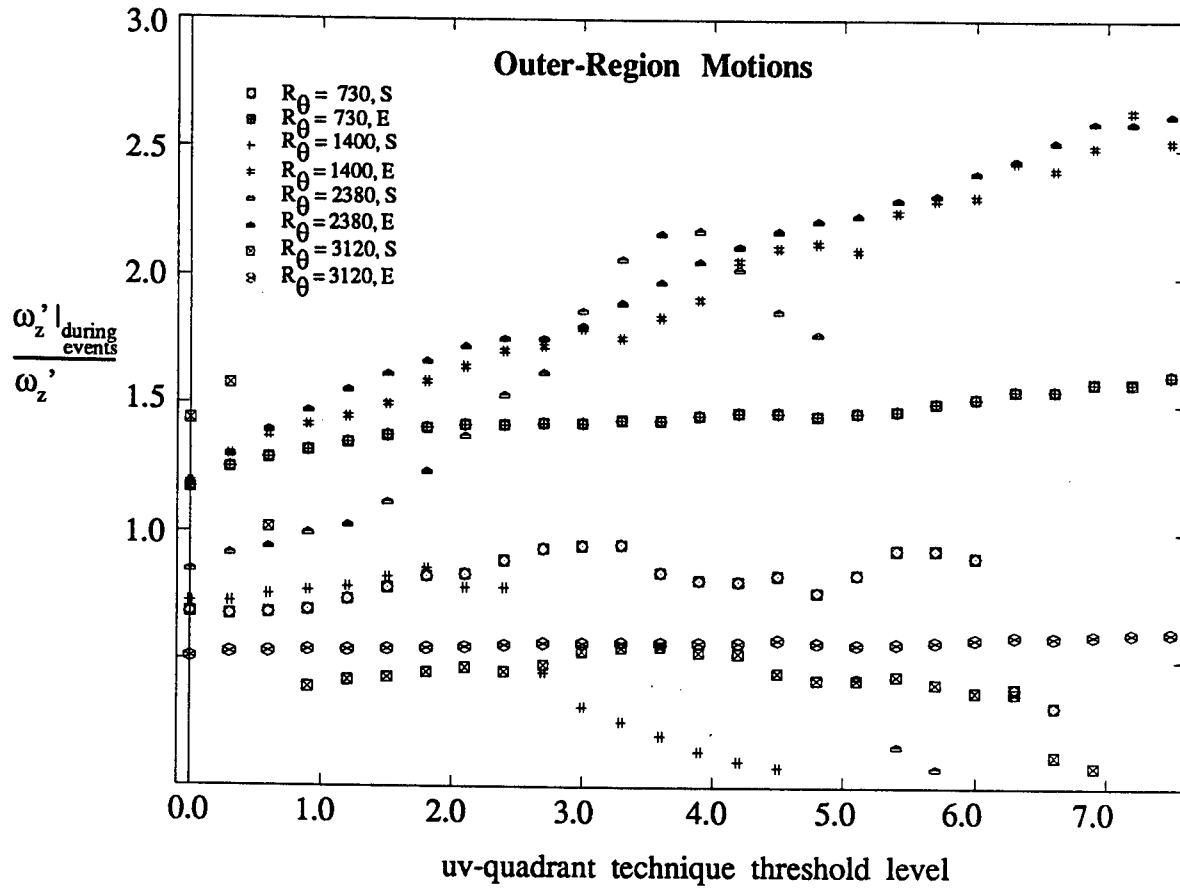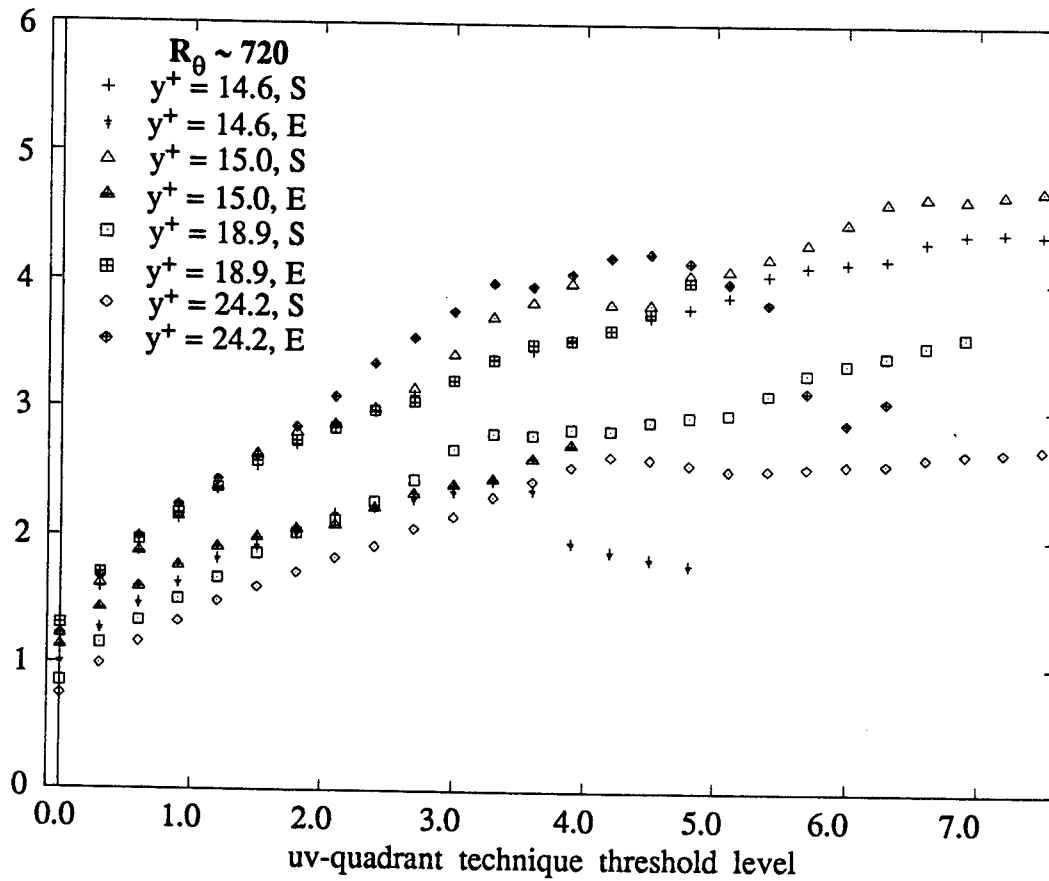
Figure 3.4.30
Average TKE During uv-quadrant
Events Normalized by TKE'
vs. Threshold (Inner-region data)

$$\frac{<u^2+v^2>|_{\substack{during \\ events}}}{(u^2+v^2)'}$$
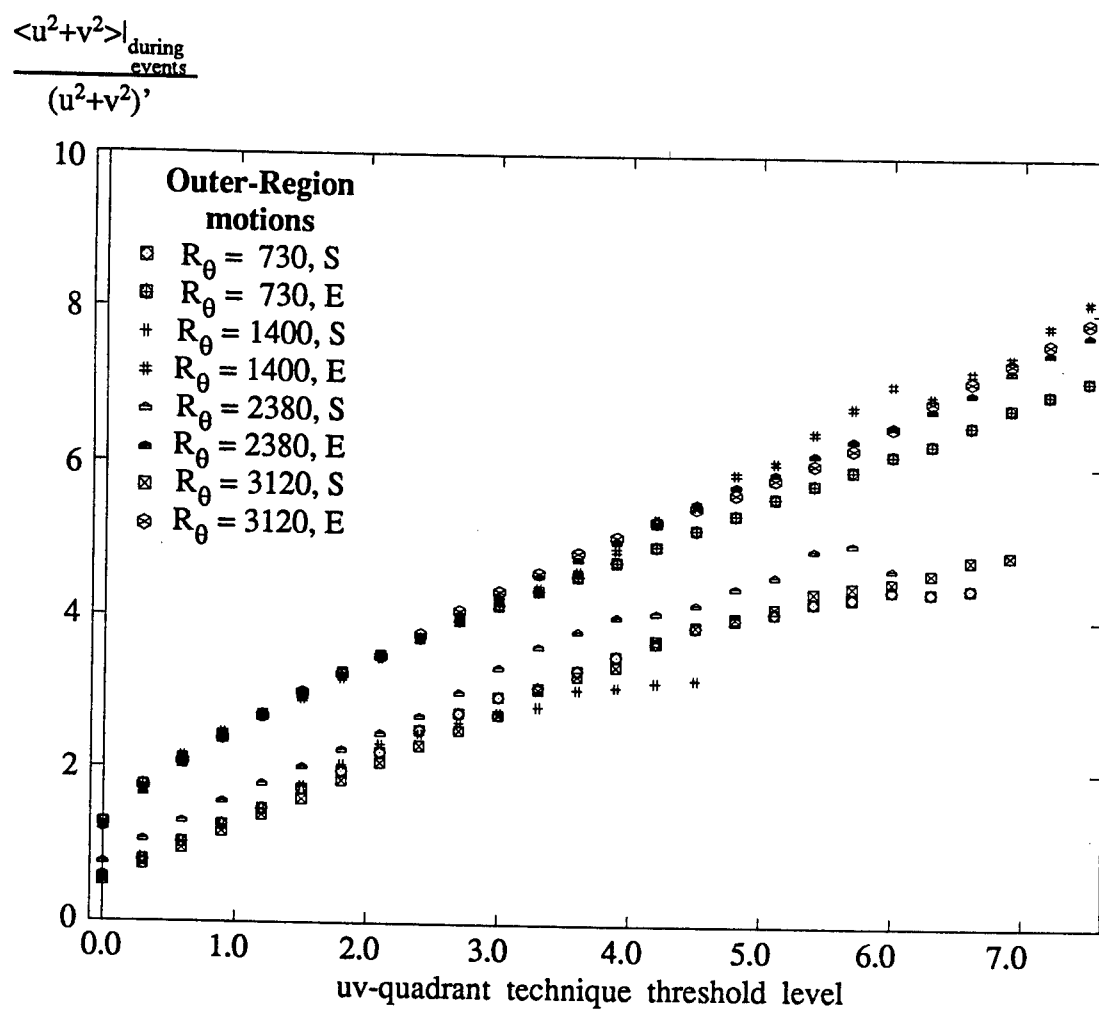
Figure 3.4.31
Average TKE During uv-quadrant
Events Normalized by TKE'
vs. Threshold (LSM data set)
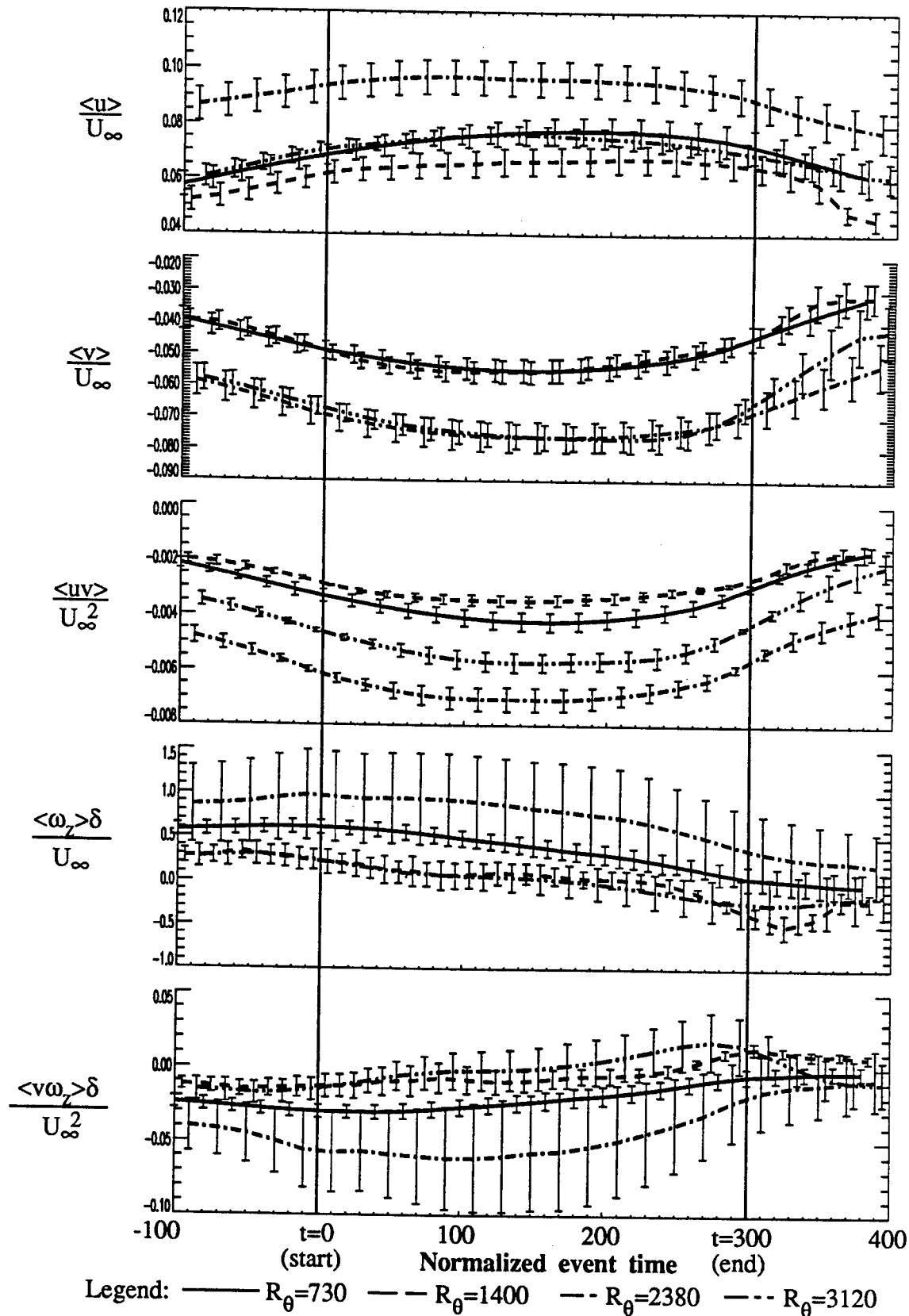
Figure 3.4.32 Outer-scaled uv-quadrant sweep ensembles. Error bars indicate 25% of an ensemble's standard deviation at each point in time
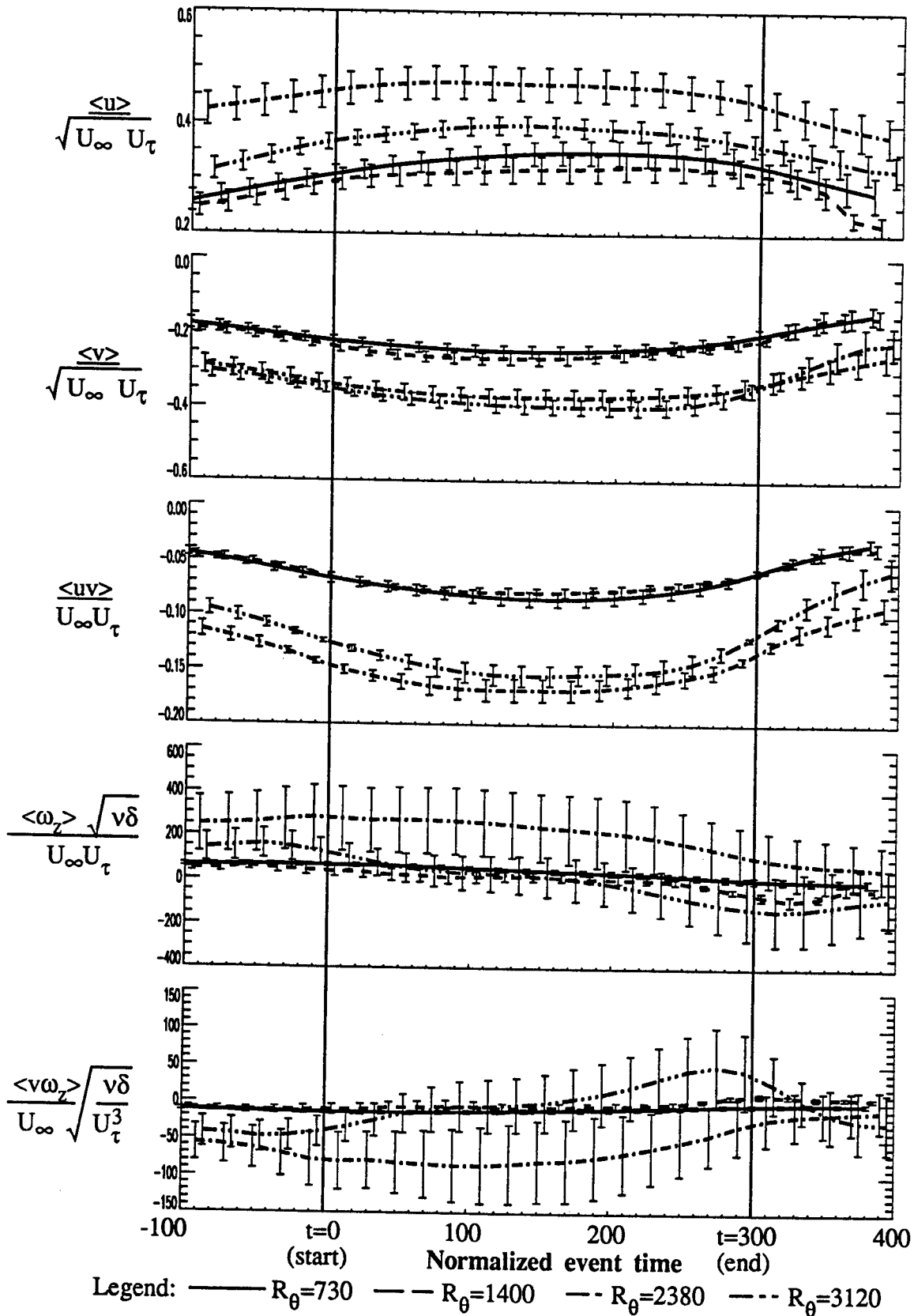
Figure 3.4.33 Mixed-scaled uv-quadrant sweep ensembles. Error bars indicate 25% of an ensemble's standard deviation at each point in time
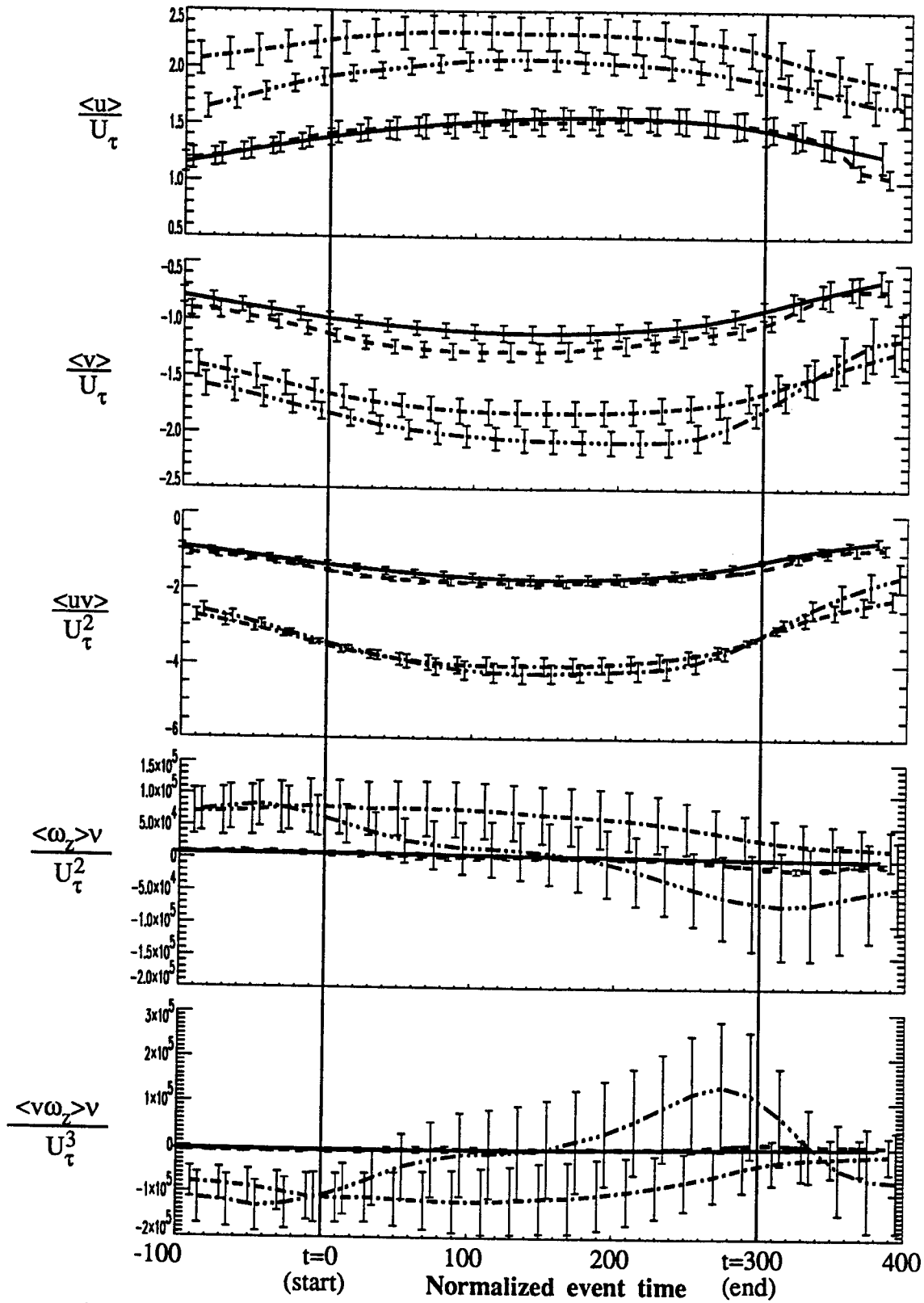
Figure 3.4.34 Inner-scaled uv-quadrant sweep ensembles. Error bars indicate 25% of an ensemble's standard deviation about each point in time
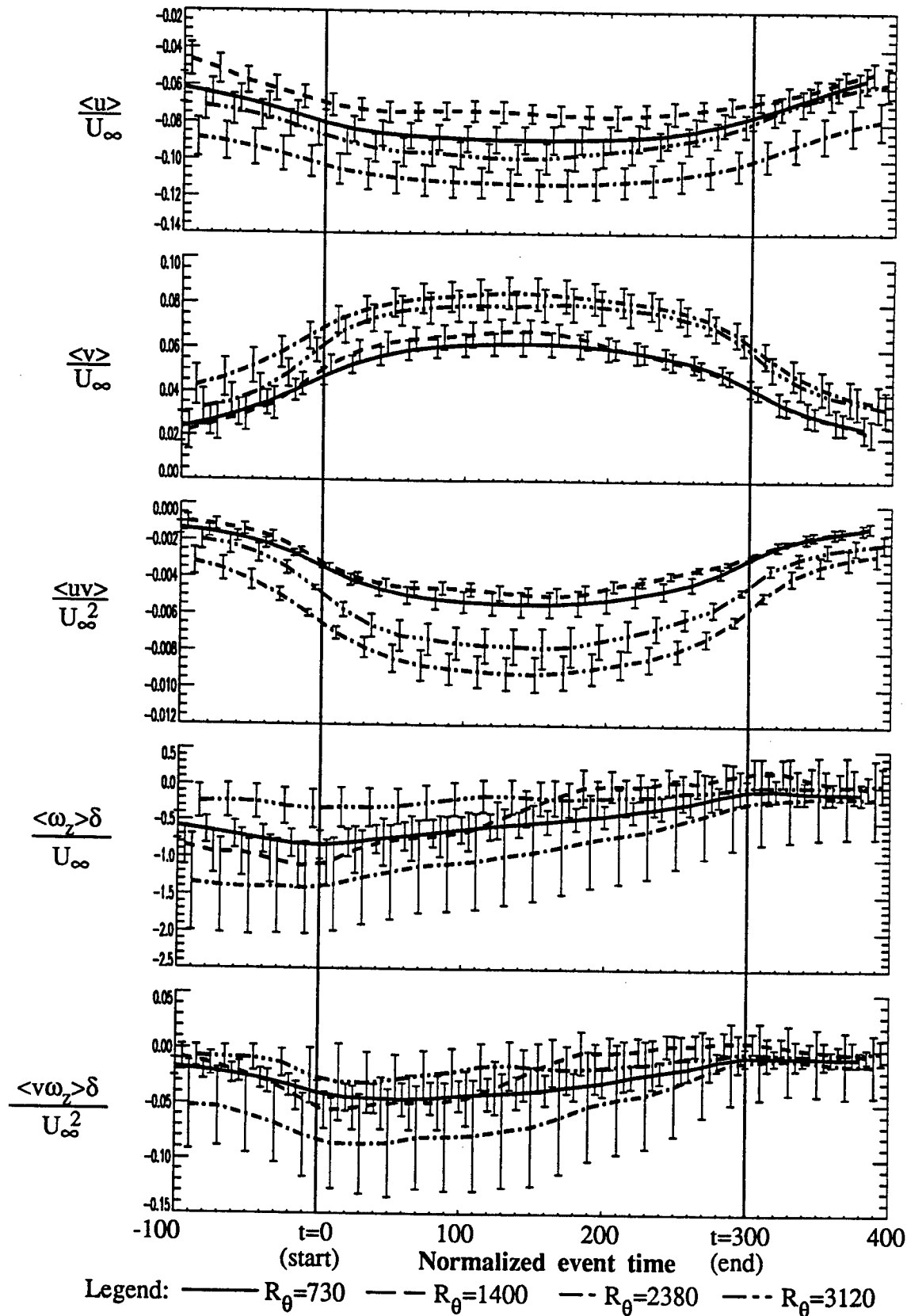
Figure 3.4.35 Outer-scaled uv-quadrant ejection ensembles. Error bars indicate 25% of an ensemble's standard deviation about each point in time
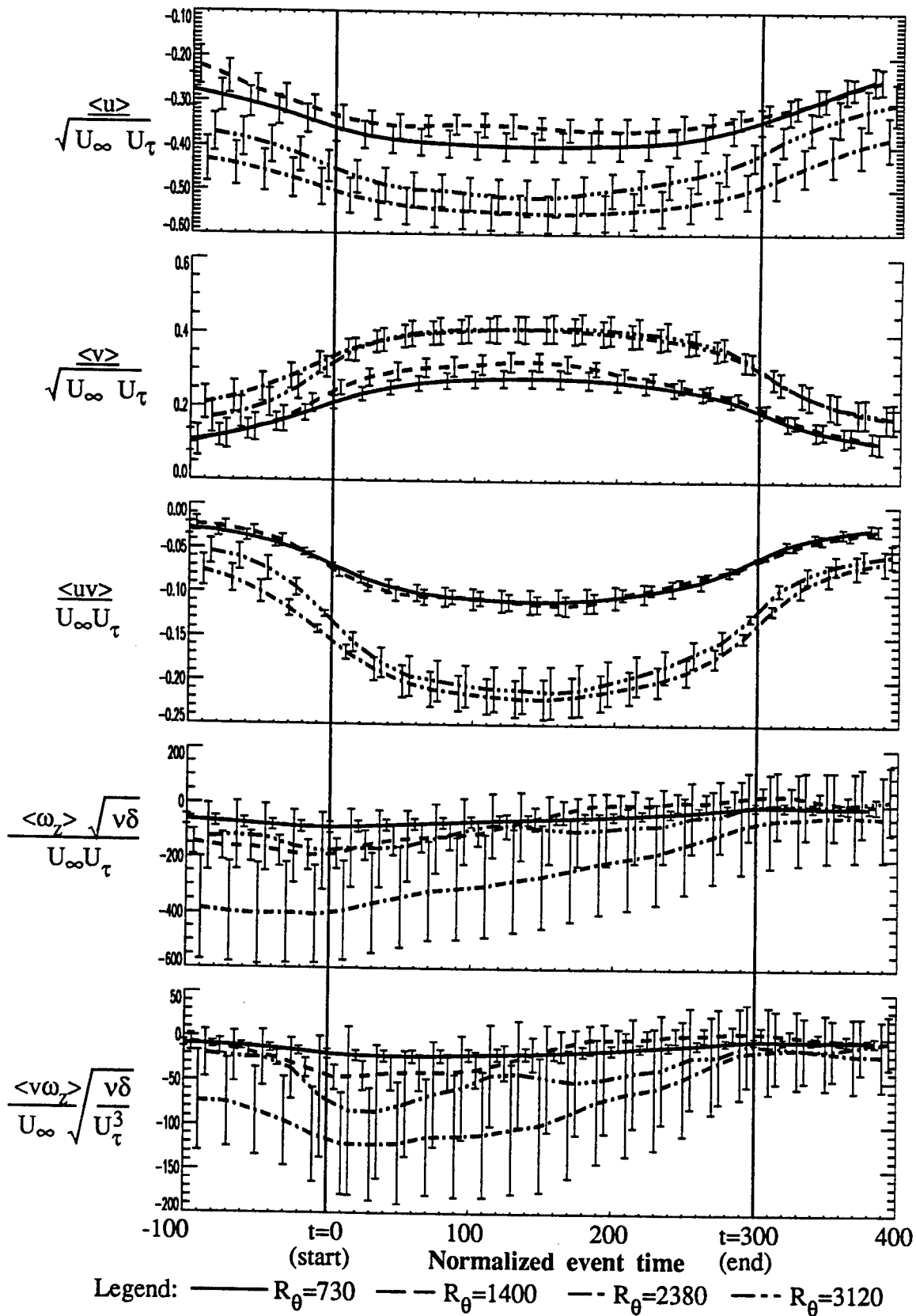
Figure 3.4.36 Mixed-scaled uv-quadrant ejection ensembles. Error bars indicate 25% of an ensemble's standard deviation about each point in time

155
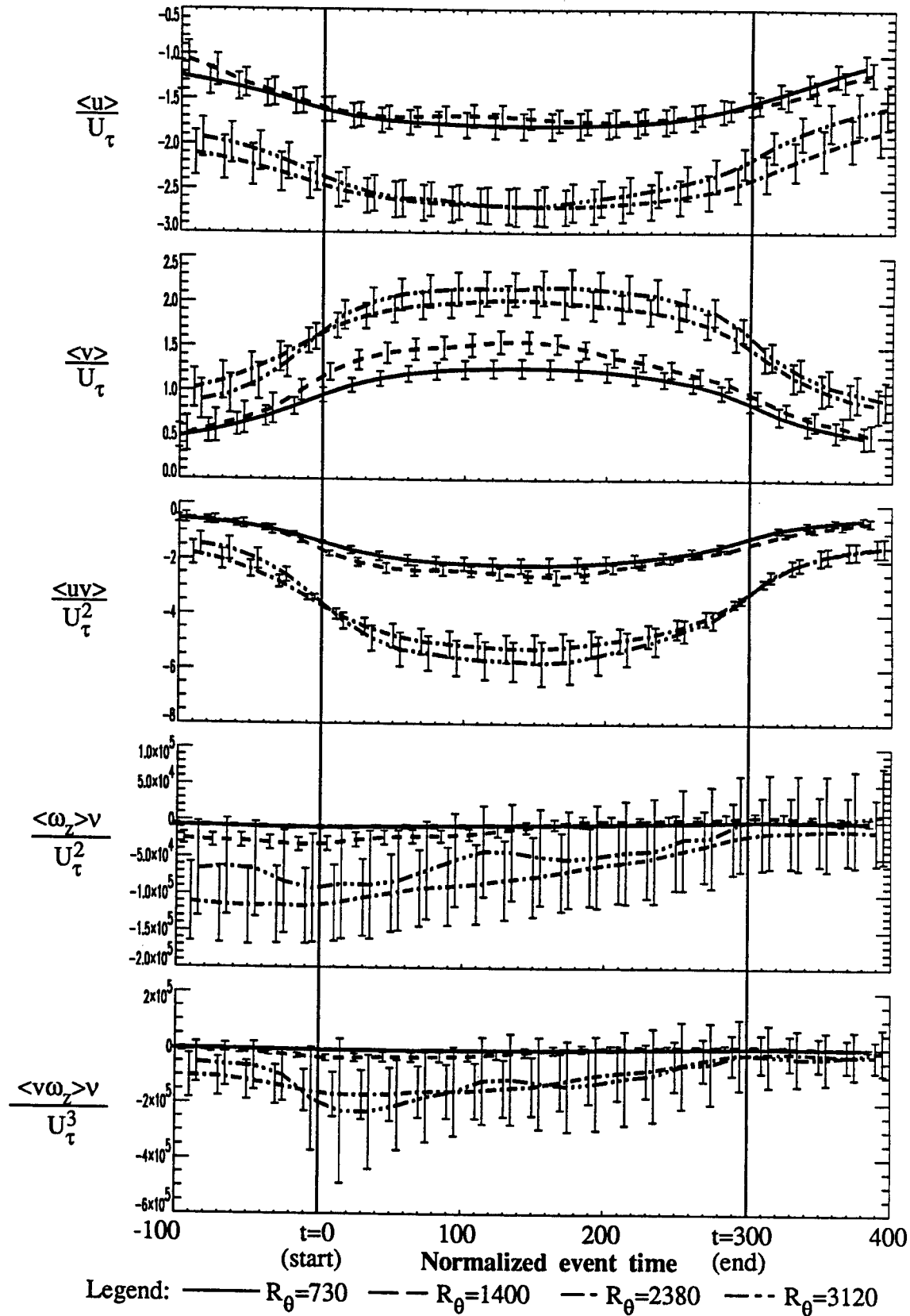
Figure 3.4.37 Inner-scaled uv-quadrant ejection ensembles. Error bars indicate 25% of an ensemble's standard deviation about each point in time
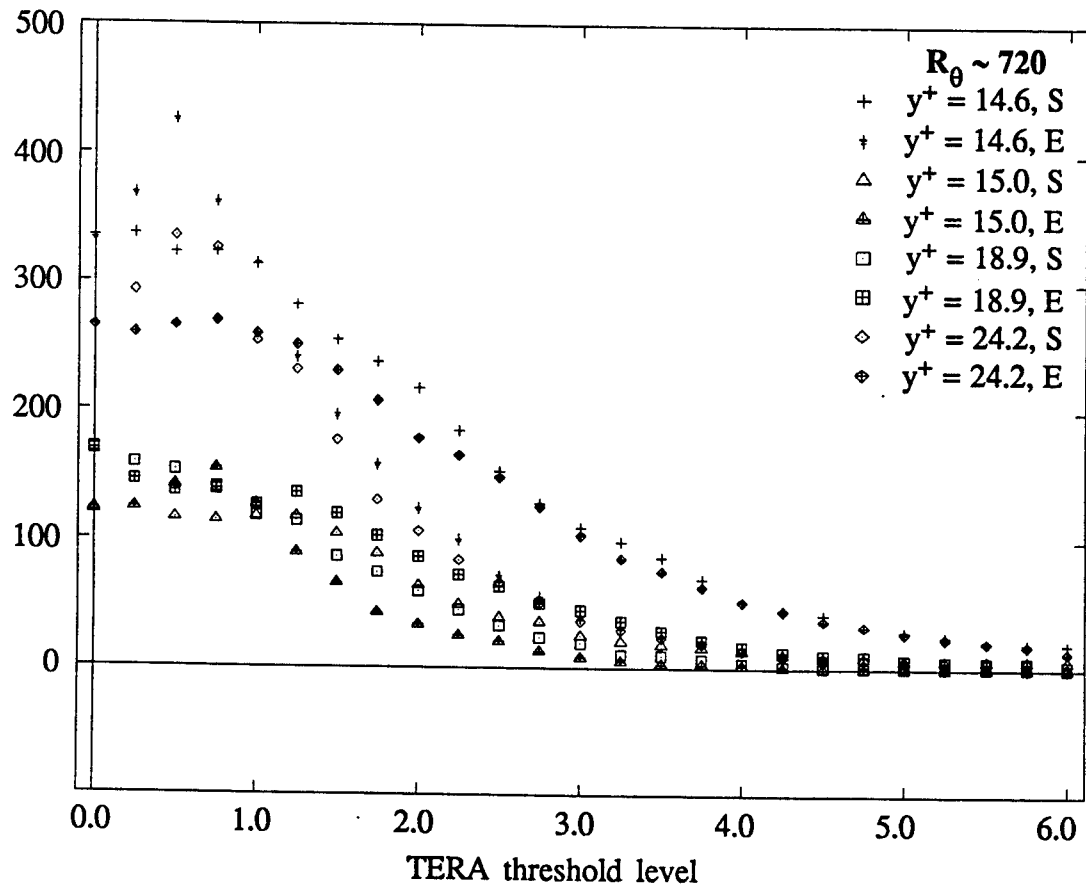
Number
of Events

Figure 3.5.1
Number of TERA Events
vs. Threshold level
(Inner-region data)
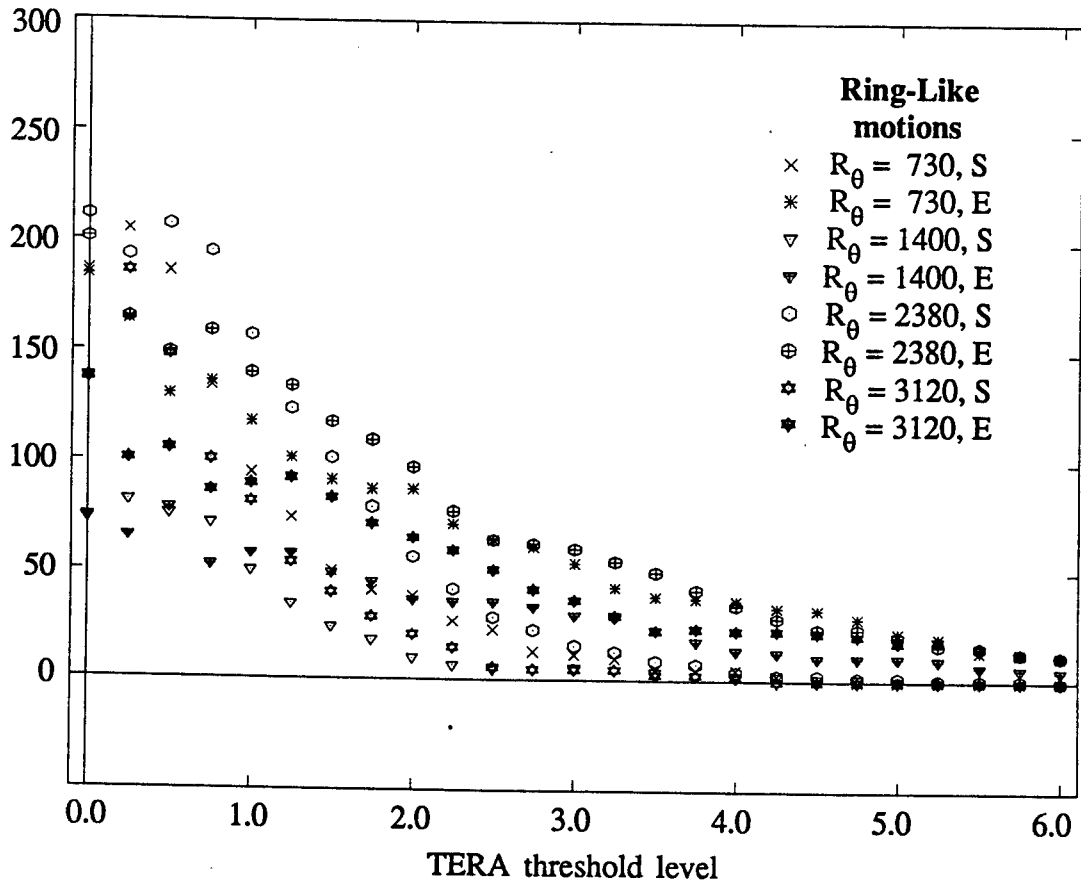
Number
of Events

Figure 3.5.2
Number of TERA Events
vs. Threshold level
(RLM data set)
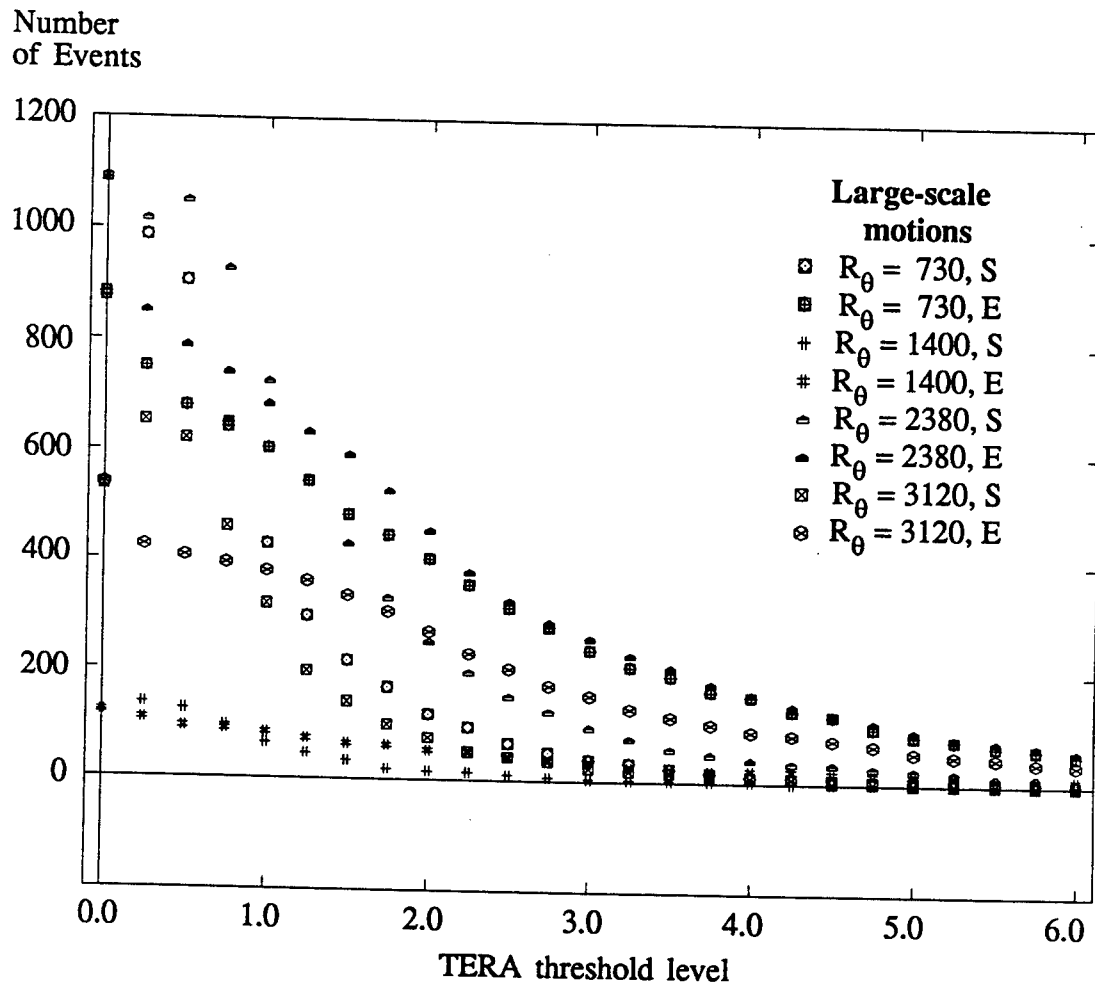
Figure 3.5.3
Number of TERA Events
vs. Threshold level
(LSM data set)
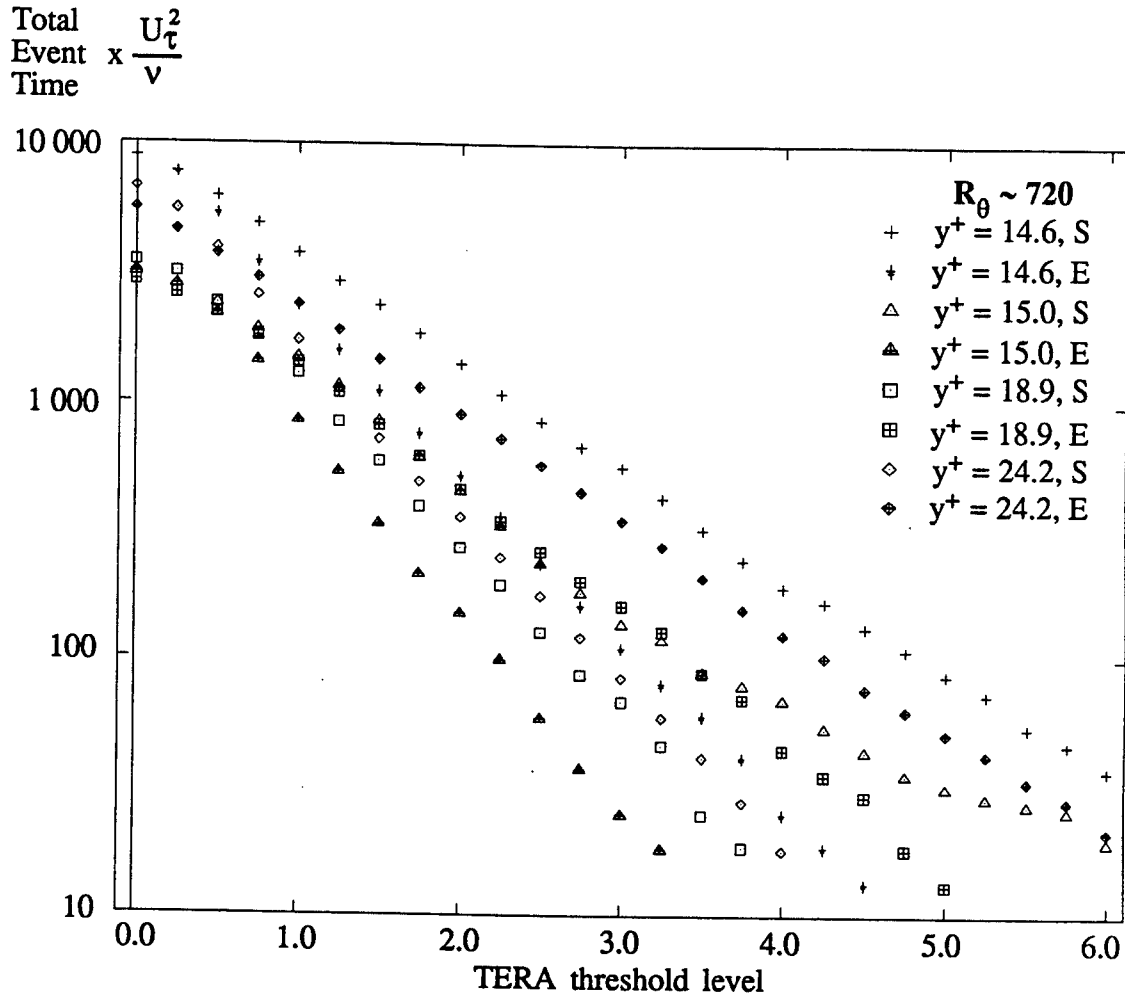
Figure 3.5.4
Inner-Scaled Total TERA Event Time
vs. Threshold (Inner-region data)

Total
Event x $\dfrac{U_\tau^2}{\nu}$
Time
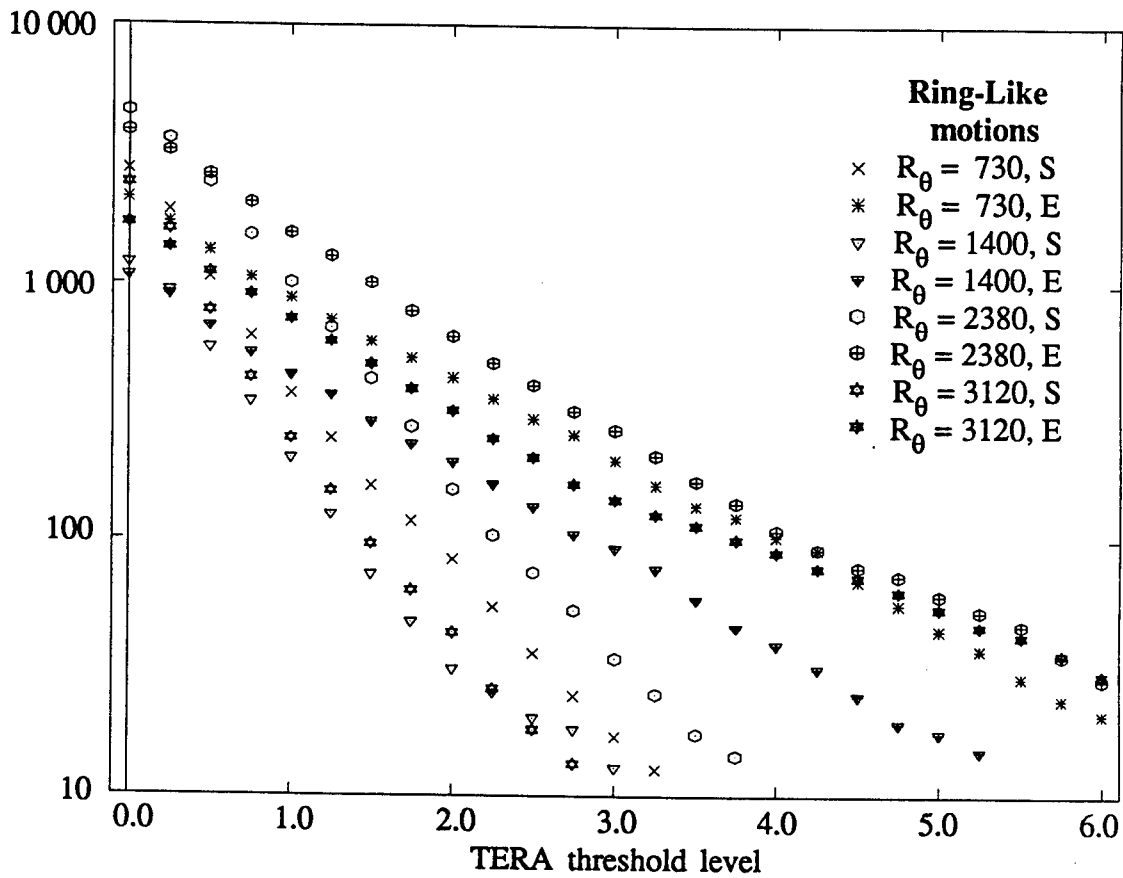
Figure 3.5.5
Inner-Scaled Total TERA Event Time
vs. Threshold (RLM data set)
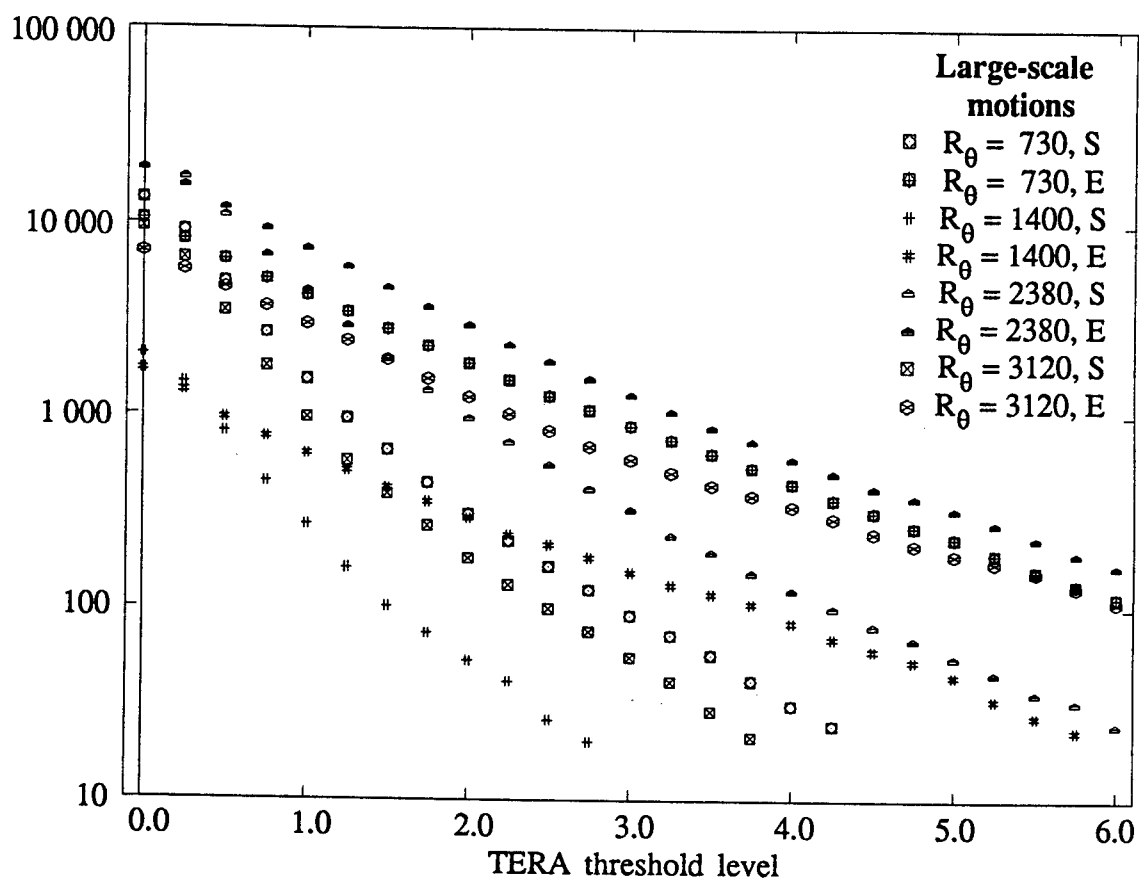
Figure 3.5.6
Inner-Scaled Total TERA Event Time
vs. Threshold (LSM data set)

Total
Event $\quad x\sqrt{\dfrac{U_\tau^2}{\nu}\dfrac{U_\infty}{\delta}}$
Time
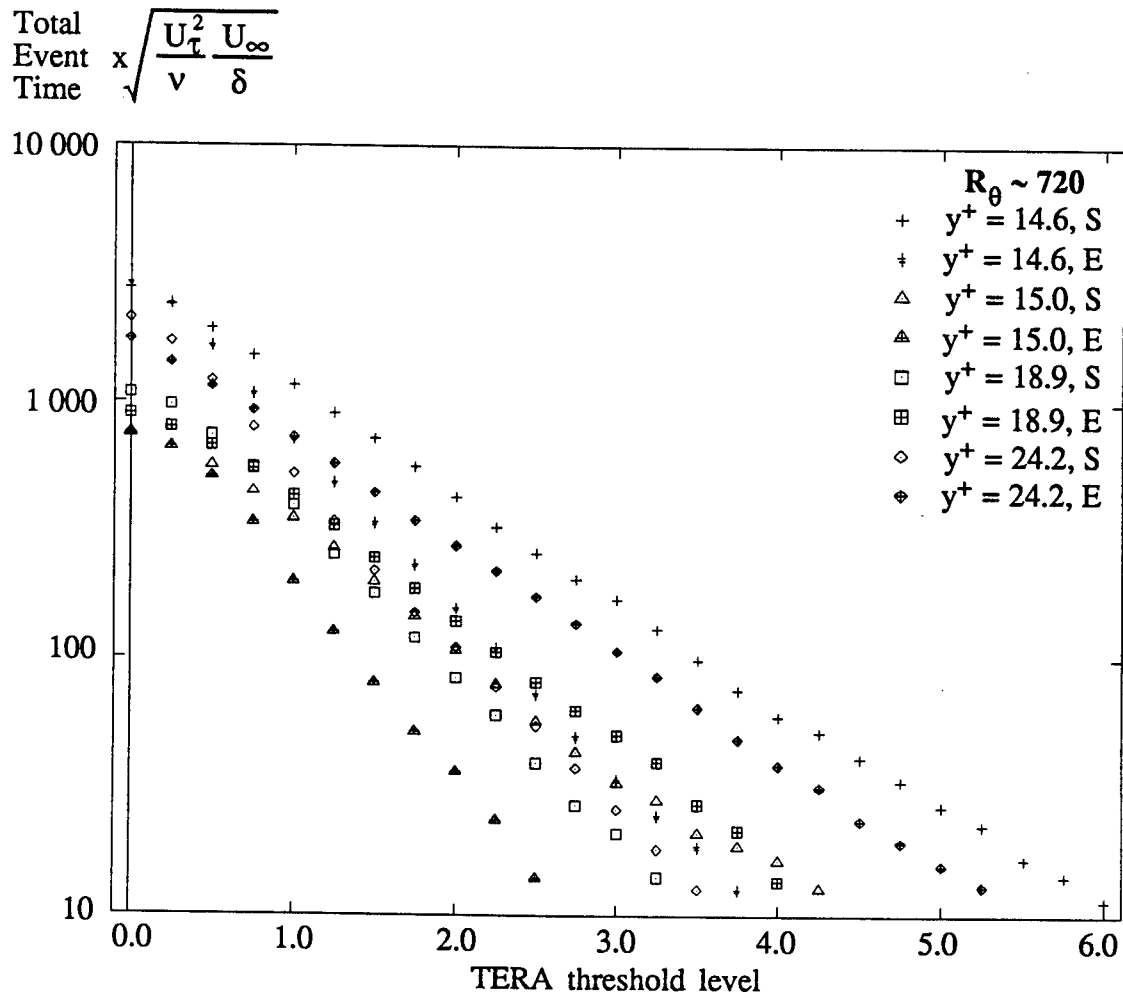
Figure 3.5.7
Total TERA Event Time (Mixed Scaling)
vs. Threshold (Inner-region data)
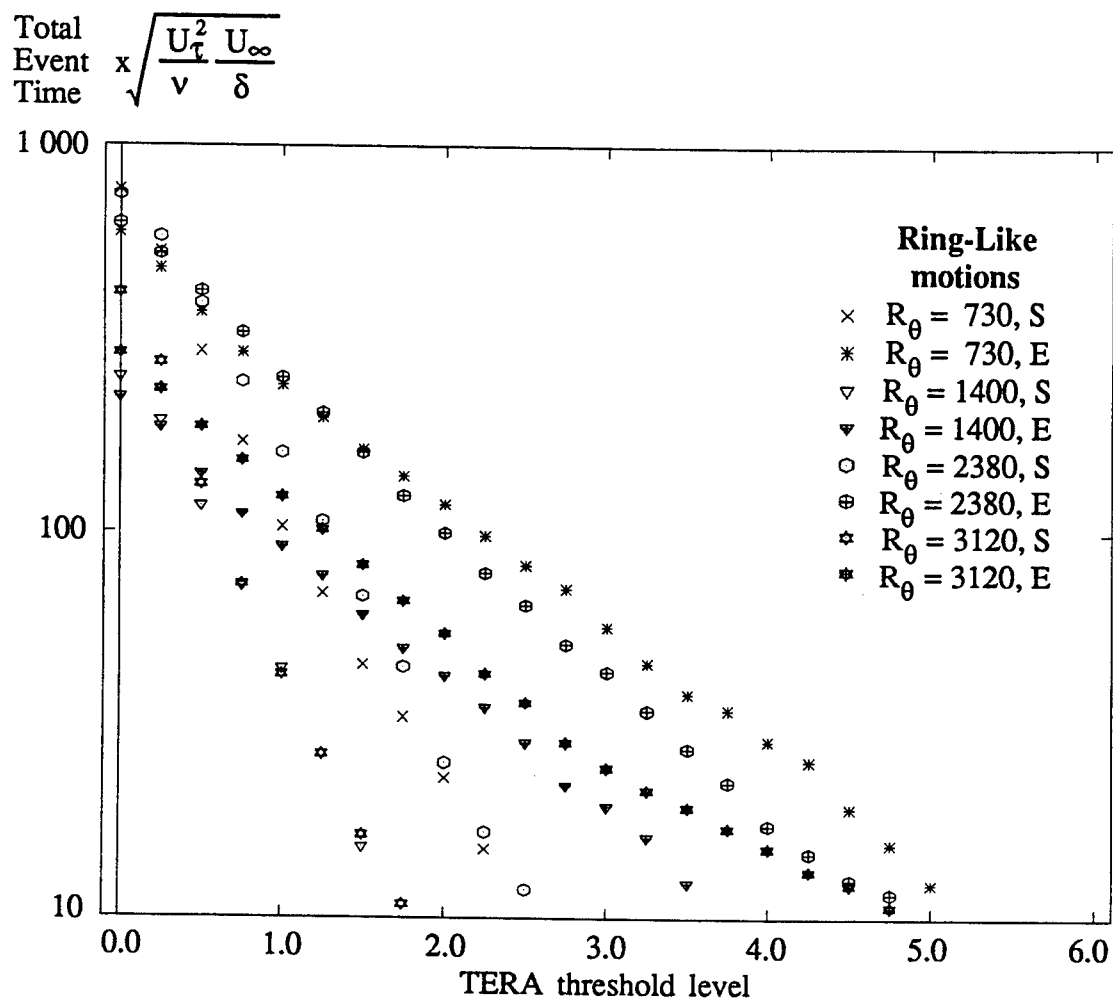
Figure 3.5.8
Total TERA Event Time (Mixed Scaling)
vs. Threshold (RLM data set)

Total
Event x $\sqrt{\dfrac{U_{\tau}^2}{\nu}\dfrac{U_{\infty}}{\delta}}$
Time

10 000

**Large-scale
motions**

⊡ $R_{\theta} = 730$, S
⊞ $R_{\theta} = 730$, E
+ $R_{\theta} = 1400$, S
✳ $R_{\theta} = 1400$, E
⬠ $R_{\theta} = 2380$, S
▲ $R_{\theta} = 2380$, E
⊠ $R_{\theta} = 3120$, S
⊗ $R_{\theta} = 3120$, E

1 000

100

10

0.0   1.0   2.0   3.0   4.0   5.0   6.0

TERA threshold level
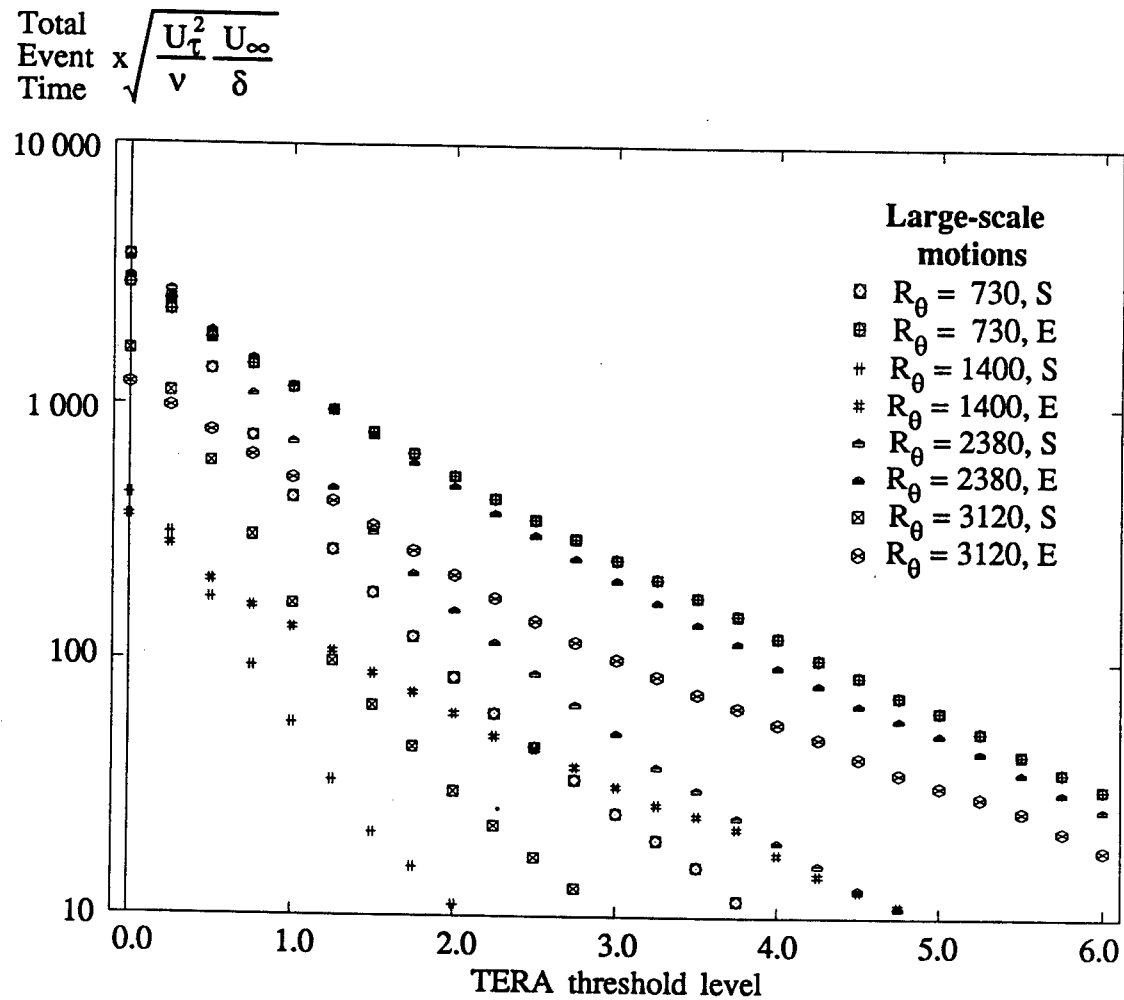
Figure 3.5.9
Total TERA Event Time (Mixed Scaling)
vs. Threshold (LSM data set)
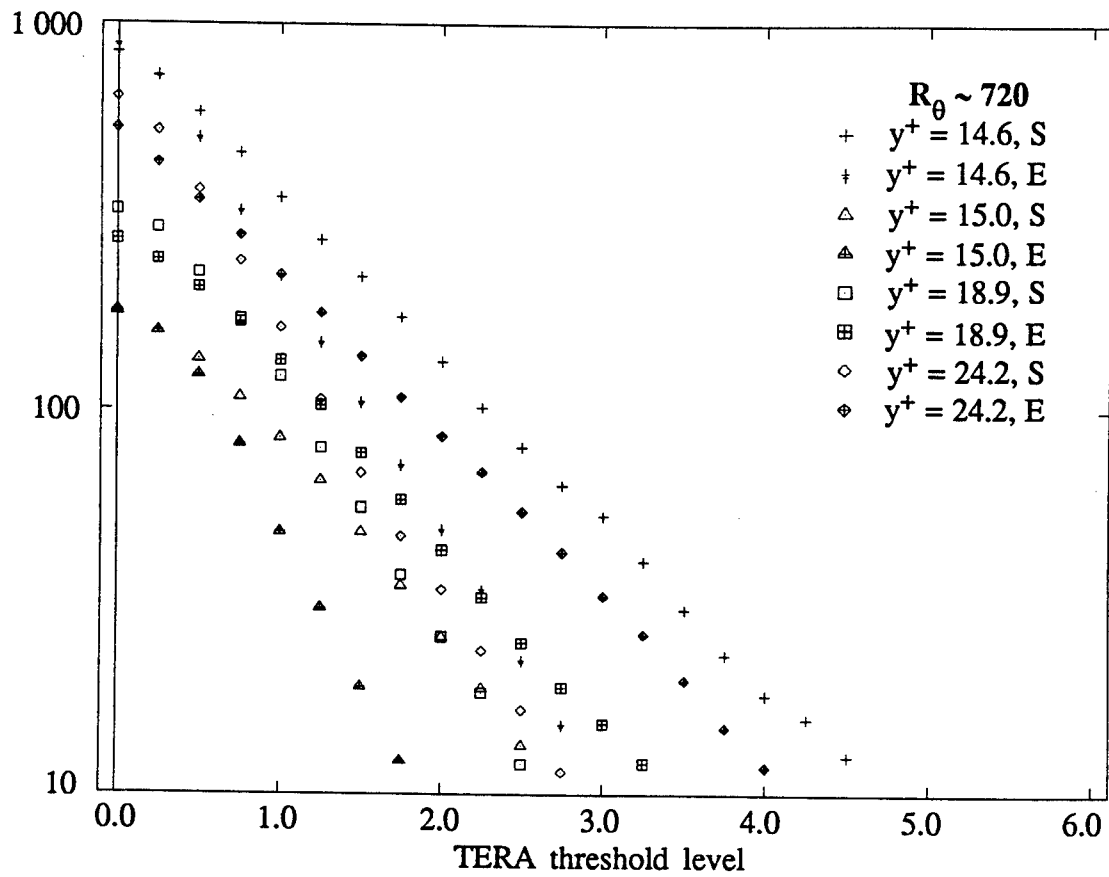
Total
Event $\mathrm{x}\, \dfrac{U_\infty}{\delta}$
Time

Figure 3.5.10
Outer-Scaled Total TERA Event Time
vs. Threshold (Inner-region data)
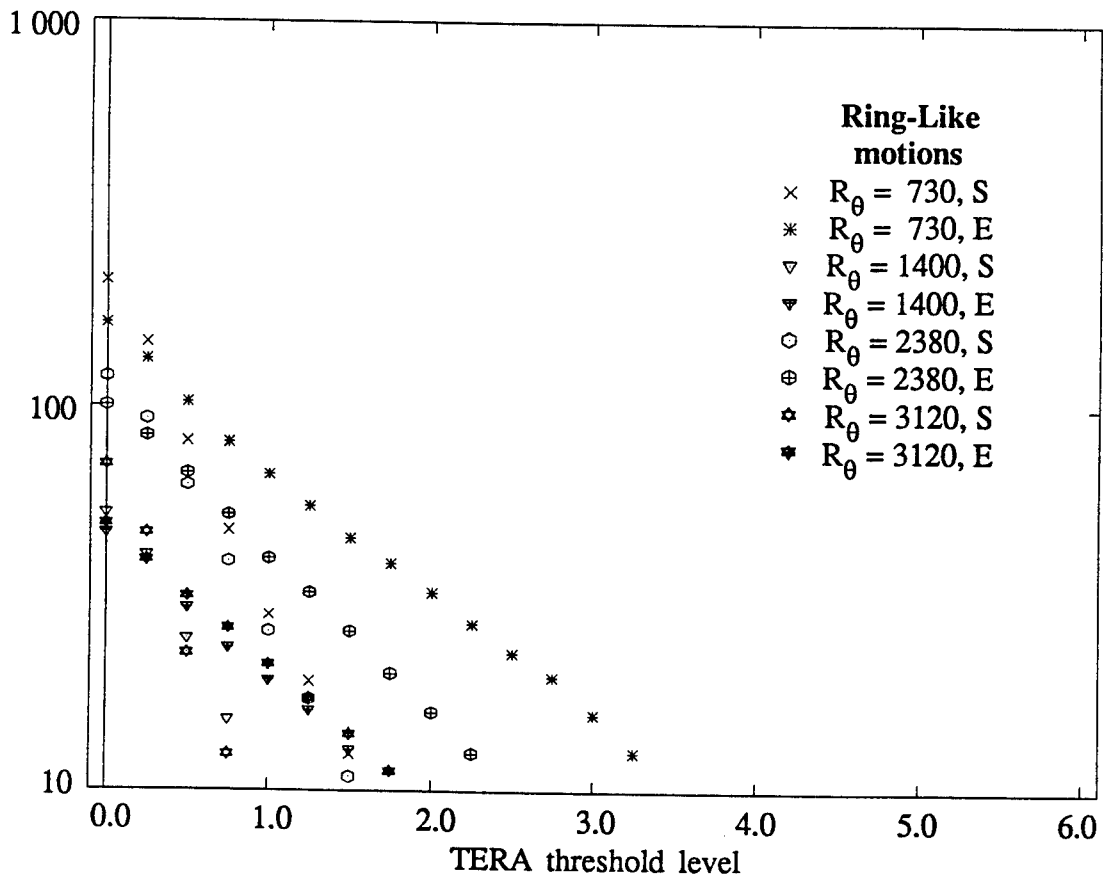
Total
Event x $\dfrac{U_\infty}{\delta}$
Time

Figure 3.5.11
Outer-Scaled Total TERA Event Time
vs. Threshold (RLM data set)
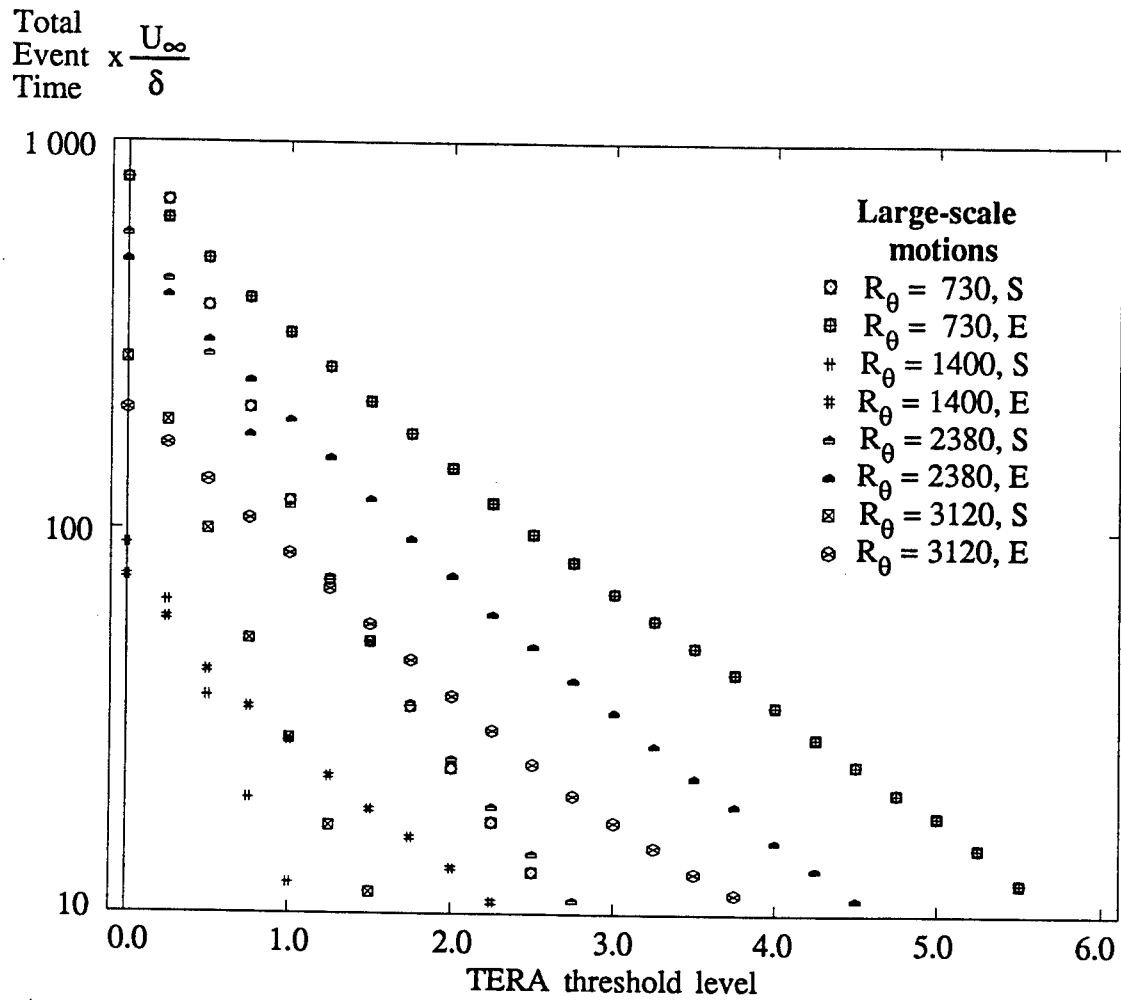
Total
Event $x \dfrac{U_\infty}{\delta}$
Time

Figure 3.5.12
Outer-Scaled Total TERA Event Time
vs. Threshold (LSM data set)
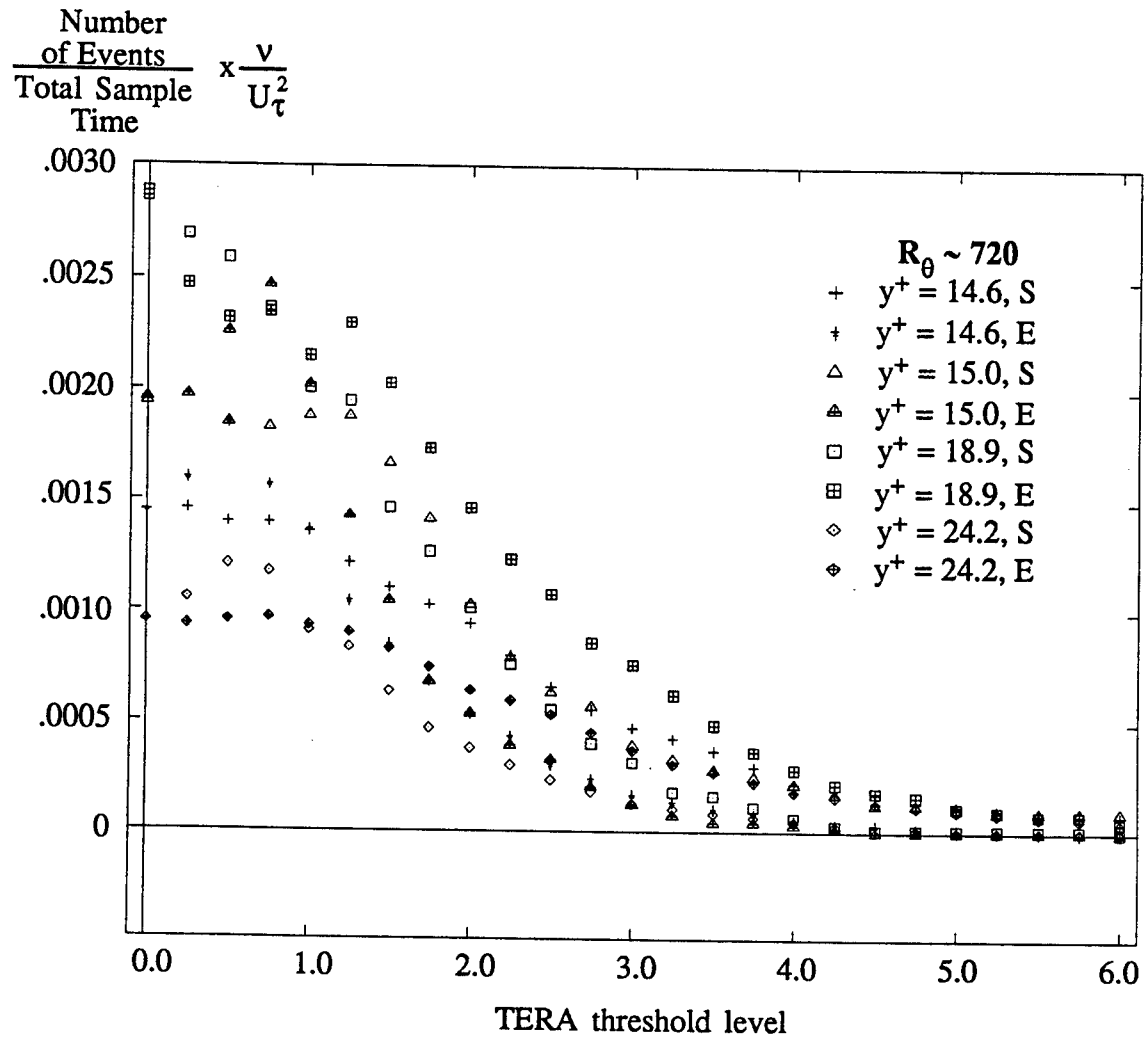
Figure 3.5.13
Inner-scaled TERA Event frequency
vs. Threshold level (Inner-region data)

$$\frac{\frac{\text{Number}}{\text{of Events}}}{\substack{\text{Total Sample}\\\text{Time}}} \times \sqrt{\frac{\nu}{U_\tau^2}\frac{\delta}{U_\infty}}$$
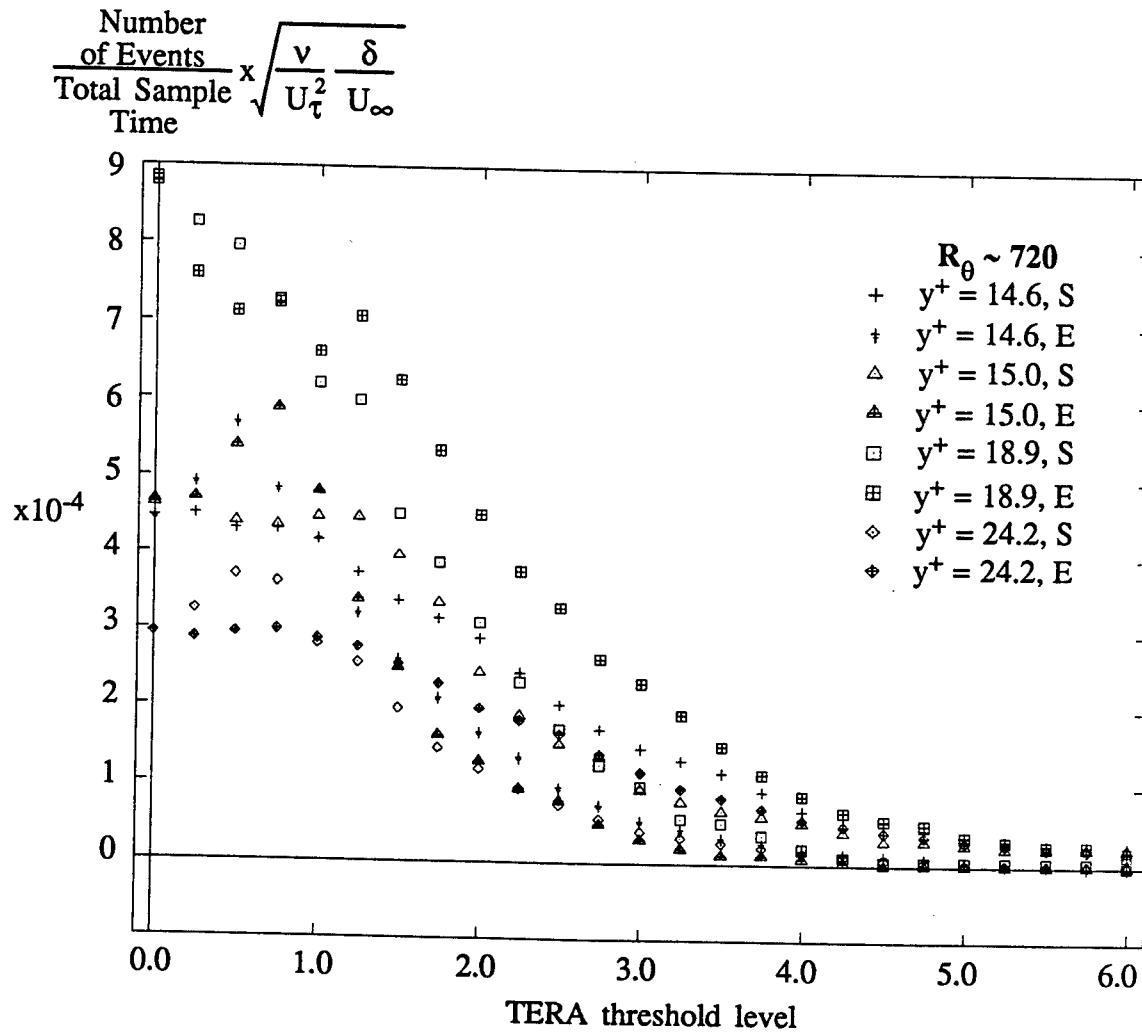
Figure 3.5.14
TERA Event frequency (Mixed-scaling)
vs. Threshold level (Inner-region data)

$$\frac{\text{Number of Events}}{\text{Total Sample Time}} \times \frac{\delta}{U_\infty}$$
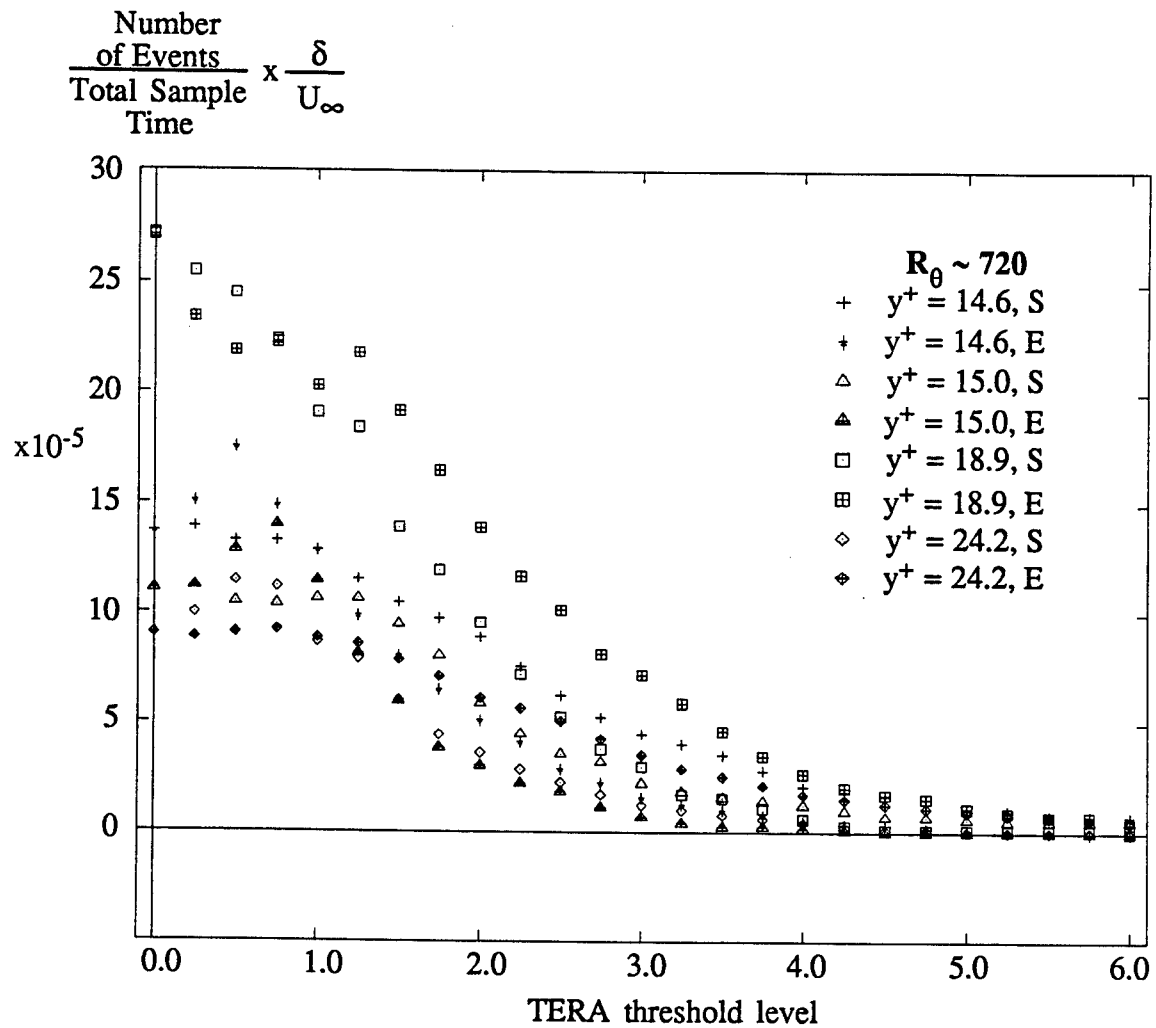
Figure 3.5.15
Outer-scaled TERA Event frequency
vs. Threshold level (Inner-region data)

$$\frac{\text{Number}}{\text{of Events}} \times \frac{\nu}{U_\tau^2}$$
Total Sample
Time

**Outer-Region
motions**

◻	$R_\theta = 730, S$
⊞	$R_\theta = 730, E$
✢	$R_\theta = 1400, S$
✚	$R_\theta = 1400, E$
◓	$R_\theta = 2380, S$
◕	$R_\theta = 2380, E$
⊠	$R_\theta = 3120, S$
⊗	$R_\theta = 3120, E$

TERA threshold level
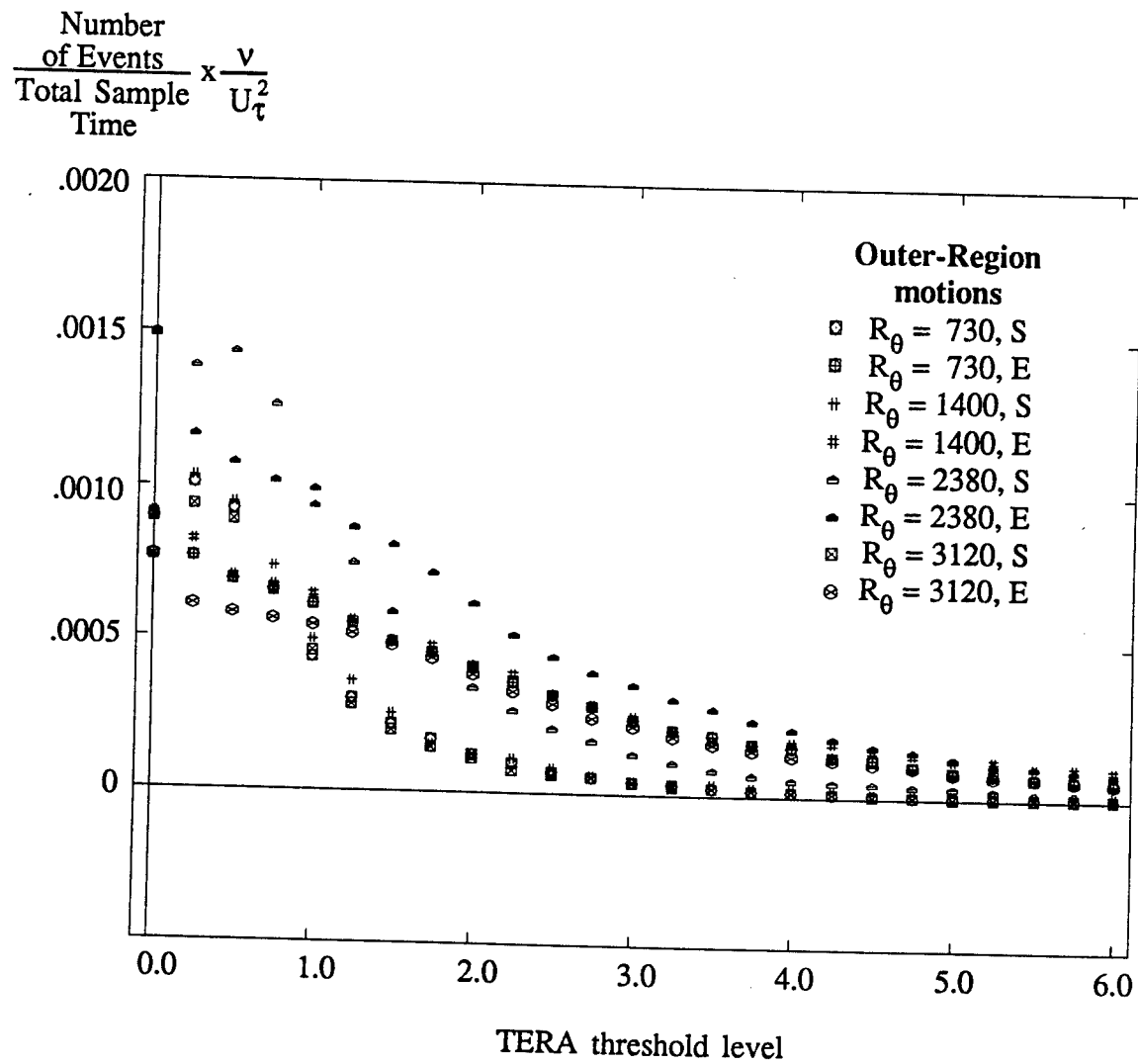
Figure 3.5.16
Inner-scaled TERA Event frequency
vs. Threshold level (LSM data set)

$$\frac{\frac{\text{Number}}{\text{of Events}}}{\frac{\text{Total Sample}}{\text{Time}}} \times \sqrt{\frac{\nu}{U_\tau^2} \frac{\delta}{U_\infty}}$$
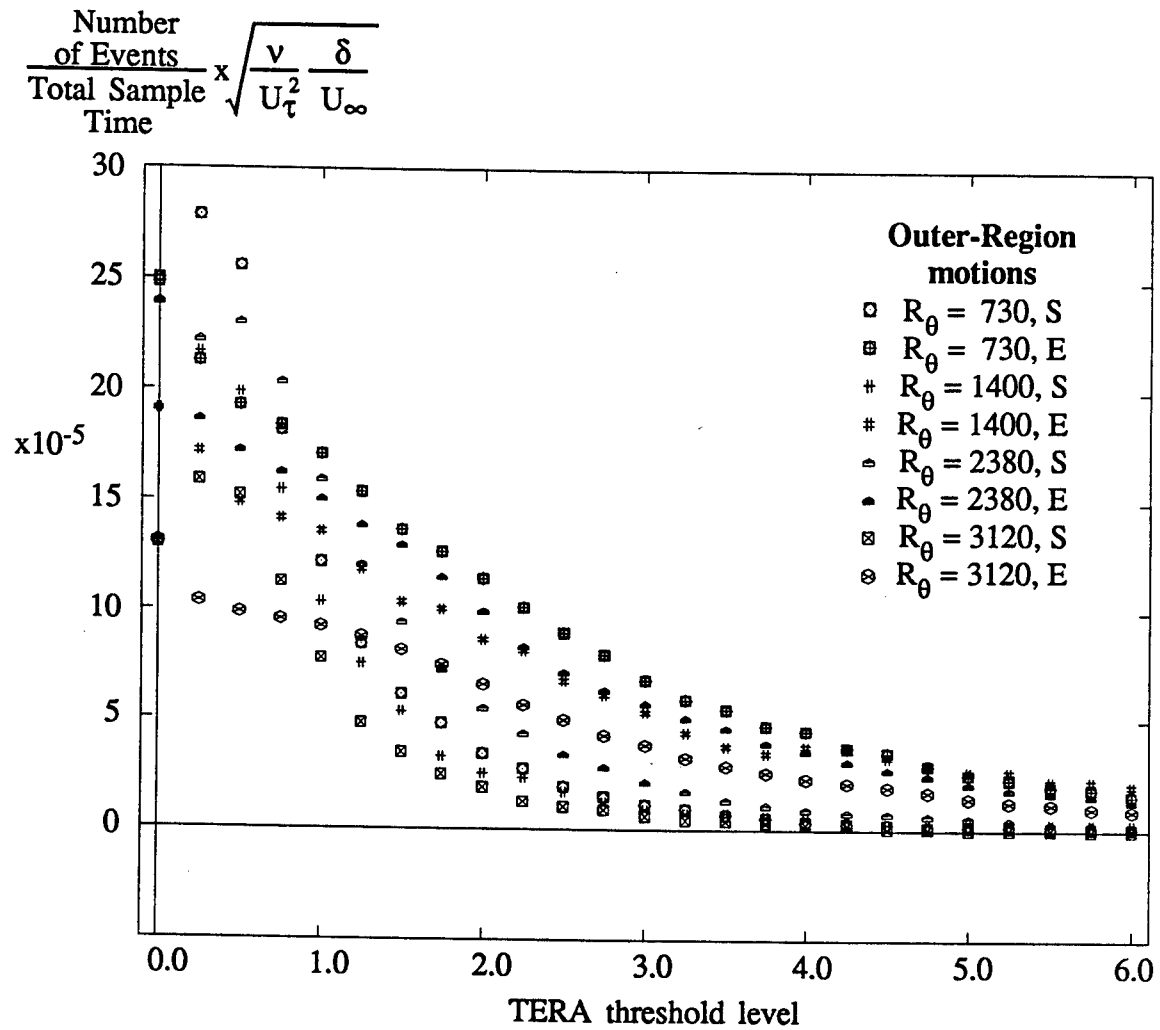
Figure 3.5.17
TERA Event frequency (Mixed-scaling)
vs. Threshold level (LSM data set)
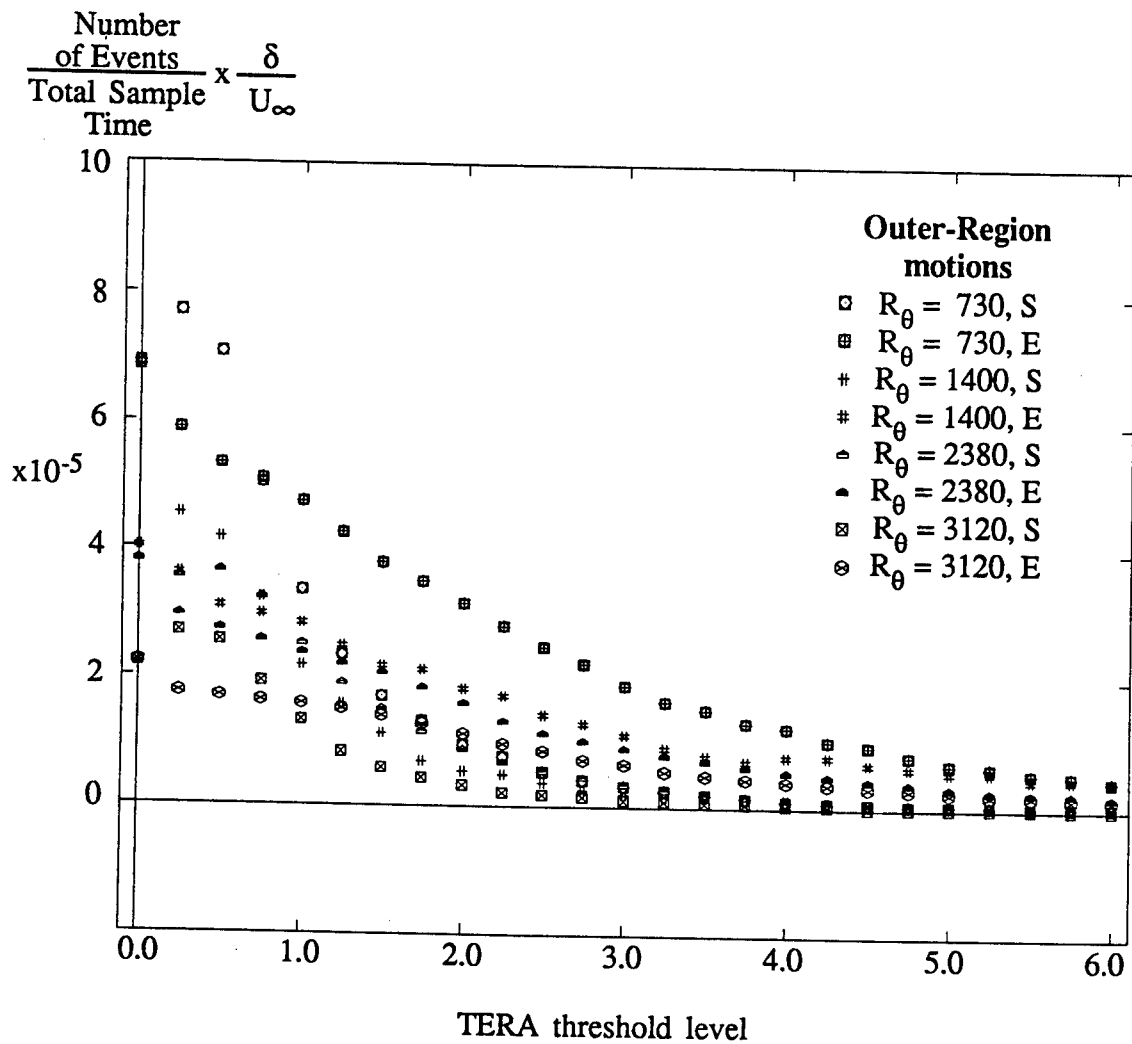
Figure 3.5.18
Outer-scaled TERA Event frequency
vs. Threshold level (LSM data set)
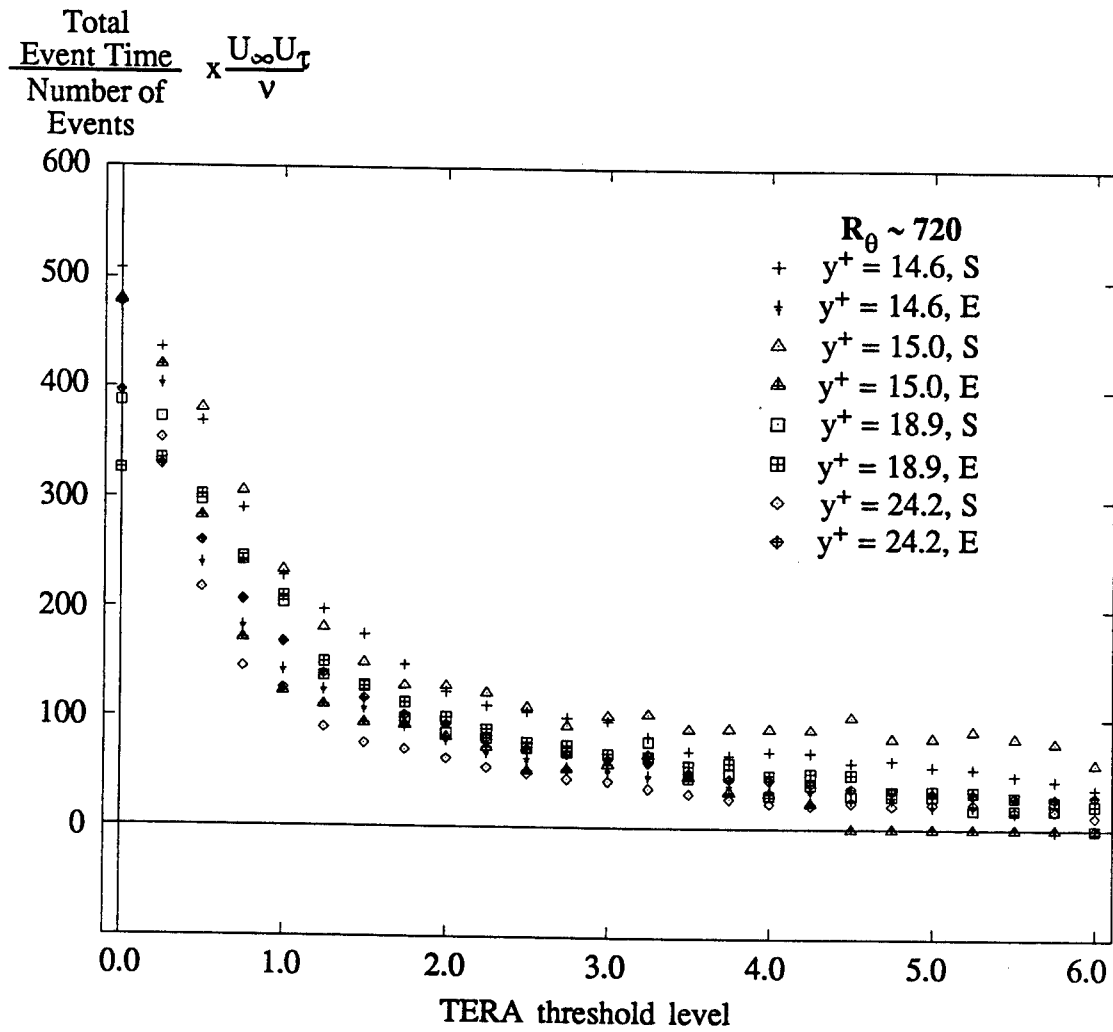
Figure 3.5.19
Inner-Scaled Average TERA Event Length
vs. Threshold (Inner-region data)

$$\frac{\text{Total}}{\underset{\text{Events}}{\underset{\text{Number of}}{\text{Event Time}}}} \text{x} \sqrt{\frac{U_\infty^2 \, U_\tau}{\delta \, \nu}}$$
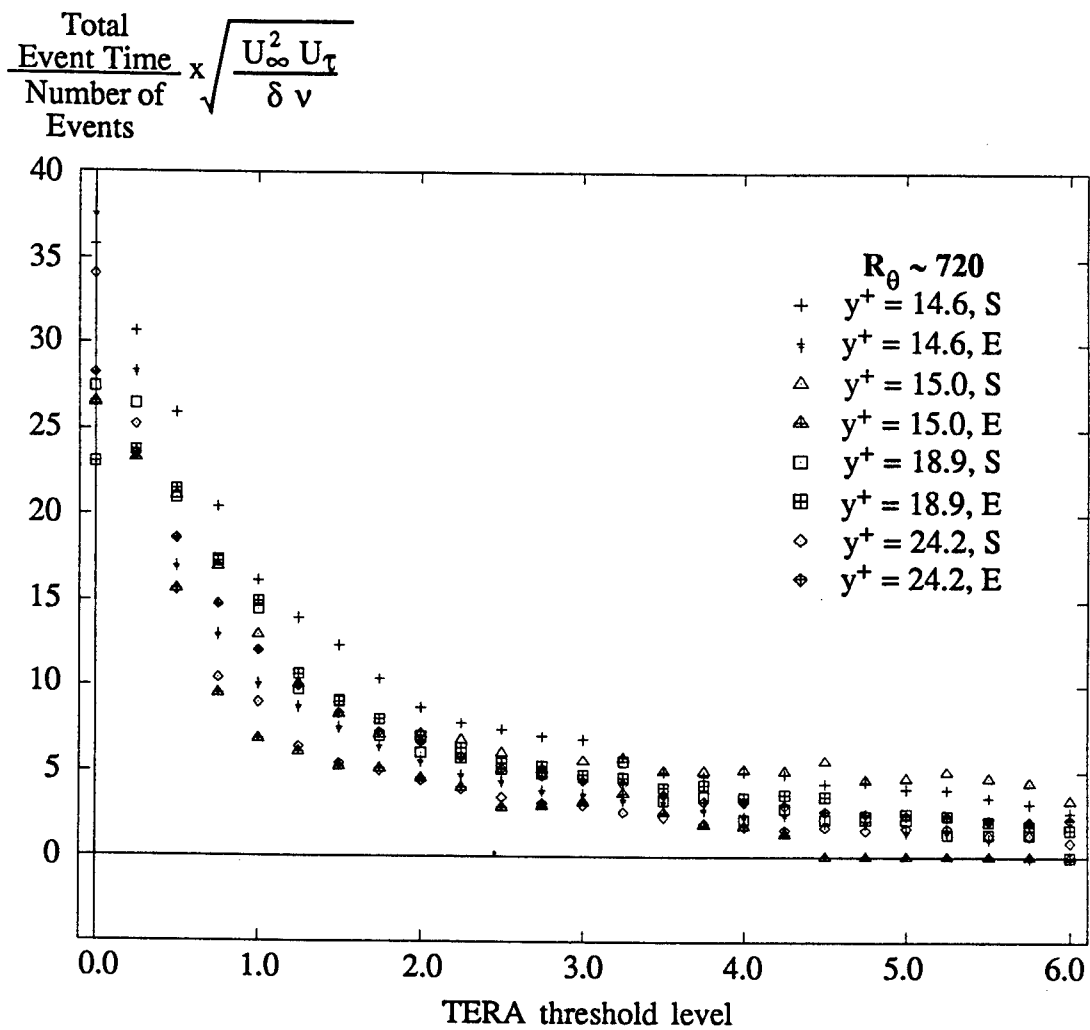
Figure 3.5.20
Average TERA Event Length (Mixed Scaling)
vs. Threshold (Inner-region data)

Total
$\dfrac{\text{Event Time}}{\text{Number of}}$ $\times \dfrac{U_\infty}{\delta}$
Events

R$_\theta$ ~ 720

+	$y^+ = 14.6$, S
✝	$y^+ = 14.6$, E
△	$y^+ = 15.0$, S
▲	$y^+ = 15.0$, E
□	$y^+ = 18.9$, S
⊞	$y^+ = 18.9$, E
◇	$y^+ = 24.2$, S
◈	$y^+ = 24.2$, E

TERA threshold level
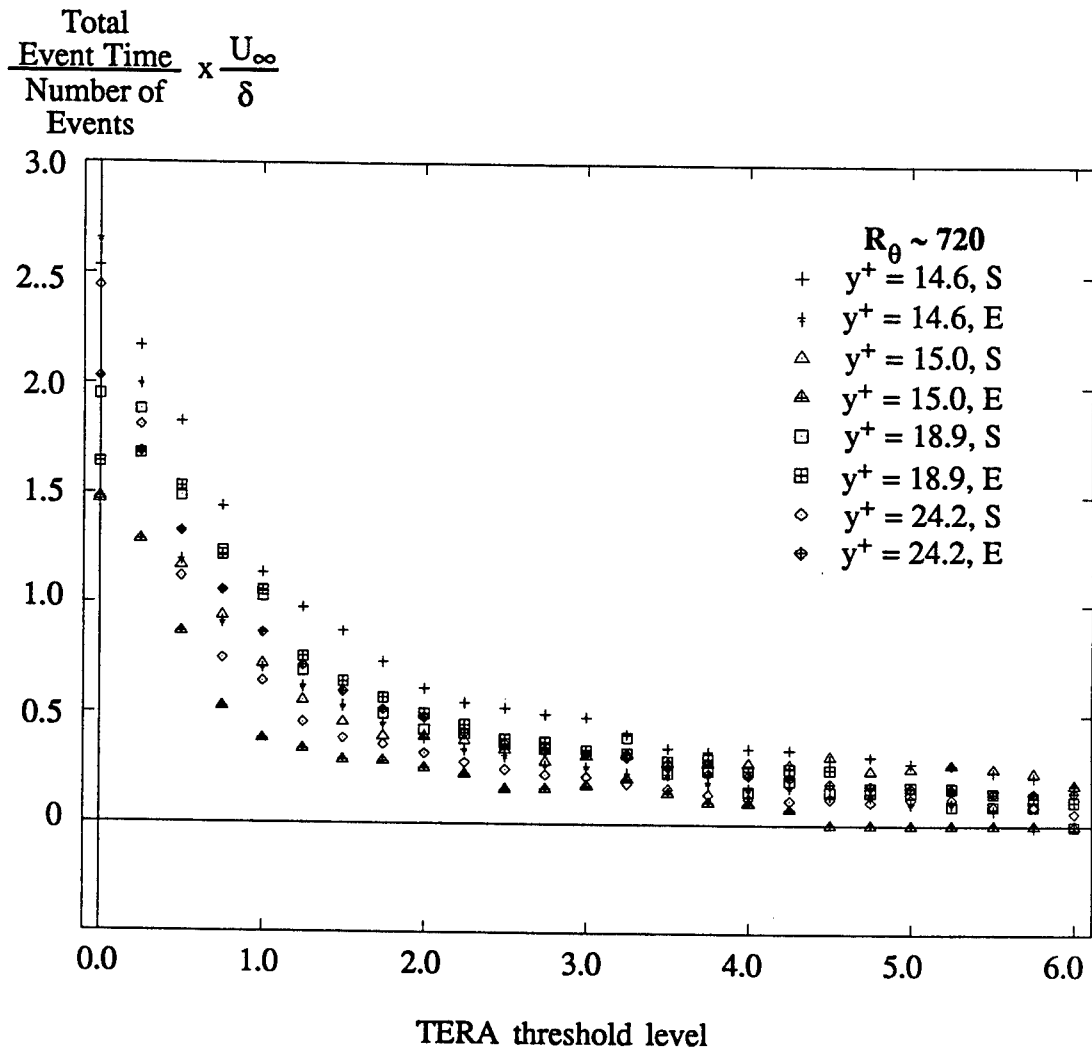
Figure 3.5.21
Outer-Scaled Average TERA Event Length
vs. Threshold (Inner-region data)
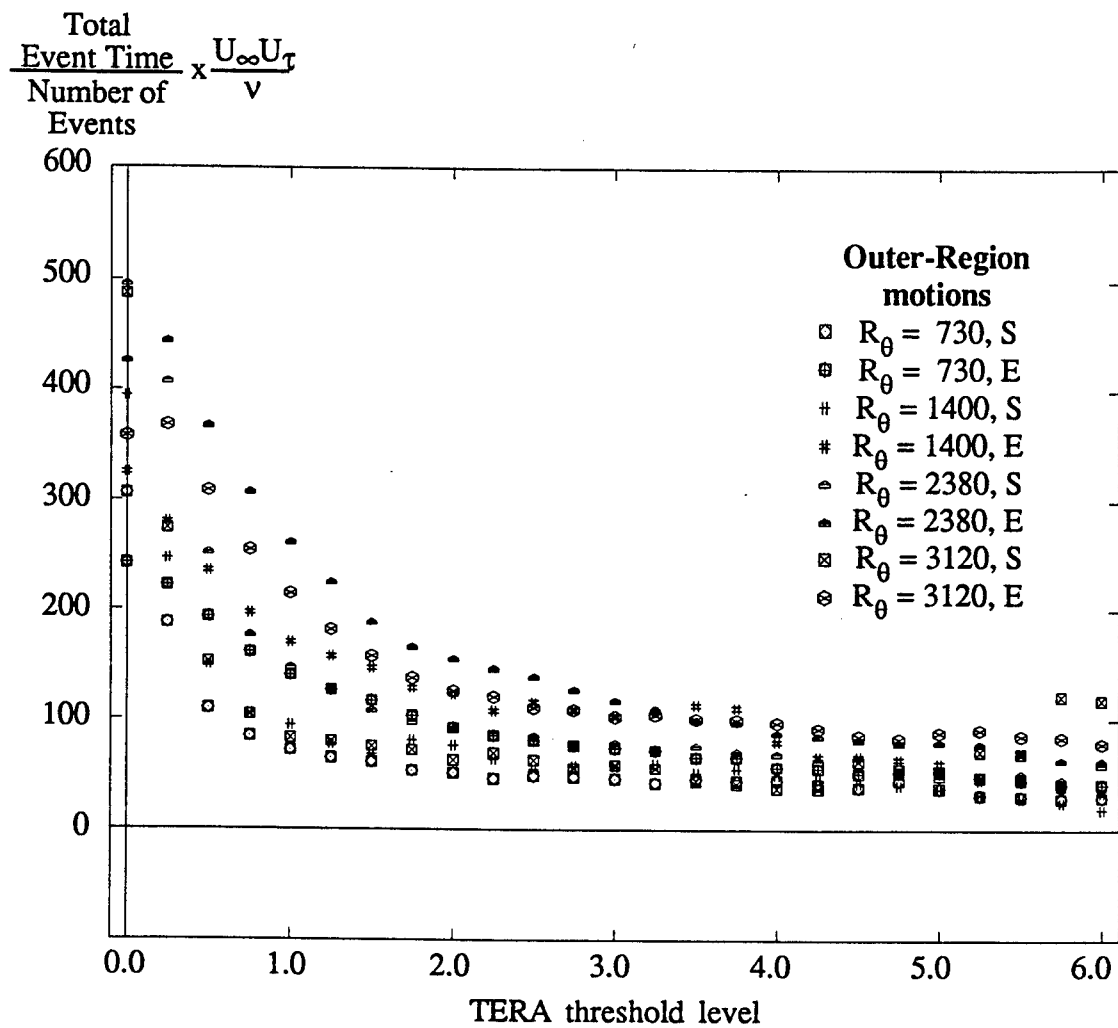
Figure 3.5.22
Inner-Scaled Average TERA Event Length
vs. Threshold (LSM data set)

$$\frac{\text{Total}}{\substack{\text{Event Time} \\ \text{Number of} \\ \text{Events}}} \times \sqrt{\frac{U_\infty^2 \, U_\tau}{\delta \, \nu}}$$
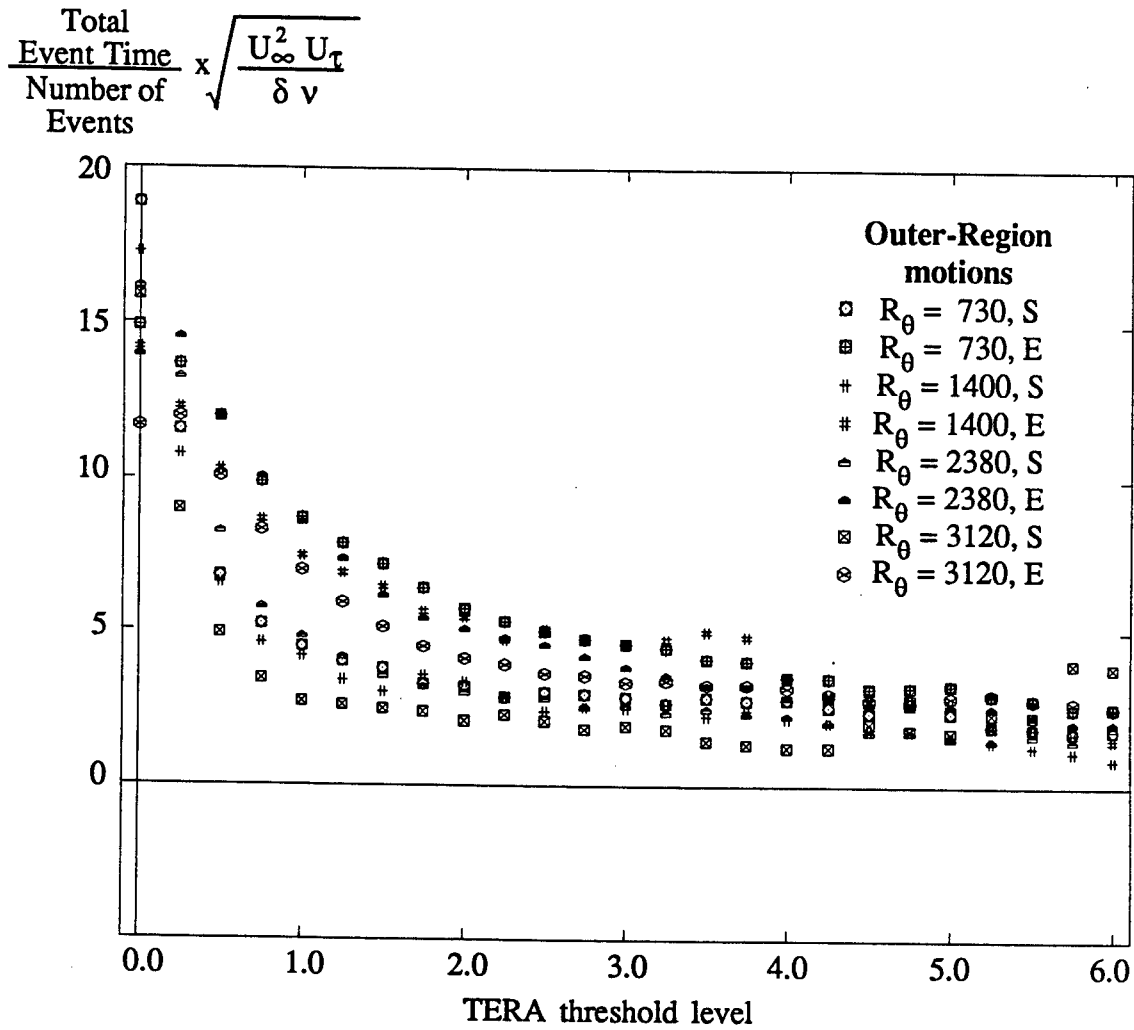
Figure 3.5.23
Average TERA Event Length (Mixed Scaling)
vs. Threshold (LSM data set)

Total
$$\frac{\underline{\text{Event Time}}}{\text{Number of}} \times \frac{U_\infty}{\delta}$$
Events
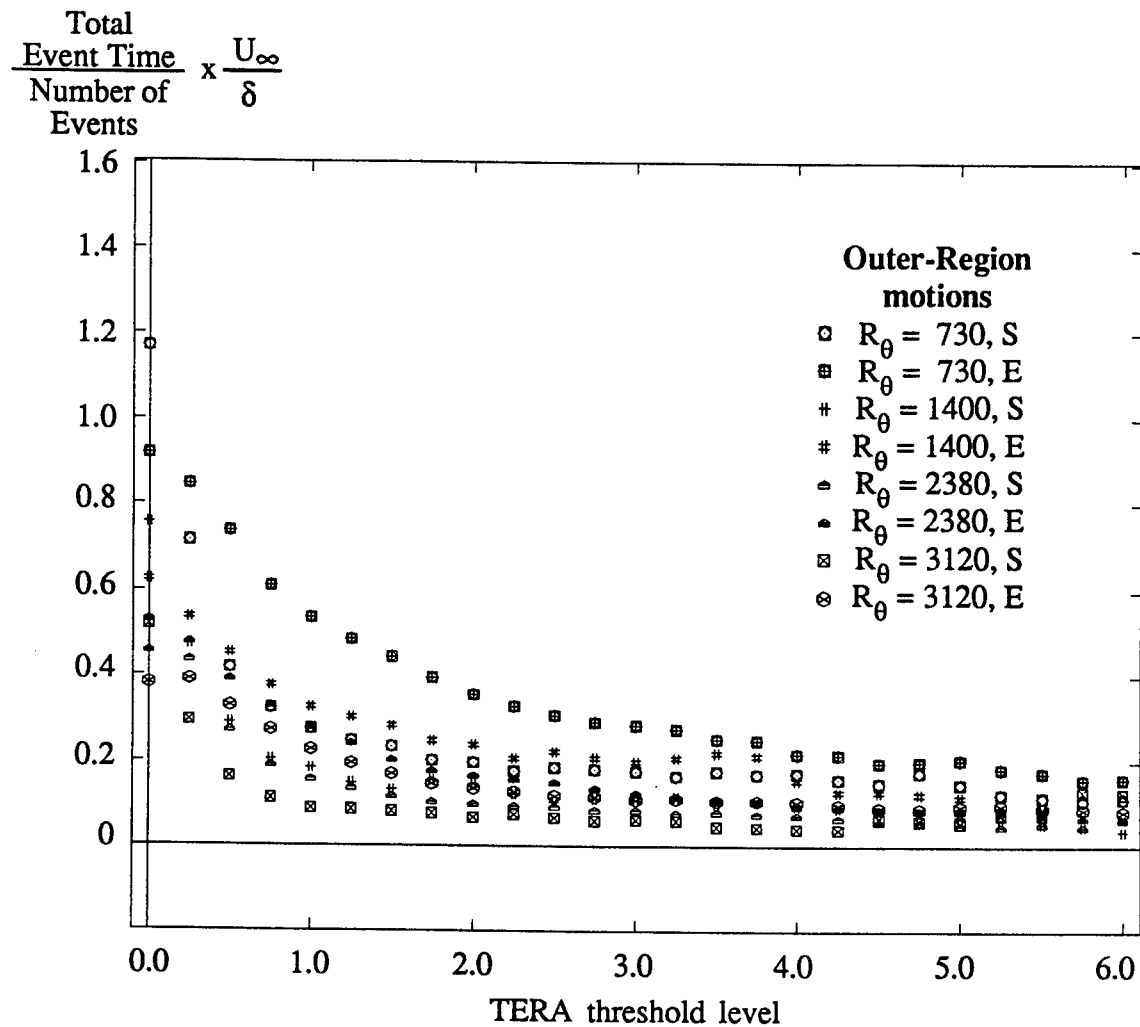
Figure 3.5.24
Outer-Scaled Average TERA Event Length
vs. Threshold (LSM data set)
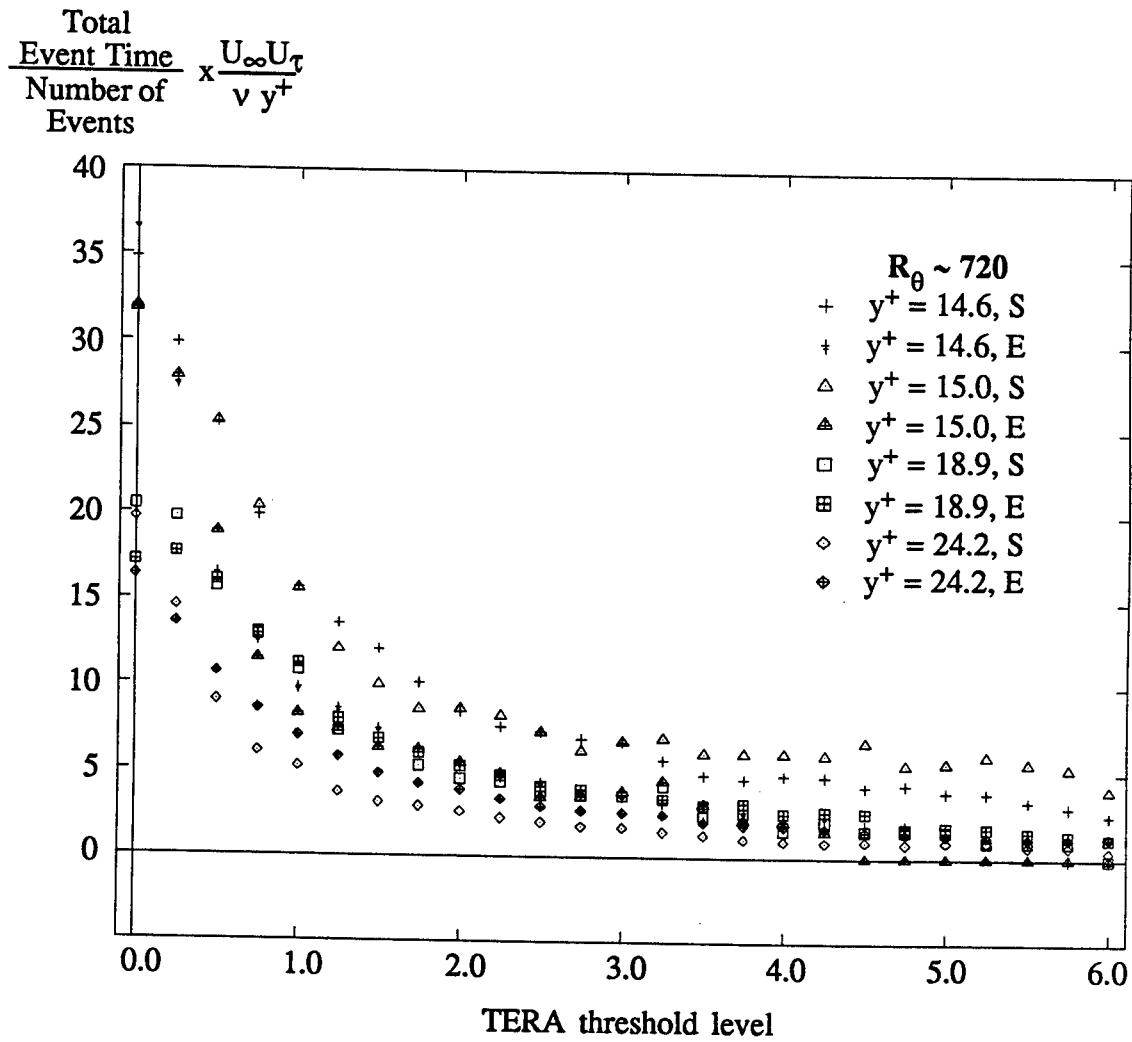
Figure 3.5.25
Average Inner-Scaled TERA
Event Length over y^+
vs. Threshold (Inner-region data)

$\int uv{<}0$ / $\int uv{<}0$

during events   all times
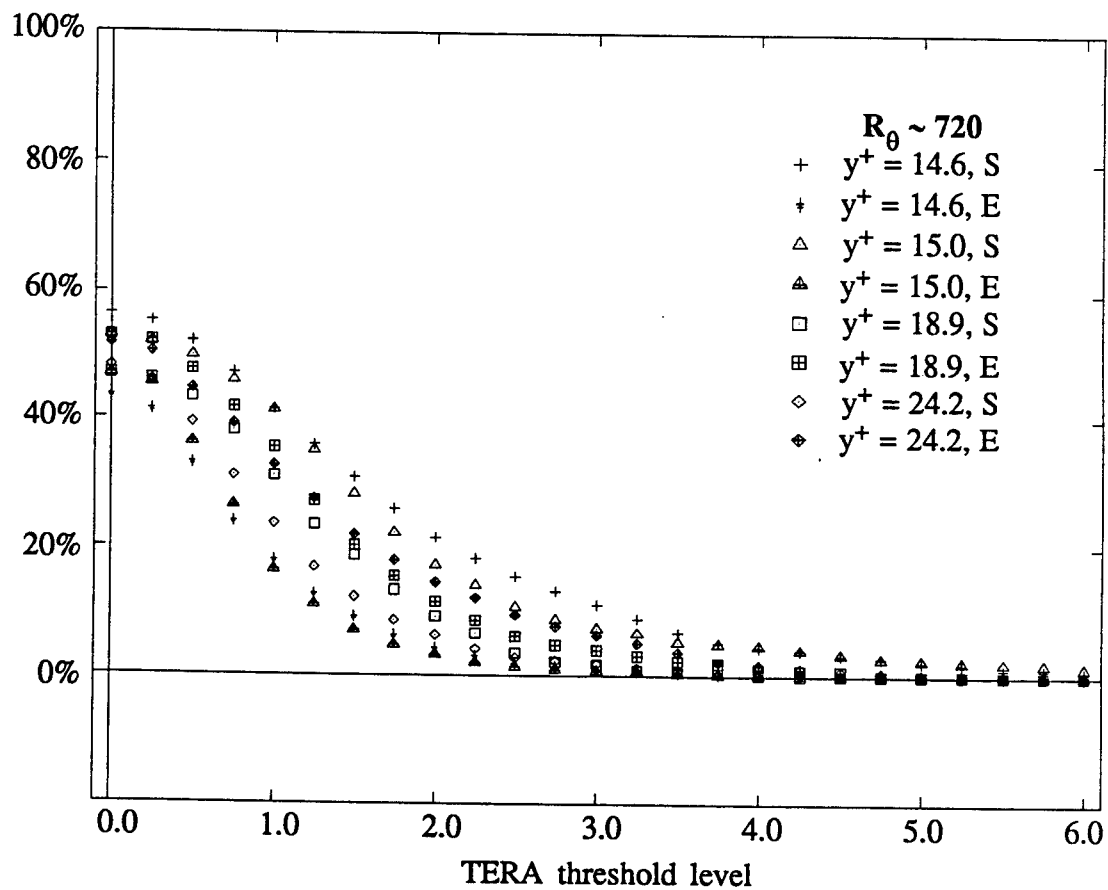
Figure 3.5.26
Percent Reynolds Stress "captured" during
TERA events vs. Threshold
(Inner-region data)

$\int uv<0 \big/ \int uv<0$
during   all times
events
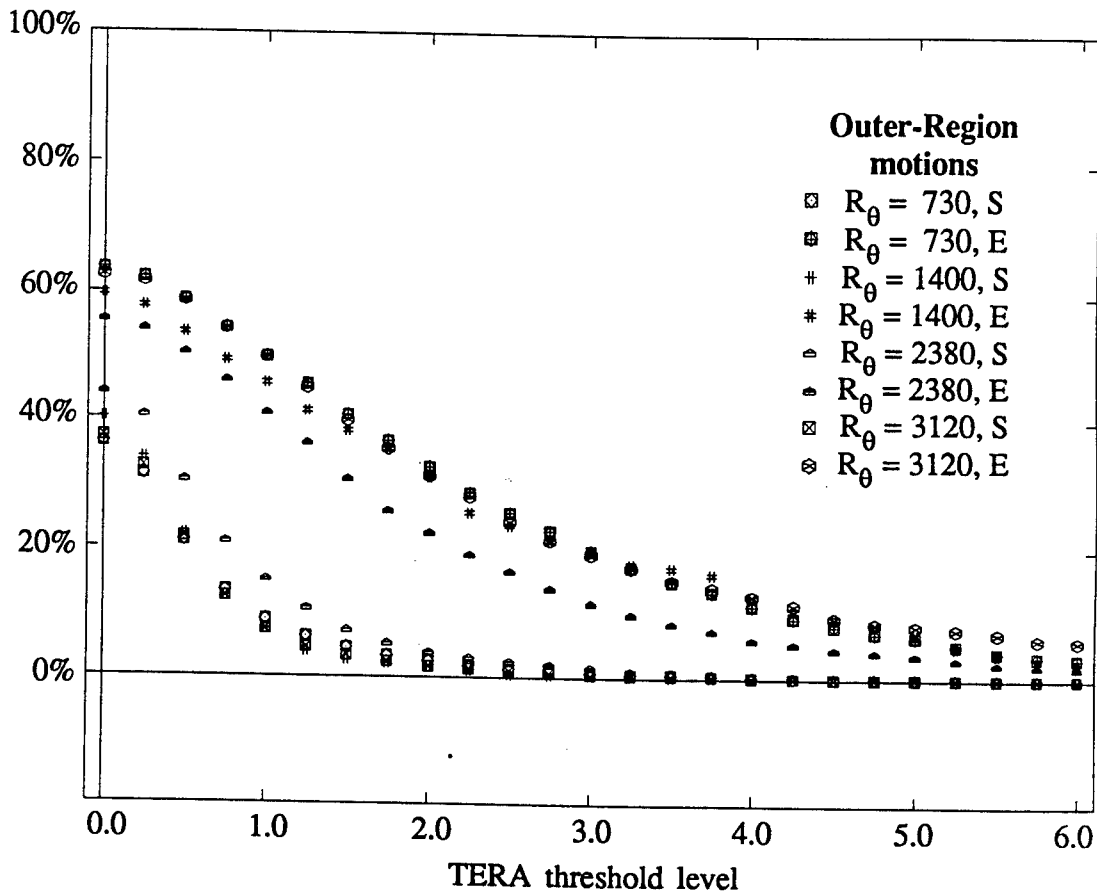
Figure 3.5.27
Percent Reynolds Stress "captured" during
TERA events vs. Threshold
(LSM data set)
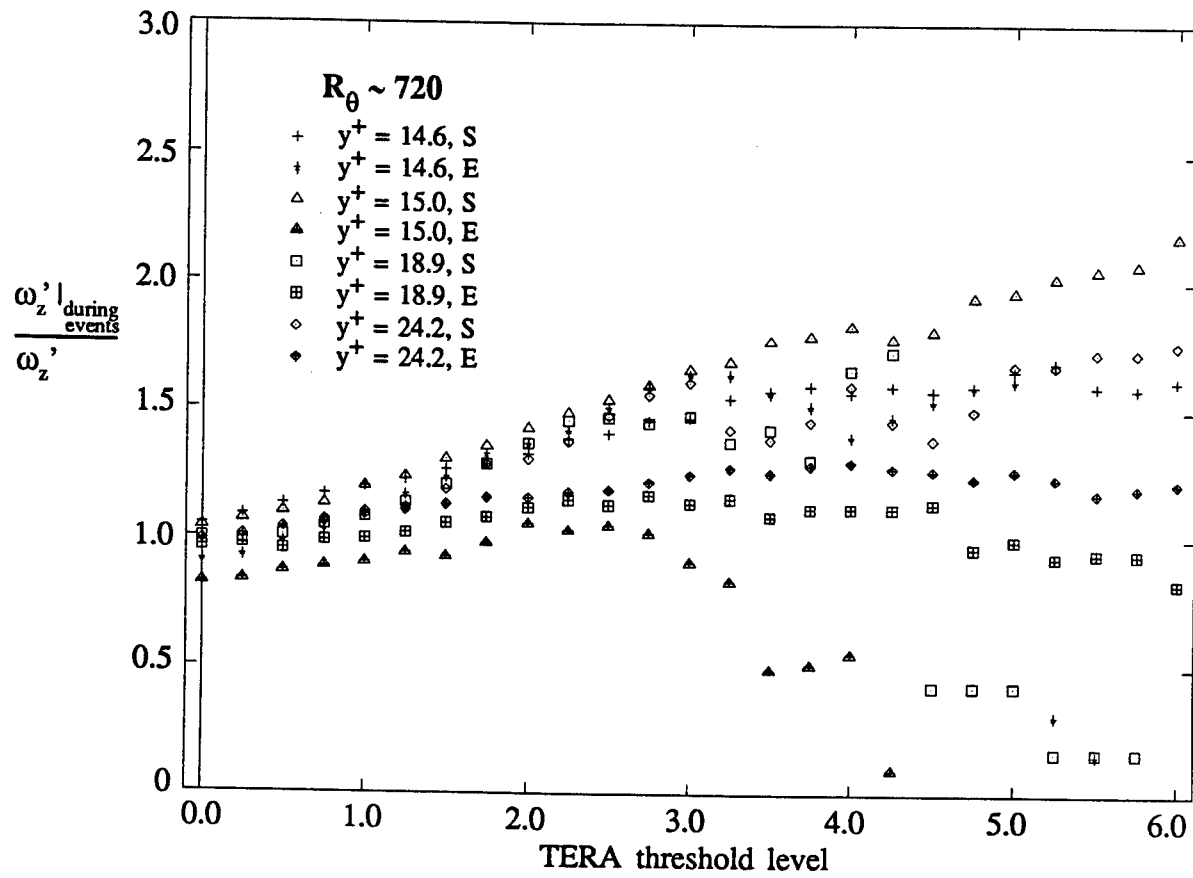
Figure 3.5.28
RMS ω_z During TERA Events
Normalized by ω_z'
vs. Threshold (Inner-region data)
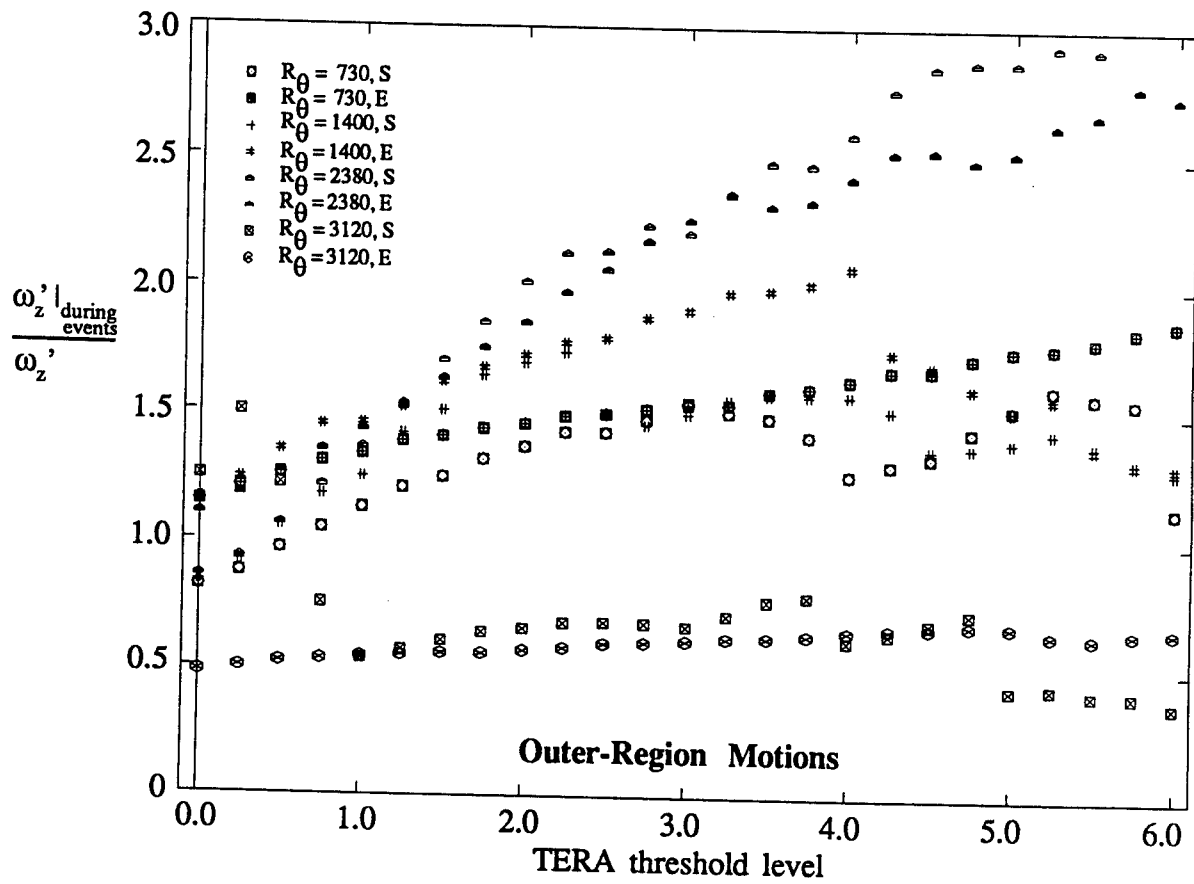
Figure 3.5.29
RMS ω_z During TERA Events
Normalized by ω_z'
vs. Threshold (LSM data set)

$$\frac{<u^2+v^2>|_{\substack{during \\ events}}}{(u^2+v^2)'}$$
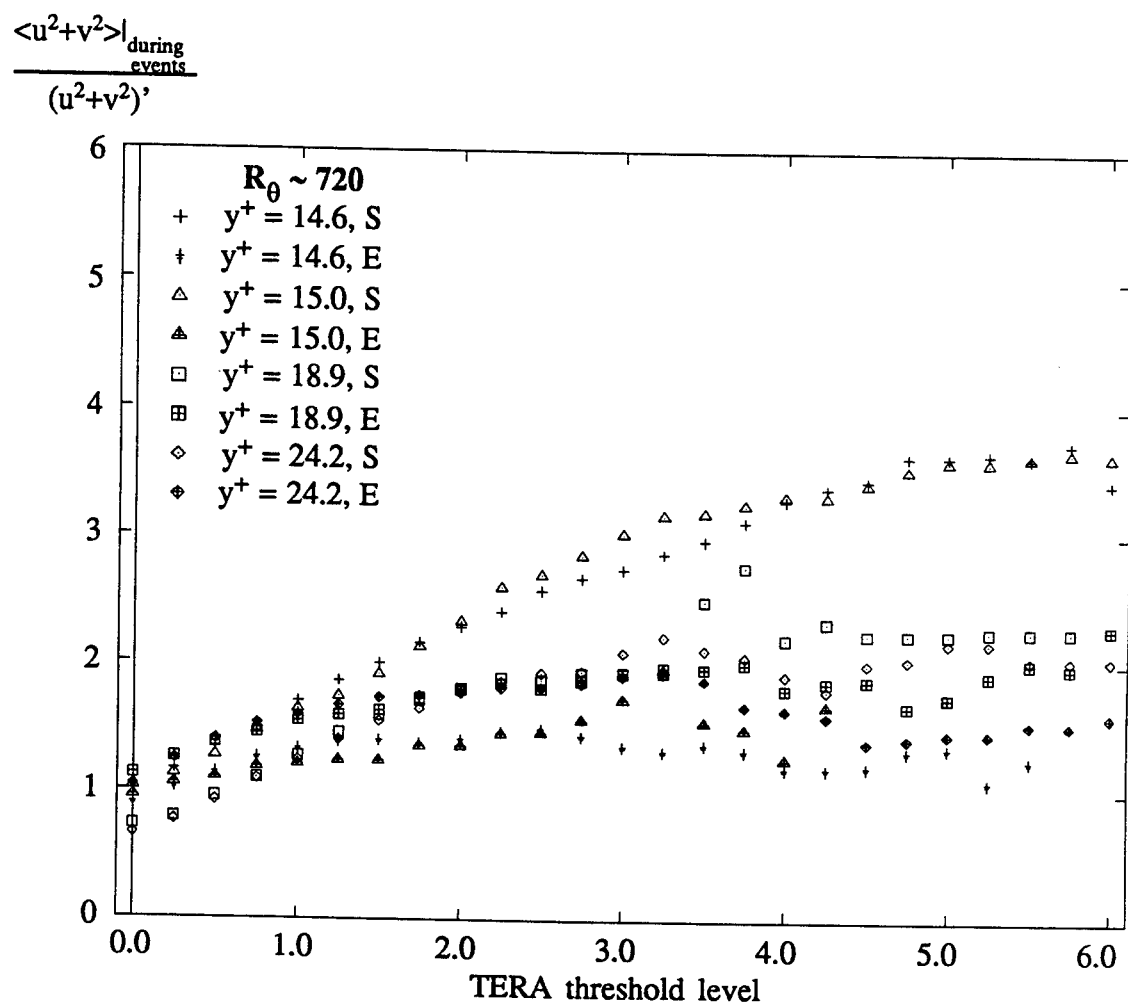
Figure 3.5.30
Average TKE During TERA
EventsNormalized by TKE'
vs. Threshold (Inner-region data)

$$\frac{<u^2+v^2>|_{during \atop events}}{(u^2+v^2)'}$$
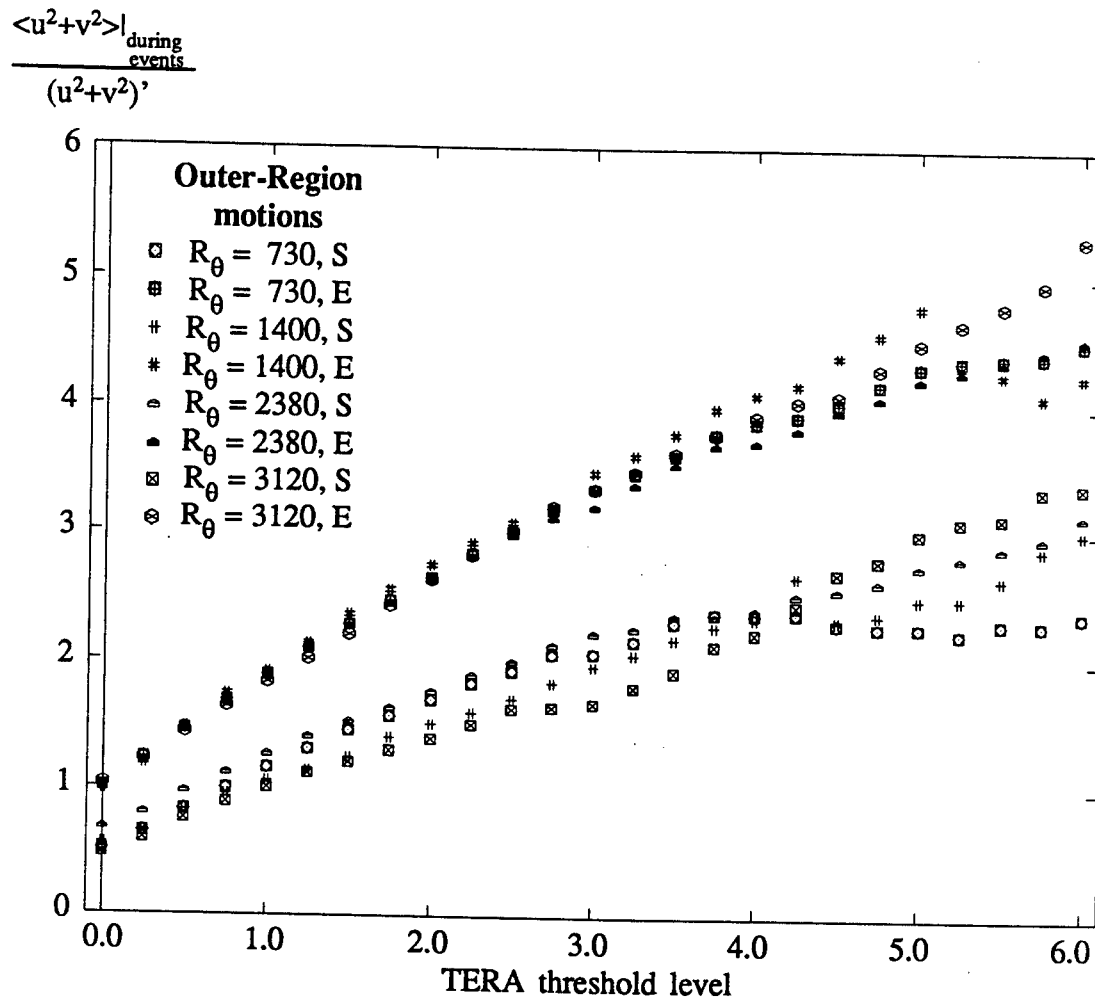
Figure 3.5.31
Average TKE During TERA
Events Normalized by TKE'
vs. Threshold (LSM data set)
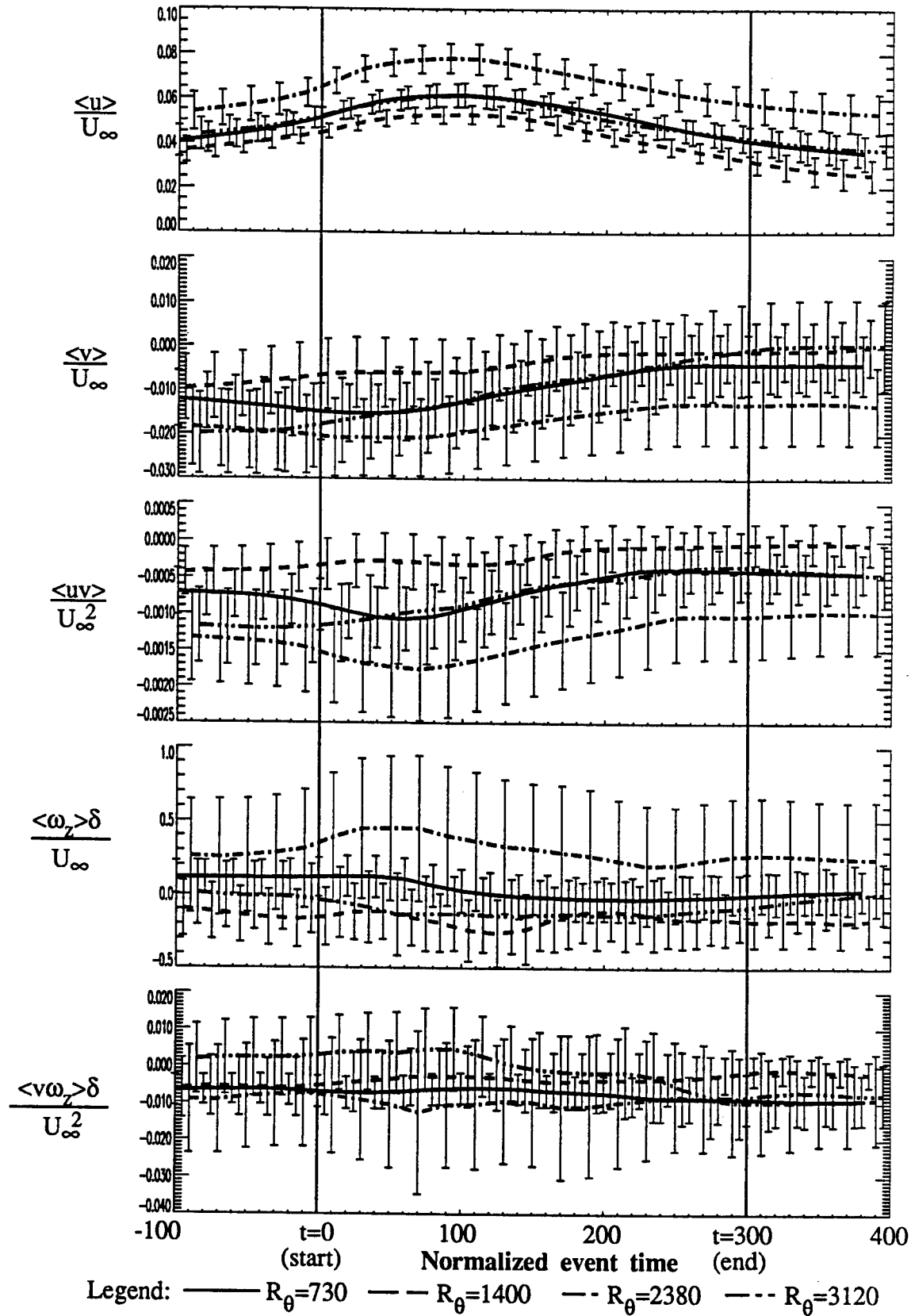
Figure 3.5.32 Outer-scaled TERA sweep ensembles. Error bars indicate 25% of an ensemble's standard deviation about each point in time
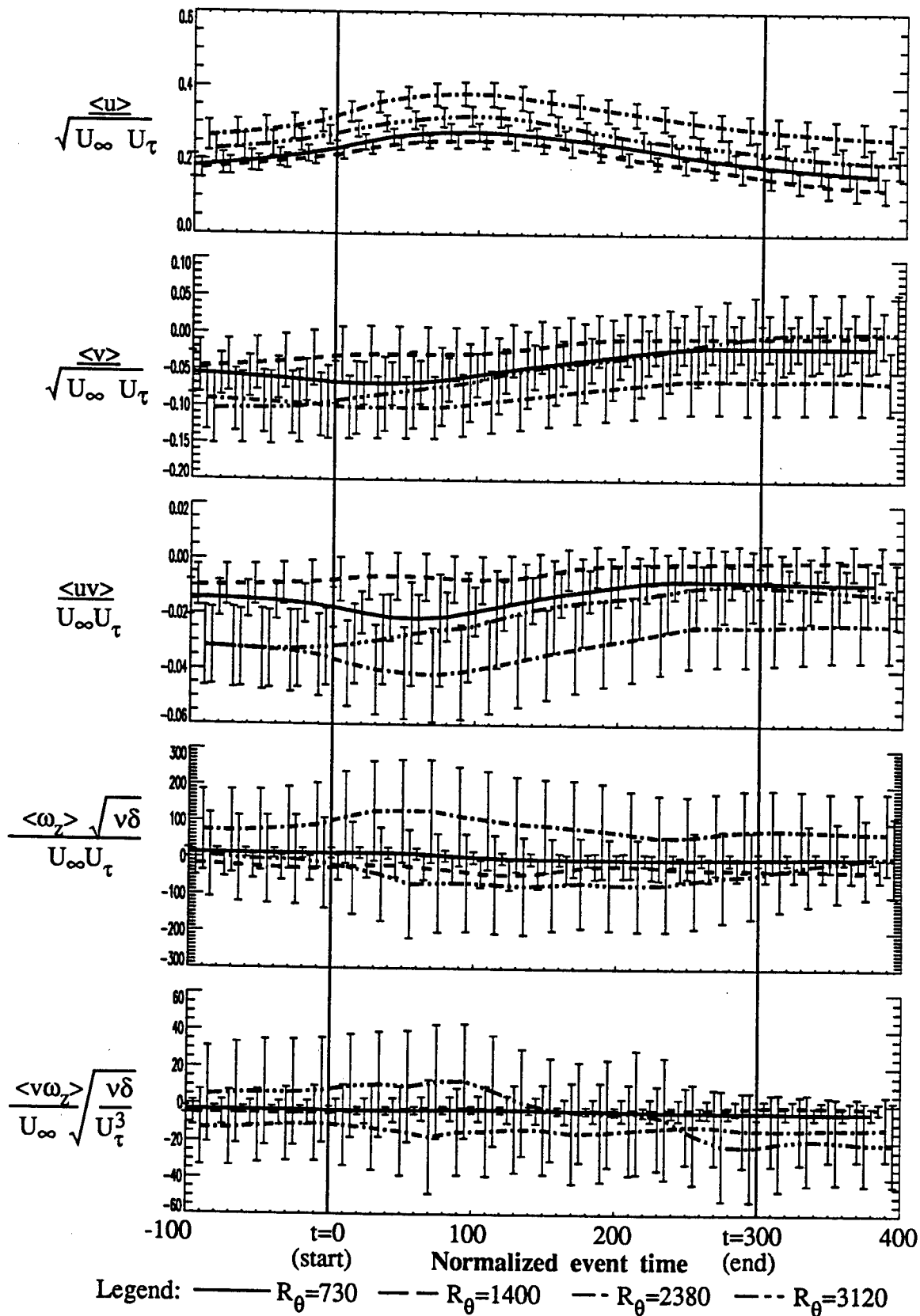
Figure 3.5.33 Mixed-scaled TERA sweep ensembles. Error bars indicate 25% of an ensemble's standard deviation about each point in time
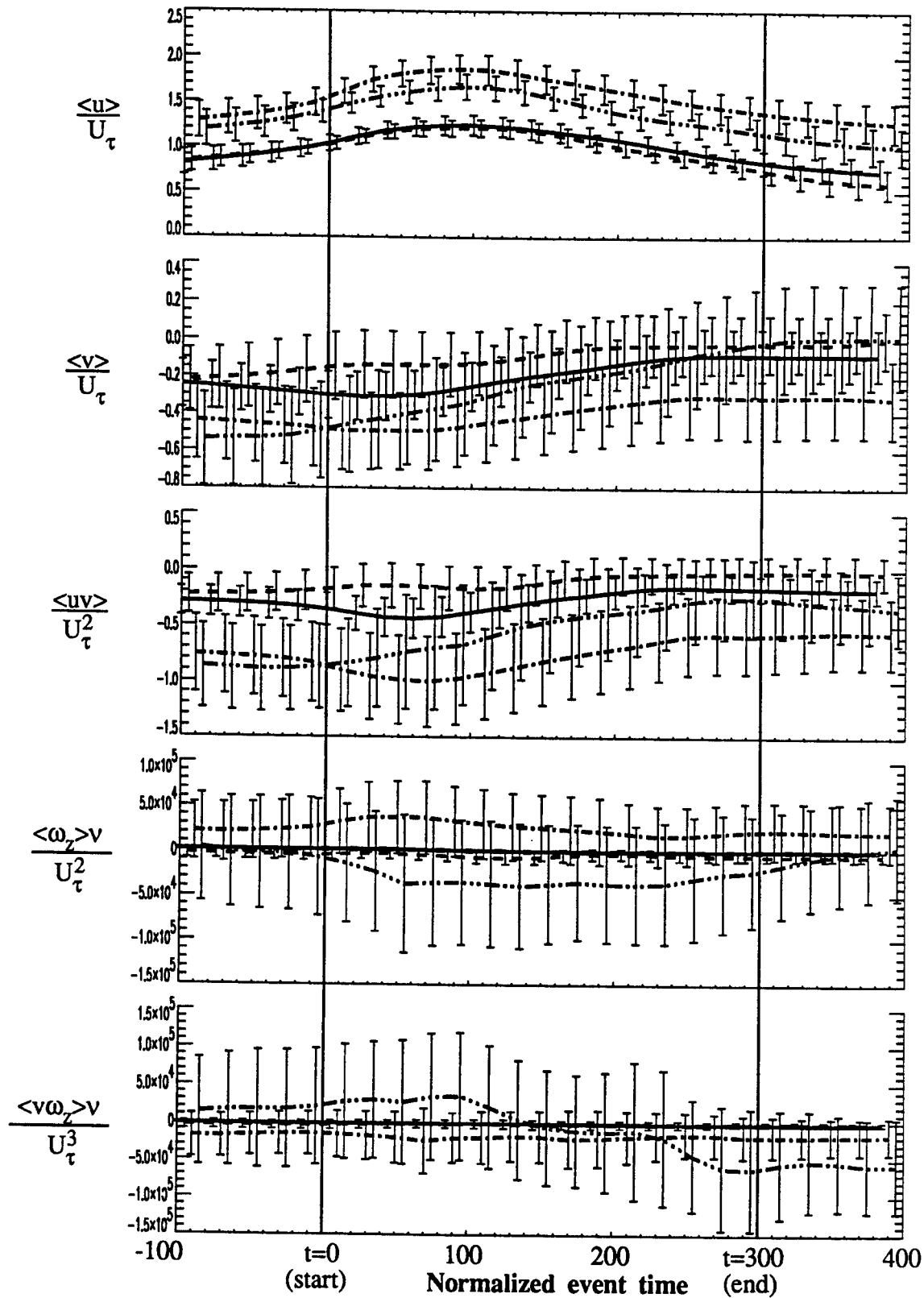
Figure 3.5.34 Inner-scaled TERA sweep ensembles. Error bars indicate 25% of an ensemble's standard deviation about each point in time
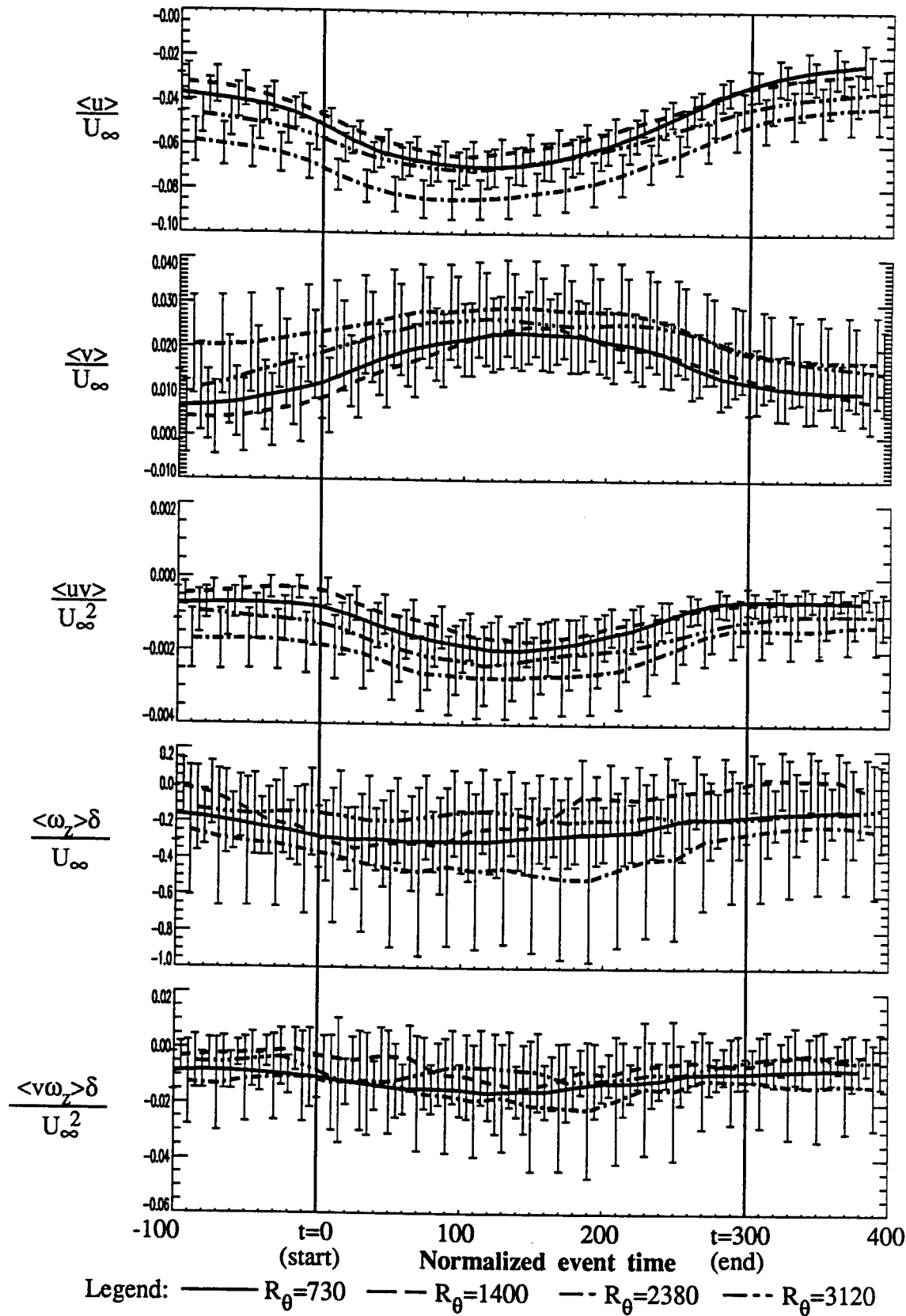
Figure 3.5.35 Outer-scaled TERA ejection ensembles. Error bars indicate 25% of an ensemble's standard deviation about each point in time
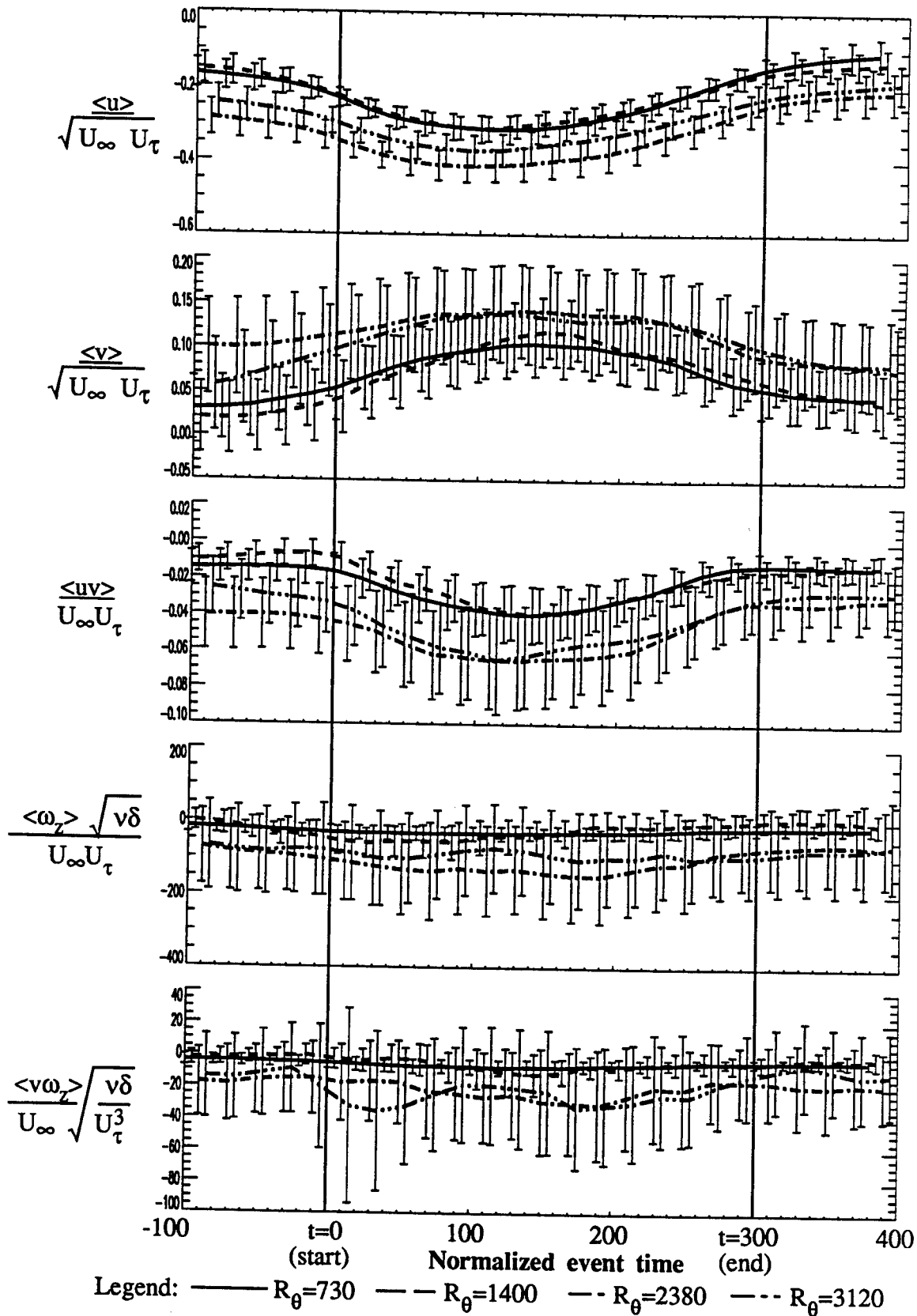
Figure 3.5.36 Mixed-scaled TERA ejection ensembles. Error bars indicate 25% of an ensemble's standard deviation about each point in time
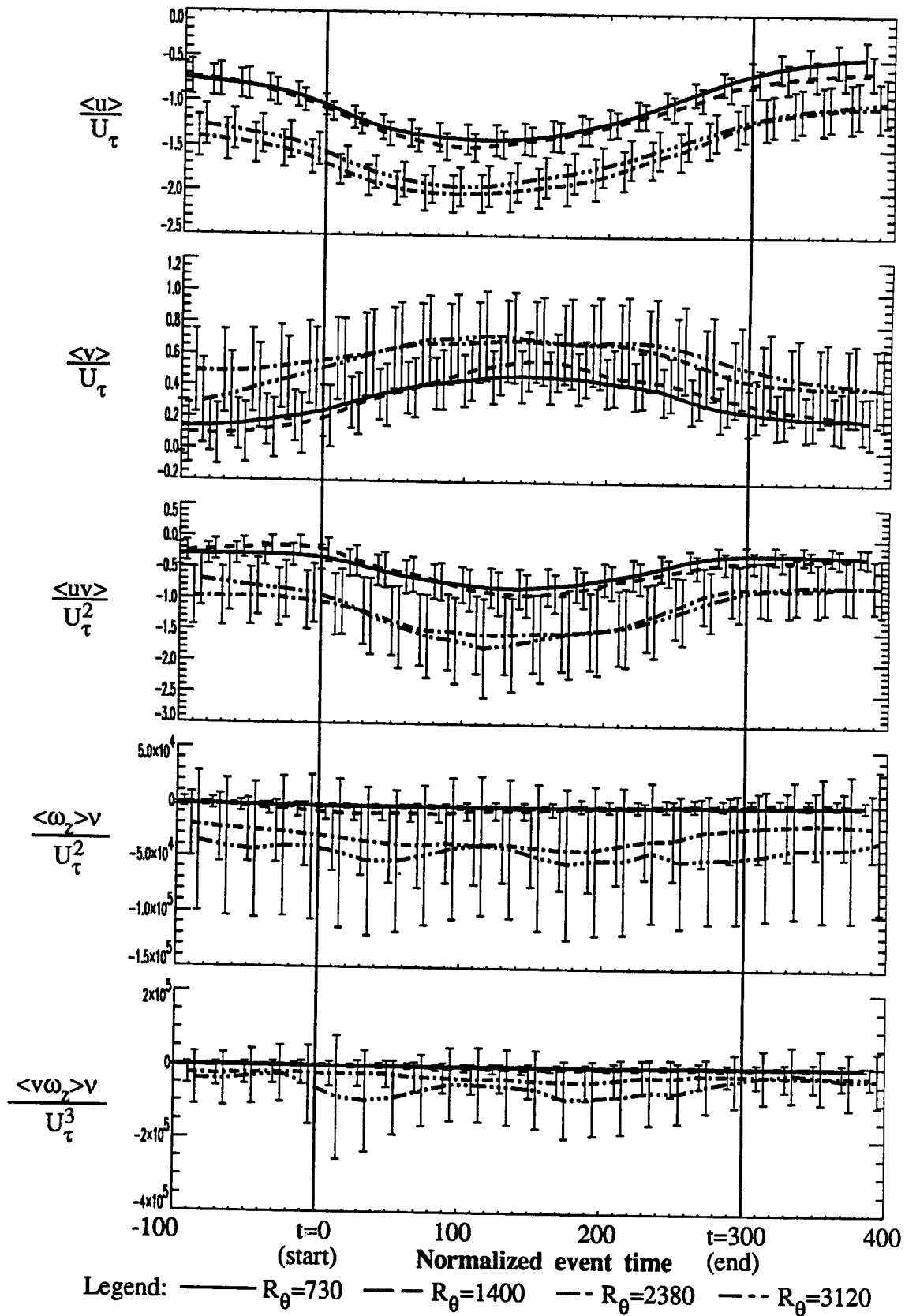
Figure 3.5.37 Inner-scaled TERA ejection ensembles. Error bars indicate 25% of an ensemble's standard deviation about each point in time
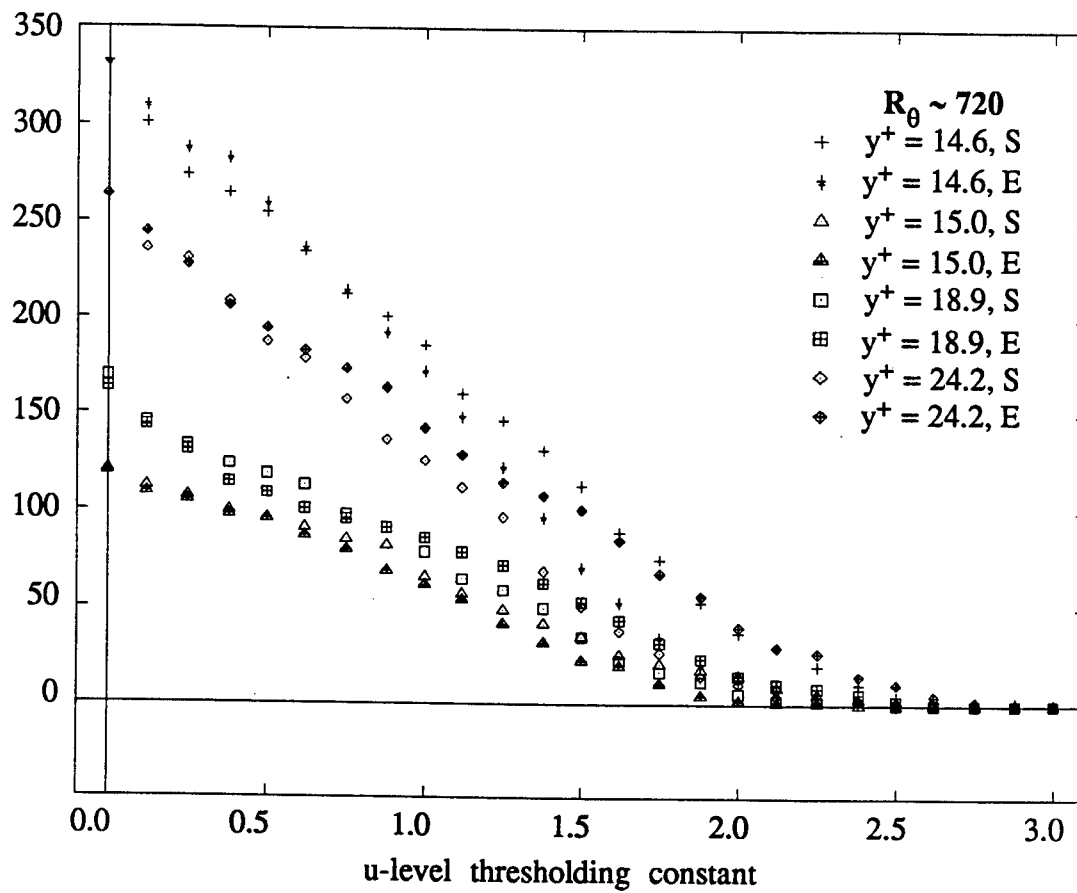
Number
of Events

Figure 3.6.1
Number of u-level Events
vs. Threshold (Inner-region data)
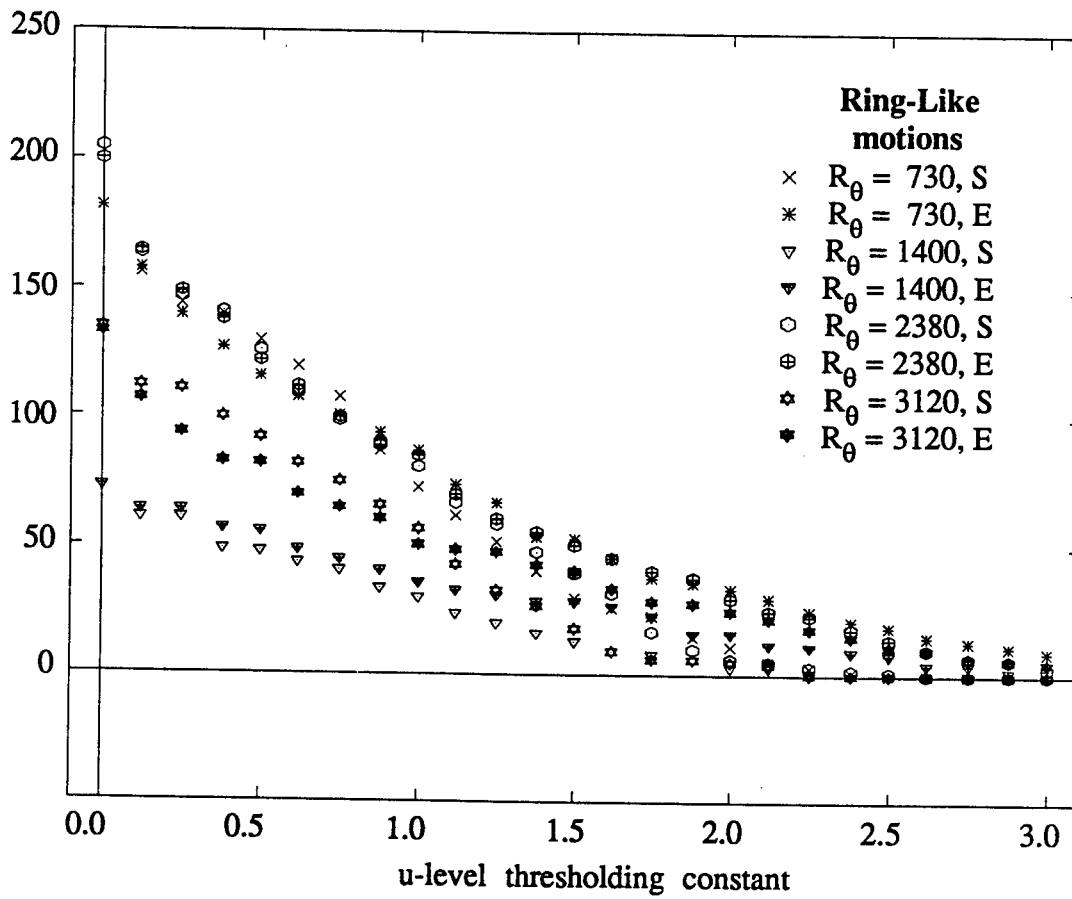
**Number
of Events**

Figure 3.6.2
Number of u-level Events
vs. Threshold (RLM data set)
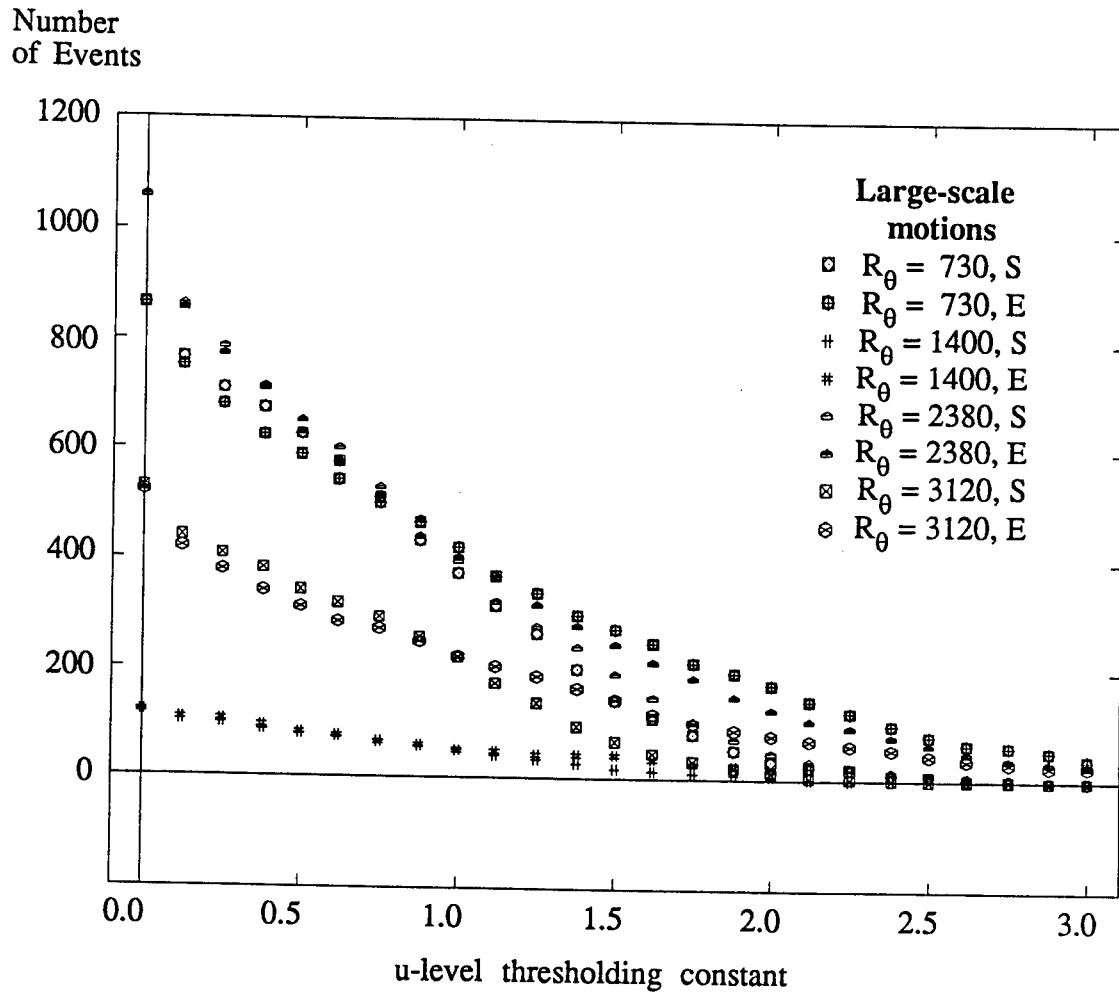
Number
of Events

Figure 3.6.3
Number of u-level Events
vs. Threshold level (LSM data set)
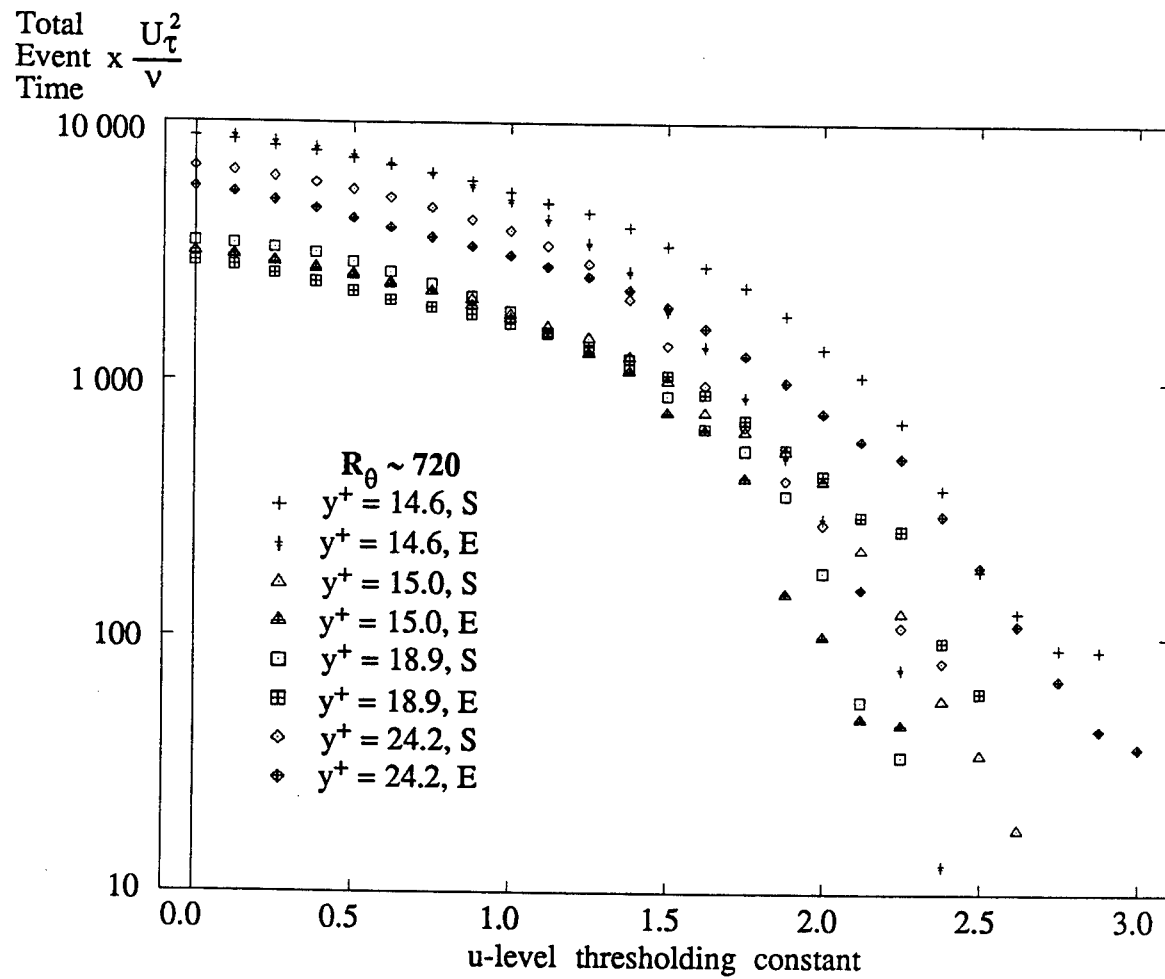
Figure 3.6.4
Inner-Scaled Total u-level Event
Time vs. Threshold
(Inner-region data)
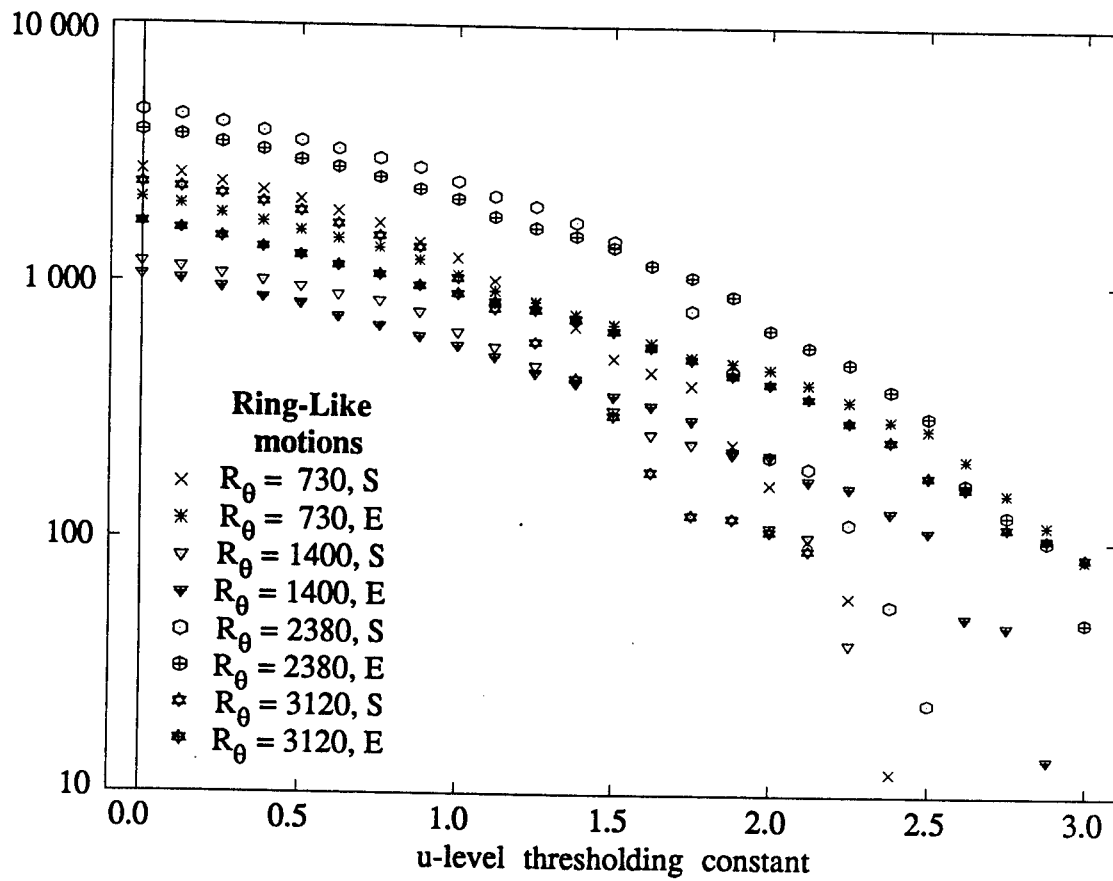
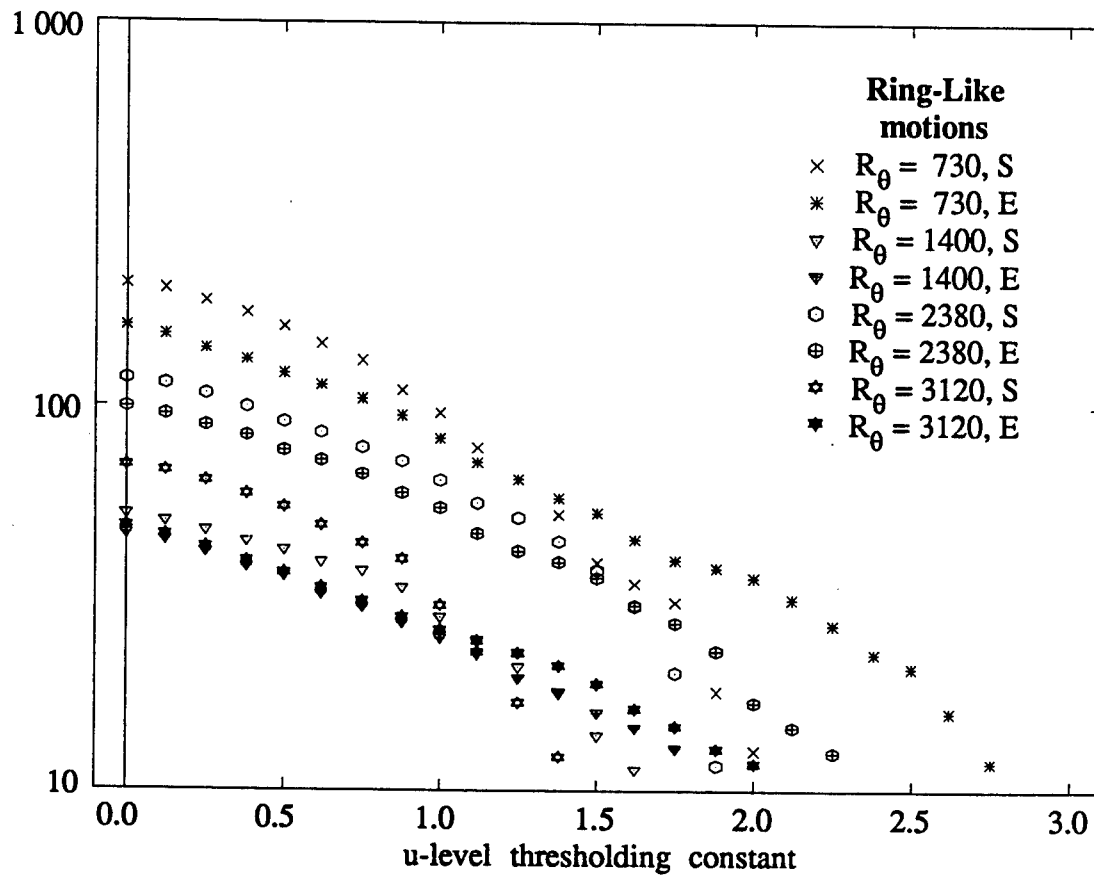**Figure 3.6.5**
Inner-Scaled Total u-level Event
Time vs. Threshold
(RLM data set)
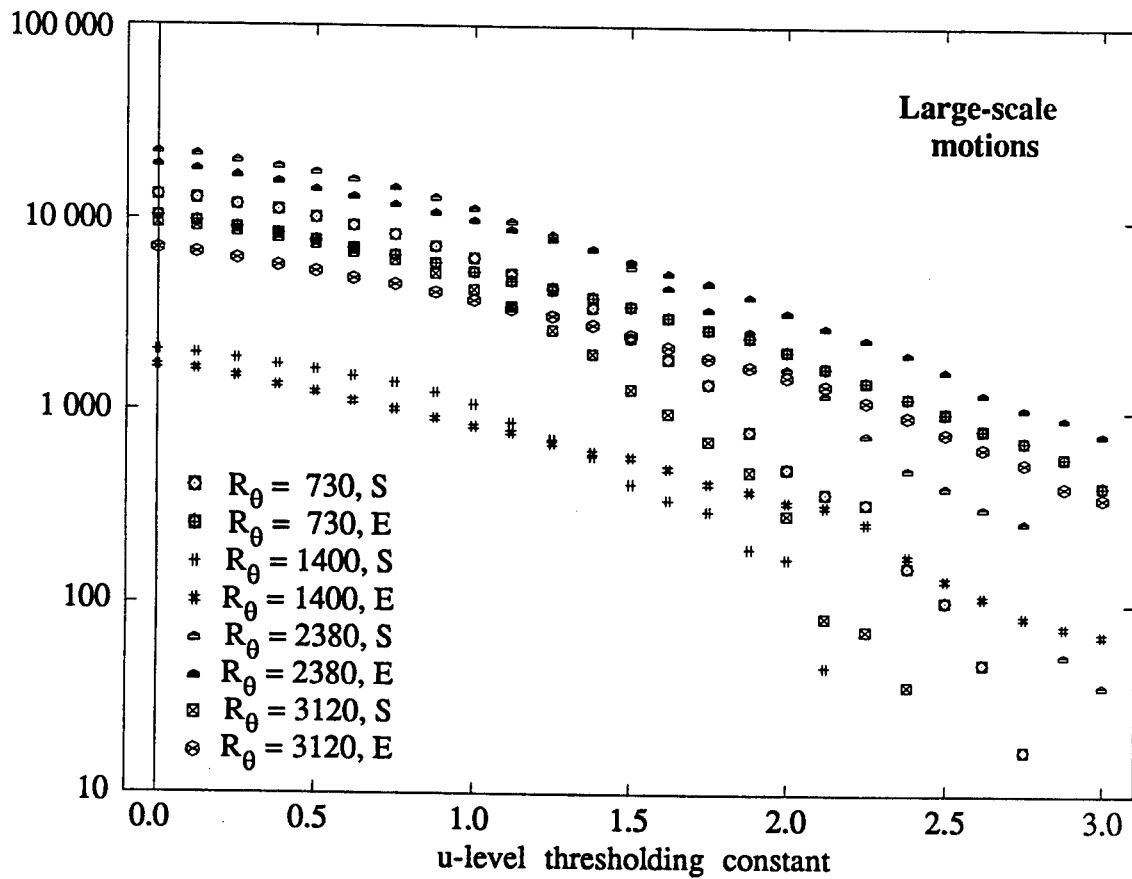
Total
Event $\times \dfrac{U_\tau^2}{\nu}$
Time

Figure 3.6.6
Inner-Scaled Total u-level
Event Time vs. Threshold
(LSM data set)

Total
Event $x\sqrt{\dfrac{U_\tau^2}{\nu}\dfrac{U_\infty}{\delta}}$
Time
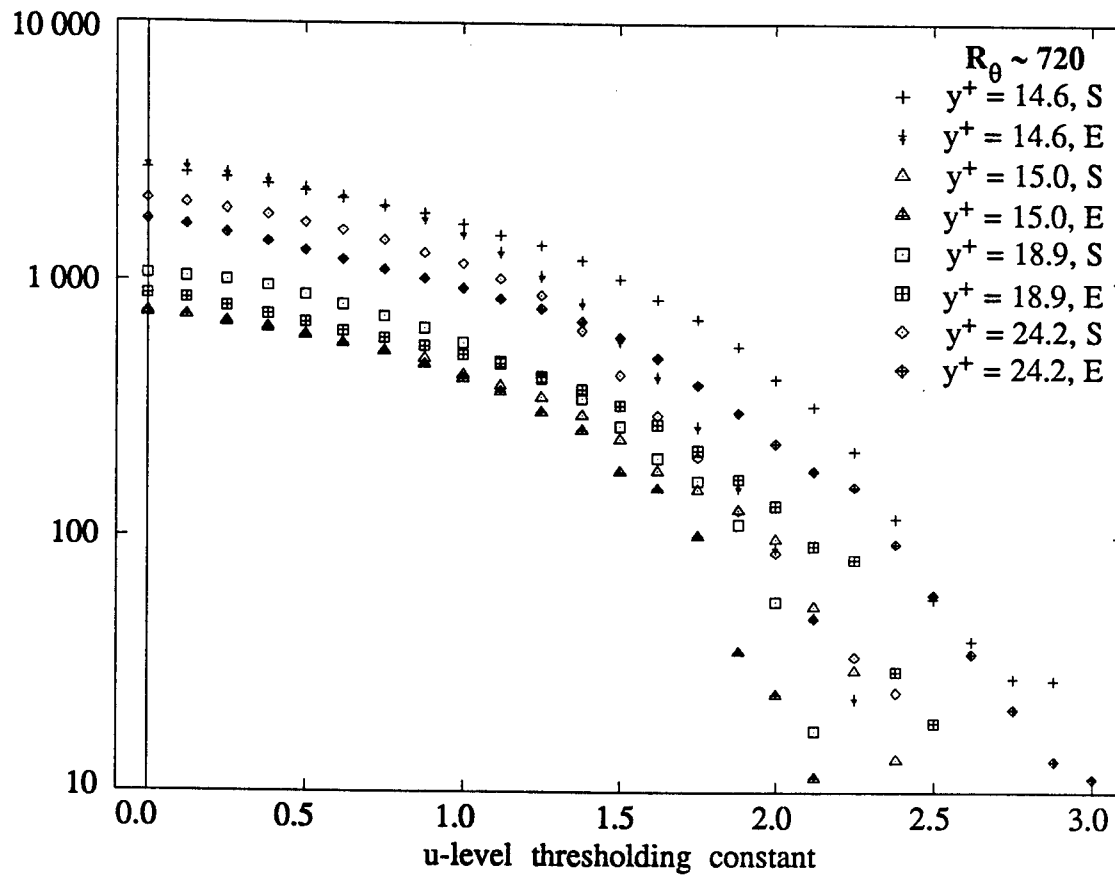
Figure 3.6.7
Total u-level Event Time
(Mixed Scaling) vs. Threshold
(Inner-region data)
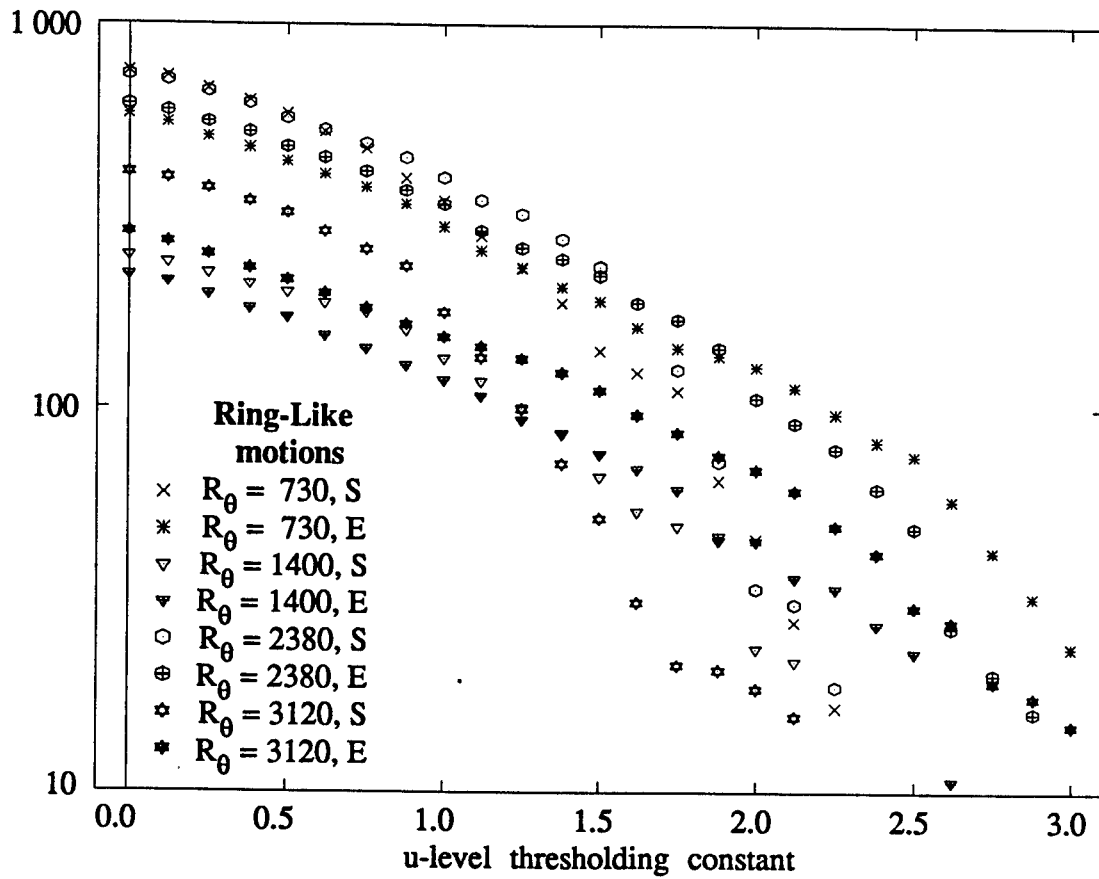
Figure 3.6.8
Total u-level Event Time
(Mixed Scaling)vs. Threshold
(RLM data set)

$$\text{Total Event Time } \quad x\sqrt{\frac{U_\tau^2}{\nu}\frac{U_\infty}{\delta}}$$
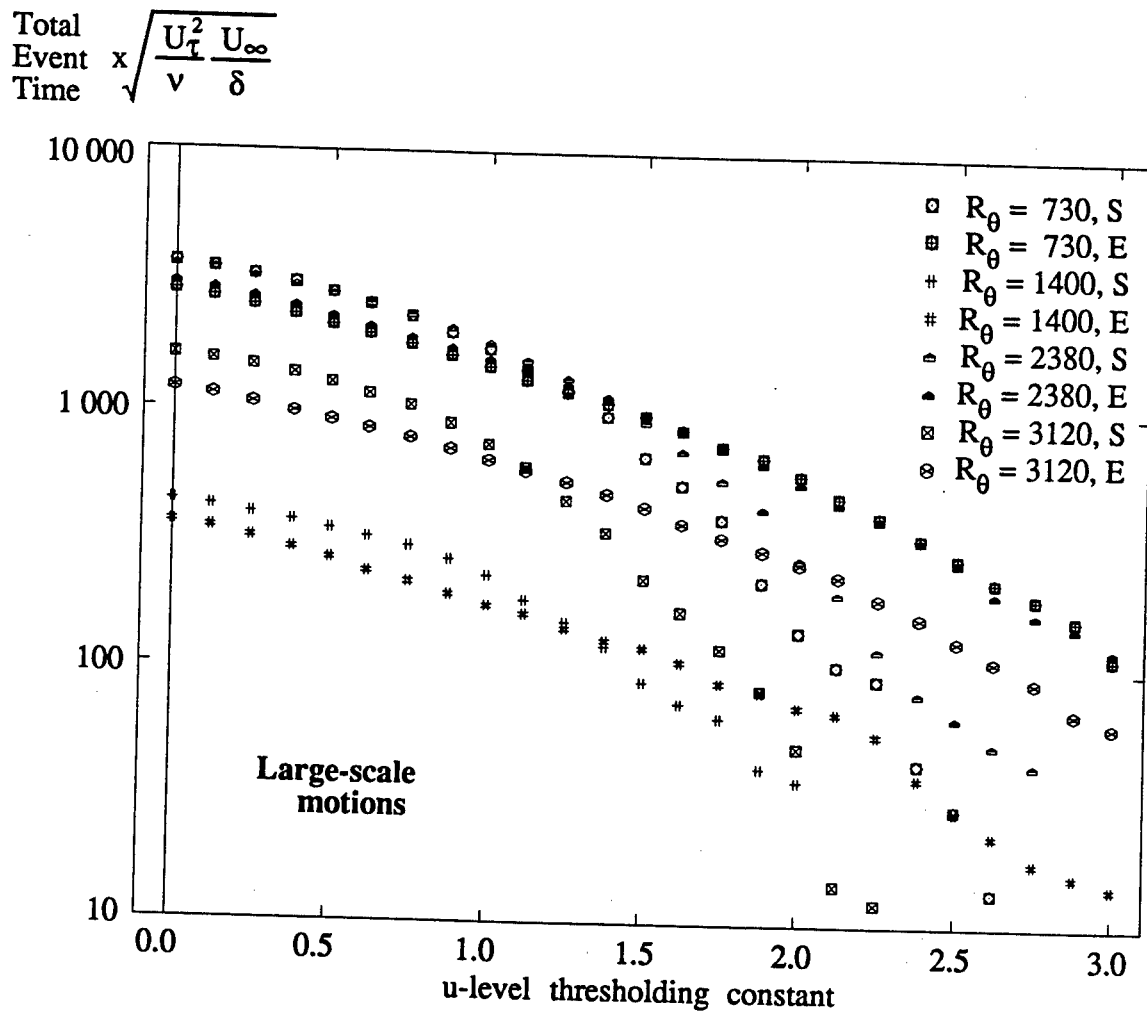
Figure 3.6.9
Total u-level Event Time
(Mixed Scaling)vs. Threshold
(LSM data set)
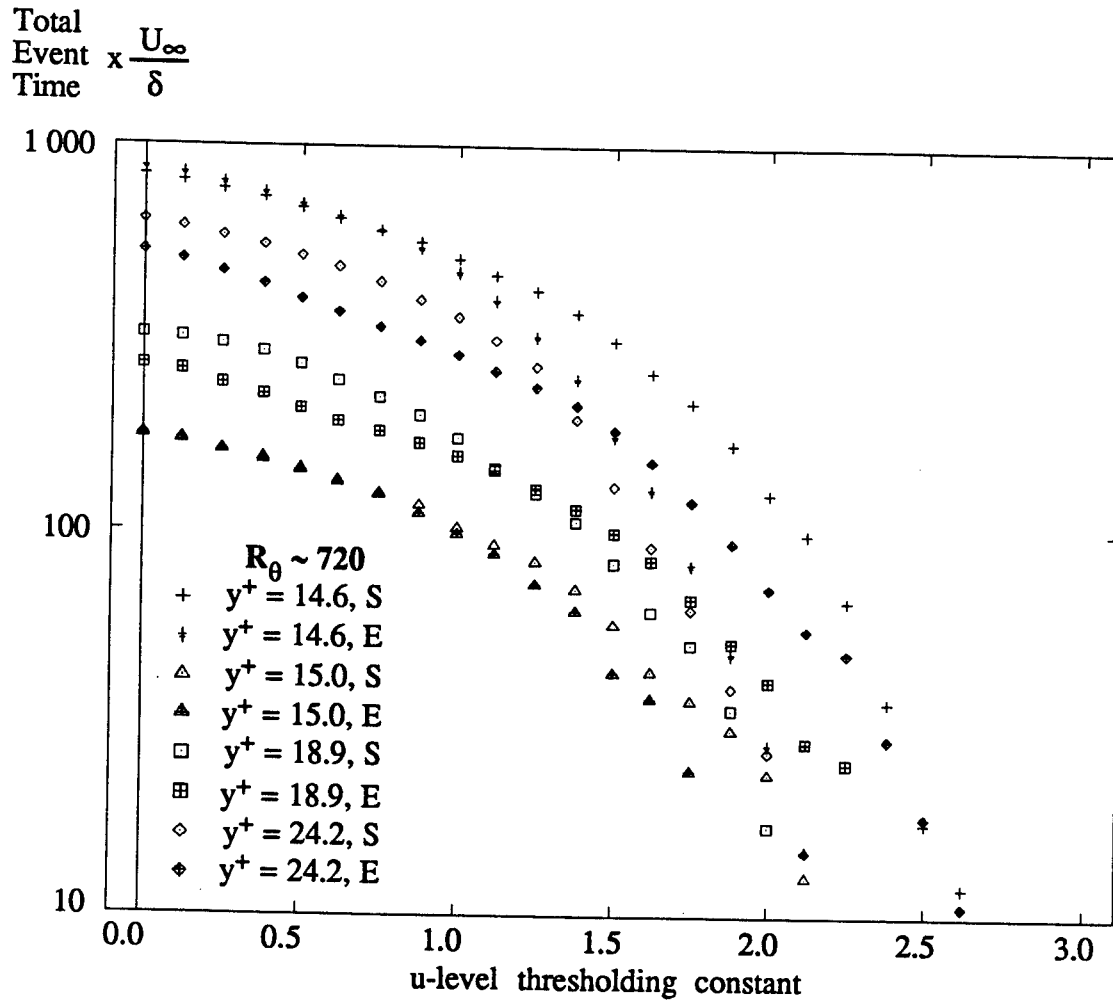
Figure 3.6.10
Outer-Scaled Total u-level
Event Time vs. Threshold
(Inner-region data)

Figure 3.6.11
Outer-Scaled Total u-level
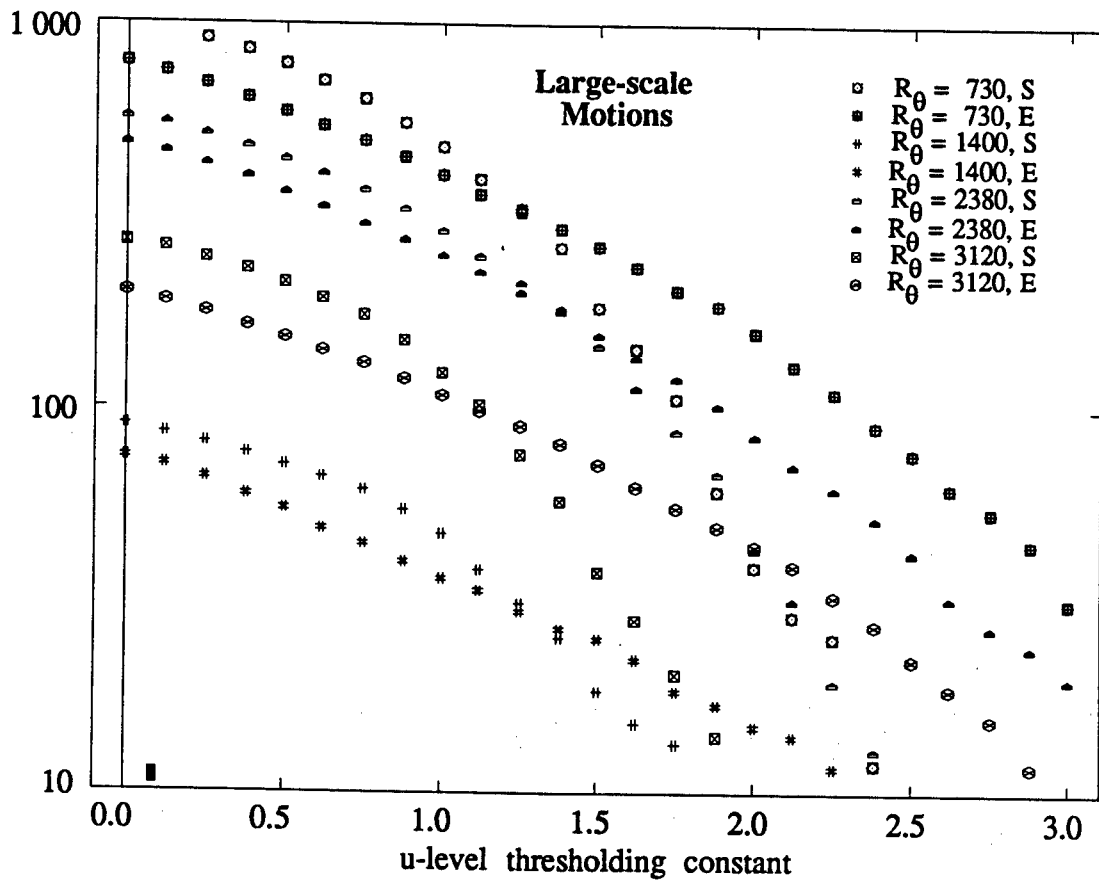Event Time vs. Threshold
(RLM data set)

Figure 3.6.12
Outer-Scaled Total u-level
Event Time vs. Threshold
(LSM data set)
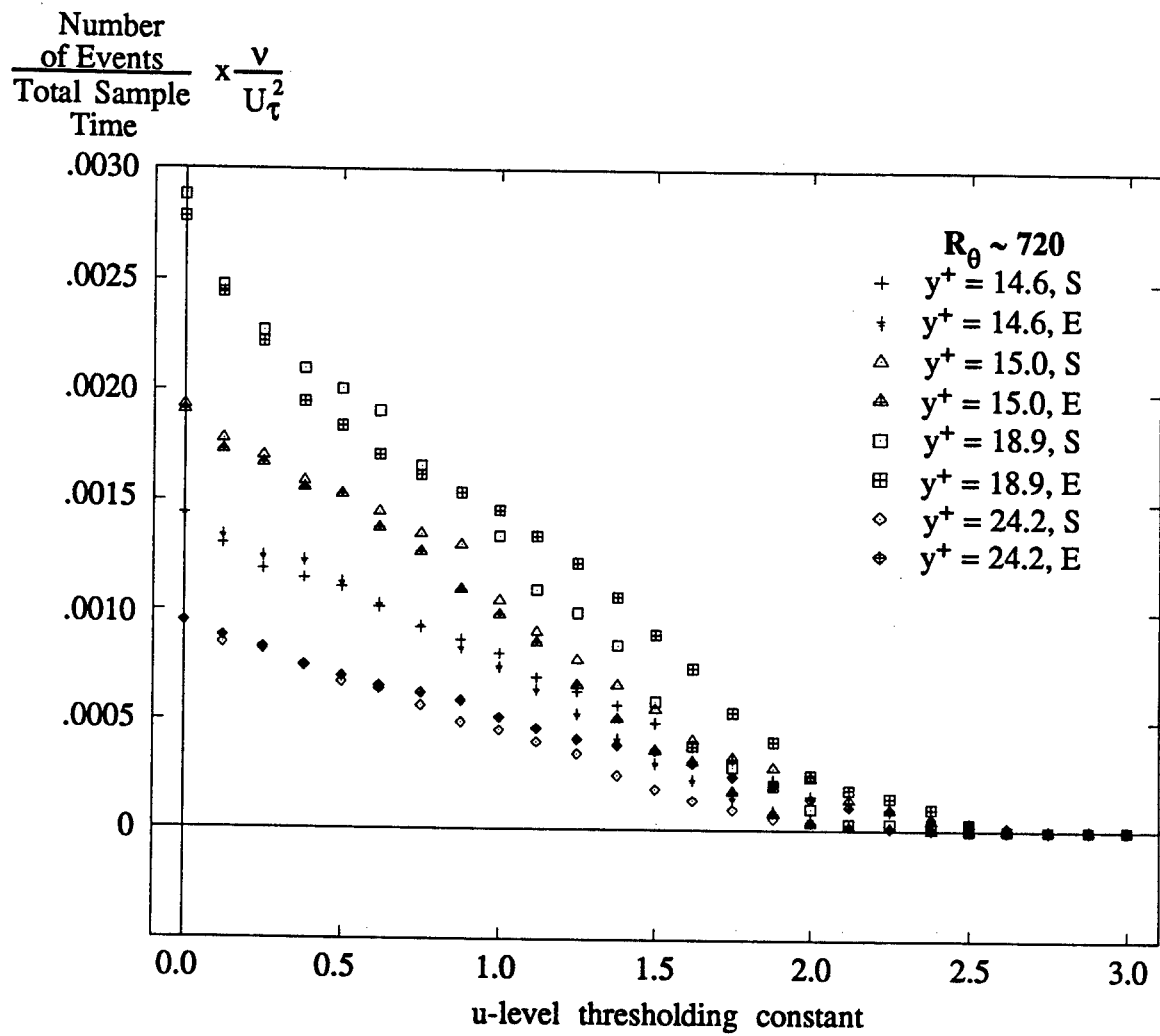
Figure 3.6.13
Inner-scaled u-level Event
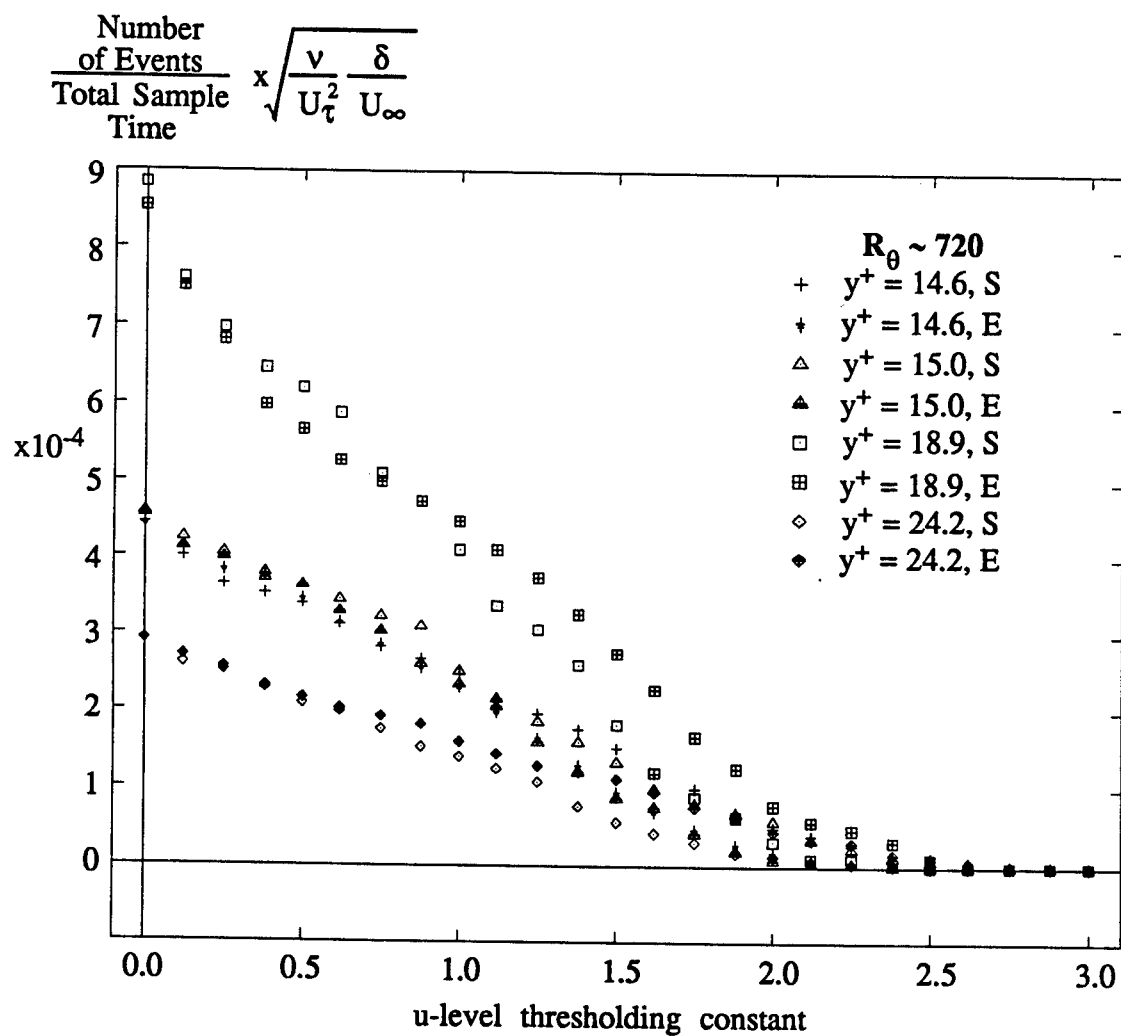frequency vs. Threshold level
(Inner-region data)

$$\frac{\text{Number}}{\text{of Events}} \quad x\sqrt{\frac{\nu}{U_\tau^2}\frac{\delta}{U_\infty}}$$
$$\frac{\text{Total Sample}}{\text{Time}}$$

Figure 3.6.14
u-level Event frequency
(Mixed-scaling) vs. Threshold
level (Inner-region data)

$$\frac{\text{Number of Events}}{\text{Total Sample Time}} \times \frac{\delta}{U_\infty}$$
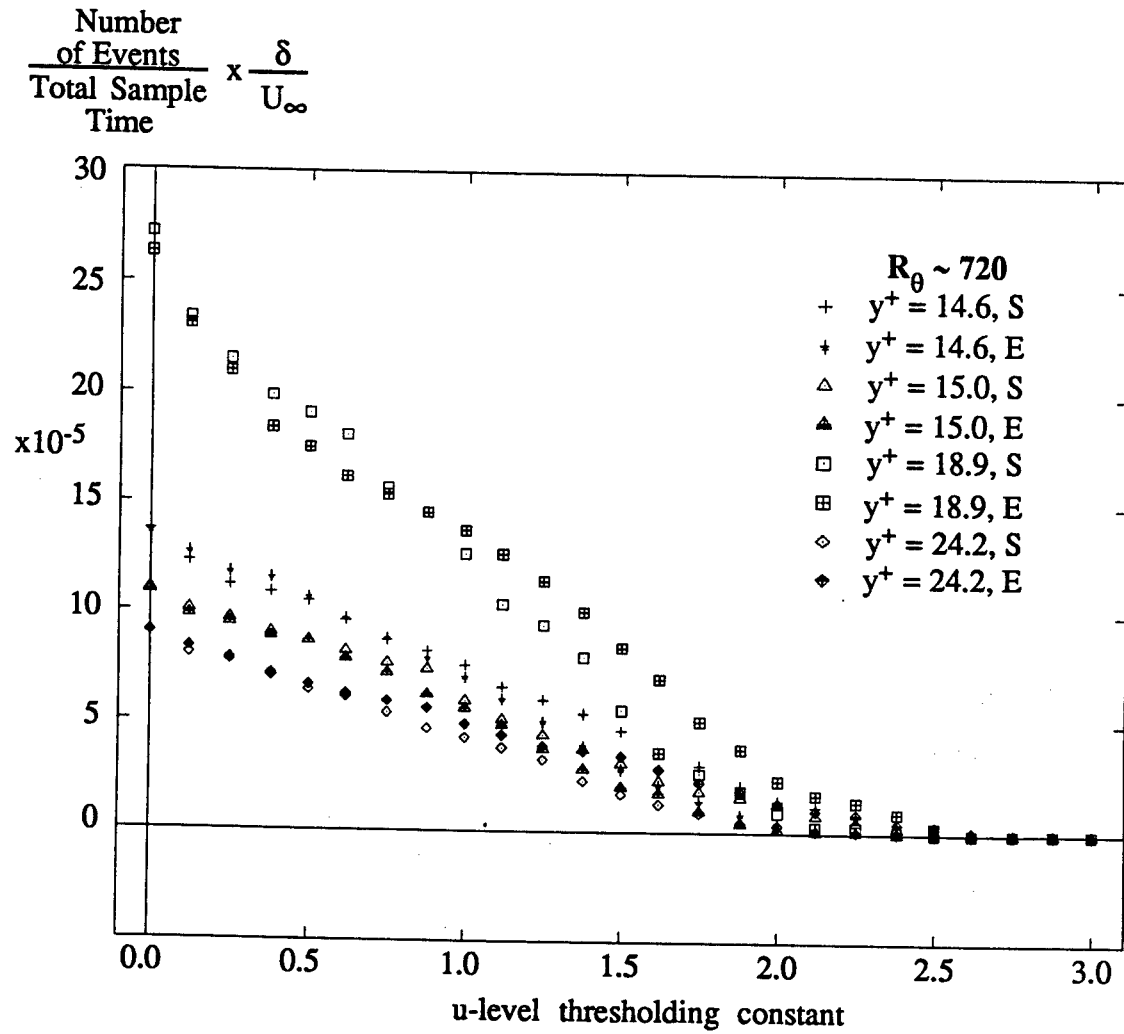
Figure 3.6.15
Outer-scaled u-level Event
frequency vs. Threshold level
(Inner-region data)

$$\frac{\text{Number}}{\text{of Events}} \times \frac{\nu}{U_\tau^2}$$

Outer-Region motions

⊡ $R_\theta = 730$, S
⊞ $R_\theta = 730$, E
╫ $R_\theta = 1400$, S
✳ $R_\theta = 1400$, E
◓ $R_\theta = 2380$, S
◆ $R_\theta = 2380$, E
⊠ $R_\theta = 3120$, S
⊗ $R_\theta = 3120$, E

u-level thresholding constant
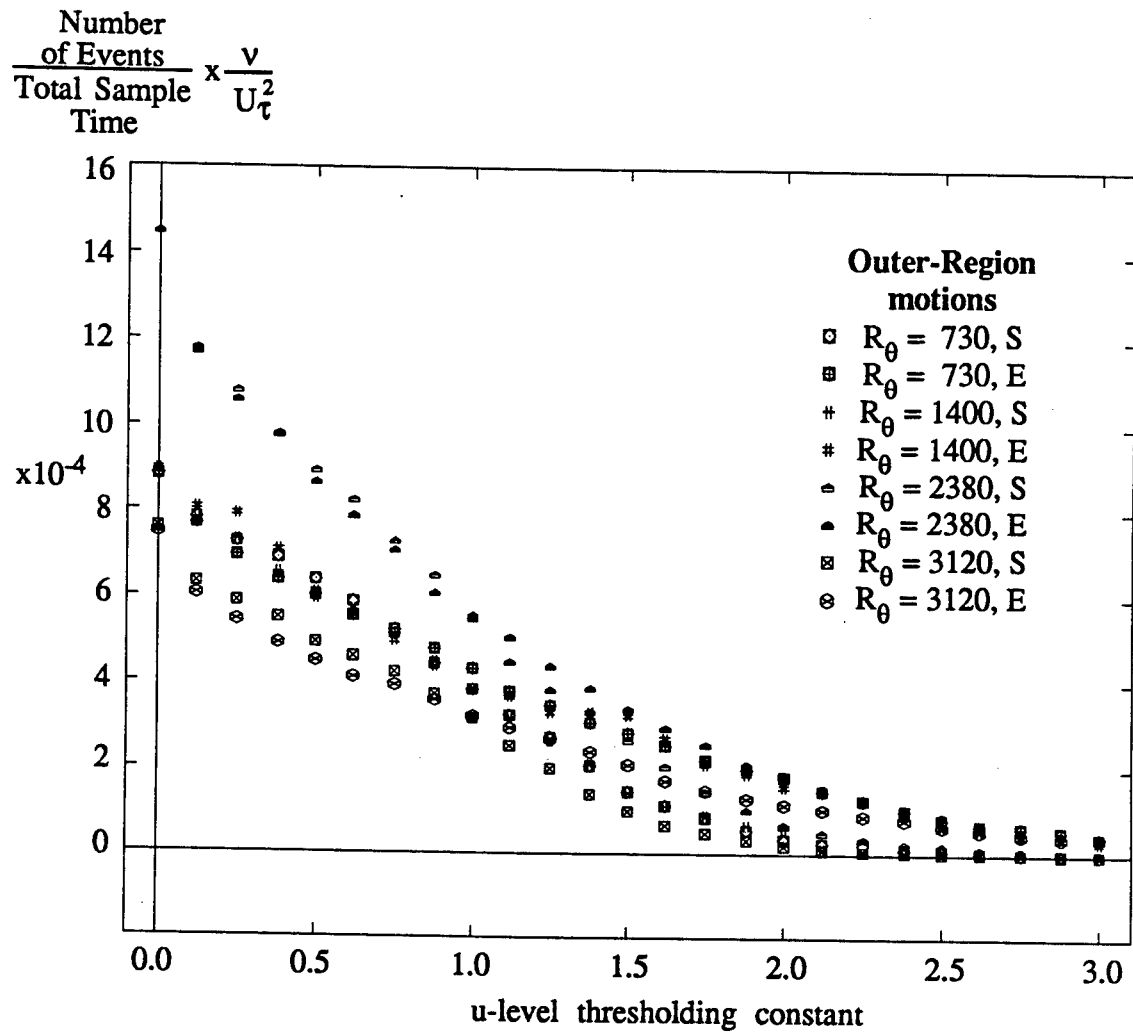
Figure 3.6.16
Inner-scaled u-level Event
frequency vs. Threshold level
(LSM data set)

$$\frac{\frac{\text{Number}}{\text{of Events}}}{\substack{\text{Total Sample} \\ \text{Time}}} \times \sqrt{\frac{\nu}{U_\tau^2} \frac{\delta}{U_\infty}}$$
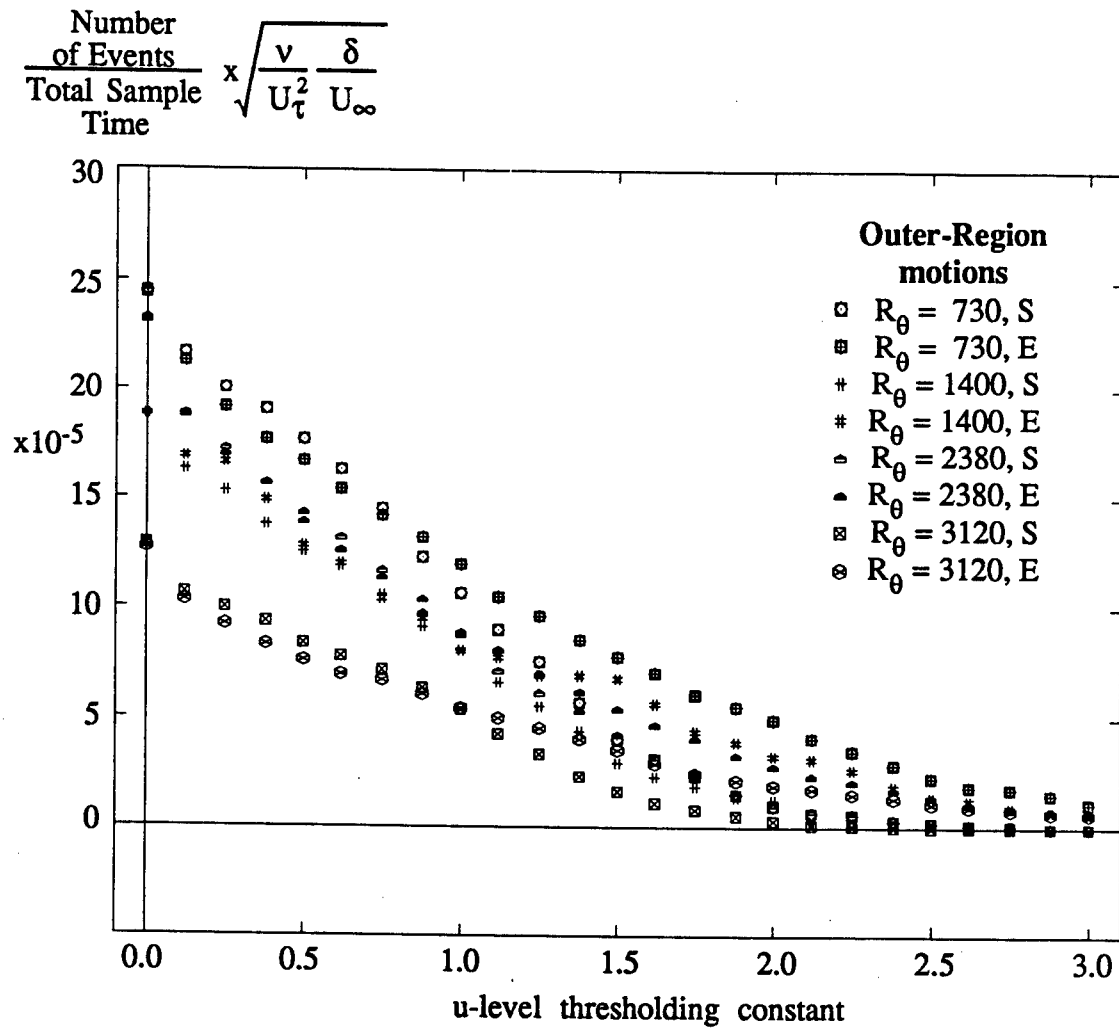
Figure 3.6.17
u-level Event frequency
(Mixed-scaling) vs. Threshold
level (LSM data set)

$$\frac{\text{Number}}{\text{of Events}}{\text{Total Sample}} \times \frac{\delta}{U_\infty}$$
$$\text{Time}$$
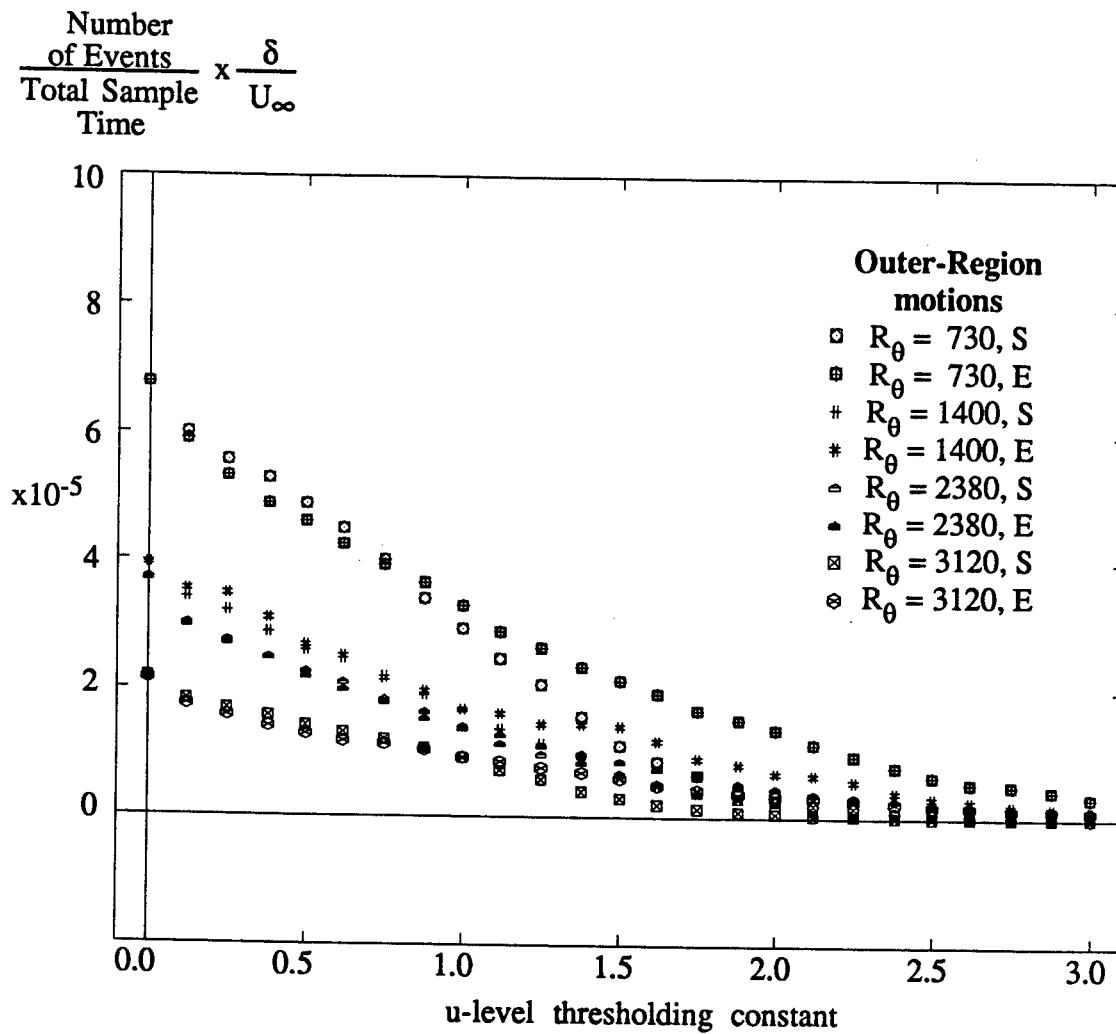
Figure 3.6.18
Outer-scaled u-level Event
frequency vs. Threshold level
(LSM data set)

Total
Event Time $\times \dfrac{U_\infty U_\tau}{\nu}$
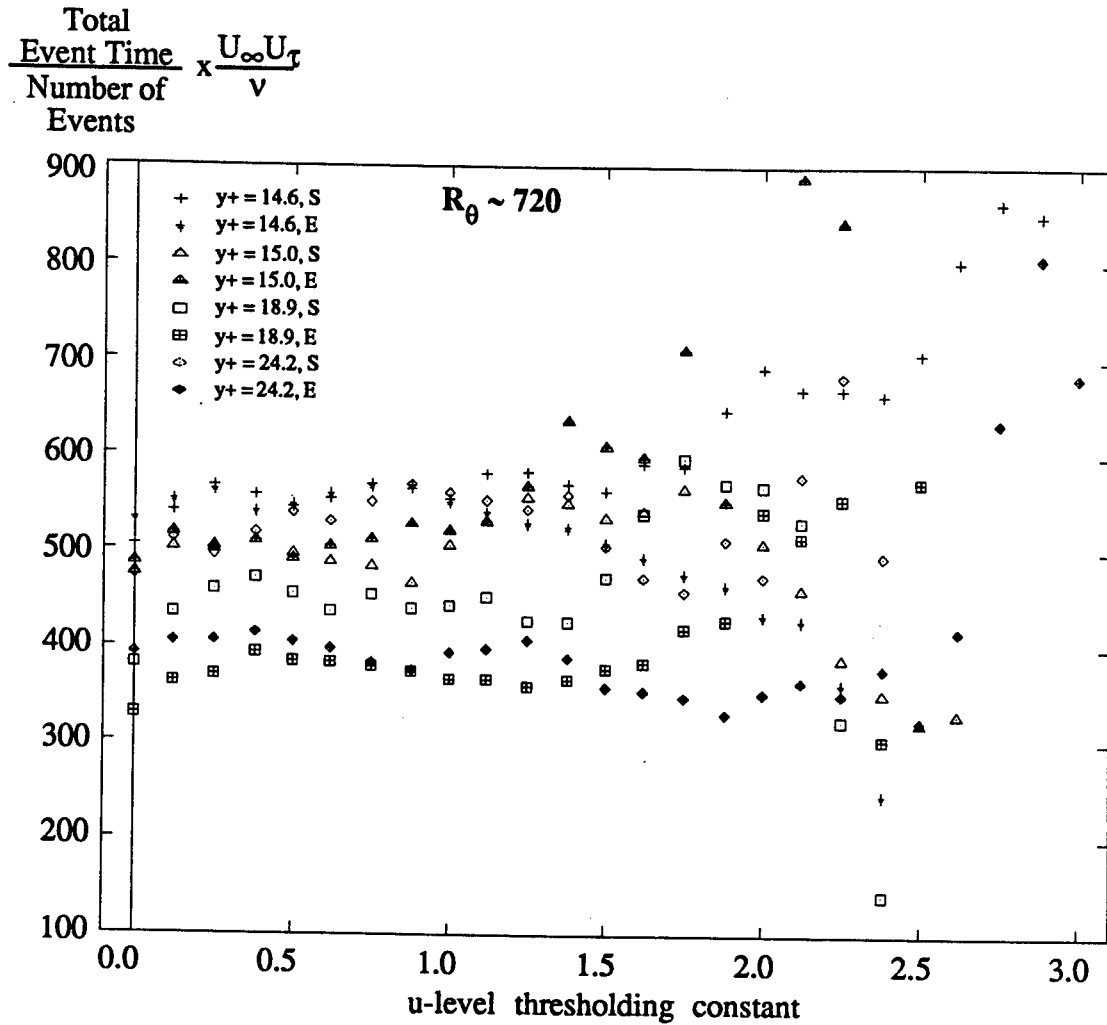Number of
Events

Figure 3.6.19
Inner-Scaled Average u-level
Event Length vs. Threshold
(Inner-region data set)
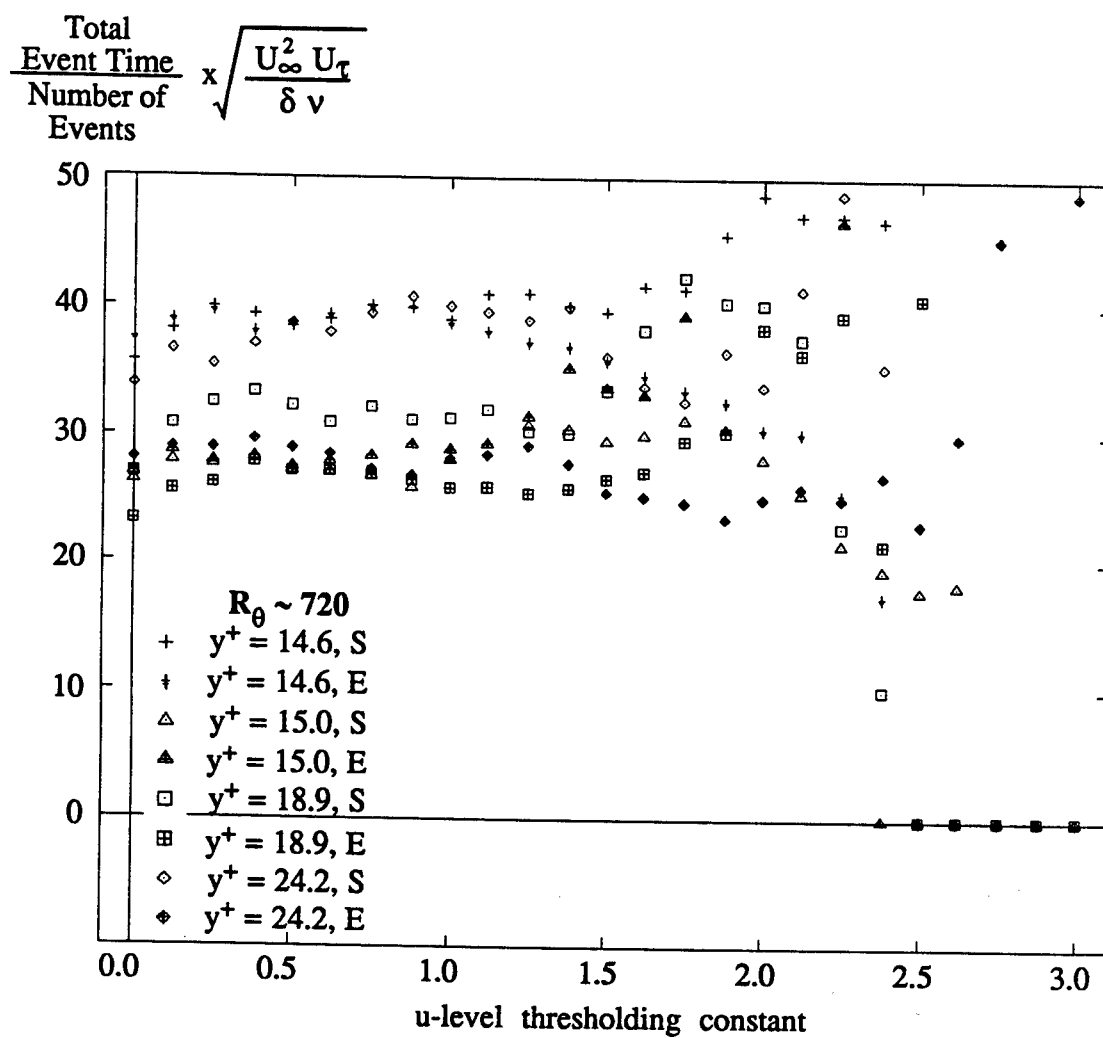
Figure 3.6.20
Average u-level Event Length
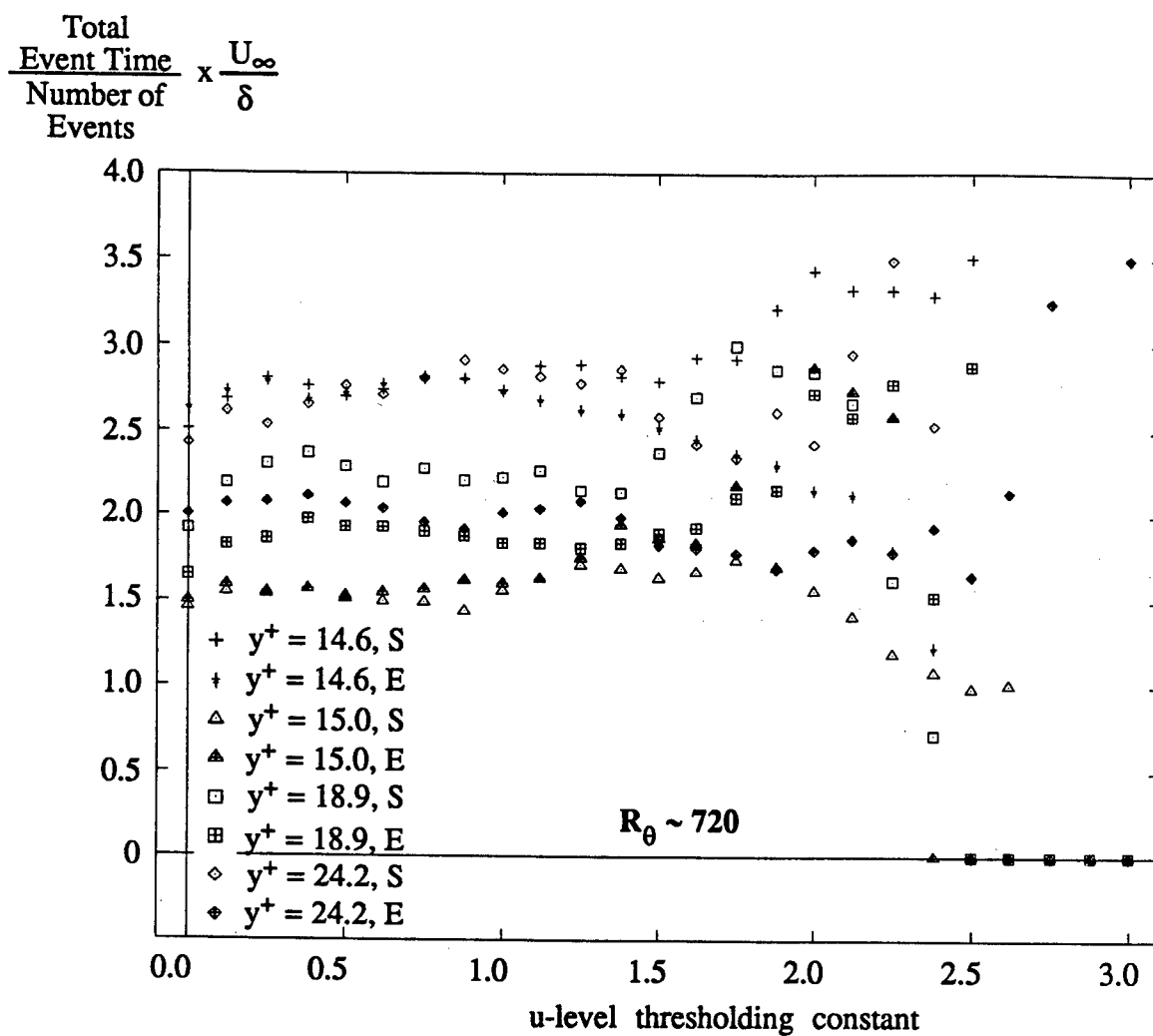(Mixed Scaling) vs. Threshold
(Inner-region data)

Total
$\dfrac{\text{Event Time}}{\text{Number of Events}} \times \dfrac{U_\infty}{\delta}$

$R_\theta \sim 720$

+ $y^+ = 14.6$, S
✝ $y^+ = 14.6$, E
△ $y^+ = 15.0$, S
▲ $y^+ = 15.0$, E
□ $y^+ = 18.9$, S
⊞ $y^+ = 18.9$, E
◇ $y^+ = 24.2$, S
◈ $y^+ = 24.2$, E

u-level thresholding constant

Figure 3.6.21
Outer-Scaled Average u-level
Event Length vs. Threshold
(Inner-region data)

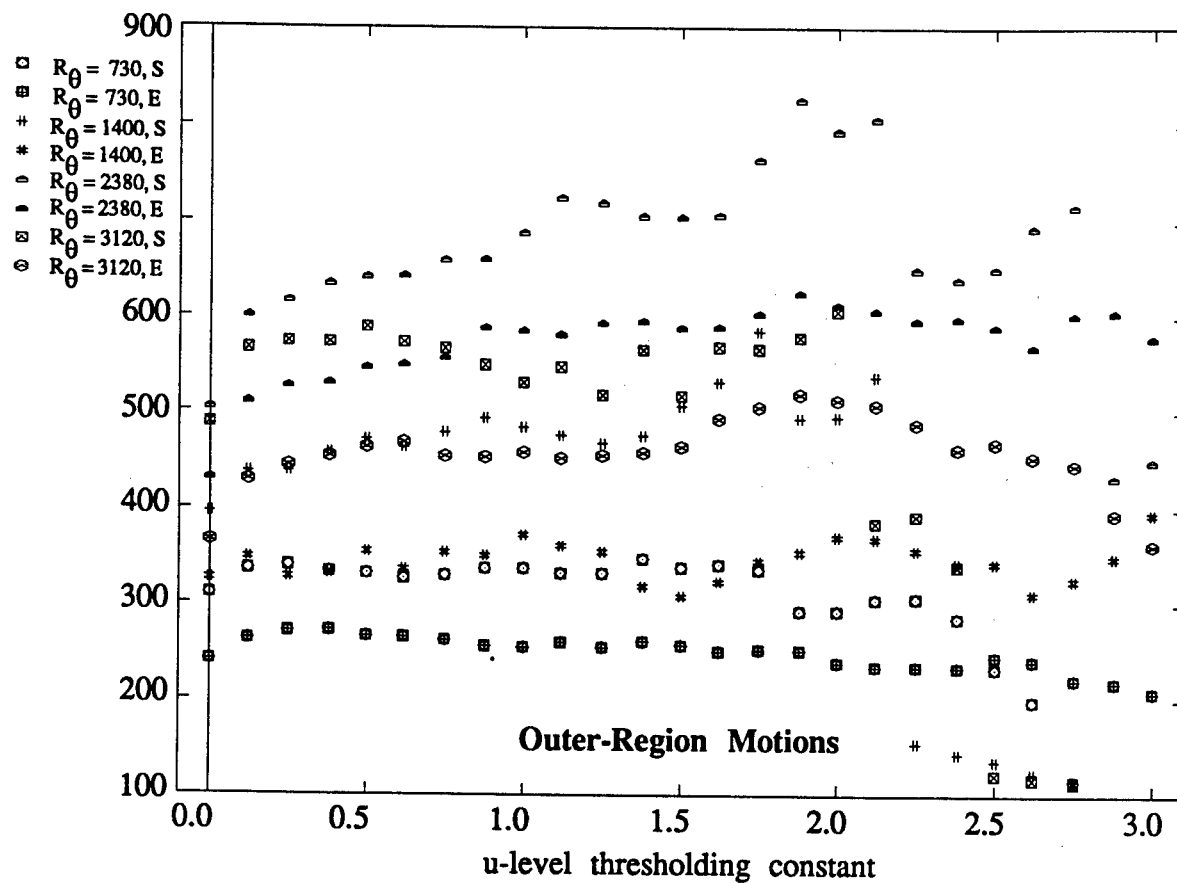$$\frac{\text{Total}}{\text{Number of}} \times \frac{U_\infty U_\tau}{\nu}$$
Event Time

Number of
Events

Figure 3.6.22
Inner-Scaled Average u-level
Event Length vs. Threshold
(LSM data set)

$$\frac{\text{Total Event Time}}{\text{Number of Events}} \times \sqrt{\frac{U_\infty^2\, U_\tau}{\delta\, \nu}}$$
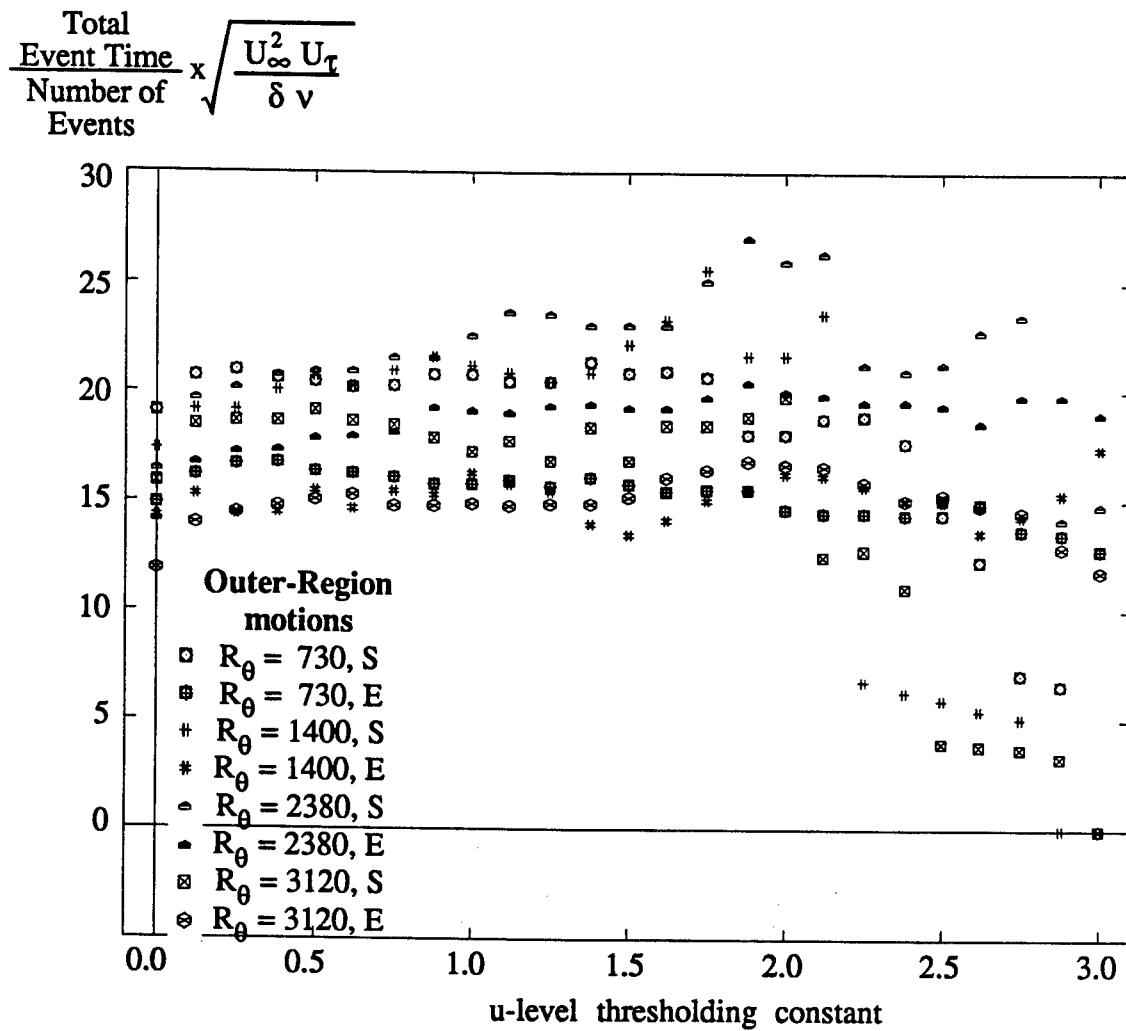
Figure 3..6.23
Average u-level Event
Length (Mixed Scaling)
vs. Threshold (LSM data set)

$$\frac{\text{Total}}{\substack{\text{Event Time} \\ \text{Number of} \\ \text{Events}}} \times \frac{U_\infty}{\delta}$$

Legend:

□ $R_\theta = 730, S$
⊞ $R_\theta = 730, E$
╫ $R_\theta = 1400, S$
✳ $R_\theta = 1400, E$
◠ $R_\theta = 2380, S$
▲ $R_\theta = 2380, E$
⊠ $R_\theta = 3120, S$
⊘ $R_\theta = 3120, E$

Outer-Region motions

u-level thresholding constant
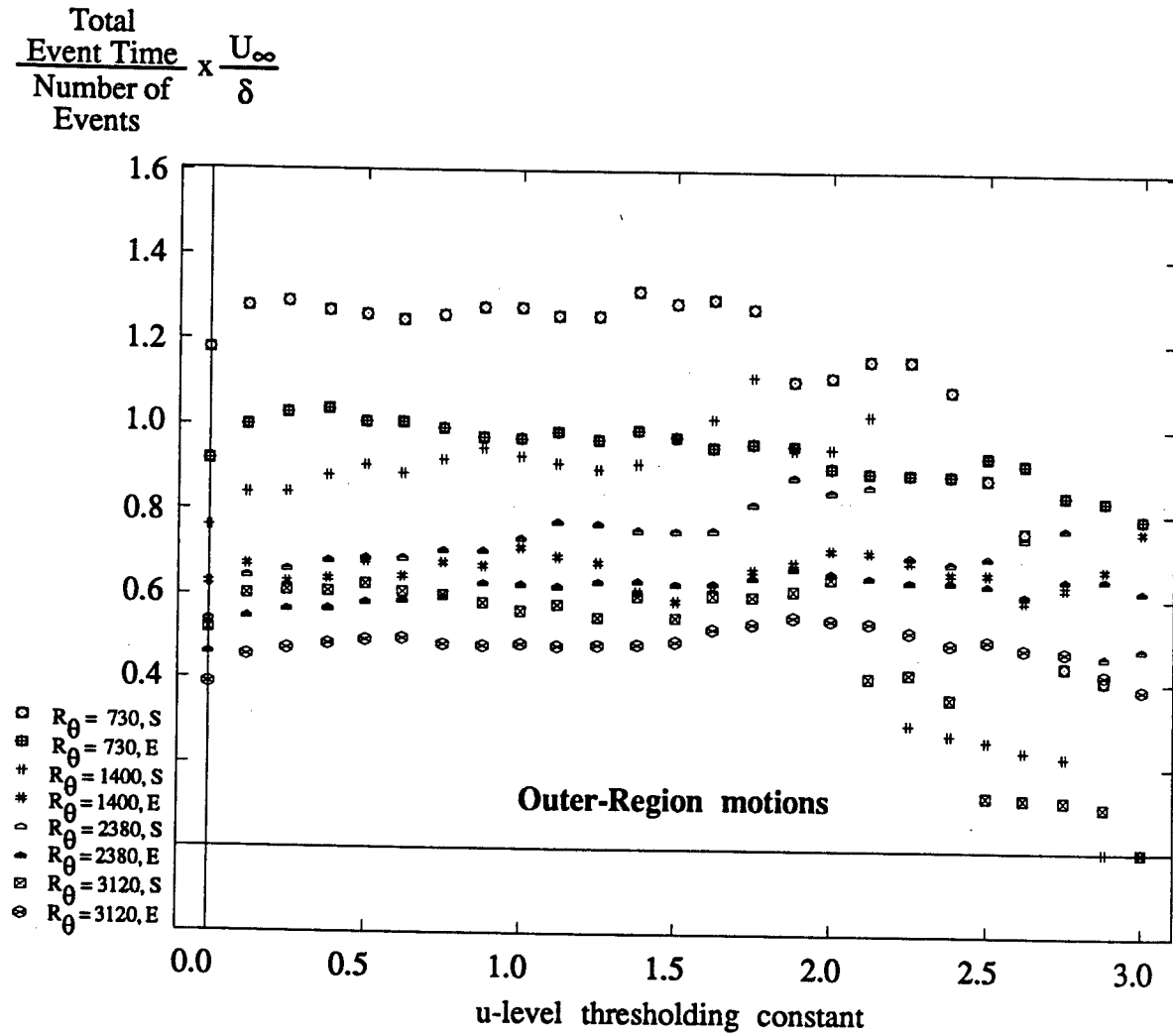
Figure 3..6.24
Outer-Scaled Average u-level
Event Length vs. Threshold
(LSM data set)

$$\frac{\text{Total}}{\frac{\text{Event Time}}{\text{Number of}}} \times \frac{U_\infty U_\tau}{\nu \, y^+}$$
Events

Legend:
- $+$ $y+ = 14.6, S$
- ┿ $y+ = 14.6, E$
- $\triangle$ $y+ = 15.0, S$
- $\blacktriangle$ $y+ = 15.0, E$
- $\square$ $y+ = 18.9, S$
- ⊞ $y+ = 18.9, E$
- $\diamond$ $y+ = 24.2, S$
- $\blacklozenge$ $y+ = 24.2, E$

$R_\theta \sim 720$

u-level thresholding constant
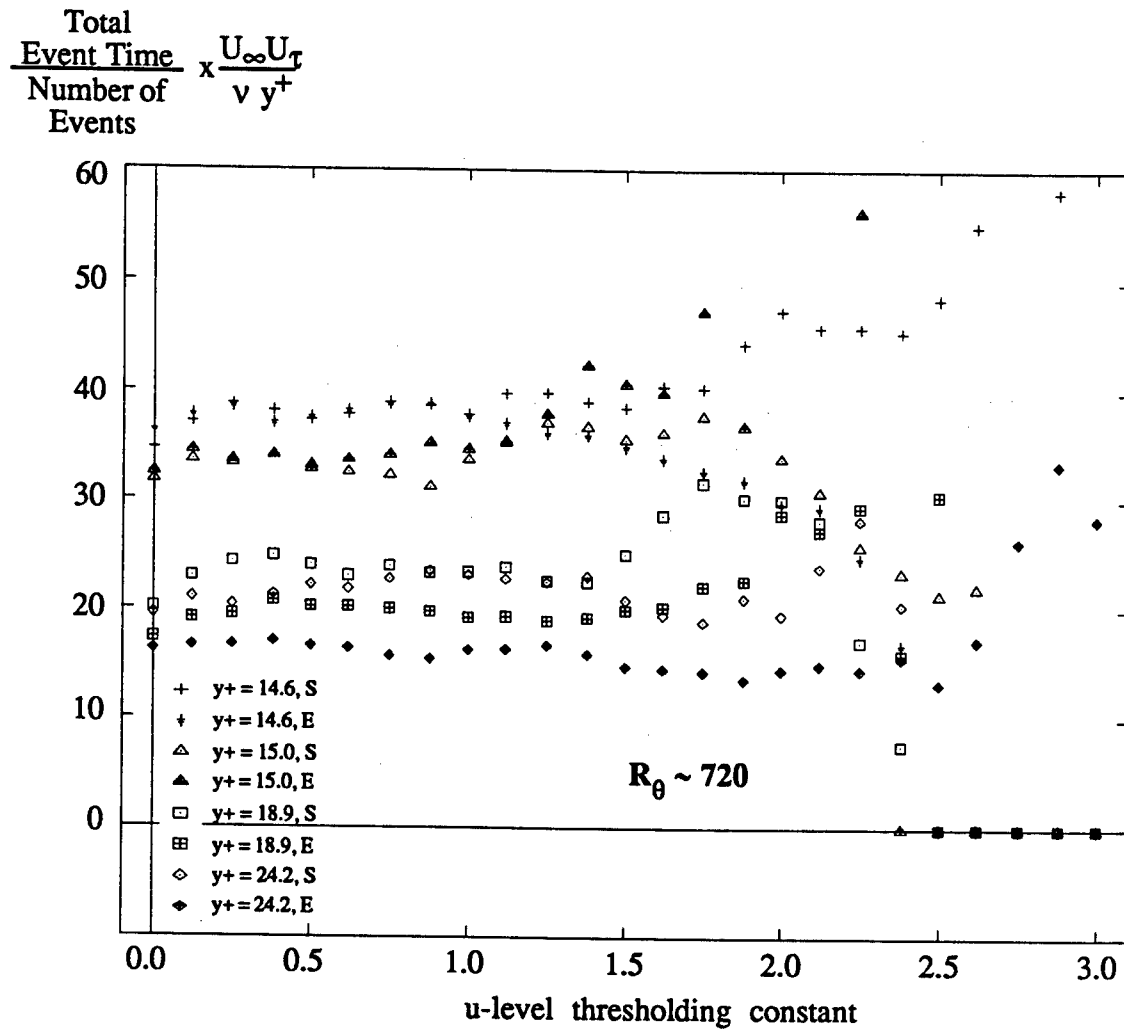
Figure 3.6.25
Inner-Scaled Average u-level
Event Length / y^+ vs. Threshold
(Inner-region data)

$\int uv<0 / \int uv<0$
during   all times
events
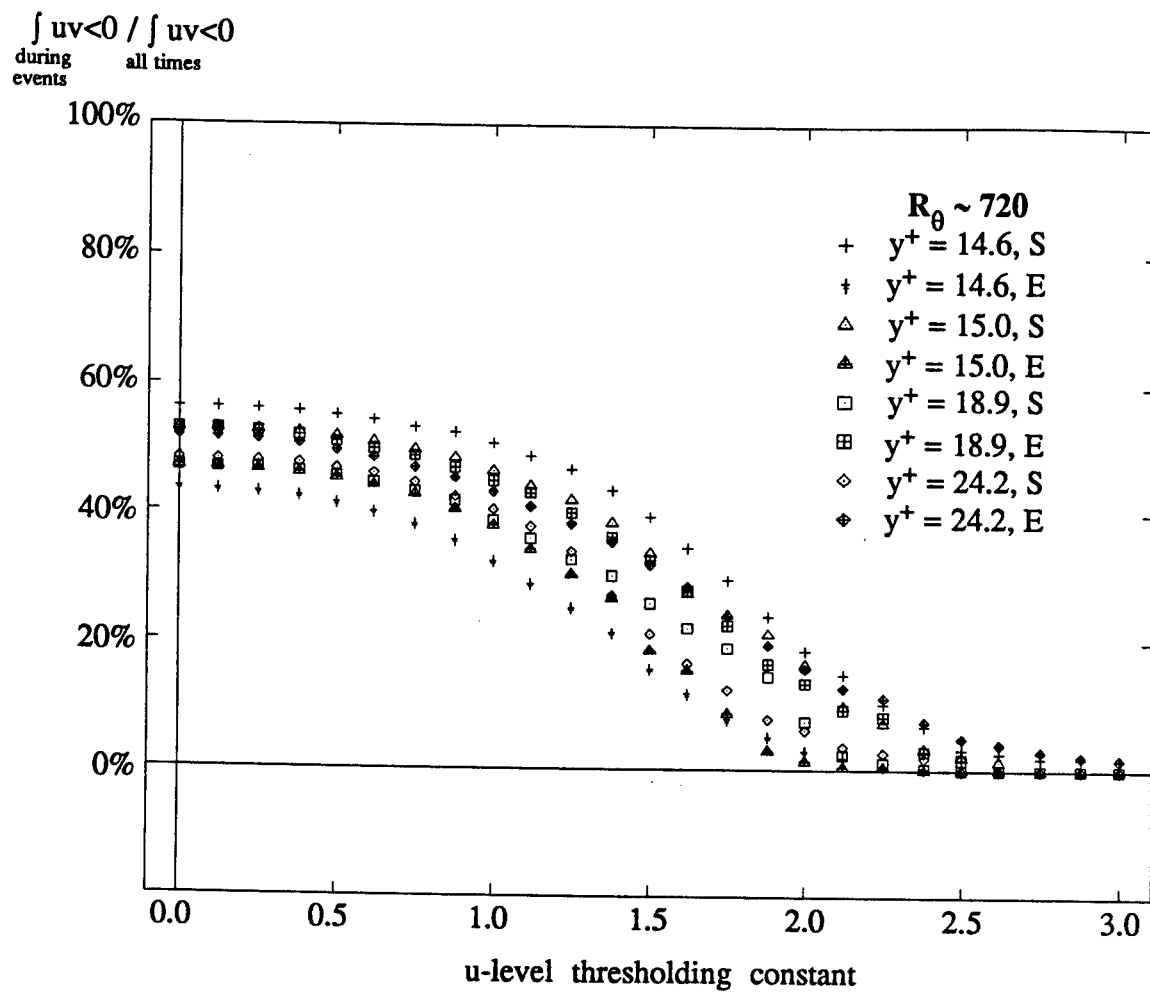
Figure 3.6.26
Percent Reynolds Stress "captured" during
u-level events vs. Threshold
(Inner-region data)

$$\int uv<0 \, / \int uv<0$$
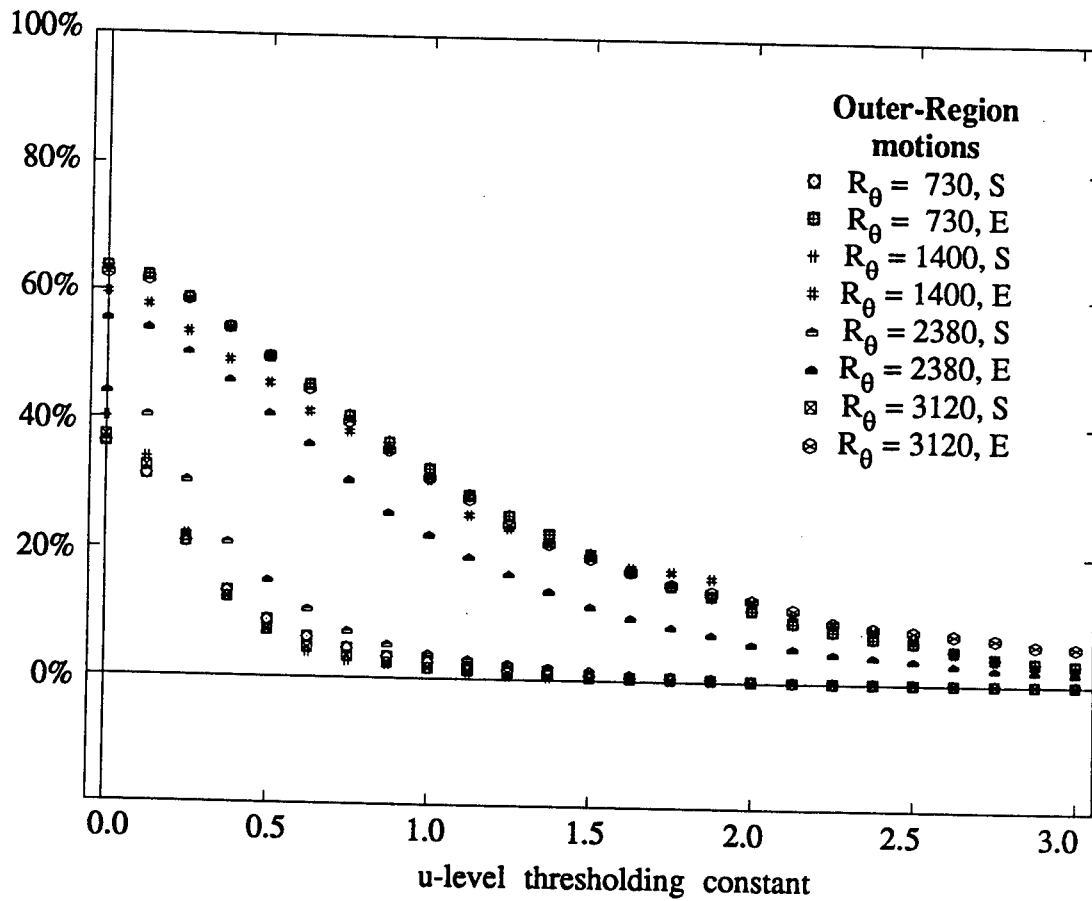during   all times
events

Figure 3.6.27
Percent Reynolds Stress "captured" during
u-level events vs. Threshold
(LSM data set)
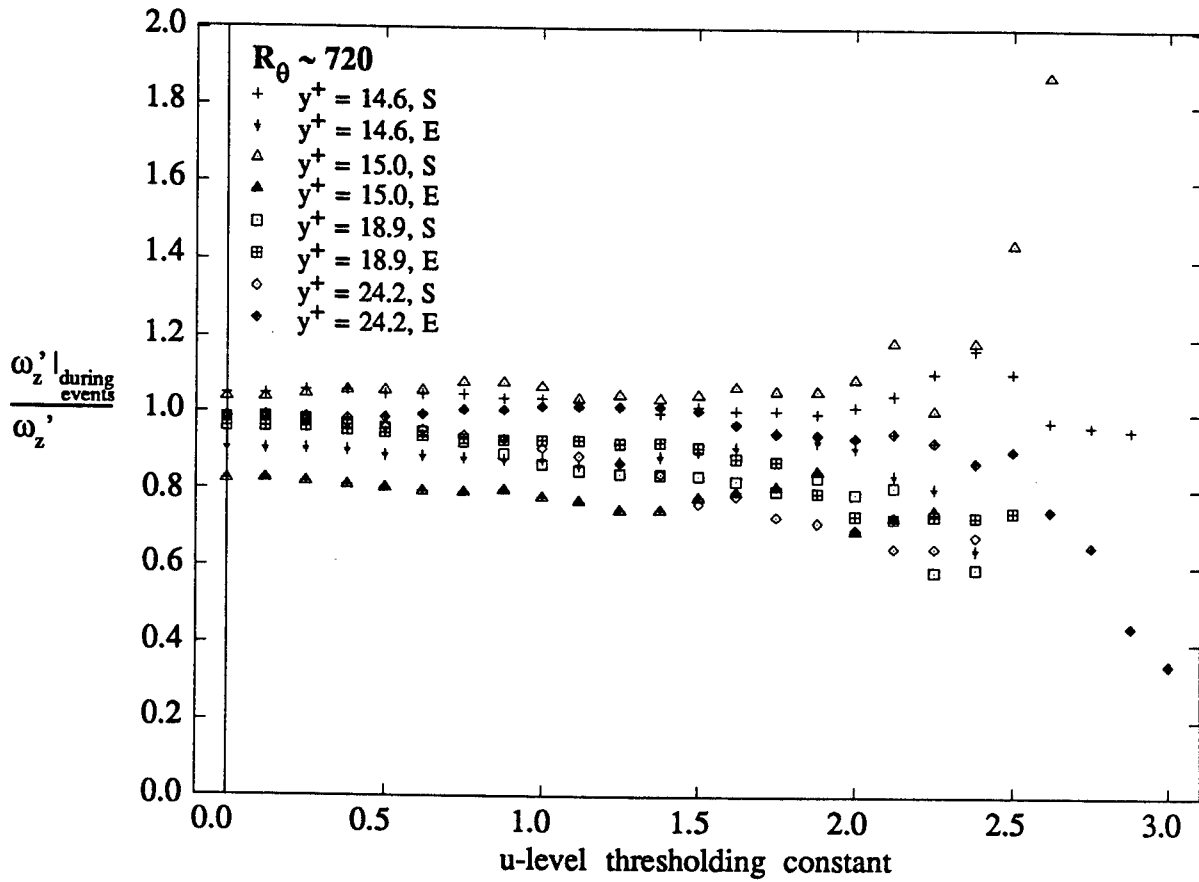
Figure 3.6.28
RMS ω_z During u-level
Evemts Normalized by ω_z'
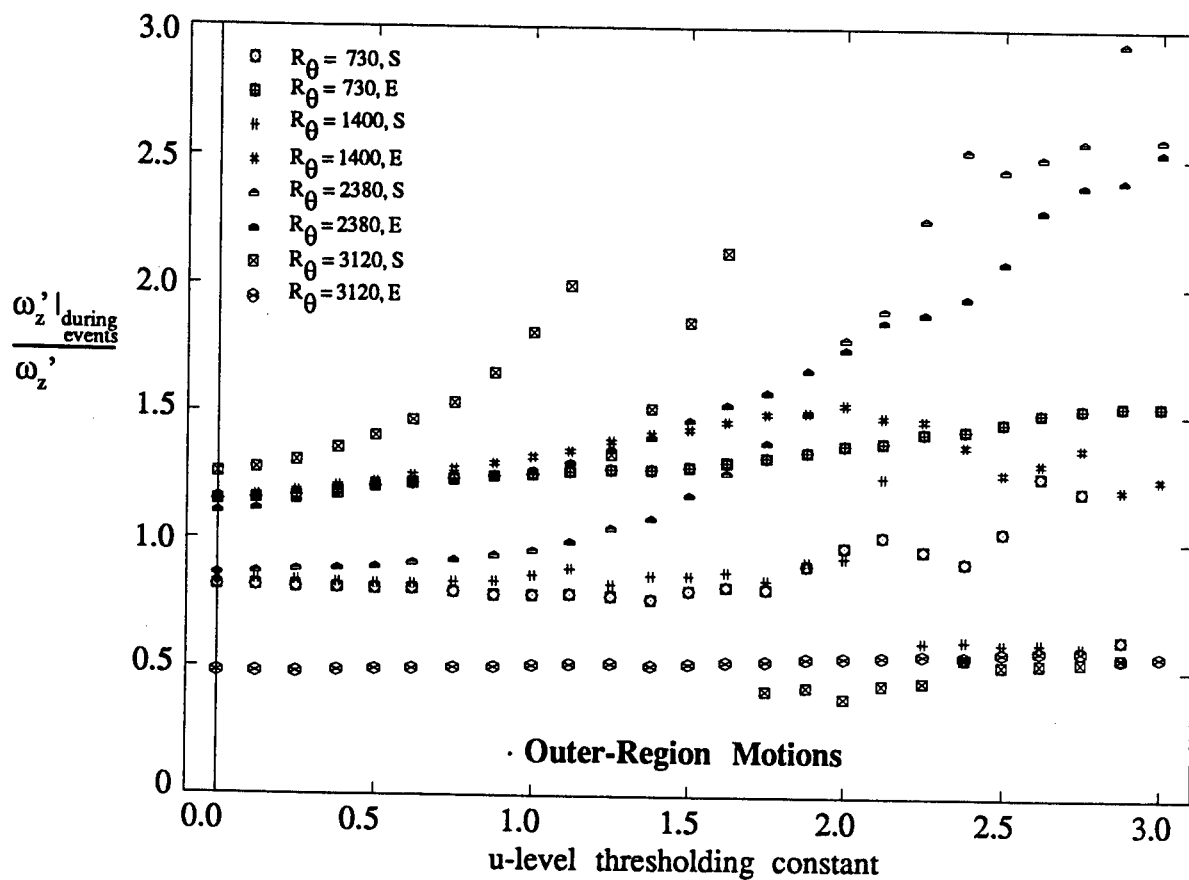vs. Threshold (Inner-region data)

Figure 3.6.29
RMS ω_z During u-level
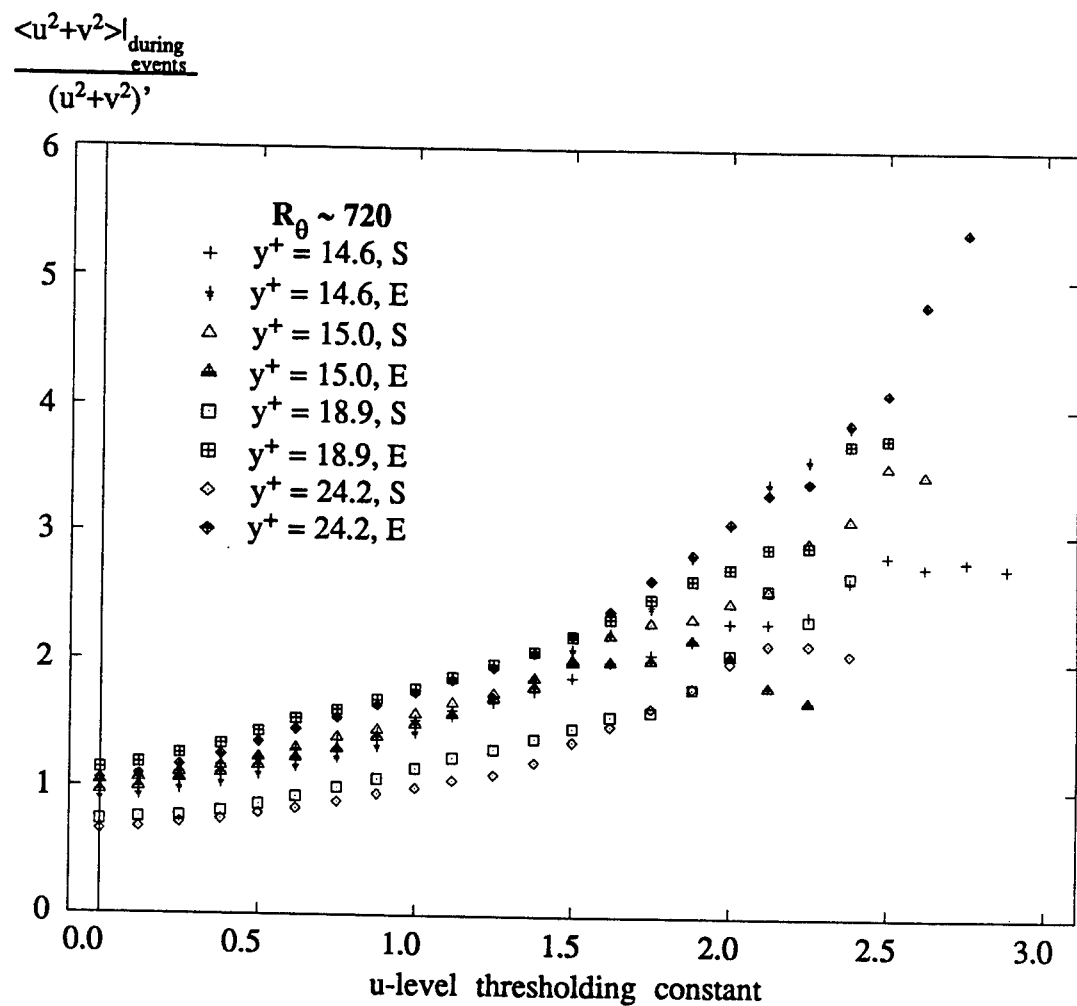Events Normalized by ω_z'
vs. Threshold (LSM data set)

Figure 3.6.30
Average TKE During u-level
Events Normalized by TKE'
vs. Threshold (Inner-region data)

$$\dfrac{<u^2+v^2>|_{\substack{during \\ events}}}{(u^2+v^2)'}$$
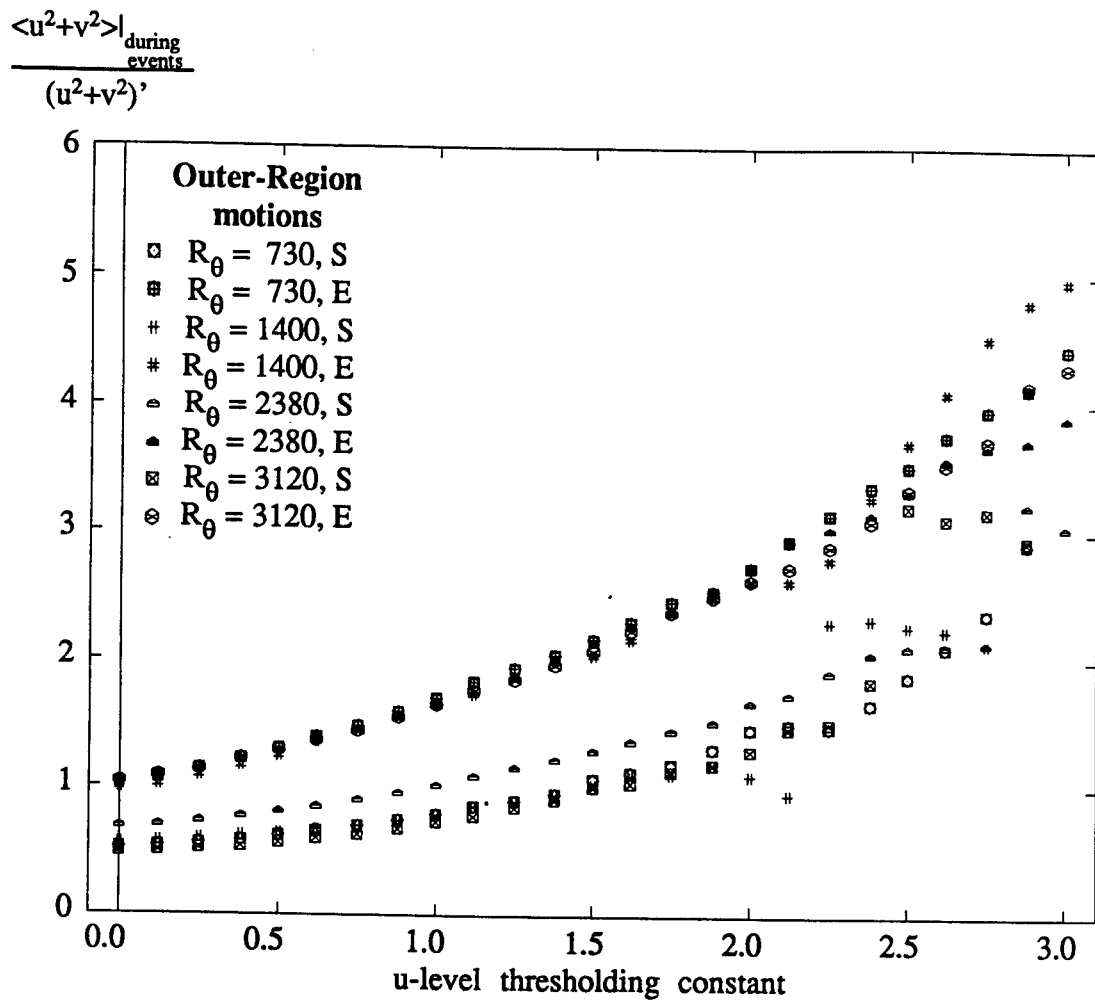

Figure 3.6.31
Average TKE During u-level
Events Normalized by TKE'
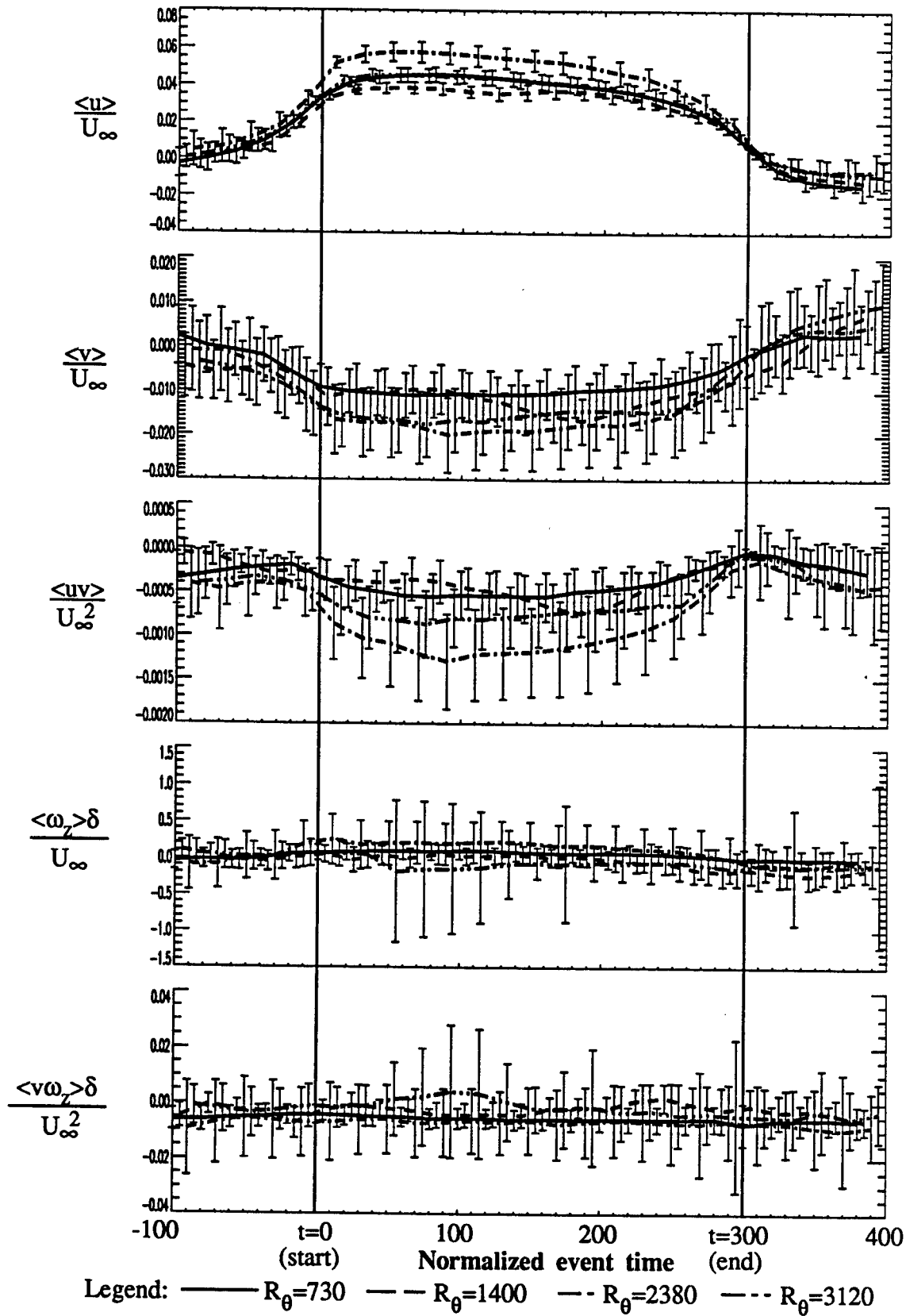vs. Threshold (LSM data set)

Figure 3.6.32 Outer-scaled u-level sweep ensembles. Error bars indicate 25% of an ensemble's standard deviation about each point in time
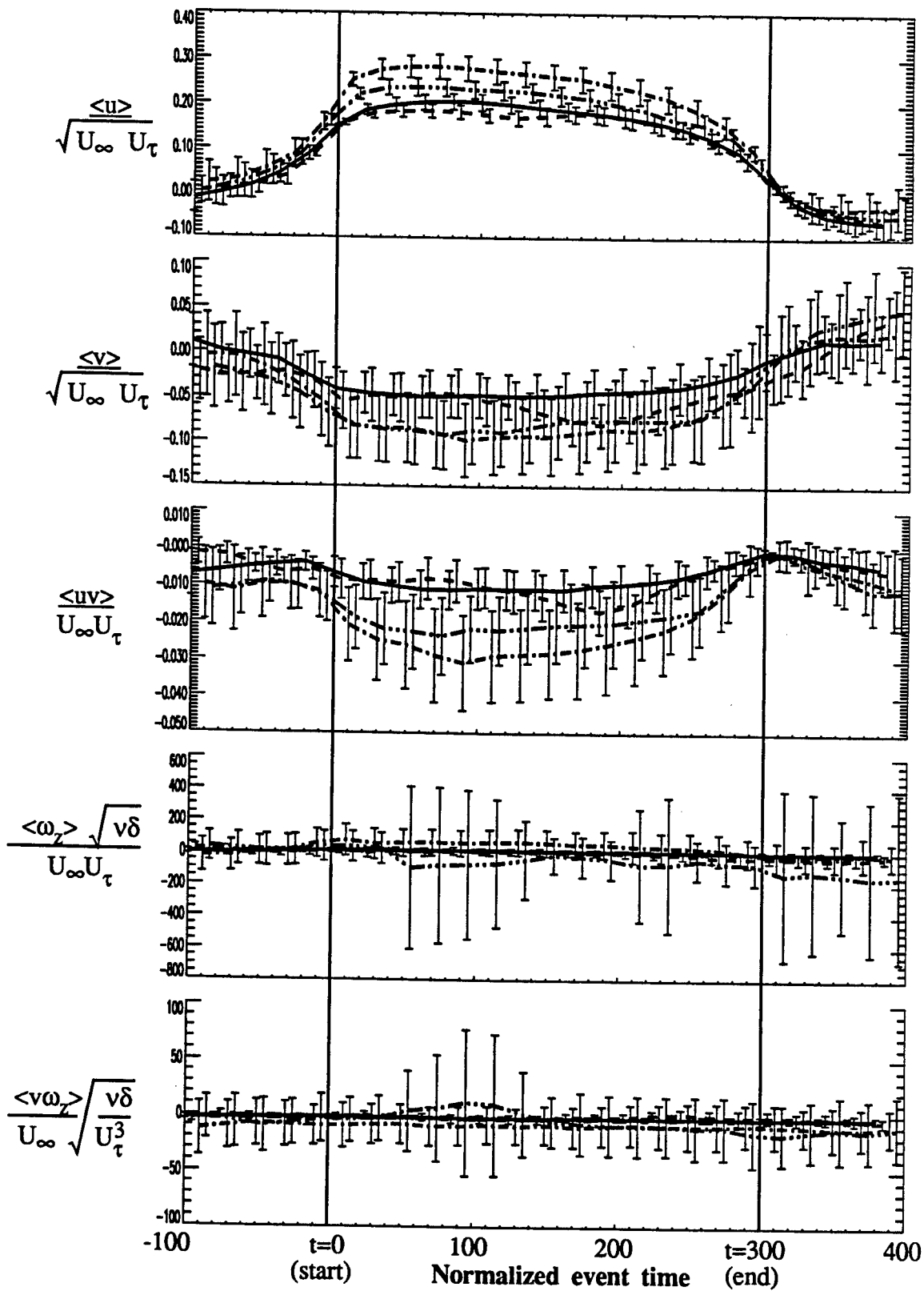
Figure 3.6.33 Mixed-scaled u-level sweep ensembles. Error bars indicate 25% of an ensemble's standard deviation about each point in time
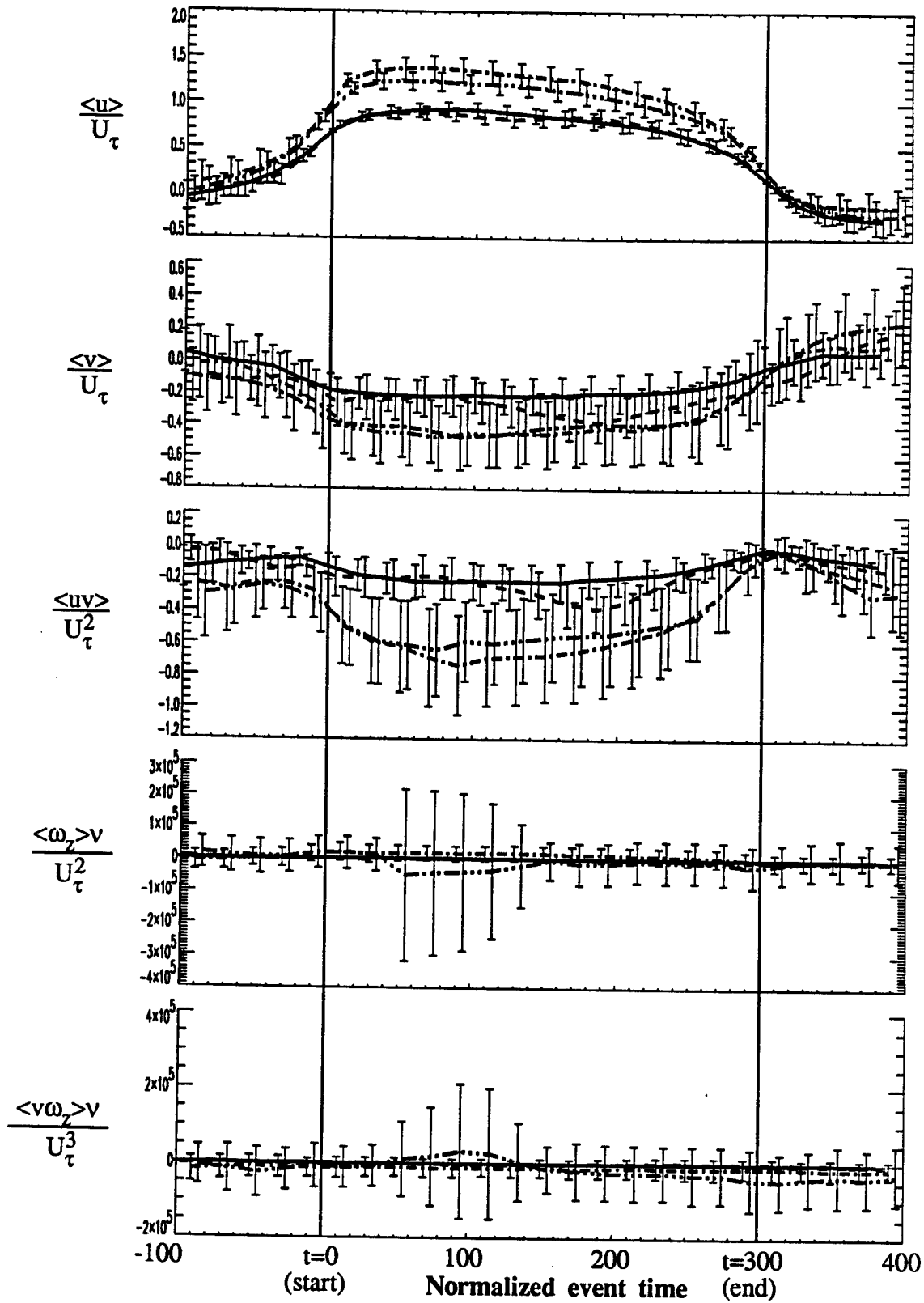
Figure 3.6.34 Inner-scaled u-level sweep ensembles. Error bars indicate 25% of an ensemble's standard deviation about each point in time

Figure 3.6.35 Outer-scaled u-level ejection ensembles. Error bars indicate 25% of an ensemble's standard deviation about each point in time

Figure 3.6.36 Mixed-scaled u-level ejection ensembles. Error bars indicate 25% of an ensemble's standard deviation about each point in time
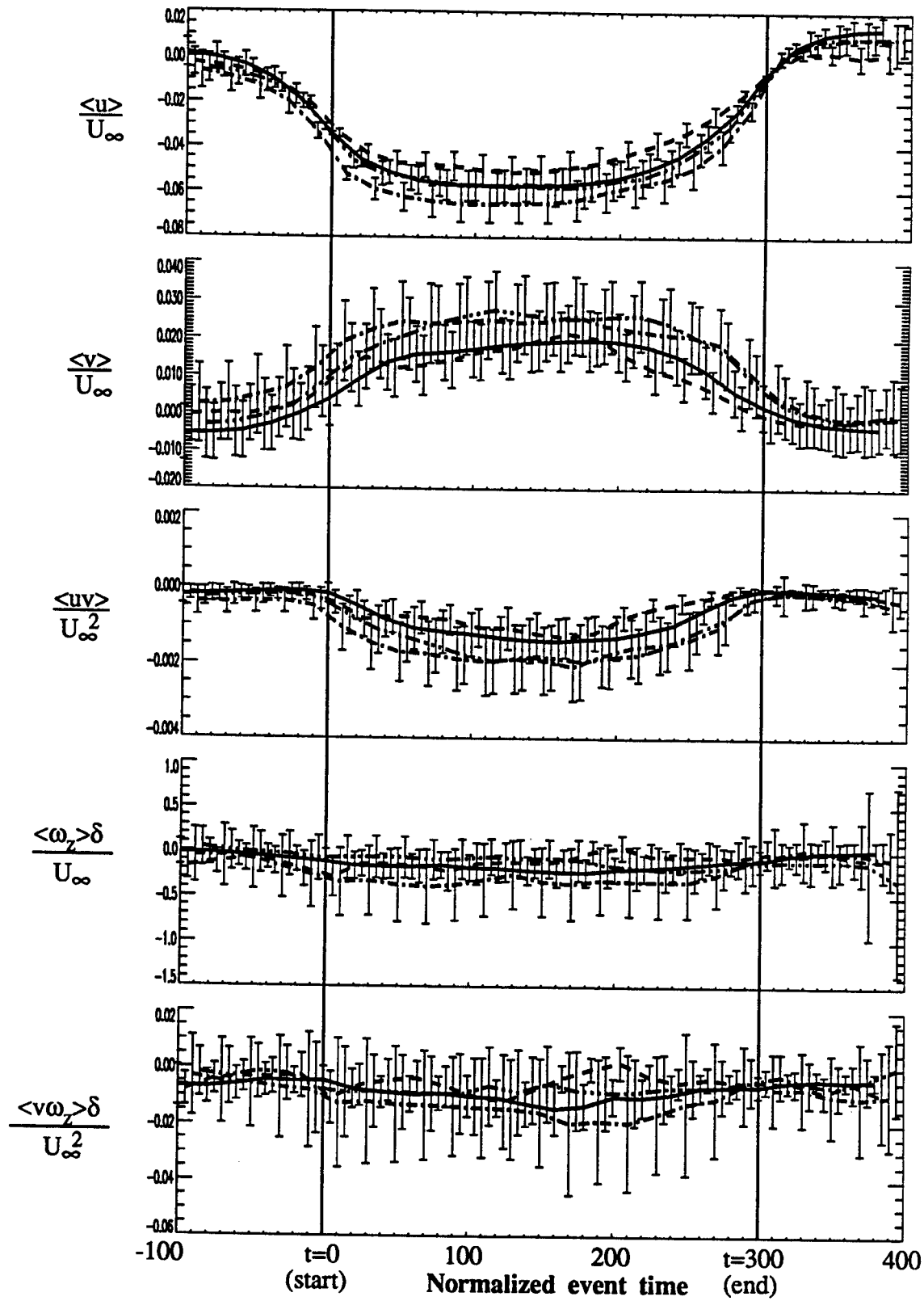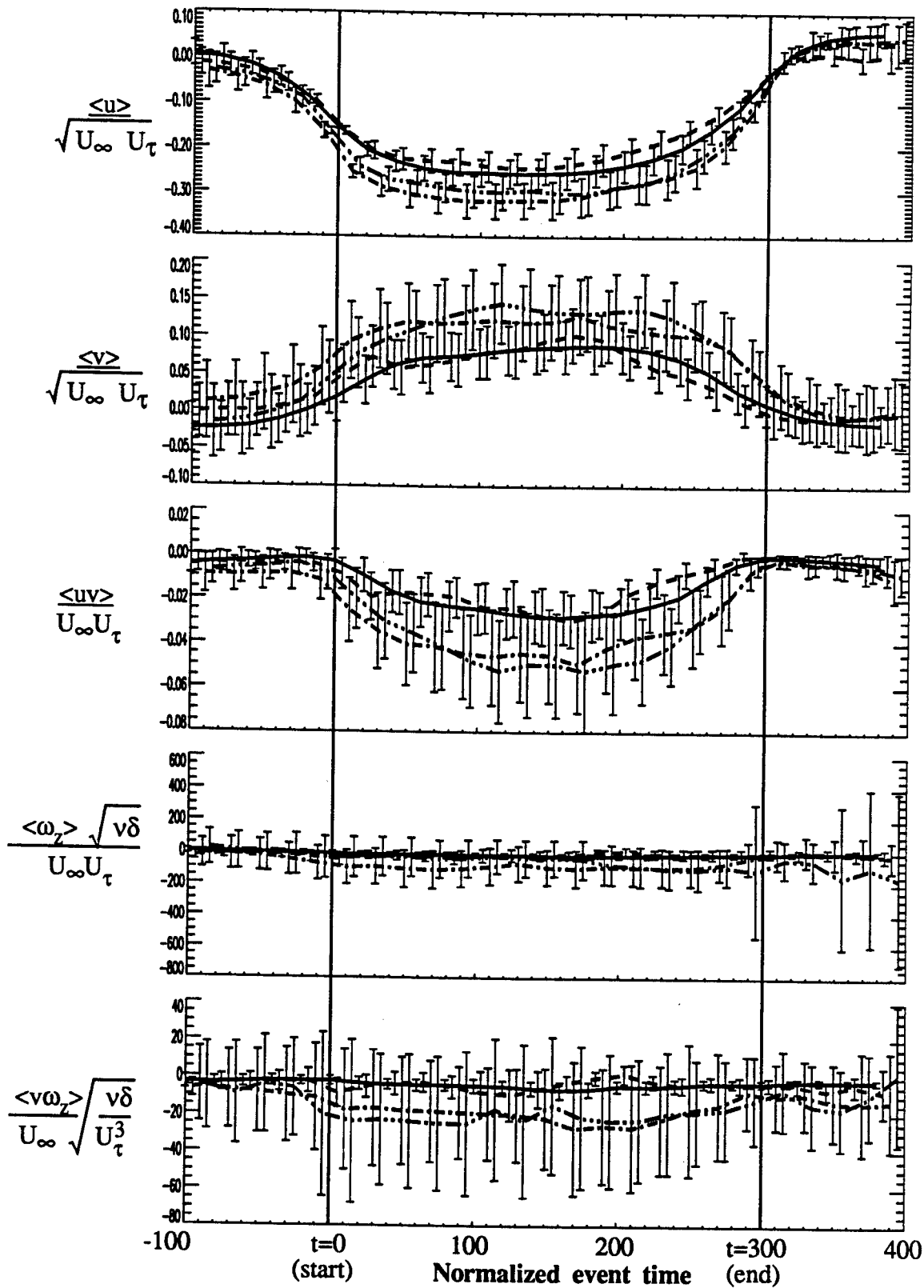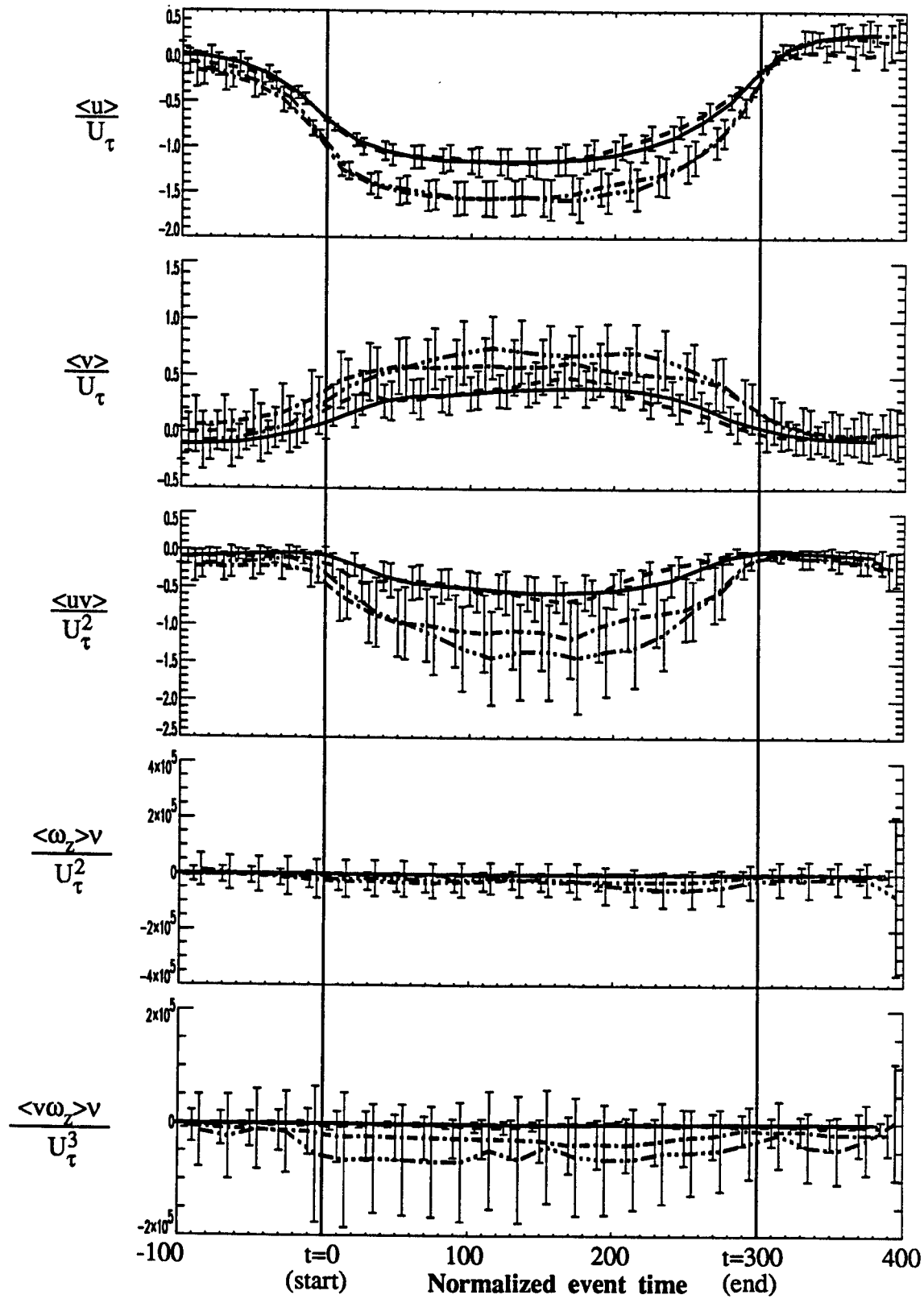
Figure 3.6.37 Inner-scaled u-level ejection ensembles. Error bars indicate 25% of an ensemble's standard deviation about each point in time
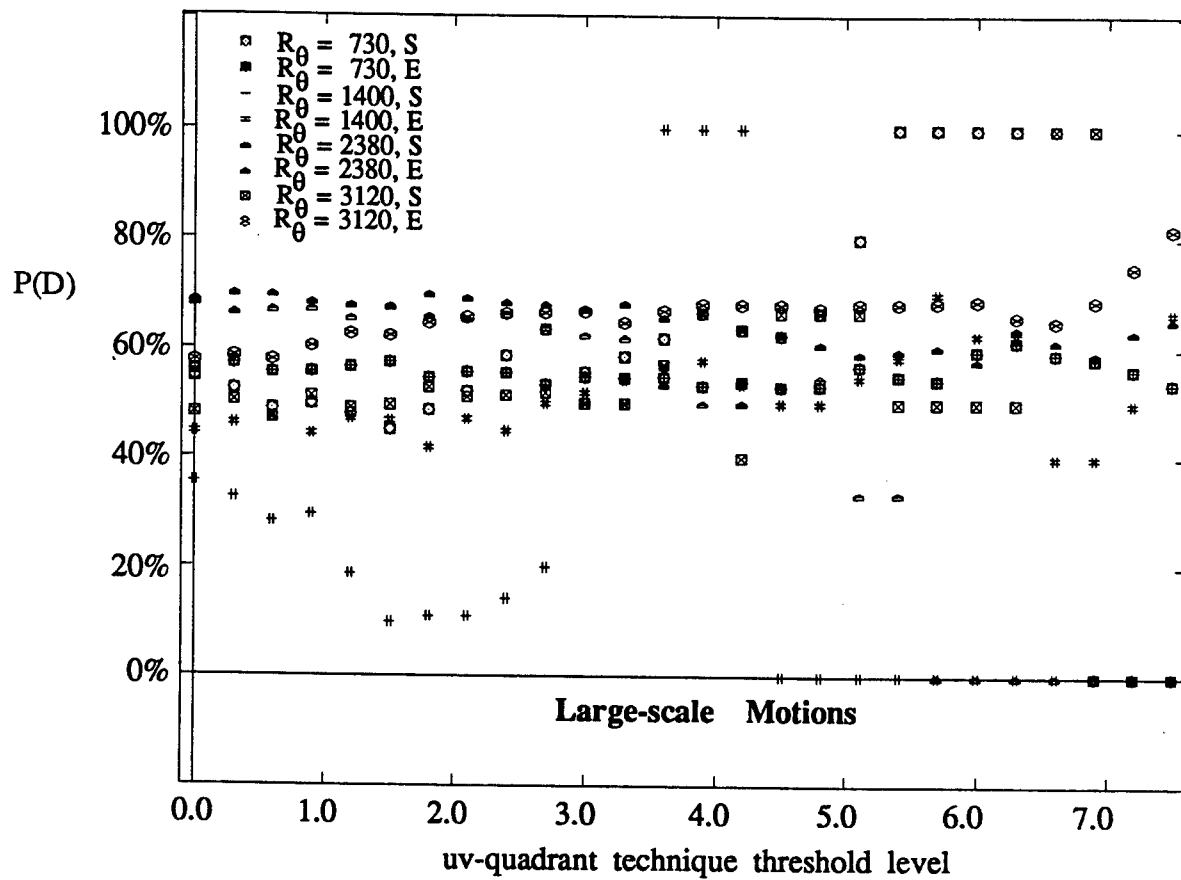
Figure 4.1.1
P(D): Probability of an LSM Detection
Occurring During a uv-quadrant Detection
vs. Threshold

Figure 4.1.2
P(D): Probability of an LSM Detection
Occurring During a TERA Detection
vs. Threshold

Figure 4.1.3
P(D): Probability of an LSM Detection
Occurring During a u-level Detection
vs. Threshold

Figure 4.1.4
P(E): Probability of a uv-quadrant Detection
Occurring During an LSM Detection
vs. Threshold

Figure 4.1.5
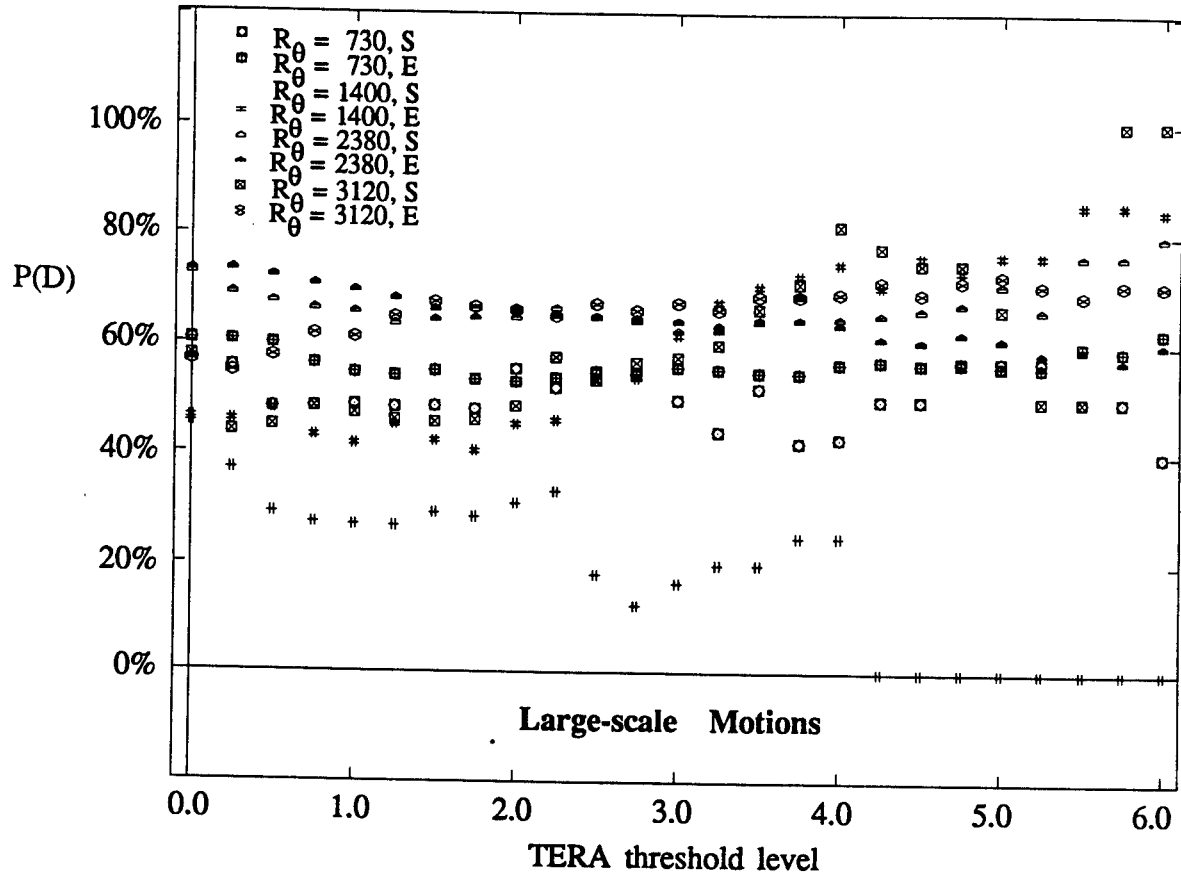P(E): Probability of a TERA Detection
Occurring During an LSM Detection
vs. Threshold

Figure 4.1.6
P(E): Probability of a u-level Detection
Occurring During an LSM Detection
vs. Threshold

Figure 4.1.7a
P(T): Probability of a uv-quadrant ejection
vs.
Phase of an LSM smoke detection
($R_\theta = 730$)

Threshold	
+	0.00
+	0.35
△	0.70
▲	1.05
□	1.40
⊞	1.75
◇	2.10
◆	2.45

Figure 4.1.7b
P(T): Probability of a uv-quadrant ejection
vs.
Phase of an LSM smoke detection
($R_\theta = 1400$)

Threshold	
+	0.00
+	0.35
△	0.70
▲	1.05
□	1.40
⊞	1.75
◇	2.10
◆	2.45

Phase of a smoke event
(Normalized event time)

Figure 4.1.7c
P(T): Probability of a uv-quadrant ejection
vs.
Phase of an LSM smoke detection
$(R_\theta = 2380)$

Threshold
+ 0.00
✦ 0.35
△ 0.70
▲ 1.05
□ 1.40
⊞ 1.75
◇ 2.10
◆ 2.45

Figure 4.1.7d
P(T): Probability of a uv-quadrant ejection
vs.
Phase of an LSM smoke detection
$(R_\theta = 3120)$

Threshold
+ 0.00
✦ 0.35
△ 0.70
▲ 1.05
□ 1.40
⊞ 1.75
◇ 2.10
◆ 2.45

Phase of a smoke event
(Normalized event time)

Figure 4.1.8a
P(T): Probability of a TERA ejection
vs.
Phase of an LSM smoke detection
$(R_\theta = 730)$

Figure 4.1.8b
P(T): Probability of a TERA ejection
vs.
Phase of an LSM smoke detection
$(R_\theta = 1400)$

Phase of a smoke event
(Normalized event time)

Figure 4.1.8c
P(T): Probability of a TERA ejection
vs.
Phase of an LSM smoke detection
$(R_\theta = 2380)$

Probability
of a probe-
based sweep
detection

Threshold
+ 0.0
＋ 0.3
△ 0.6
▲ 0.9
□ 1.2
⊞ 1.5
◇ 1.8
◆ 2.1

75%

50%

25%

0%

25%

50%

75%

Probability
of a probe-
based ejection
detection

-100   t=0   100   200   t=300   400

Figure 4.1.8d
P(T): Probability of a TERA ejection
vs.
Phase of an LSM smoke detection
$(R_\theta = 3120)$

Probability
of a probe-
based sweep
detection

Threshold
+ 0.0
＋ 0.3
△ 0.6
▲ 0.9
□ 1.2
⊞ 1.5
◇ 1.8
◆ 2.1

75%

50%

25%

0%

25%

50%

75%

Probability
of a probe-
based ejection
detection

-100   t=0   100   200   t=300   400
       (start)   **Phase of a smoke event**   (end)
       (Normalized event time)

Figure 4.1.9a
P(T): Probability of a u-level ejection
vs.
Phase of an LSM smoke detection
$(R_\theta = 730)$

Figure 4.1.9b
P(T): Probability of a u-level ejection
vs.
Phase of an LSM smoke detection
$(R_\theta = 1400)$

Figure 4.1.9c
P(T): Probability of a u-level ejection
vs.
Phase of an LSM smoke detection
$(R_\theta = 2380)$

Figure 4.1.9d
P(T): Probability of a u-level ejection
vs.
Phase of an LSM smoke detection
$(R_\theta = 3120)$

Figure 4.2.1
P(D): Probability of an RLM Detection
Occurring During a uv-quadrant Detection
vs. Threshold

Figure 4.2.2
P(D): Probability of an RLM Detection
Occurring During a TERA Detection
vs. Threshold

Figure 4.2.3
P(D): Probability of an RLM Detection
Occurring During a u-level Detection
vs. Threshold

Figure 4.2.4
P(E): Probability of a uv-quadrant Detection
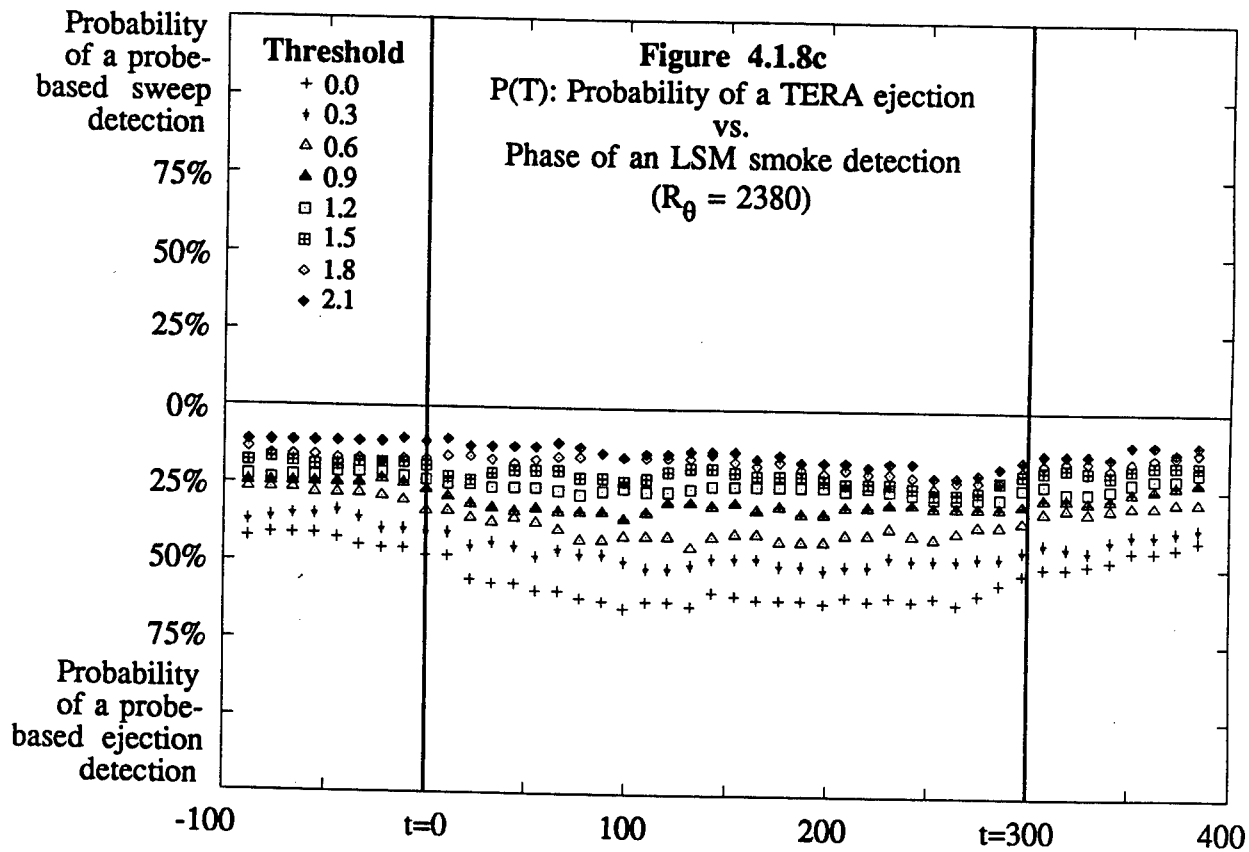Occurring During an RLM Detection
vs. Threshold

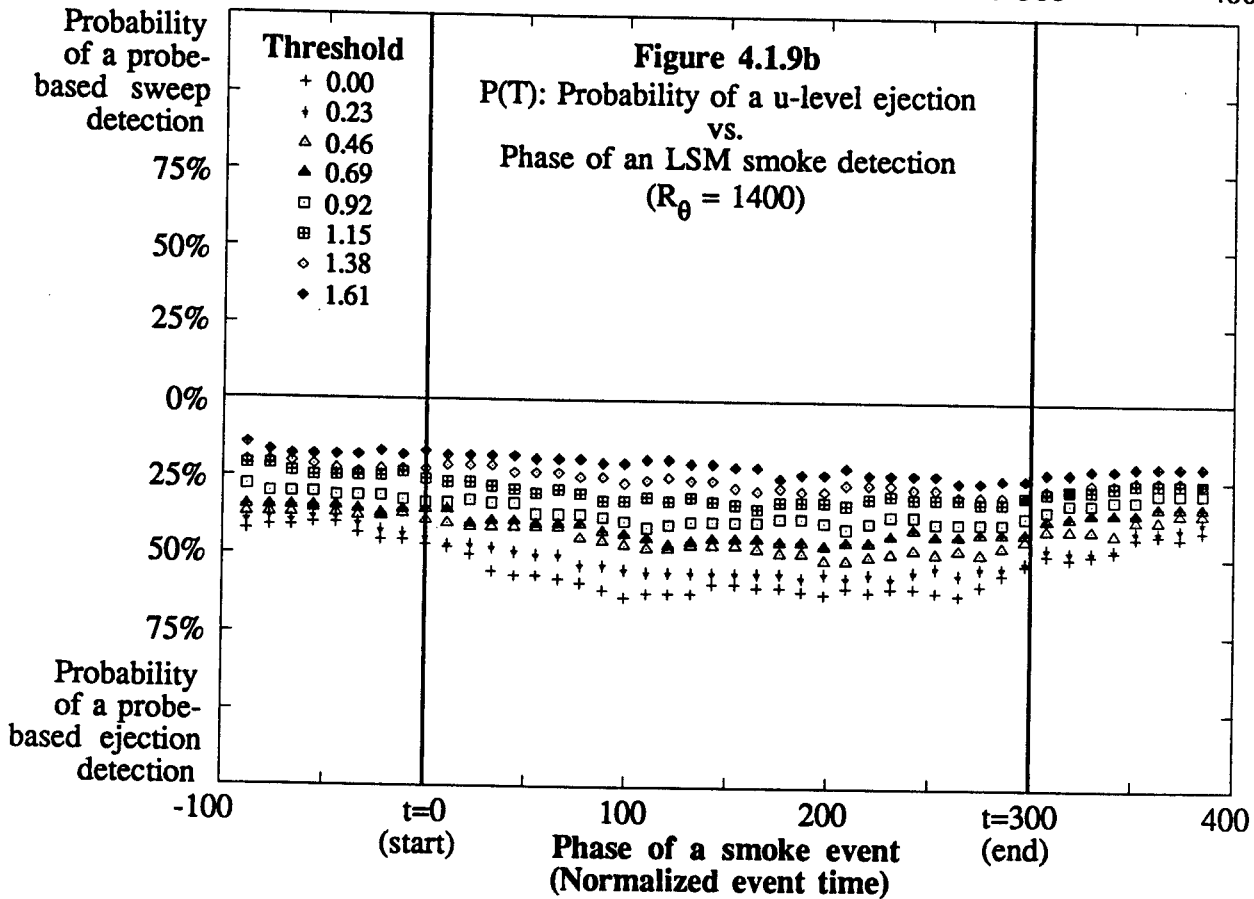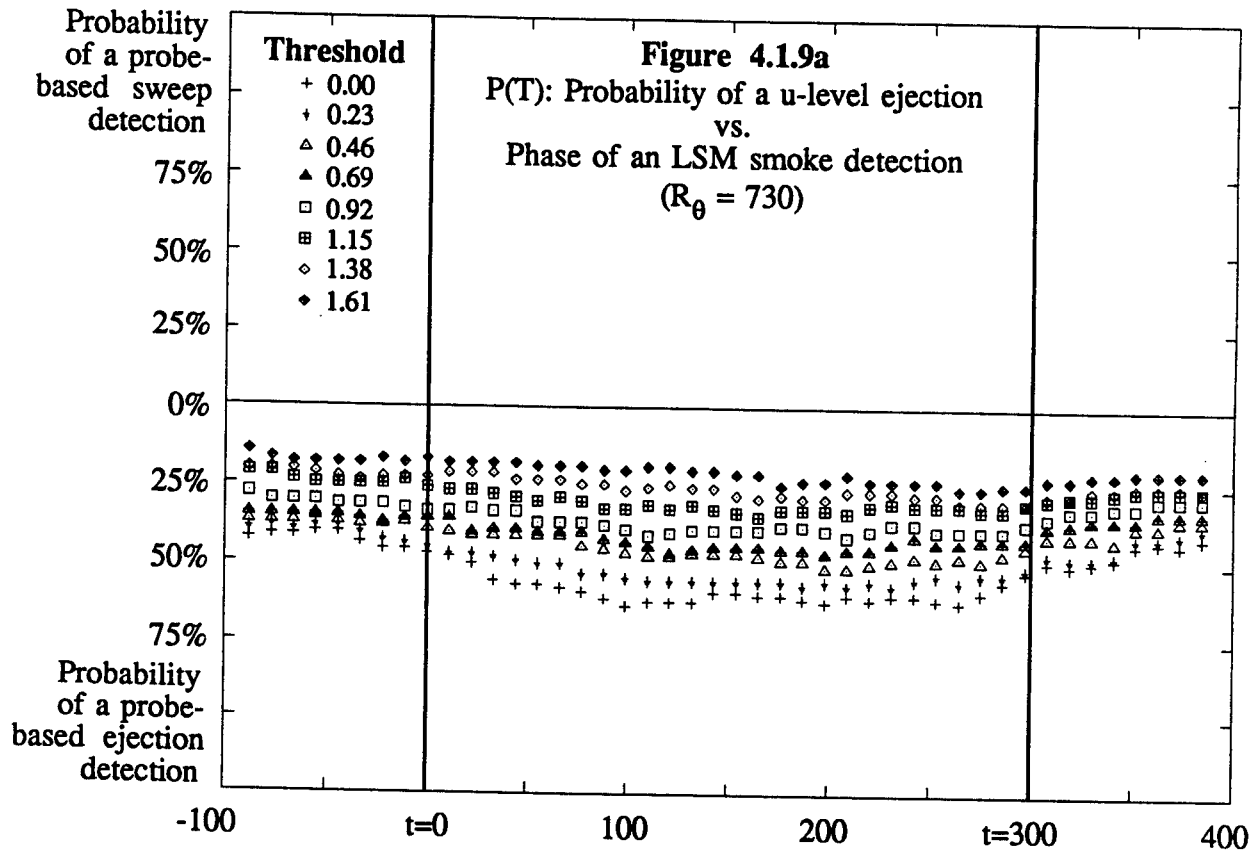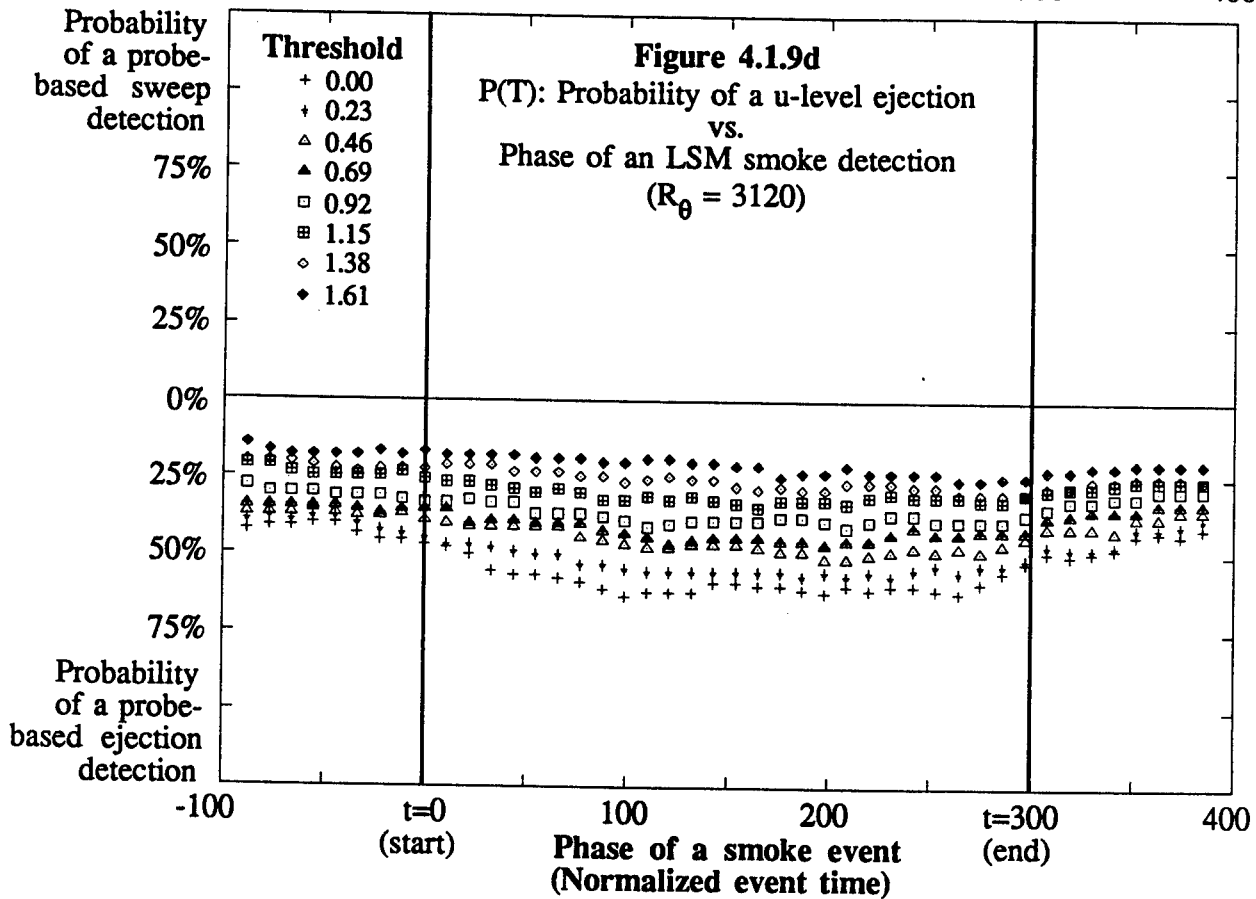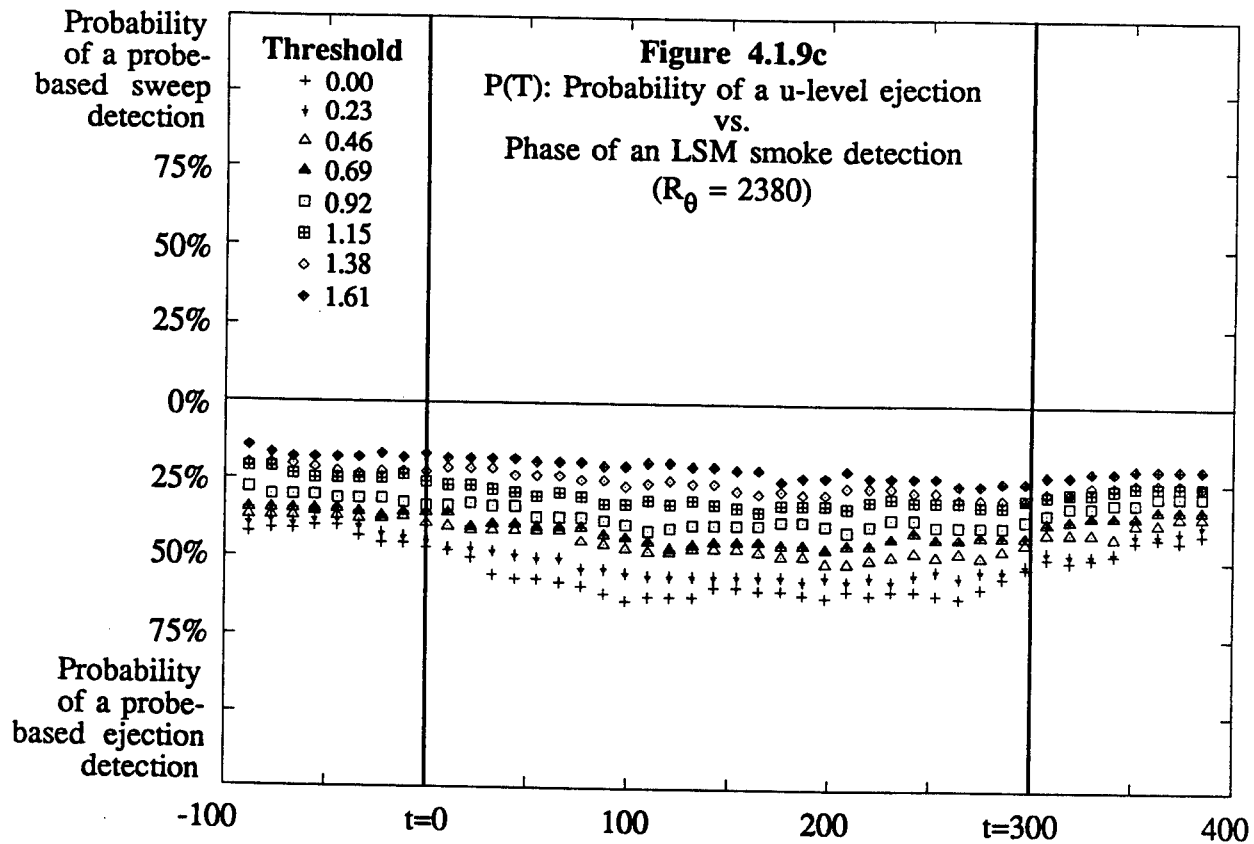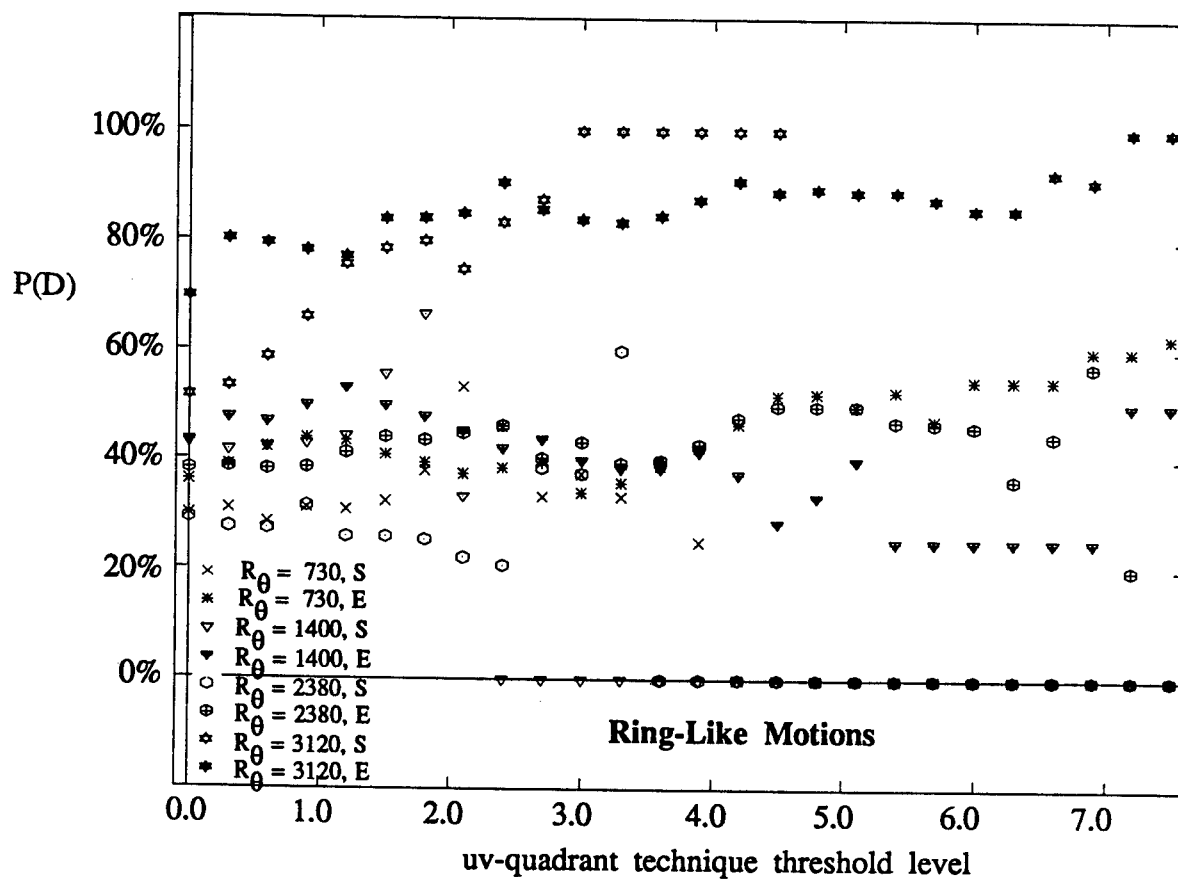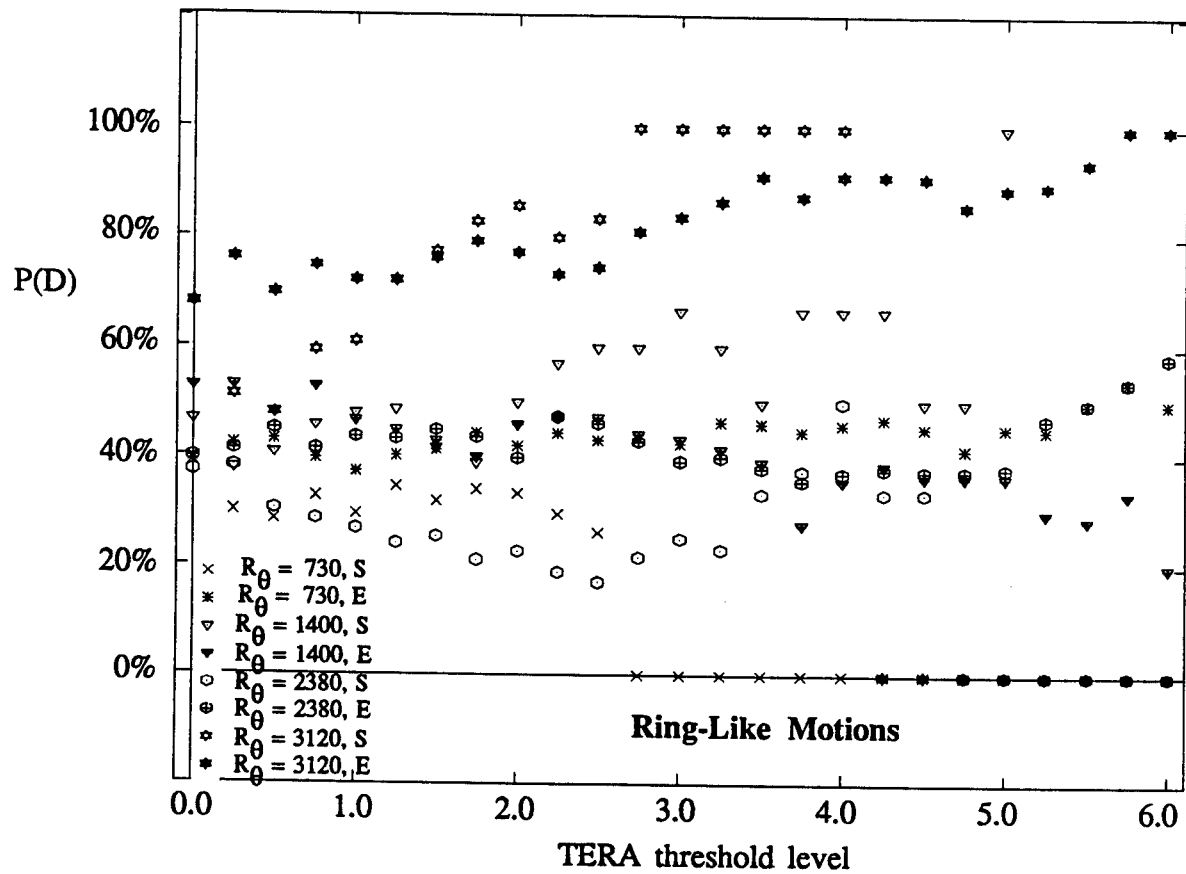**Figure 4.2.5**
P(E): Probability of a TERA Detection
Occurring During an RLM Detection
vs. Threshold

Figure 4.2.6
P(E): Probability of a u-level Detection
Occurring During an RLM Detection
vs. Threshold

Figure 4.2.7a
P(T): Probability of a uv-quadrant ejection
vs.
Phase of an RLM smoke ejection
$(R_\theta = 730)$

Figure 4.2.7b
P(T): Probability of a uv-quadrant sweep
vs.
Phase of an RLM smoke sweep
$(R_\theta = 730)$

Phase of a smoke event
(Normalized event time)

Figure 4.2.8a
P(T): Probability of a uv-quadrant ejection
vs.
Phase of an RLM smoke ejection
$(R_\theta = 1400)$

Figure 4.2.8b
P(T): Probability of a uv-quadrant sweep
vs.
Phase of an RLM smoke sweep
$(R_\theta = 1400)$

Phase of a smoke event
(Normalized event time)

Figure 4.2.9a
P(T): Probability of a uv-quadrant ejection
vs.
Phase of an RLM smoke ejection
$(R_\theta = 2380)$

Figure 4.2.9b
P(T): Probability of a uv-quadrant sweep
vs.
Phase of an RLM smoke sweep
$(R_\theta = 2380)$

Figure 4.2.10a
P(T): Probability of a uv-quadrant ejection
vs.
Phase of an RLM smoke ejection
$(R_\theta = 3120)$

Figure 4.2.10b
P(T): Probability of a uv-quadrant sweep
vs.
Phase of an RLM smoke sweep
$(R_\theta = 3120)$

Phase of a smoke event
(Normalized event time)

Figure 4.2.11a
P(T): Probability of a TERA ejection
vs.
Phase of an RLM smoke ejection
$(R_\theta = 730)$

Threshold
+ 0.0
∔ 0.3
△ 0.6
▲ 0.9
□ 1.2
⊞ 1.5
◇ 1.8
◆ 2.1

Figure 4.2.11b
P(T): Probability of a TERA sweep
vs.
Phase of an RLM smoke sweep
$(R_\theta = 730)$

Threshold
+ 0.0
∔ 0.3
△ 0.6
▲ 0.9
□ 1.2
⊞ 1.5
◇ 1.8
◆ 2.1

Phase of a smoke event
(Normalized event time)

Figure 4.2.12a
P(T): Probability of a TERA ejection
vs.
Phase of an RLM smoke ejection
$(R_\theta = 1400)$

Figure 4.2.12b
P(T): Probability of a TERA sweep
vs.
Phase of an RLM smoke sweep
$(R_\theta = 1400)$

Phase of a smoke event
(Normalized event time)

Figure 4.2.13a
P(T): Probability of a TERA ejection
vs.
Phase of an RLM smoke ejection
$(R_\theta = 2380)$

Threshold
+ 0.0
⁺ 0.3
△ 0.6
▲ 0.9
□ 1.2
⊞ 1.5
◇ 1.8
◆ 2.1

Probability of a probe-based sweep detection

75%
50%
25%
0%
25%
50%
75%

Probability of a probe-based ejection detection

-100   t=0   100   200   t=300   400

Figure 4.2.13b
P(T): Probability of a TERA sweep
vs.
Phase of an RLM smoke sweep
$(R_\theta = 2380)$

Threshold
+ 0.0
⁺ 0.3
△ 0.6
▲ 0.9
□ 1.2
⊞ 1.5
◇ 1.8
◆ 2.1

Probability of a probe-based sweep detection

75%
50%
25%
0%
25%
50%
75%

Probability of a probe-based ejection detection

-100   t=0   100   200   t=300   400
        (start)   (end)
     Phase of a smoke event
     (Normalized event time)

Figure 4.2.14a
Probability of a TERA ejection
vs.
Phase of an RLM smoke ejection
$(R_\theta = 3120)$

Threshold
+ 0.0
✦ 0.3
△ 0.6
▲ 0.9
□ 1.2
⊞ 1.5
◇ 1.8
◆ 2.1

Figure 4.2.14b
Probability of a TERA sweep
vs.
Phase of an RLM smoke sweep
$(R_\theta = 3120)$

Threshold
+ 0.0
✦ 0.3
△ 0.6
▲ 0.9
□ 1.2
⊞ 1.5
◇ 1.8
◆ 2.1

Phase of a smoke event
(Normalized event time)

Figure 4.2.15a
P(T): Probability of a u-level ejection
vs.
Phase of an RLM smoke ejection
$(R_\theta = 730)$

Figure 4.2.15b
P(T): Probability of a u-level sweep
vs.
Phase of an RLM smoke sweep
$(R_\theta = 730)$

Figure 4.2.16a
P(T): Probability of a u-level ejection
vs.
Phase of an RLM smoke ejection
$(R_\theta = 1400)$

Figure 4.2.16b
P(T): Probability of a u-level sweep
vs.
Phase of an RLM smoke sweep
$(R_\theta = 1400)$

Figure 4.2.17a
P(T): Probability of a u-level ejection
vs.
Phase of an RLM smoke ejection
$(R_\theta = 2380)$

Figure 4.2.17b
P(T): Probability of a u-level sweep
vs.
Phase of an RLM smoke sweep
$(R_\theta = 2380)$

Phase of a smoke event
(Normalized event time)

Figure 4.2.18a
P(T): Probability of a u-level ejection
vs.
Phase of an RLM smoke ejection
$(R_\theta = 3120)$

Figure 4.2.18b
P(T): Probability of a u-level sweep
vs.
Phase of an RLM smoke sweep
$(R_\theta = 3120)$

Phase of a smoke event
(Normalized event time)

Figure 4.3.1
P(D): Probability of an Inner-Region Visual Detection
Occurring During a uv-quadrant Detection
vs. Threshold

Figure 4.3.2
P(D): Probability of an Inner-Region Visual
Detection Occurring During a u-level
Detection vs. Threshold

Figure 4.3.3
P(D): Probability of an Inner-Region Visual
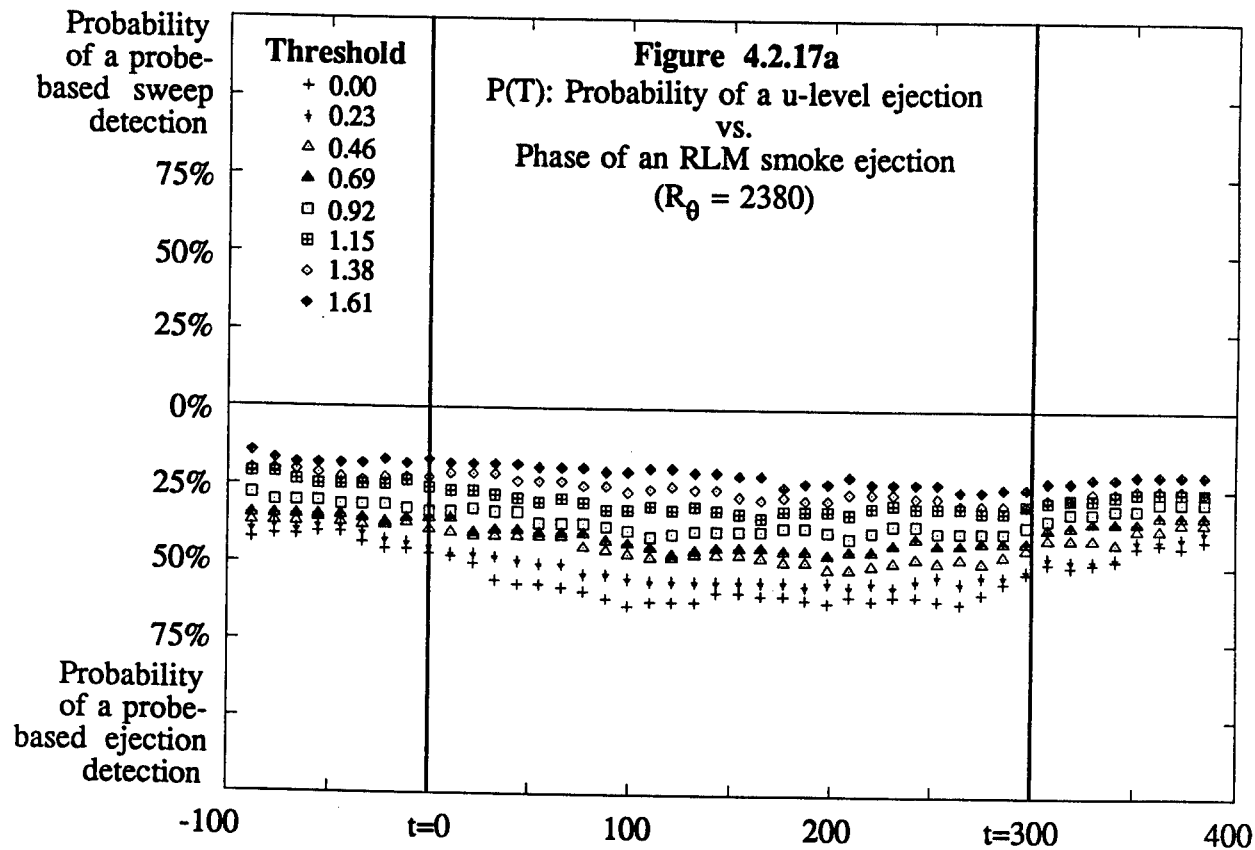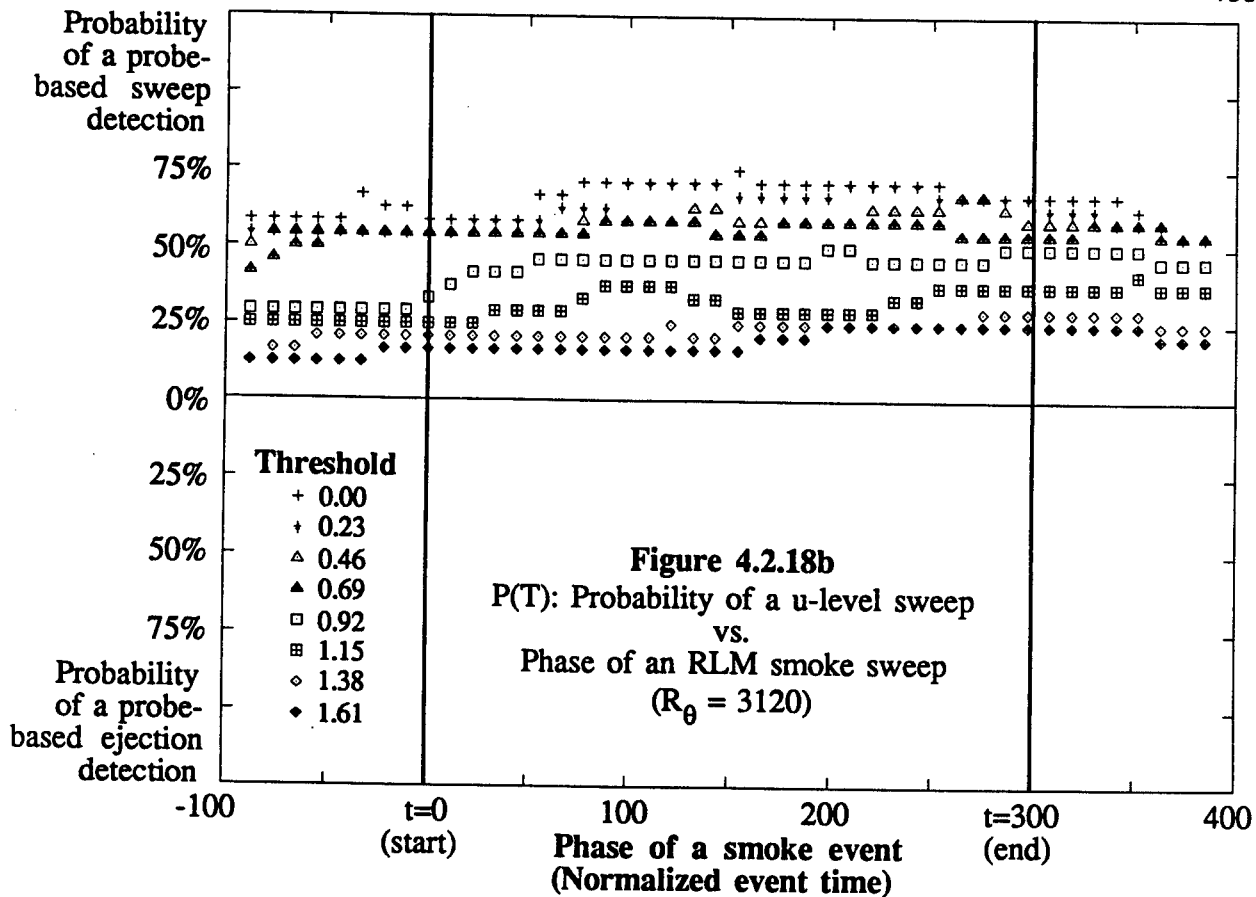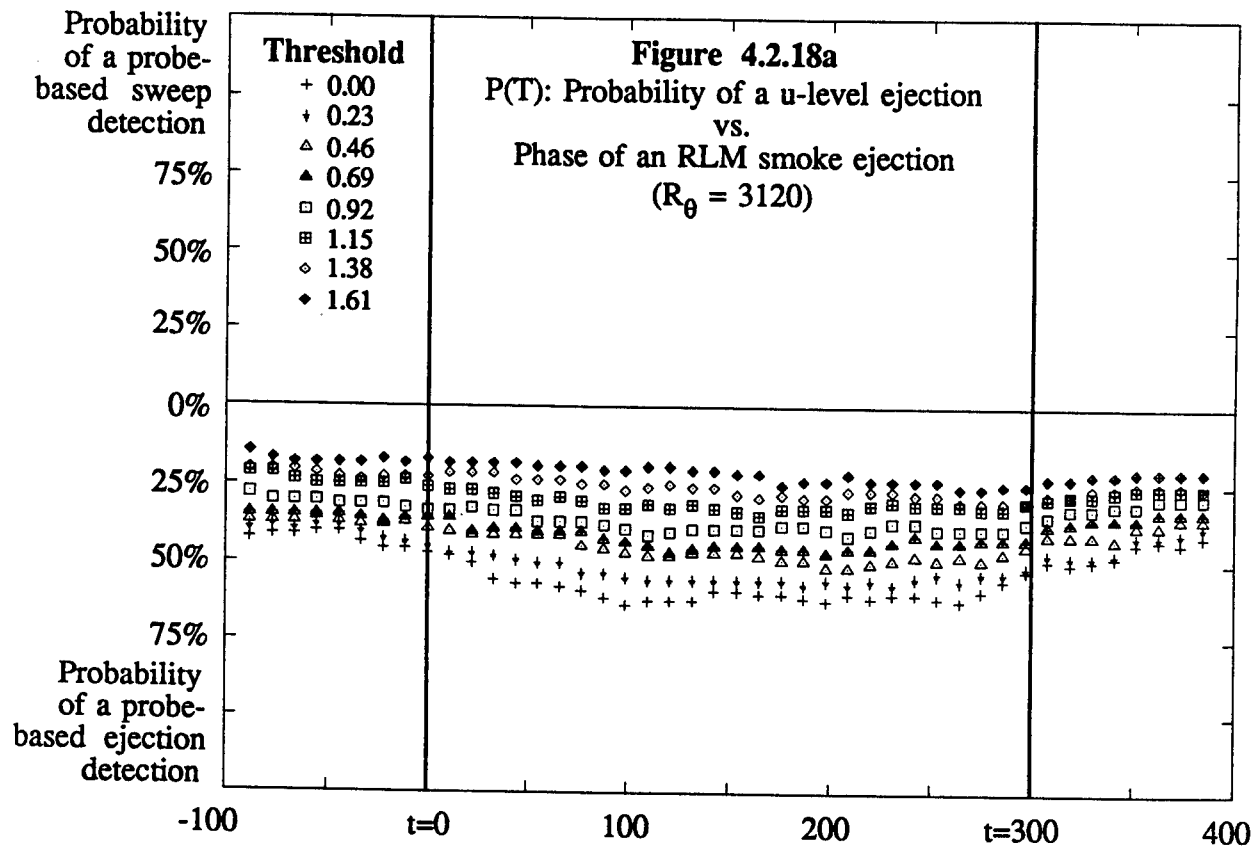Detection Occurring During a TERA Detection
vs. Threshold

Figure 4.3.4
P(E): Probability of a uv-quadrant Detection
Occurring During an Inner-Region Visual Detection
vs. Threshold

Figure 4.3.5
P(E): Probability of a TERA Detection
Occurring During an Inner-Region Visual
Detection vs. Threshold

Figure 4.3.6
P(E): Probability of a u-level Detection
Occurring During an Inner-Region
Visual Detection vs. Threshold

Figure 4.3.7a
P(T): Probability of a uv-quadrant ejection
vs.
Phase of an inner-region smoke ejection
$(y^+ = 14.6)$

Figure 4.3.7b
P(T): Probability of a uv-quadrant sweep
vs.
Phase of an inner-region smoke sweep
$(y^+ = 14.6)$

Phase of a smoke event
(Normalized event time)

Figure 4.3.8a
P(T): Probability of a uv-quadrant ejection
vs.
Phase of an inner-region smoke ejection
$(y^+ = 15.0)$

Figure 4.3.8b
P(T): Probability of a uv-quadrant sweep
vs.
Phase of an inner-region smoke sweep
$(y^+ = 15.0)$

Phase of a smoke event
(Normalized event time)

Figure 4.3.9a

P(T): Probability of a uv-quadrant ejection
vs.
Phase of an inner-region smoke ejection
$(y^+ = 18.9)$

Figure 4.3.9b

P(T): Probability of a uv-quadrant sweep
vs.
Phase of an inner-region smoke sweep
$(y^+ = 18.9)$

Figure 4.3.10a
P(T): Probability of a uv-quadrant ejection
vs.
Phase of an inner-region smoke ejection
$(y^+ = 24.2)$

Figure 4.3.10b
P(T): Probability of a uv-quadrant sweep
vs.
Phase of an inner-region smoke sweep
$(y^+ = 24.2)$

Phase of a smoke event
(Normalized event time)

Figure 4.3.11a
P(T): Probability of a TERA ejection
vs.
Phase of an inner-region smoke ejection
$(y^+ = 14.6)$

Threshold
+ 0.0
✦ 0.3
△ 0.6
▲ 0.9
□ 1.2
⊞ 1.5
◇ 1.8
◆ 2.1

Figure 4.3.11b
P(T): Probability of a TERA sweep
vs.
Phase of an inner-region smoke sweep
$(y^+ = 14.6)$

Threshold
+ 0.0
✦ 0.3
△ 0.6
▲ 0.9
□ 1.2
⊞ 1.5
◇ 1.8
◆ 2.1

Phase of a smoke event
(Normalized event time)

Figure 4.3.12a
P(T): Probability of a TERA ejection
vs.
Phase of an inner-region smoke ejection
$(y^+ = 15.0)$

Figure 4.3.12b
P(T): Probability of a TERA sweep
vs.
Phase of an inner-region smoke sweep
$(y^+ = 15.0)$

Phase of a smoke event
(Normalized event time)

Figure 4.3.13a
P(T): Probability of a TERA ejection
vs.
Phase of an inner-region smoke ejection
$(y^+ = 18.9)$

Figure 4.3.13b
P(T); Probability of a TERA sweep
vs.
Phase of an inner-region smoke sweep
$(y^+ = 18.9)$

Phase of a smoke event
(Normalized event time)

Figure 4.3.14a
P(T): Probability of a TERA ejection
vs.
Phase of an inner-region smoke ejection
$(y^+ = 24.2)$

Figure 4.3.14b
P(T): Probability of a TERA sweep
vs.
Phase of an inner-region smoke sweep
$(y^+ = 24.2)$

Figure 4.3.15a
P(T): Probability of a u-level ejection
vs.
Phase of an inner-region smoke ejection
$(y^+ = 14.6)$

Figure 4.3.15b
P(T): Probability of a u-level sweep
vs.
Phase of an inner-region smoke sweep
$(y^+ = 14.6)$

Phase of a smoke event
(Normalized event time)

Probability
of a probe-
based sweep
detection

Threshold
+ 0.00
╈ 0.23
△ 0.46
▲ 0.69
□ 0.92
⊞ 1.15
◇ 1.38
◆ 1.61

Figure 4.3.16a
P(T): Probability of a u-level ejection
vs.
Phase of an inner-region smoke ejection
$(y^+ = 15.0)$

Probability
of a probe-
based ejection
detection

Probability
of a probe-
based sweep
detection

Threshold
+ 0.00
╈ 0.23
△ 0.46
▲ 0.69
□ 0.92
⊞ 1.15
◇ 1.38
◆ 1.61

Figure 4.3.16b
P(T): Probability of a u-level sweep
vs.
Phase of an inner-region smoke sweep
$(y^+ = 15.0)$

Probability
of a probe-
based ejection
detection

t=0
(start)

Phase of a smoke event
(Normalized event time)

t=300
(end)

Probability
of a probe-
based sweep
detection

75%

50%

25%

0%

Threshold
+ 0.00
✦ 0.23
△ 0.46
▲ 0.69
▫ 0.92
⊞ 1.15
◇ 1.38
◆ 1.61

Figure 4.3.17a
P(T): Probability of a u-level ejection
vs.
Phase of an inner-region smoke ejection
$(y^+ = 18.9)$

25%

50%

75%

Probability
of a probe-
based ejection
detection

-100   t=0   100   200   t=300   400

Probability
of a probe-
based sweep
detection

75%

50%

25%

0%

25%

Threshold
+ 0.00
✦ 0.23
△ 0.46
▲ 0.69
▫ 0.92
⊞ 1.15
◇ 1.38
◆ 1.61

50%

Figure 4.3.17b
P(T): Probability of a u-level sweep
vs.
Phase of an inner-region smoke sweep
$(y^+ = 18.9)$

75%

Probability
of a probe-
based ejection
detection

-100   t=0   100   200   t=300   400
       (start) **Phase of a smoke event** (end)
             (Normalized event time)

Figure 4.3.18a
P(T): Probability of a u-level ejection
vs.
Phase of an inner-region smoke ejection
$(y^+ = 24.2)$

Threshold
+ 0.00
✦ 0.23
△ 0.46
▲ 0.69
□ 0.92
⊞ 1.15
◇ 1.38
◆ 1.61

Figure 4.3.18b
P(T): Probability of a u-level sweep
vs.
Phase of an inner-region smoke sweep
$(y^+ = 24.2)$

Threshold
+ 0.00
✦ 0.23
△ 0.46
▲ 0.69
□ 0.92
⊞ 1.15
◇ 1.38
◆ 1.61

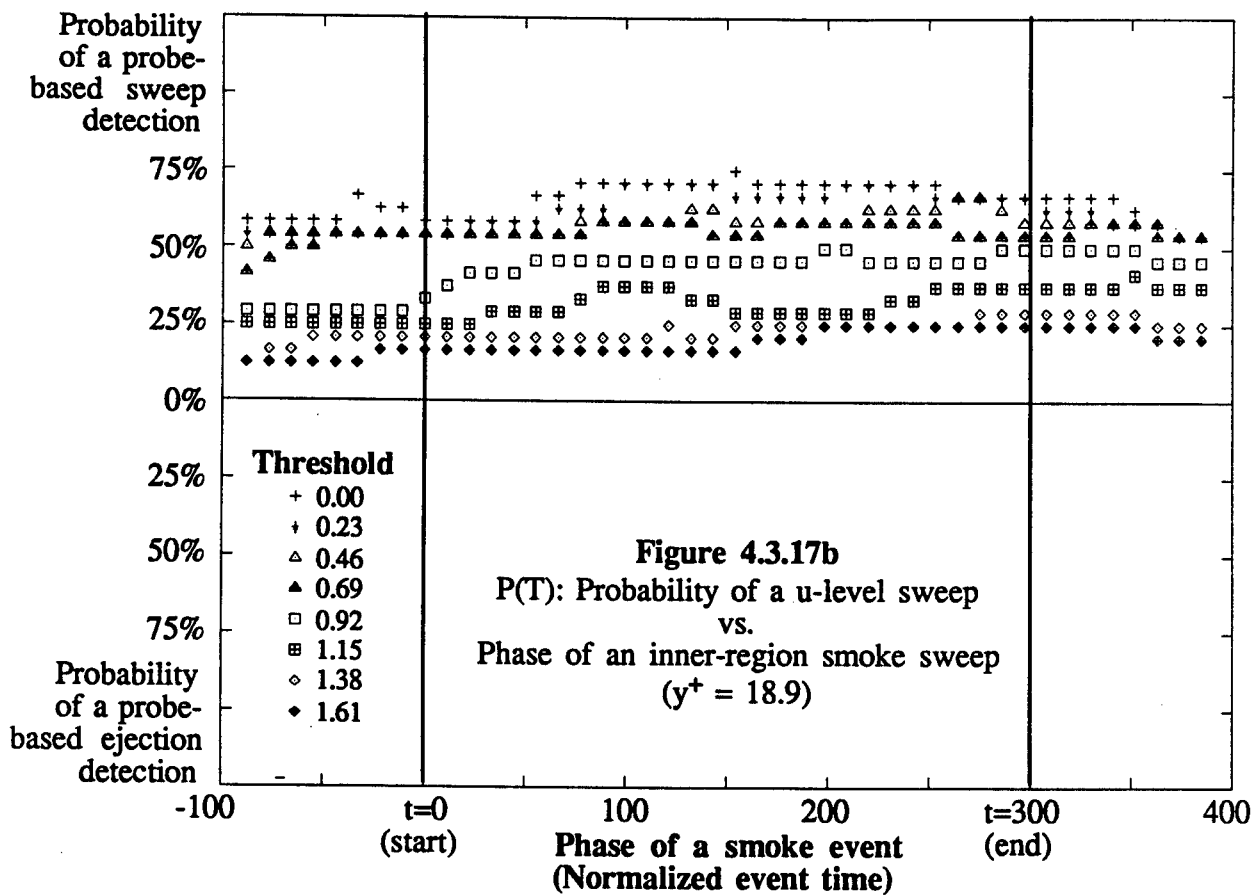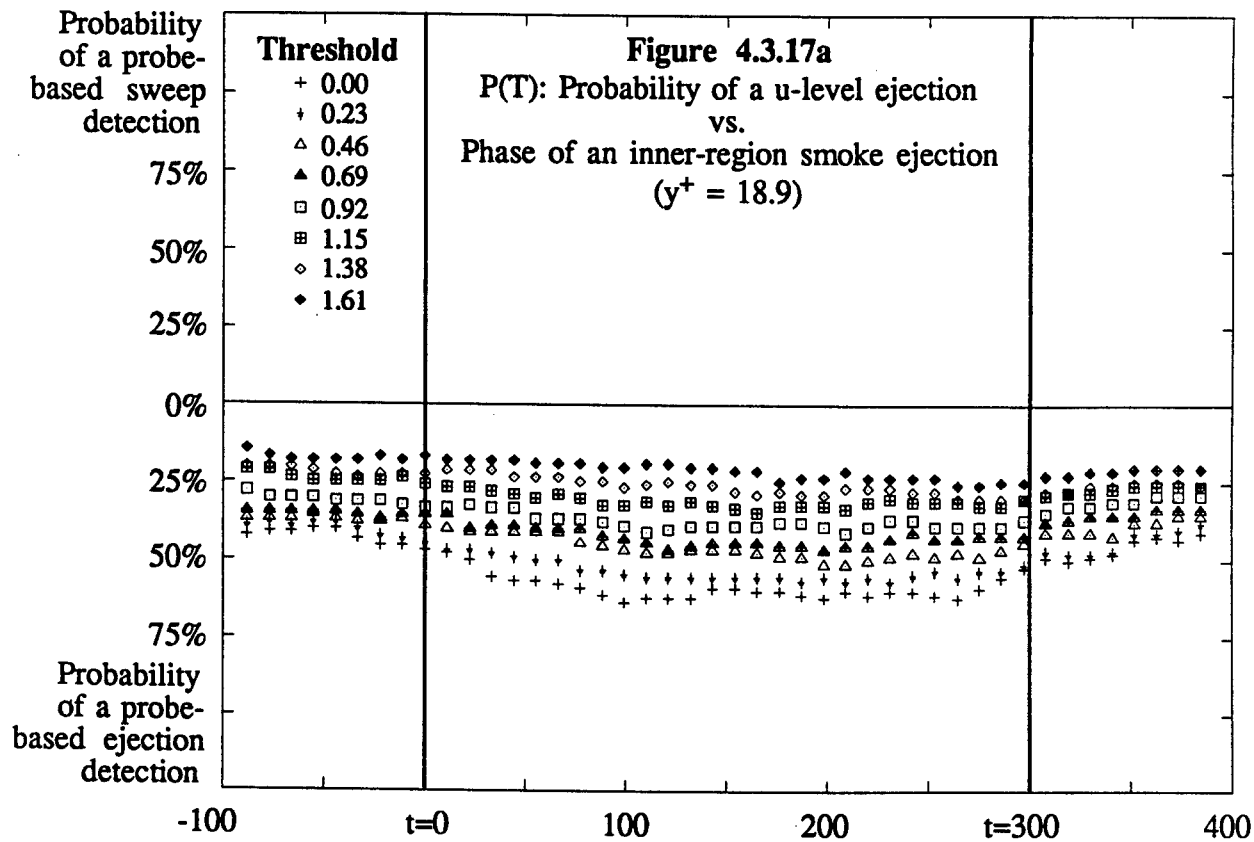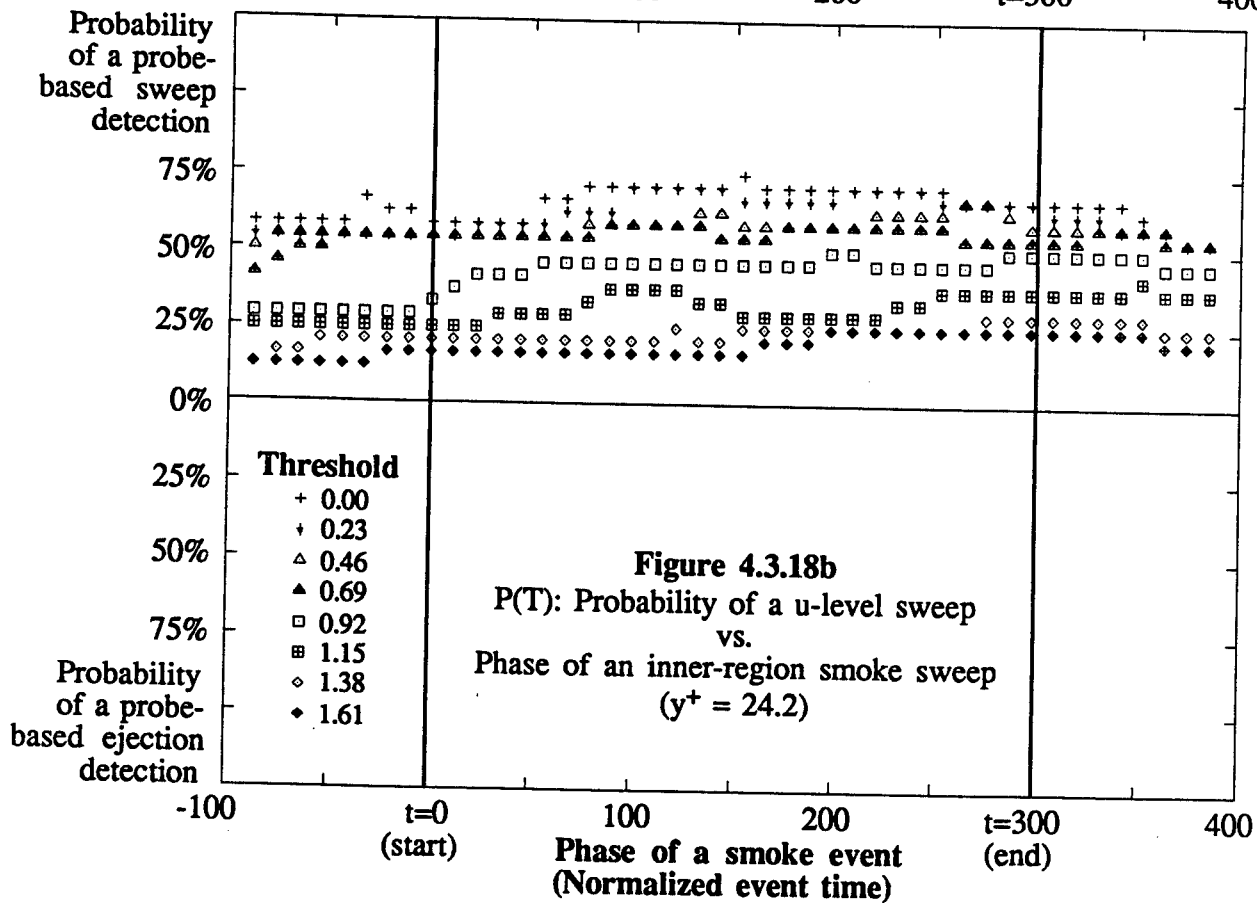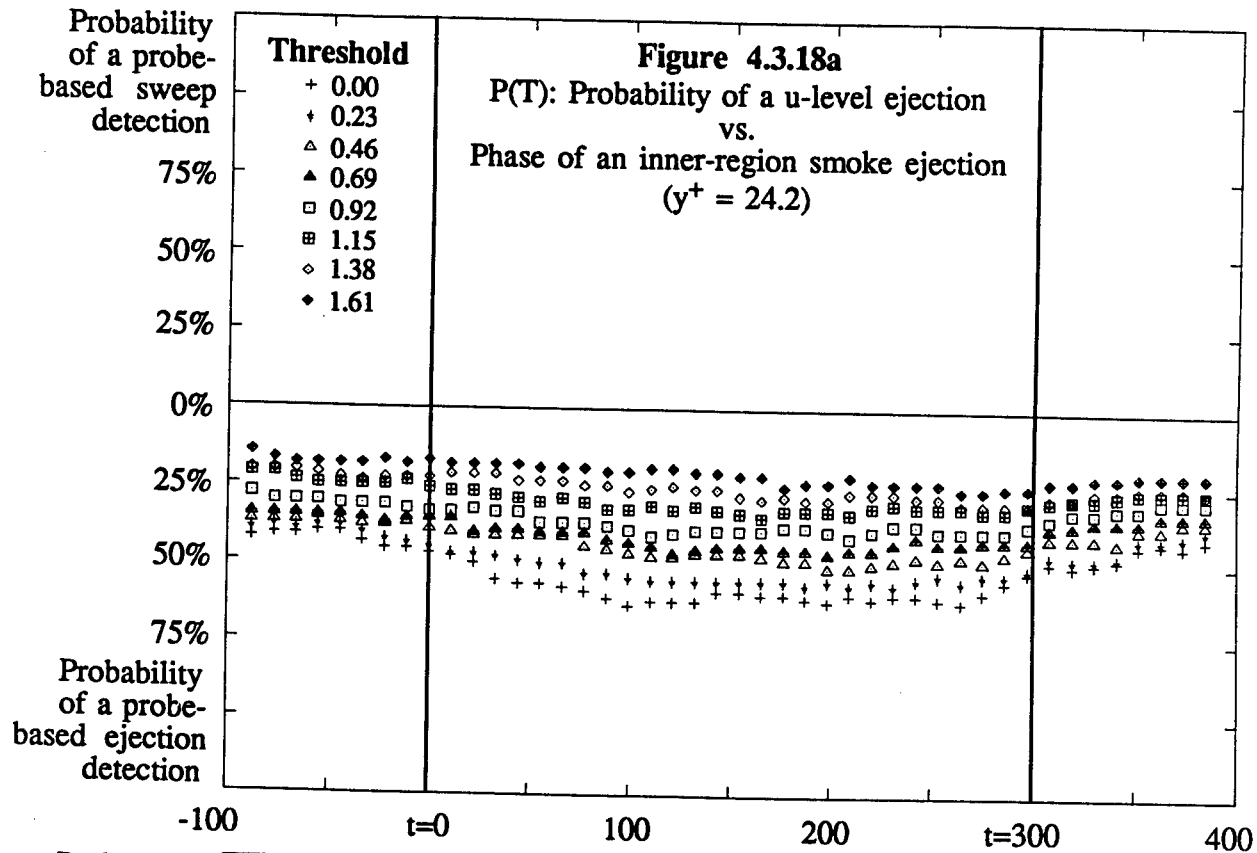Phase of a smoke event
(Normalized event time)

REFERENCES

Alfredsson, P. H. and Johansson, A. V. 1984 On the Detection of Turbulence-Generating Events. *J. Fluid Mech* **139**, 325.

Blackwelder, R. F. and Haritonidis, J. H. 1983 Scaling of the Bursting Frequency in Turbulent Boundary Layers. *J. Fluid Mech* **132**, 87.

Blackwelder, R. F. and Kaplan, R. E. 1972 Intermittent Structures in Turbulent Boundary Layers. **NATO-AGARD CP 93**. Technical Editing and Reproduction, London.

Blackwelder, R. F. and Kaplan, R. E. 1976 On the Wall Structure of the Turbulent Boundary Layer. *J. Fluid Mech* **76**, 89.

Bogard, D. G. 1982 **Investigation of Burst Structures in Turbulent Channel Flows Through Simultaneous Flow Visualization and Velocity Measurements.** Ph.D. dissertation, Purdue University, West Lafayette, Indiana.

Bogard, D. G. and Tiederman, W. G. 1986 Burst Detection with Single-Point Velocity Measurements. *J. Fluid Mech* **162**, 389.

Brodkey, R. S., Wallace, J. M., and Eckelman, H. 1974 *J. Fluid Mech* **63**, 209.

Browne, L. W. B., Antonia, R. A. and Chua, L. P. 1989 *Experiments in Fluids* **7**, 201.

Corino, E. R. and Brodkey, R. S. 1969 *J. Fluid Mech* **37**, 1.

Economikos, L., Shoemaker, C., Russ, K., Brodkey, R. S., and Jones D. 1990 Toward Full-Field Measurements of Instantaneous Visualizations of Coherent Structures in Turbulent Shear Flows. *Experimental Thermal and Fluid Science* **3**, 74.

Falco, R. E. 1974 Some Comments on Turbulent Boundary Layer Structure Inferred from the Movements of a Passive Contaminant. AIAA Paper 74-99.

Falco, R. E. 1977 Coherent Motions in the Outer Region of Turbulent Boundary Layers. *Physics of Fluids* **20**, 124.

Falco, R. E., Chu, C. C., Hetherington, M. H., and Gendrich, C. P. 1988 Circulation of an Airfoil Starting Vortex Obtained From Instantaneous Vorticity Measurements Over an Area. AIAA Paper 88-3620-CP, July, 1988.

Falco, R. E. and Gendrich, C. P. 1989 The Turbulence Burst Detection Algorithm of Z. Zaric', in **Near Wall Turbulence**, (ed. S. J. Kline) Hemisphere Press, 1989.

Foss, J. F., Klewicki, C. L. and Disimile, P. J. 1986 **NASA CR 178098.**

Gendrich, C. P., Falco, R. E., and Klewicki, J. C. 1989 Comparison of Event Detection Schemes Used in Both the Inner and Outer Regions of Turbulent Boundary Layers. Presented at the 42nd Annual Meeting of the Division of Fluid Dynamics of the American Physical Society, November, 1989.

Hinze, J. O. 1975 **Turbulence**. McGraw-Hill, Inc.

Kim, H. T., Kline, S. J., and Reynolds, W. C. 1971 *J. Fluid Mech* **50**, 133.

Klewicki, J. C. 1989 **On the Interactions Between the Inner and Outer Region Motions in Turbulent Boundary Layers**. Ph.D. dissertation, Michigan State University, East Lansing, Michigan.

Kline, S. F., Reynolds, W. C., Schraub, F. A. and Runstadler, P. W. 1967 *J. Fluid Mech* **30**, 741.

Kline, S. J. 1988 Quasi-Coherent Structures in the Turbulent Boundary Layer: Part I. Status Report on a Community-wide Summary of the Data. Private communication resulting from the Zoran P. Zaric' Memorial International Seminar on Near-Wall Turbulence, May, 1988.

Kline, S. J. and Falco, R. E. (eds.) 1980 Summary of the AFOSR/MSU Research Specialists Workshop on Coherent Structure in Turbulent Boundary Layers. **AFOSR TR 80-0290.**

Laufer, J. 1975 *Ann. Rev. Fluid Mech.* **7**, 307.

Lovett, J. A. 1982 The Flow Fields Responsible for the Generation of Turbulence Near the Wall in Turbulent Shear Flows. M.S. thesis, Michigan State University, East Lansing, Michigan.

Lu, S. S. and Willmarth, W. W. 1973 Measurements of the Structure of Reynolds Stress in a Turbulent Boundary Layer. *J. Fluid Mech* **60**, 481.

Luchik, T. S. and Tiederman, W. G. 1987 Timescale and Structure of Ejections and Bursts in Turbulent Channel Flows. *J. Fluid Mech* **174**, 529.

Offen, G. R. and Kline S. J. 1973 *Dept Mech. Engineering, Stanford University, Report* **TMC-4**.

Rao, K., Narasimha, R. and Badri Narayanan, M. A. 1971 *J. Fluid Mech* **48**, 339.

Signor, D. B. 1982 A Study of Intermediate Scale Motions in the Outer Region of Turbulent Boundary Layers. M.S. thesis, Michigan State University, East Lansing, Michigan.

Subramanian, C. S., Rajagopalan, S., Antonia, R. A., and Chambers, A. J. 1982 Comparison of Conditional Sampling and Averaging Techniques in a Turbulent Boundary Layer. *J. Fluid Mech* **123**, 335.

Tennekes, H. and Lumley, J. 1972 A First Course in Turbulence. MIT Press.

Wallace, J. M., Eckelmann, H. and Brodkey, R. S. 1972 The Wall Region in Turbulent Shear Flow. *J. Fluid Mech* **54**, 39.

Wark, C. E., Offutt, P. W., and Adrian, R. J. 1990 Structure of Turbulence Using PIV in Wall-Bounded Shear Flow. Presented at the 43rd Annual Meeting of the Division of Fluid Dynamics of the American Physical Society, November, 1990.

Wei, T. and Willmarth, W. W. 1990 Reynolds Number Effects on the Structure of a Turbulent Channel Flow. Accepted for publication in *J. Fluid Mech.*

Willmarth, W. W. and Lu, S. S. 1972 Structure of the Reynolds Stress Near the Wall. *J. Fluid Mech* **55**, 65.